Role of Cavitation, Surfactants, and their Synergism in Transdermal Sonophoresis

by

Baris E. Polat

Bachelor of Science in Chemical Engineering
Carnegie Mellon University

Submitted to the Department of Chemical Engineering in partial fulfillment of the requirements of the degree of

Doctor of Philosophy in Chemical Engineering

at the

MASSACHUSETTS INSTITUTE OF TECHNOLOGY

June 2011

Author.....
Department of Chemical Engineering
May 16, 2011

Certified by.....
Daniel Blankschtein
Professor, Thesis Supervisor

.....
Robert Langer
Institute Professor, Thesis Supervisor

Accepted by.....
William M. Deen
Professor of Chemical Engineering
Chairman, Committee for Graduate Students

Role of Cavitation, Surfactants, and their Synergism in Transdermal Sonophoresis

by

Baris E. Polat

Submitted to the Department of Chemical Engineering on May 16, 2011
in partial fulfillment of the requirements of the degree of
Doctor of Philosophy in Chemical Engineering

Abstract

The research described in this thesis represents a significant advancement in the current mechanistic understanding of low-frequency ultrasound-mediated transdermal drug delivery. Specifically, while prior research has focused on a more general understanding of the mechanisms associated with low-frequency sonophoresis (LFS), this thesis directly investigates the mechanisms associated with phenomena that occur due to LFS skin treatment. These include a deeper understanding of: i) the reasons for heterogeneous perturbation of skin treated with LFS, ii) the physical mechanism that causes synergism between LFS and chemical penetration enhancers (CPEs), iii) the interactions between traditional and non-traditional surfactants in LFS skin treatments, and iv) the effects of LFS and LFS/CPEs on skin structural perturbation.

In the first study of this thesis, the intrinsic properties and formation mechanisms of localized-transport regions (LTRs), and the surrounding less-perturbed non-LTRs, of low-frequency sonophoresis-treated skin are investigated. By independently analyzing LTR, non-LTR, and total skin samples treated at multiple LFS frequencies, it was found that the pore radii (r_{pore}) within non-LTRs are *frequency-independent*, ranging from 18.2 – 18.5 Å, but significantly larger than r_{pore} of native skin samples (13.6 Å). Conversely, r_{pore} within LTRs *increases significantly with decreasing frequency* from 161 Å, to 276 Å, and to ∞ (>300 Å) for LFS/SLS-treated skin at 60 kHz, 40 kHz, and 20 kHz, respectively. These findings suggest that different mechanisms contribute to skin permeability enhancement within each skin region. Therefore, it was proposed that the enhancement mechanism within LTRs is the *frequency-dependent process* of cavitation-induced microjet collapse at the skin surface, while the increased r_{pore} values in non-LTRs are likely due to SLS perturbation, with enhanced penetration of SLS into the skin resulting from the *frequency-independent process* of acoustic streaming.

Next, the effects of a non-traditional surfactant on LFS treatment were analyzed through a case study with the commonly used fluorescent dye sulforhodamine B (SRB). SRB is often considered to be a purely hydrophilic molecule, having no impact on bulk or interfacial properties of aqueous solutions. However, it was demonstrated that SRB is in fact an amphiphile, with the ability to adsorb at an air/water interface and to incorporate into sodium lauryl sulfate (SLS) micelles. In fact, SRB reduced the surface tension of water by up to 23 mN/m, and the addition of SRB to an aqueous SLS solution was found to induce a significant decrease in the critical micelle concentration (cmc) of SLS. Molecular dynamics revealed that SRB has defined polar "head" and non-polar "tail" regions when adsorbed at the air/water interface as a monomer. These findings have significant implications into LFS-mediated transdermal drug delivery, as the inclusion of SRB into an LFS coupling solution can cause a synergistic increase in skin permeability enhancement. However, in the presence of SLS, SRB actually causes an antagonistic effect due to the resulting change in bulk and interfacial properties.

The next investigation of this thesis focused on understanding the synergism between LFS and CPEs (e.g., surfactants). In spite of identifying that the origin of this synergism is the increased penetration and subsequent dispersion of CPEs in the skin in response to LFS treatment, no prior study had proposed a mechanism to explain *how* LFS induces the observed increased transport of CPEs. In this study, a physical mechanism by which the transport of *all* CPEs is expected to have significantly increased flux into the localized-transport regions (LTRs) of LFS-treated skin was proposed. Specifically, the collapse of acoustic cavitation microjets within LTRs was shown to induce a convective flux. In addition, because amphiphilic molecules are able to adsorb onto the gas/water interface of cavitation bubbles, amphiphiles were shown to have an additional adsorptive flux. In this sense, the cavitation bubbles were shown to effectively act as carriers for amphiphilic molecules, delivering surfactants directly into the skin when they collapse at the skin surface as cavitation microjets. The flux equations derived for the LTRs and non-LTRs of LFS-treated skin, compared to that for untreated skin, explained how the transport of all CPEs, and to an even greater extent amphiphilic CPEs, increases during LFS treatment. The flux model was supported with experiments involving a non-amphiphilic CPE (propylene glycol) and both nonionic and ionic amphiphilic CPEs (octyl glucoside and SLS), by measuring the flux of each CPE into untreated skin and the LTRs and non-LTRs of LFS-treated skin. Data showed excellent agreement with the expected trends from the flux model.

The final study of this thesis investigated the effect of SLS on skin structural perturbation when utilized simultaneously with LFS. Pig full-thickness skin (FTS) and pig split-thickness skin (STS) treated with LFS/SLS and LFS were analyzed in the context of the aqueous porous pathway model to quantify skin perturbation through changes in skin pore radius and porosity-to-tortuosity ratio (ε/τ). In addition, skin treatment times required to attain specific levels of skin electrical resistivity were analyzed to draw conclusions about the effect of SLS on reproducibility and predictability of skin perturbation. It was found that LFS/SLS-treated FTS, LFS/SLS-treated STS, and LFS-treated FTS exhibited similar skin perturbation. However, LFS-treated STS exhibited significantly higher skin perturbation, suggesting greater structural changes to the less robust STS induced by the purely physical enhancement mechanism of LFS. Evaluation of ε/τ values revealed that LFS/SLS-treated FTS and STS have similar transport pathways, while LFS-treated FTS and STS have lower ε/τ values. In addition, LFS/SLS treatment times were much shorter than LFS treatment times for both FTS and STS. Moreover, the simultaneous use of SLS and LFS not only results in synergistic enhancement, as reflected in the shorter skin treatment times, but also in more predictable and reproducible skin perturbation.

In conclusion, the research conducted in this thesis has contributed to the advancement of the molecular and cellular-level understanding of phenomena associated with LFS-mediated transdermal skin permeability enhancement. Additionally, the insights provided by this thesis could lead to the development of optimized LFS treatment protocols and improved LFS coupling solution formulations. This would permit attaining the desired skin permeability using milder LFS treatment conditions and smaller skin treatment areas. This could also lead to lower power requirements of LFS devices, thereby leading to miniaturization of devices and the creation of more commercially-viable LFS equipment.

Thesis Advisor: Daniel Blankschtein
Title: Professor of Chemical Engineering

Thesis Advisor: Robert Langer
Title: David H. Koch Institute Professor

Acknowledgements

There are many people to thank that have contributed to the completion of this thesis. First, I would like to acknowledge the tremendous impact of my advisors, Professor Daniel Blankschtein and Professor Robert Langer. I have learned from Professor Blankschtein to be thorough and critical in both research and writing. He has invested a tremendous amount of time and effort in the completion of this thesis, for which I am immeasurably grateful. From Professor Langer I have learned to think in terms of the big picture, to believe in the science and technologies I have worked on, and to not be afraid of asking, and attempting to answer, difficult problems. Although my advisors are vastly different in the way in which they operate, they complement each other perfectly, and I could not imagine a better situation in which to have done my doctoral research than under the mutual guidance of Professor Blankschtein and Professor Langer.

Secondly, I would like to thank my committee members, Professor William Deen, Professor Douglas Hart, and Dr. Joseph Kushner IV, for the time they have invested, and support they have provided, during my thesis work at MIT. Each have contributed to my scientific and professional development, as well as in improving the quality of the research presented in this thesis. I would also like to thank my friends, colleagues, and collaborators for their important role during my time here at MIT. To the person I consider my closest friend in the lab, Jonathan Mendenhall, life at MIT over the last five years would not have been as enjoyable without our meaningless, and sometimes meaningful, conversations. Special thanks to my fellow transdermal team member, Jennifer Seto, I believe we have achieved quite a bit over our time at MIT, which I do not think would have been possible had either of us worked on this project alone. I would also like to thank all my colleagues and collaborators at MIT, including those in the Blankschtein

Lab: Jaisree Iyer, Shangchao Lin, Srinivas Moorkanikkara, Brian Stephenson, Diviya Sinha, Carl Schoellhammer, Chih-Jen Shih, and Vishnu Sresht; those in the Langer Lab: Avi Schroeder, Giovanni Traverso, Gizem Orbey, Chris Alabi, and Hila Epstein-Barash; my UROP, Pedro Figueroa Albertorio; and my collaborator in the chemistry department, Brett VanVeller. All of these people have had a tremendous, positive impact on me, both professionally and personally.

Most importantly, however, I would like to express my deepest gratitude to my incredible family. The two people who have had the greatest impact on me becoming the person that I am today, of course, are my parents, Suna and Osman. Over my entire life you never let me doubt my ability to accomplish anything I put my mind to, and you have always given me every opportunity in your power to allow me to reach my goals. I can honestly say that without you, I would not be where I am today. I would also like to thank my sister, Bikem. I am proud to be your brother and I hope that I have been a positive influence in your life.

To my wife, Julia, I cannot express in words how much you mean to me and how important you are to me in every way. When we both began graduate school, we were young, naïve, newlyweds, and I am still amazed at how much we have accomplished together over the last six years. I know that together, we will be able to accomplish anything we want, but most importantly, we will do it together. I would also like to thank my wonderful in-laws, Elena and Sergey, for always being there for us. And finally, to my beautiful, intelligent daughters, Laila and Serra: You have been the joy of my life over the last 4 years. There is nothing that has provided me more pleasure and pride than being your father and coming home to your smiling faces each and every day. You have changed my life in so many positive ways. This thesis is dedicated to both of you.

Table of Contents

List of Figures

List of Tables

Chapter 1
Introduction

1.1 Transdermal Delivery

The transdermal route provides an attractive alternative method of drug administration compared to oral delivery and hypodermic injections. With respect to oral delivery, advantages include: (i) minimization of first-pass metabolic effects, (ii) bypassing of the harsh gastro-intestinal tract that can cause degradation or denaturing of macromolecules, and (iii) decreased side effects from dyspeptic drugs.[1, 2] Furthermore, advantages of transdermal delivery over hypodermic injections include: (i) non-invasive delivery, (ii) decreased pain and increased patient compliance, (iii) decreased generation of dangerous medical sharps, and (iv) less risk of needle contamination, disease transmission, and needle misuse.[1, 2] Transdermal delivery also allows for sustained release profiles for both systemic and localized drug delivery, which is not always possible with oral or injectable formulations. However, the innate structure of the skin provides a very robust barrier to drug delivery. In fact, only very small and hydrophobic molecules, such as clonidine, estradiol, fentanyl, nicotine, nitroglycerine, scopolamine, and testosterone, have been successfully administered at therapeutic levels through intact skin.[1, 2] This has led to the so-called "500 Dalton Rule", which states that for a drug to be deliverable through native skin, it

must have a molecular weight of less than 500 Daltons and, in general, be hydrophobic.[3] The reason for these limitations is that the primary barrier for transdermal transport is the outermost layer of the epidermis, the stratum corneum, which is typically only 10-20 μm in thickness (see Figure 1-1). The stratum corneum is a non-viable cell layer that is comprised of highly-crosslinked keratinocytes (or corneocytes), embedded in a continuous matrix of skin lipids (see Figure 1-2).

To increase the permeability of skin, one can generally use one of two approaches. First, if the drug being administered is sufficiently small, chemical modification can be utilized to increase its lipophilicity, without directly affecting the structure of the skin.[4] Furthermore, one can also increase the driving force for permeation using various strategies, including supersaturation of the delivery vehicle, increasing the vehicle-to-skin partition coefficient, or by electroosmotic flow induced by iontophoresis, without directly affecting the skin structure.[5] Conversely, one can use a chemical or physical enhancer to decrease the barrier properties of the skin without modifying the drug itself. Chemical enhancers include molecules such as surfactants or oils, and operate by denaturing keratinocytes, disordering/fluidizing lipid bilayers, or creating segregated phases in the stratum corneum.[1, 2] There are many types of physical enhancers for transdermal delivery, such as iontophoresis (application of a continuous, low-voltage electric field),[6] electroporation (application of pulsed, high-voltage electricity),[6] thermal or laser ablation,[7] liquid or powder jet injectors,[8] or the use of high- or low-frequency ultrasound (sonophoresis). Low-frequency sonophoresis (LFS), in particular, offers advantages over other transdermal delivery methods. Specifically, with LFS, the extent of skin perturbation, and the resulting skin permeability enhancement, can be controlled by varying the application time and

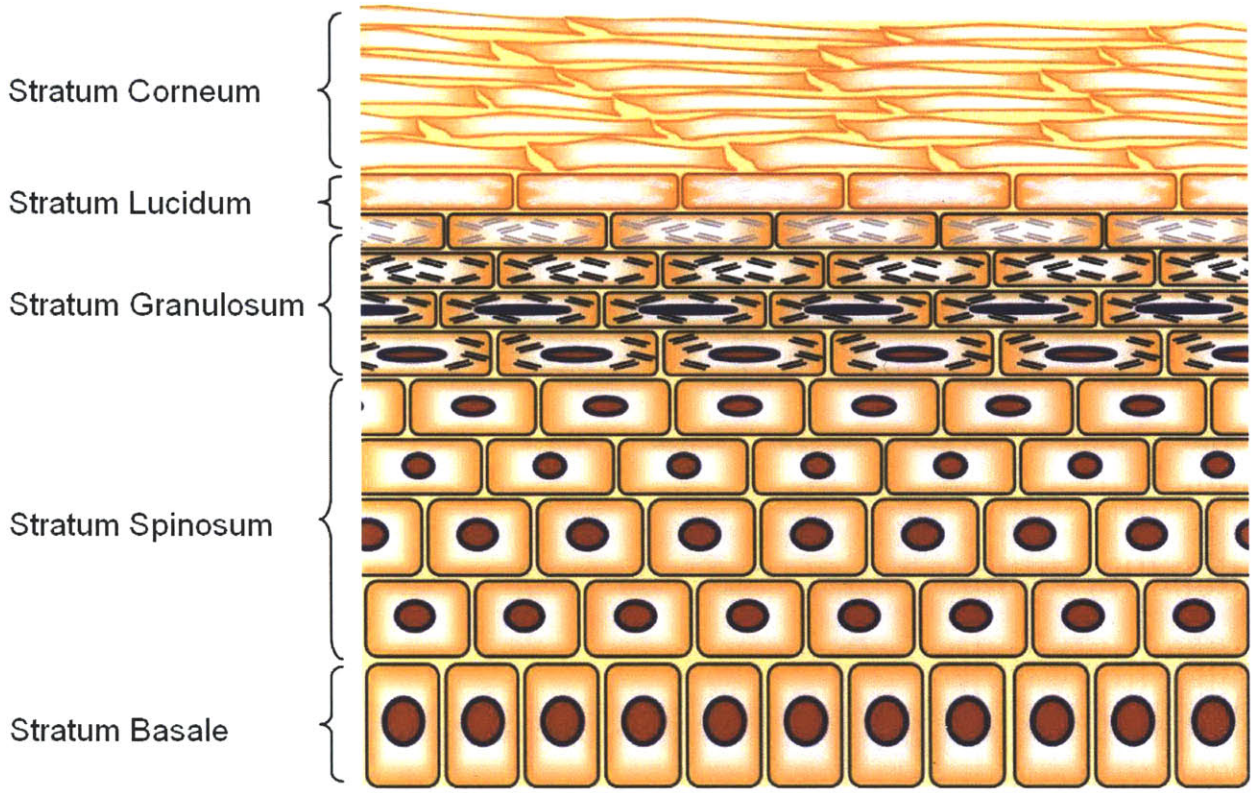

Figure 1-1. Cross-sectional schematic of the stratified layers of the epidermis. The stratum corneum provides the skin with the majority of its barrier properties, being comprised of anucleate corneocytes embedded in a lipid matrix. Legend: corneocytes ( ), keratinocytes with a nucleus ( ), keratinocytes containing granules ( ), and lipids ( ).

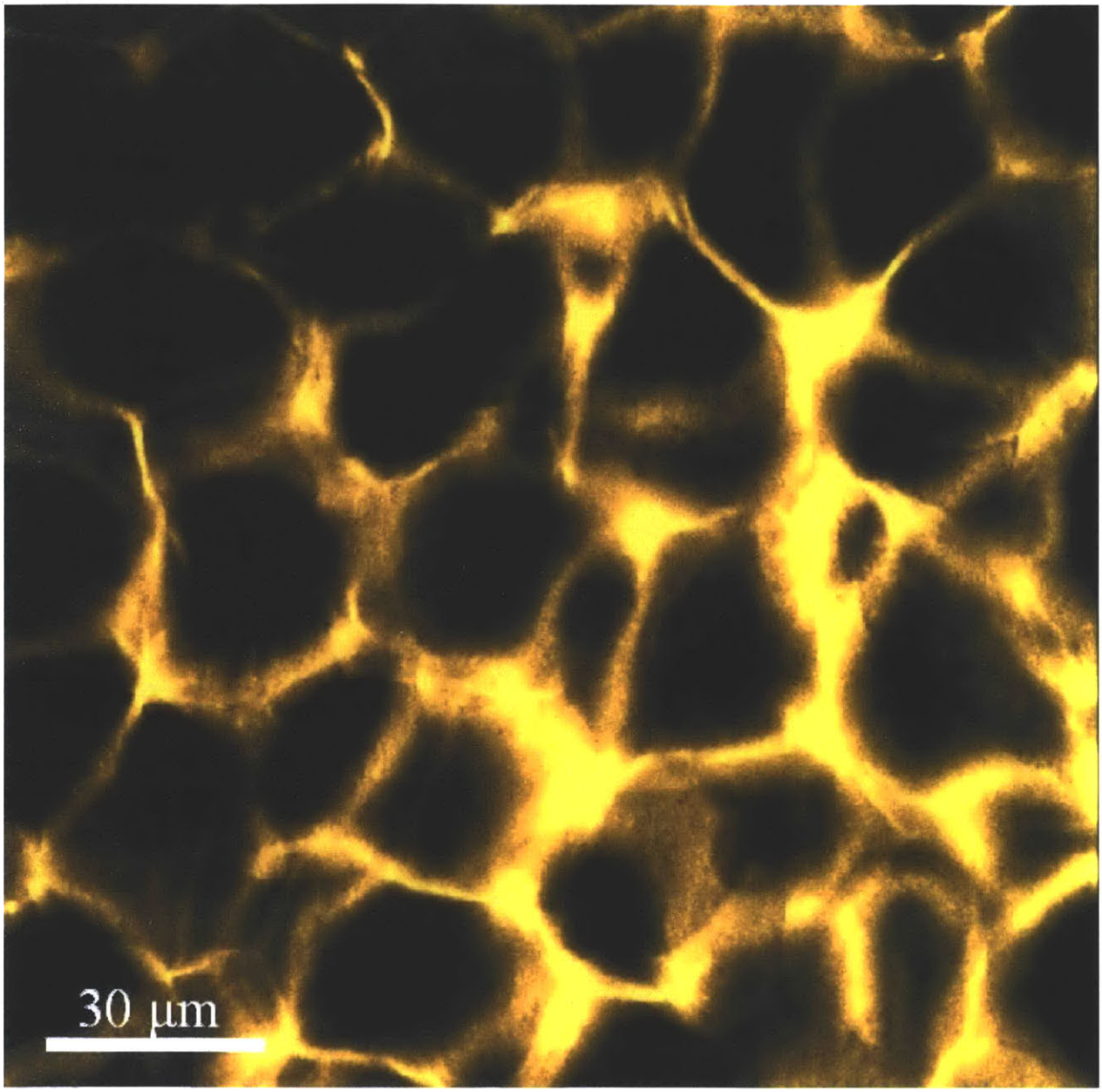

Figure 1-2. Two-photon microscopy image of the honeycomb structure of the stratum corneum. The lipid bilayers are stained with the fluorescent dye rhodamine B – hexyl ester. The dark, approximately hexagonal, regions are the highly cross-linked corneocytes, where the dye cannot penetrate deeply.

other ultrasound parameters.[9-13] Therefore, systemic, regional, and local delivery is possible with LFS. The size of aqueous skin pores created by LFS can also be controlled by varying the frequency and the intensity of the ultrasound utilized.[11, 14, 15] Moreover, LFS allows for pretreatment of the skin, prior to application of a drug-containing patch, so that the actual LFS treatment is only on the order of seconds and the device does not need to be worn constantly.[16-19] Finally, LFS has shown promise in delivering both macromolecules and hydrophilic permeants transdermally,[20, 21] as well as in non-invasively monitoring blood analytes, such as blood glucose.[22, 23]

1.1.1 Historical Perspective on Ultrasound-Mediated Transdermal Delivery

The use of ultrasound to deliver therapeutic compounds through the skin is generally referred to as sonophoresis (also known as phonophoresis)[24], and dates back to the 1950s.[25, 26] In these early studies, the most common applications involved the use of therapeutic or high-frequency sonophoresis (HFS, frequencies $\geq$ 0.7 MHz) for the local delivery of corticosteroids. HFS continued to be used for nearly four decades, with researchers investigating frequencies as high as 16 MHz.[27, 28] Typical skin penetration enhancements observed with HFS are between 1-10 fold.[20, 27, 29, 30] However, a crucial shift in the mechanistic understanding of sonophoresis occurred when the importance of acoustic cavitation was recognized.[28, 31-34] By exploiting the fact that cavitational effects exhibit an inverse relationship with ultrasound frequency,[35] Mitragotri *et al.* hypothesized that low-frequency sonophoresis (LFS), in the range 20 – 100 kHz, should be more effective than HFS in enhancing skin permeability.[20, 30]

In these studies, it was shown that LFS at 20 kHz is up to three orders of magnitude more effective than HFS at 1 MHz. In the past decade, research has focused primarily on the use of LFS for transdermal drug delivery, due to the much greater enhancement ratios attained at these lower frequencies, while research with HFS has focused on topical or regional delivery. More background into transdermal delivery can be found in the following reviews: [36-38].

1.2 Background

1.2.1 Ultrasound Basics and their Implications in Sonophoresis

An ultrasound wave is a longitudinal compression wave with frequency above that of the audible range of human hearing (above 20 kHz). Sound waves propagate by causing local oscillatory motion of particles in the medium through which they are traveling. As the wave displaces particles at a given location, the local density and pressure of the medium increases or decreases depending on whether that location is in a rarefaction (low pressure) or compression (high pressure) cycle of the wave.[39] Many interesting phenomena occur in aqueous solution due to the resulting oscillation between low and high pressure, which will be discussed in Section 1. 2.1.1.

Ultrasound waves are created by first generating an electric signal which is subsequently amplified before being sent to the ultrasound horn. Once the electric signal reaches the ultrasound horn, it is converted into a mechanical wave by piezoelectric crystals (which change their static dimensions in response to an electric field[40]) through the tip of the transducer, which is then transmitted to the desired medium. Two characteristics of ultrasound waves are most significant in sonophoresis: the amplitude and the frequency. The amplitude of the

ultrasound wave is proportional to the displacement of the ultrasound horn during each half cycle. The frequency of the ultrasound wave corresponds to the number of times that the transducer tip is displaced per second of application time. Commonly used frequencies for sonophoresis are generally separated into two groups: (i) low-frequency sonophoresis (LFS), which includes frequencies in the range 20 – 100 kHz, and (ii) high-frequency sonophoresis (HFS), which includes frequencies in the range 0.7 – 16 MHz (the range of both therapeutic and high-frequency ultrasound), but most commonly 1 – 3 MHz. This distinction is made because of the different mechanisms of enhancement associated with LFS and HFS, as discussed in Section 1.3. The range of frequencies between ~100 kHz and 700 kHz, which is referred to as intermediate ultrasound, is not included in either (i) or (ii) above because this range of frequencies has not been thoroughly investigated in the context of transdermal drug delivery, and therefore, the primary enhancement mechanisms are not as well understood. The most likely reason that LFS and HFS have been utilized historically for transdermal delivery applications, while intermediate ultrasound has not, is because of the lack of commercially available ultrasound equipment in the range 100 – 700 kHz.

Additional experimental variables that are important in sonophoresis include: i) the ultrasound duty cycle (ratio of the time that ultrasound is on), ii) the distance between the ultrasound horn and the skin (horn-to-skin distance), iii) treatment time, and iv) composition of the ultrasound coupling medium (the medium between the ultrasound horn and the skin, which can be an aqueous solution or a gel-like formulation). Commonly used ultrasound duty cycles are 10% (e.g., 0.1s ON and 0.9 s OFF),[10, 13, 20, 21, 30, 41-43] 50% (e.g., 5 s ON and 5 s OFF),[11, 14, 15, 23, 44-57] or continuous application.[12, 41, 58-62] Ultrasound pulsing is common because

it decreases thermal effects associated with ultrasound by allowing time for heat to dissipate from the coupling medium during the treatment. Many different horn-to-skin distances have been utilized in sonophoretic research, ranging from placing the ultrasound horn in contact with the skin (zero tip displacement) to as far as 4.0 cm from the skin surface.[11, 58] The most common tip displacements reported for use with LFS range from 0.3 cm to 1.0 cm.[9, 10, 12-15, 20, 21, 23, 30, 41, 42, 44-46, 48-56, 60, 62-69] With HFS, it is much more common to have smaller tip displacements, almost in contact with the skin, for reasons that will become clear when the enhancement mechanisms associated with HFS and LFS are discussed in Section 1.3. Treatment times can also vary greatly, from a few seconds,[17-19, 70] to a few minutes,[14, 15, 51, 56] or even to cases where steady-state is attained, which can take many hours to days.[13, 21, 71] Finally, formulation of the coupling medium is also a very important variable in sonophoresis. The viscosity, surface tension, density, acoustic impedance, and other bulk and interfacial properties of the coupling medium can all play significant roles in determining the extent of skin permeability enhancement observed as a result of the ultrasound treatment. Furthermore, the coupling medium can contain an active ingredient (e.g., a drug) or can include a chemical enhancer (co-enhancer), such as a surfactant. Because of the mechanisms associated with LFS and HFS (see Section 1.3), LFS coupling media are typically aqueous formulations, while HFS coupling media are typically gels. In both cases, the coupling solution has an acoustic impedance which is similar to that of the skin, such that there is no significant reflection of the ultrasound wave at the interface between the skin and the coupling medium. The mechanistic effects associated with the formulation used will be discussed further in Sections 1.3 and 1.4.

1.2.1.1 Acoustic Cavitation

Although all the mechanisms responsible for skin permeability enhancement by sonophoresis are not fully understood, it is generally accepted that the main contributor is acoustic cavitation, particularly in the case of LFS.[42, 59, 60, 72] The term cavitation can take multiple definitions depending on the source of the stress acting upon the system. Strictly speaking, cavitation is the process by which a liquid is pulled apart when it is acted upon by a force in excess of its tensile strength, causing the formation of voids in the system.[73] However, due to inhomogeneities in all real liquids, such as those induced by the presence of dissolved gases, microscopic gas bubbles, or other particulates, the theoretical tensile strength of a liquid is never observed in practice.[73] For this reason, cavitation in all systems is observed far below the theoretical limit, even in extremely purified liquids. This definition of cavitation is not well suited for systems involving acoustic pressure variations, as is the case with sonophoresis. Instead, acoustic cavitation can be loosely defined as the process by which any of the following occurs: i) small gas bubbles already present in a liquid pulsate or grow, ii) gas bubbles form in the bulk or on nuclei due to acoustic pressure variations, or iii) the occurrence of any other type of growth, splitting, or interaction of gas bubbles due to acoustic pressure oscillations in solution.[74]

Cavitation can be further divided into two types: stable and transient. Stable cavitation is defined as the pulsation of cavitation bubbles over many acoustic pressure cycles without collapse. Transient cavitation is defined as the rapid and uncontrolled growth of cavitation bubbles over several pressure cycles, eventually leading to their collapse into smaller bubbles or, if near a surface such as the skin, to the formation of a microjet.[75] A microjet results from the asymmetry in bubble collapse pressure near an interface. Depending on the properties of the

interface, the bubble can either generate a jet towards the interface, away from the interface, or collapse in an alternate shape.[76] The collapse of a cavitation bubble as a microjet directed towards the interface tends to occur near more rigid surfaces[76] and has been implicated in causing skin perturbation during LFS treatment.[14, 15, 54, 59] The growth of gaseous bubbles in response to ultrasound occurs by a process called rectified diffusion, which is discussed in Section 1.2.1.2.

It is important to stress that the resonant radius of cavitation bubbles exhibit an inverse relationship with the applied ultrasound frequency.[35] Specifically, the linear resonant bubble radius is defined by the equation $r_{res} = C / f$, where r_{res} and f are the resonant bubble radius and the applied ultrasound frequency, respectively, and C is a constant that depends on the properties of the solution in which cavitation is occurring.[35] Therefore, high-frequency ultrasound will generate bubble populations having smaller radii than low-frequency ultrasound. For example, the linear resonant bubble radius of an air bubble in water, which is assumed to be incompressible and inviscid, for ultrasound at 20 kHz is 150 μm, while at 3 MHz it is only 1 μm (see the equation above).[77, 78] The average size of cavitation bubbles in a given system will dictate where cavitation can occur in that system. For example, if the resonant bubble radius is larger than the dimensions of the skin voids available for cavitation to occur, it is unlikely that cavitation within the skin itself can play a significant role in skin permeability enhancement.[79] Therefore, cavitation within the skin is much more likely to occur with HFS, when the resonant bubble radius is on the order of microns or smaller, rather than with LFS. This will be discussed further in Section 1.3. Moreover, Ueda *et al.* have shown, through acoustic spectroscopy measurements, that the amount of transient cavitation generated in the coupling medium between

the ultrasound horn and the skin membrane increases with decreasing ultrasound frequency, in the range 41 kHz – 445 kHz.[62] This suggests that not only cavitation bubble size, but also transient cavitation itself increases with decreasing ultrasound frequency, which has implications on the level of enhancement that can be achieved at lower ultrasound frequencies, relative to higher ultrasound frequencies (see discussion on mechanisms in Section 1.3).

1.2.1.2 Rectified Diffusion

Cavitation cannot be thought of as an isolated phenomenon, because it is strongly linked to many other processes that cause unique behavior in acoustically cavitating systems. For example, the process of rectified diffusion causes oscillating cavitation bubbles to grow under an acoustic pressure field.[80, 81] It is this growth and the eventual collapse of cavitation bubbles that is believed to cause skin permeability enhancement during LFS.[59] During rectified diffusion, a bubble encountering a negative-pressure half-cycle of an acoustic field will grow due to the expansion of the gas inside the bubble. In addition, some of the liquid surrounding the bubble will diffuse through the boundary layer and vaporize, causing the amount of gas in the bubble to increase. In the subsequent positive-pressure half-cycle, the bubble will collapse to a size which is much smaller than that in its previous state. Depending on the temperature and the composition of the gas and liquid phases, some of the vapor will condense and join the liquid phase surrounding the bubble. This process favors bubble growth for two main reasons: (i) the "area" effect, and (ii) the "shell" effect.[82] The "area" effect simply occurs because the surface area of a bubble in the expanded state is much greater than in the collapsed state. Therefore, there is much greater area for diffusion into the bubble to occur in the expanded state than for diffusion out of the bubble to occur in the collapsed state. The "shell" effect occurs due to the

existence of a diffusion boundary layer (see Figure 1-3), or shell, through which gas or vapor transfers between the gas phase of the bubble and the surrounding liquid phase. When the bubble is in an expanded state and the concentration of gas in the bubble is at its lowest point (Figure 1-3, right-hand side), the shell is thin and, therefore, there is a larger concentration gradient for diffusion into the bubble. Conversely, in the collapsed state, the boundary layer is thicker, because of the rapid collapse of the bubble, and therefore, the driving force for diffusion out of the bubble decreases. Opposing the forces of bubble growth is the Laplace pressure, caused by the surface tension of the bubble. The Laplace pressure, ΔP_L, is given by: $\Delta P_L = 2\gamma/r$, where γ and r are the surface tension and radius of the gas bubble, respectively. If the radius of the gas bubble is exceedingly small, the Laplace pressure will be extremely large, causing the gas bubble to dissolve back into the bulk phase once the ultrasound is turned off.[83] In this respect, the duty cycle of the applied ultrasound can also play an important role. If the pulse rate is rapid, cavitation bubbles may not have sufficient time to grow, and therefore, when the ultrasound is in the OFF period of the duty cycle, bubbles may dissolve back into the solution,[84] and will be unable to contribute to skin permeability enhancement in subsequent cycles.

Rectified diffusion is most important to cavitation when the amount of liquid vaporized in the negative-pressure half-cycle is greater than the amount of vapor condensing in the positive-pressure half-cycle. In this case, there is net growth of the bubble through each consecutive pressure cycle of the acoustic wave. If this process proceeds quickly, with rapid bubble growth over a few cycles, the event is considered a transient cavitation bubble and the bubble will either collapse in the bulk or can generate a microjet near an interface.[75] The occurrence of transient

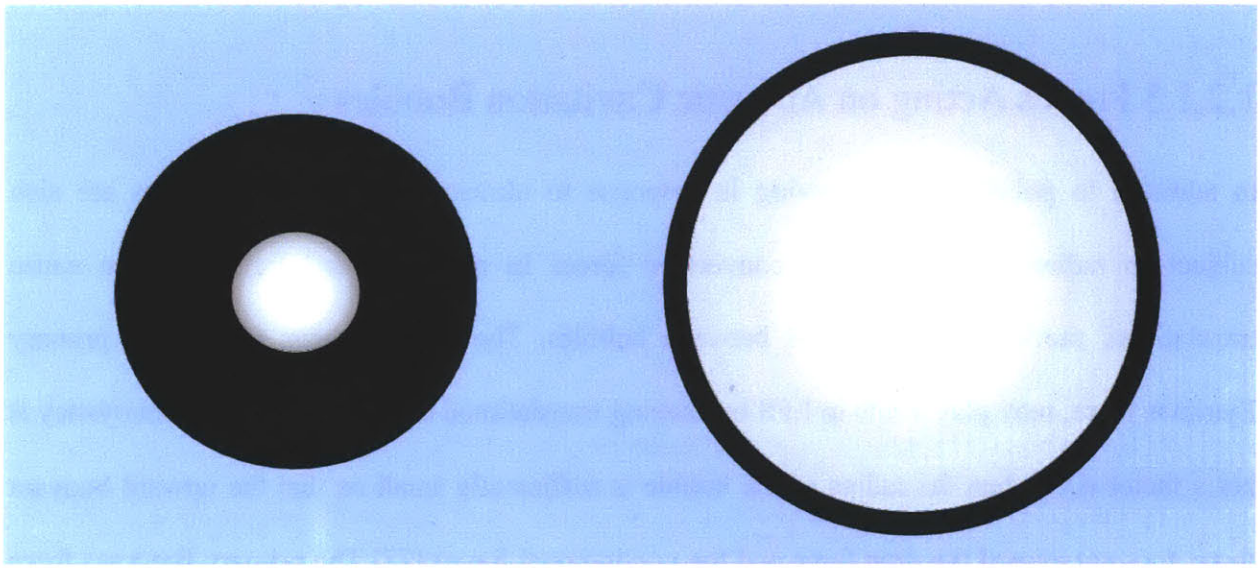

Figure 1-3. Relative thickness of the diffusion boundary layer (in black) of a spherical cavitation bubble in the collapsed state (in the compression cycle, left) and in the expanded state (in the rarefaction cycle, right).

cavitation depends on the ultrasound frequency, its amplitude, and the size of the cavitation bubble.[78] On the other hand, if this process proceeds slowly and an equilibrium is reached, a stable cavitation bubble will result and the bubble will continue to oscillate during many pressure cycles.[82, 85] The importance of transient and stable cavitation to ultrasound-induced skin permeability enhancement will be discussed further in Section 1.3.

1.2.1.3 Forces Acting on Acoustic Cavitation Bubbles

In addition to pulsating and growing in response to ultrasound, cavitation bubbles are also subject to radiation pressure and convective forces in an ultrasound field that can cause translational motion or interactions between bubbles. The first of these forces, the primary Bjerknes force, may play a role in LFS by causing translational bubble motion when buoyancy is not a factor (i.e. when the radius of the bubble is sufficiently small so that the upward buoyant force does not exceed the drag force and the gravitational force).[77] The primary Bjerknes force occurs as a result of the coupling of bubble oscillation with the applied acoustic pressure gradient. It causes bubbles that are smaller than the resonant bubble radius, at the applied frequency, to move up pressure gradients, or towards pressure antinodes, and bubbles that are larger than the resonant bubble radius to move down pressure gradients, or towards pressure nodes.[77] The effect of the primary Bjerknes force can be beneficial to LFS because, under typical operating conditions, the distance between the ultrasound transducer and the skin is less than one-fourth of the ultrasound wavelength, λ (in water at 20 kHz, λ = 7.5 cm), corresponding to the first pressure antinode ($\lambda/4 \sim 1.9$ cm). Therefore, any small bubble produced in the coupling medium between the ultrasound transducer and the skin will tend to move towards the surface of the skin as a result of this force. Even more significant than the primary Bjerknes

force, however, is acoustic streaming, which is the convection-induced motion of cavitation bubbles due to the movement of the ultrasound horn itself.[73] Acoustic streaming causes the bulk fluid to move in the direction of the applied ultrasound field, which in the case of LFS is towards the skin surface. This causes smaller bubbles, which do no experience significant buoyancy, to also move towards the surface of the skin. Furthermore, this bulk fluid movement causes rigorous mixing of the coupling medium, which can have implications on enhancing mechanisms in areas of the skin where cavitation microjets do not occur (see Section 1.4.1).[24] This also implies that, at higher ultrasound intensities, when bubbles grow rapidly and larger bubbles are formed, bubbles will collect at the surface of the ultrasound transducer due to buoyancy, causing decreased process efficiency (which has been observed in practice[11]).

A second force of interest in LFS is what is referred to as the secondary Bjerknes force. This force can cause the mutual attraction or repulsion of oscillating cavitation bubbles, and occurs as a result of the coupling of the sound field emitted by each oscillating bubble.[86, 87] However, the secondary Bjerknes force can also cause other, higher-order, phenomena such as acoustic streamers (the formation of stable pairs of bubbles that oscillate about an equilibrium distance from each other and move through an ultrasound field) and cavitation bubble clouds (localized collections of cavitation bubbles in an ultrasound field).[88-90] These phenomena may be significant in sonophoresis, particularly with respect to the recently recognized heterogeneous transport observed with LFS, as localized collections of cavitation bubbles may induce skin perturbation solely in discrete regions (see Section 1.4.1).[51, 54]

1.2.2 Modes of Skin Treatment with Sonophoresis

Ultrasound is applied to skin primarily in one of two ways: i) as a pretreatment of the skin prior to contact with a drug or permeant (which will hereafter be referred to as "pretreatment"), or ii) as a simultaneous application of ultrasound through a coupling medium containing the drug or permeant (which will hereafter be referred to as "simultaneous treatment"). Simultaneous treatment causes enhancement of drug transport in two ways: i) by structural changes to the skin that increase skin permeability, and ii) through convection-related mechanisms that occur only when ultrasound is applied.[91] Conversely, the pretreatment method only enhances skin permeability by mechanism (i), because the drug is applied only after ultrasound treatment is completed. The simultaneous protocol is still common in studies that utilize HFS.[92-96] With LFS, both types of skin treatments have been investigated in the past, although the most common type of current treatment is the pretreatment method, including in clinical use of the technology.[17-19, 70] This is mainly because of three reasons. First, the action of ultrasound on drugs, or other active ingredients, can cause degradation of the molecules or other chemical reactions to occur. This can result in loss of activity or effectiveness of the therapeutic compound and may also cause undesired reactions that generate unknown species which could have deleterious biological effects.[97] Second, for clinical applications, simultaneous treatment requires that patients wear the ultrasound device for the duration of the treatment, while pretreatment has the advantage of requiring only that a patch be applied following a brief, ~10 second, ultrasound treatment.[91] Finally, the use of LFS for transdermal drug delivery has resulted in the ability to increase skin permeability to a greater extent than previously possibly with HFS,[20, 30] making it feasible for pretreatment of the skin to deliver therapeutic levels of

drugs, without the need for the additional convection mechanism associated with the simultaneous treatment.

1.3 Mechanisms of Skin Permeability Enhancement in Sonophoresis

1.3.1 Non-Cavitational Mechanisms of Enhancement in Sonophoresis

In addition to cavitation, which will be discussed in Sections 1.3.2 – 1.3.4, there are several other mechanisms whose roles on skin permeability enhancement in sonophoresis have been investigated. These include: i) convection (acoustic streaming and resulting boundary-layer reduction),[30, 79] ii) thermal effects,[30, 41, 79, 98] iii) mechanical or radiation pressure effects,[29, 79] iv) lipid extraction,[43], and v) increase in the solution-membrane interfacial transfer rate,[99] among others.

1.3.1.1 Convection-Related Mechanisms

It is important to recognize that the mechanisms of enhancement depend on the skin treatment protocol used. For example, utilizing the simultaneous treatment protocol, enhancement of drug permeation by convection is quite feasible. However, using a pretreatment protocol, convection cannot play any role in the enhancement of transport because the drug is not present in the coupling medium during the ultrasound treatment. Nevertheless, even with simultaneous treatment protocols, there have been conflicting claims about the role of convection in enhancing drug delivery. One likely explanation for this seeming incongruity is the skin model and skin thickness utilized. For example, using 20 kHz LFS (intensity of 1.6 W/cm^2) applied simultaneously with mannitol or sucrose, Tang *et al.* showed that convection only plays a

significant role in transport across heat-stripped human skin (which contains solely the epidermis), while it was not significant in the case of the thicker split-thickness (0.7 mm) or full-thickness (≥1.4 mm) pig skin models.[21] Similarly, Mitragotri *et al.* showed that convection did not affect mannitol permeability in full-thickness pig skin (20 kHz, 7 W/cm^2).[10] In other words, the skin permeability to mannitol was the same regardless of whether mannitol was present in the LFS coupling medium or was applied post-treatment.

Other studies, however, have suggested that convection can be important using LFS. For example, Tachibana *et al.* showed that the analgesic effect of 2% lidocaine, simultaneously applied with 48 kHz ultrasound (0.17 W/cm^2), was greater than when applied with an aqueous formulation instead of with a gel.[100] These authors concluded that the most likely reason for this observation was that ultrasound-induced convective streaming processes (such as acoustic streaming, see Section 1.2.1.3) were enhancing the bioavailability of lidocaine at the skin surface in the less-viscous aqueous formulation. In addition to the studies using LFS, a number of HFS studies have investigated the effect of convective processes as potential mechanisms of therapeutic delivery. Using cellophane membranes as a model, Lenart *et al.* deduced that with 1 MHz HFS treatment (1.2-6.0 W/cm^2), the main mechanism of increased diffusion of electrolytes was due to the formation of acoustic microcurrents.[101] In addition, utilizing 1 MHz HFS (1.5-3.0 W/cm^2), Levy *et al.* concluded that a combination of convective mixing and cavitation were the main mechanisms of enhanced delivery of mannitol, inulin, and physostigmine.[33] Simonin also demonstrated, using a theoretical analysis, that convective reduction of the boundary layer above the skin by stirring of the donor compartment could decrease the overall resistance of the

membrane by about 10%.[79] Convection has also been cited as a possible mechanism in other HFS studies,[102] while it has not been implicated in several others.[29, 34, 103, 104]

1.3.1.2 Thermal Effects

Thermal effects have been studied in great detail with respect to sonophoresis, because attenuation of an ultrasound wave leads to heating of the medium that the wave traverses. An increase in temperature can increase skin permeability by: i) increasing the kinetic energy and diffusivity of drug compounds, ii) dilating points of entry of the skin (e.g., hair follicles and sweat glands), iii) facilitating drug absorption, and iv) enhancing circulation of blood in the treated area (in *in vivo* experiments).[29, 79] Because thermal effects are directly proportional to the ultrasound intensity and duty cycle, reports have differed on the importance of heating as a mechanism of sonophoresis. Many studies have concluded that thermal effects do not play a role in HFS (1-16 MHz, 0.2-3.0 W/cm^2) enhanced transdermal transport, although the temperature in the donor solution was not observed to increase more than 1-2 °C in these studies.[28, 33, 103] Conversely, and not surprisingly, in studies that observed much larger temperature increases (in excess of 10 °C), thermal effects were found to play a role in increasing permeant transport, although a temperature increase alone could not explain the full enhancement observed with the HFS treatment (1 MHz, 1 W/cm^2).[102] Meidan *et al.* even concluded that heating is the main mechanism of action with HFS.[98] A study of sonophoresis, at an intermediate frequency of 150 kHz (2 W/cm^2), also concluded that thermal effects may be a significant mechanism of increased flux of hydrophilic permeants.[105] However, recent studies, especially those conducted with LFS at higher amplitudes, have paid more attention to controlling and minimizing thermal effects. This is because significant increases in temperature, and sustained

exposure to high temperatures, can lead to many harmful side effects, such as epidermal detachment, burns, and necrosis of the viable epidermis or underlying tissues.[41] Therefore, most current sonophoresis treatment protocols require periodic replacement of the coupling medium to minimize heating. Thermal effects have therefore been shown not to play a significant role in LFS studies.[42, 43, 60] For example, in Chapter 2 I will show that heating a solution to 37 °C does not increase the skin uptake of sodium lauryl sulfate (SLS) to a statistically significant extent, compared to controls at 25 °C, in 20 minutes of exposure (a typical duration for an *in vitro* LFS treatment, with replacement of the coupling medium every 2 minutes).[14, 15] However, similar to observations with HFS, if the temperature is allowed to increase in the LFS experiments, and the increased temperature is maintained for an extended time, thermal effects will play a role. For example, Merino *et al.* demonstrated that during a 2-hour treatment using 20 kHz LFS (4.5-15.0 W/cm^2, 10% duty cycle), thermal effects could explain up to 25% of the observed mannitol transport, with the temperature increasing as much as 20 °C during the treatments.[57] These authors also stated that the remaining enhancement was likely due to cavitation (see Sections 1.3.2 – 1.3.4).

1.3.1.3 Other Proposed Mechanisms

Other mechanisms of enhancement have also been reported in the literature, albeit less often. One potential mechanism that has been considered is the direct force of the acoustic wave on the skin membrane or on the interface between the skin and the coupling medium.[101, 106] However, an investigation by Simonin has shown that this effect is exceedingly small and is therefore negligible relative to the overall skin permeability enhancement.[79] A unique study by Alvarez-Roman *et al.* showed that up to 30% of the stratum corneum lipids can be extracted into

the coupling medium during LFS exposure (20 kHz, 15 W/cm^2).[43] These authors proposed that the decrease in skin lipids could explain previously observed phenomena such as: i) decreased skin electrical resistance, ii) increased water permeability, and iii) sustained permeability enhancement post-treatment. However, Alvarez-Roman *et al.* suggested that cavitation in the coupling medium is the most likely mechanism for the observed non-uniform enhancement across the skin surface, as well as a possible reason for the lipid extraction itself.[43] Therefore, lipid extraction due to LFS is likely a result of other enhancement mechanisms (e.g., cavitation), and not a direct mechanism of the LFS treatment. Finally, Julian and Zentner proposed that 20 kHz LFS (~13-46 W/cm^2) increased the diffusion of benzoic acid and hydrocortisone across model membranes (polydimethylsiloxane or cellulose) by decreasing the activation energy for diffusion, and thereby increasing the diffusion coefficients and partition coefficients between the solution and the membrane for these compounds.[99] However, no physical explanation was given as to how the ultrasound caused these changes, other than possible thermal effects. A subsequent theoretical analysis by Simonin to identify a microscopic physical interpretation as to why ultrasound decreases the interfacial energy barrier was unsuccessful.[79] Therefore, it is again possible that the proposed energy barrier reduction mechanism results simply from thermal effects (note the high amplitudes utilized in this study[99], which are reported above), instead of being a direct mechanism itself.

1.3.2 The Role of Cavitation in HFS

In some of the first mechanistic investigations using HFS, Kost *et al.* and Levy *et. al.* hypothesized that cavitation could play a role in transdermal delivery with sonophoresis.[32, 33] It was then shown by microscopy-based histological examination that cavitation within the skin

is a significant mechanism at 10 MHz and 16 MHz.[28] A following theoretical analysis suggested that, at frequencies above 1 MHz, cavitation within skin appendages (such as hair follicles) could explain observed skin permeability enhancements using HFS, although it was unlikely that cavitation within the stratum corneum lipid bilayers could occur.[79] However, the most significant experimental study into the mechanisms of HFS, at frequencies between 1-3 MHz, was conducted by Mitragotri *et al.*, and showed that cavitation within the skin is the primary mechanism of skin permeability enhancement.[34] Moreover, the microscopy-based findings showed that cavitation occurs within cavities near the corneocytes of the stratum corneum, leading to the hypothesis that the direct interaction of the oscillating cavitation bubbles induces disordering of the stratum corneum lipid bilayers, causing the observed increase in skin permeability (see Figure 1-4).[34]

1.3.3 The Role of Cavitation in LFS

The role of cavitation as the primary mechanism of skin permeability enhancement during LFS was demonstrated by Tang *et al.* in a series of experiments involving the selective suppression of cavitation inside and outside the skin.[42] First, to show that cavitation outside the skin plays a more significant role than cavitation inside the skin, a highly viscous liquid, castor oil, was used in place of water in the coupling medium. This, in effect, completely suppressed cavitation in the coupling medium outside the skin, while not changing the conditions inside the skin significantly. It is important to note that the acoustic impedance of both water and castor oil are similar to that of skin, and therefore, the efficiency of energy transfer between the coupling medium and the skin is similar using either type of formulation. In the next series of experiments, a high-pressure diffusion cell was built, allowing for the suppression of cavitation

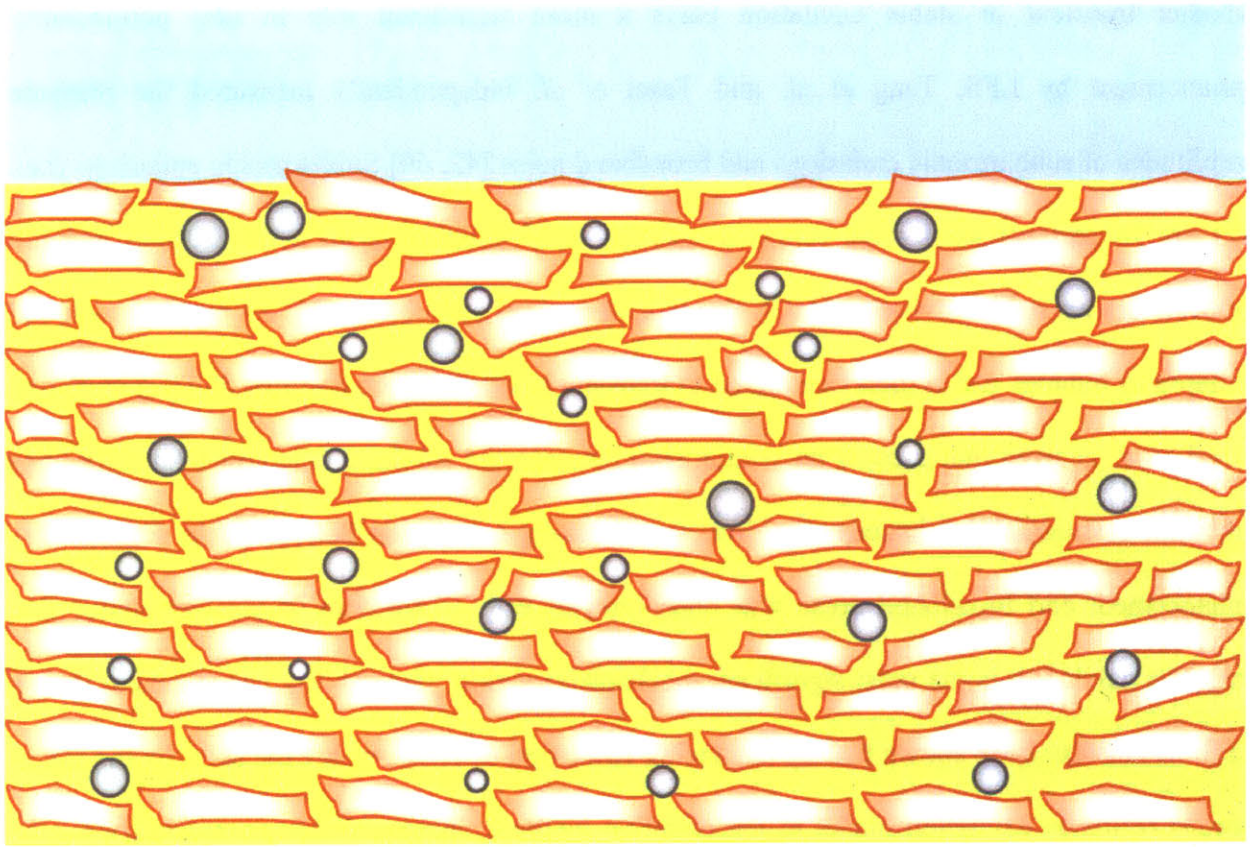

Figure 1-4. Illustration of cavitation bubbles inducing disordering within the stratum corneum under HFS. Legend: Keratinocytes ( ), cavitation bubbles ( ), lipid bilayers ( ), and coupling medium ( ).

in the entire system, both outside and inside the skin, by generating high static pressure. In both the castor oil and high-pressure studies, no significant change in skin permeability was observed compared to passive controls, and therefore, it was concluded that cavitation outside the skin was indeed the most important mechanism of skin permeability enhancement.[42] To elucidate whether transient or stable cavitation plays a more significant role in skin permeability enhancement by LFS, Tang *et al.* and Tezel *et al.* independently measured the pressure amplitudes of subharmonic emissions and broadband noise.[42, 60] Subharmonic emissions (i.e., $f/2$) are in part caused by the repeated oscillation of bubbles in an acoustic field and are associated with stable cavitation.[107] Broadband noise is associated with the rapid growth and collapse of bubbles and is therefore linked to transient cavitation. The findings of Tang *et al.* and Tezel *et al.* showed that there is no relationship between the sub-harmonic emission recordings and skin permeability enhancement. However, a strong correlation between skin permeability enhancement and broadband noise was observed.[42, 60] Therefore, it was concluded that transient cavitation is the most significant mechanism of skin permeability enhancement during LFS. It has also been shown that by enhancing cavitation activity outside the skin, by the use of porous resins as cavitation nuclei in the coupling medium, increased skin permeability can be attained. This further demonstrates the significance of cavitation outside the skin in causing skin permeability enhancement using LFS.[49]

The findings above, however, did not elucidate: (i) which types of transient cavitation events (microjets or shockwaves) lead to the observed enhancement of skin permeability, and (ii) the location of these transient cavitation events in the coupling medium: at the surface of the skin,

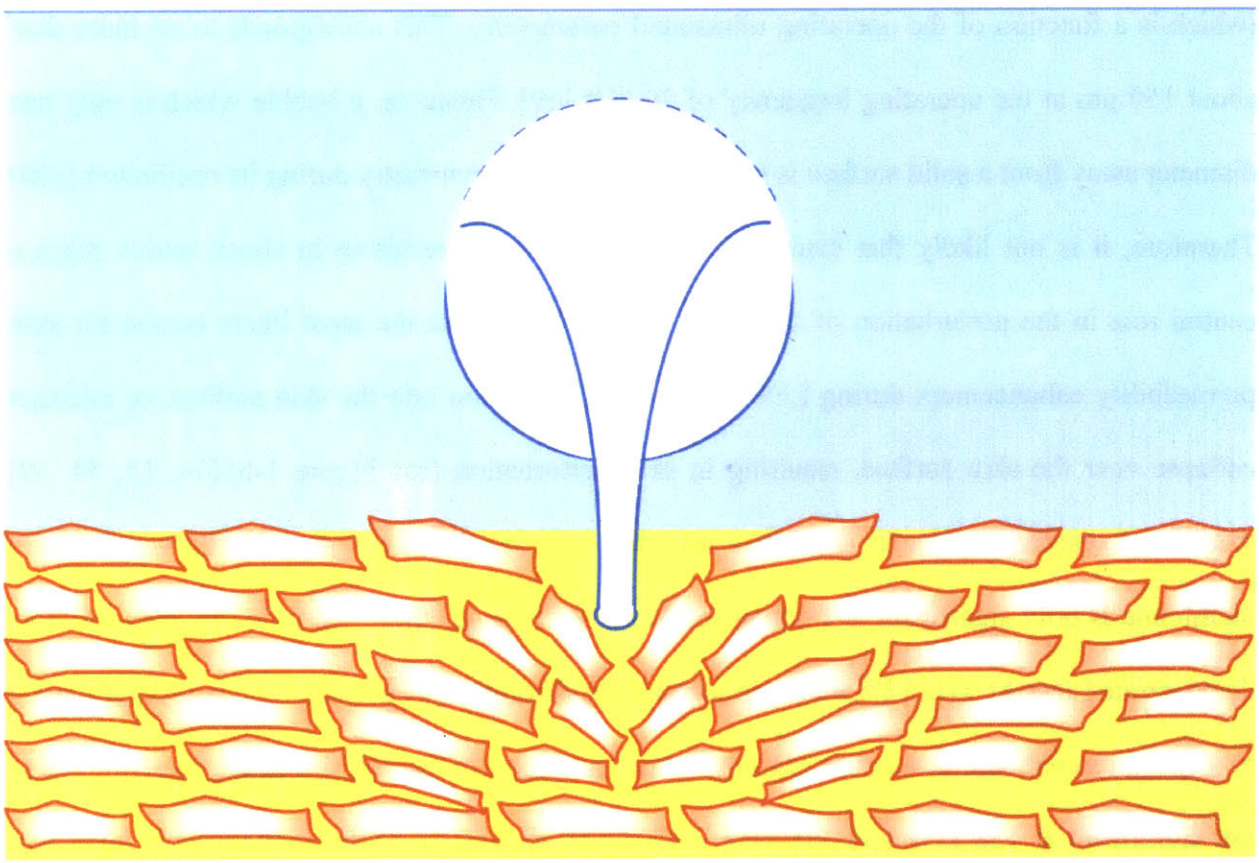

Figure 1-5. Illustration of a cavitation bubble asymmetrically collapsing into the stratum corneum as a microjet under LFS. Legend: Keratinocytes ( ), lipid bilayers ( ), and coupling medium ( ).

close to the surface of the skin, or in the bulk. Tezel *et al.* were able to show that the critical distance of a bubble from the skin surface required to cause disruption to the surface is approximately one maximum bubble radius.[59] The maximum bubble radius is the largest radius to which the bubble expands to in the negative pressure half-cycle of the ultrasound field (which is a function of the operating ultrasound parameters). This corresponds to no more than about 150 μm at the operating frequency of 20 kHz.[59] However, a bubble which is only one diameter away from a solid surface is not likely to maintain symmetry during its oscillation.[108] Therefore, it is not likely that symmetric bubble oscillation resulting in shock waves plays a central role in the perturbation of the skin. This indicates that the most likely reason for skin permeability enhancement during LFS is microjet penetration into the skin surface, or microjet collapse near the skin surface, resulting in skin perturbation (see Figure 1-5).[14, 15, 54, 59] Additional research by Ueda *et al.* has revealed that transient cavitation in the vicinity of a membrane is only significant at frequencies in the LFS range. [62] Specifically, these authors demonstrated that 41 kHz LFS treatment caused the disruption of a rhodamine B layer adsorbed to a gelatin membrane in discrete regions, while cavitation in the vicinity of the membrane was not significant at 158 kHz and 445 kHz, because no disruption of the rhodamine B layer was observed.[62] Ueda *et al.* also demonstrated that transient cavitation generation increases with decreasing ultrasound frequency, which scales directly with the membrane permeability.[62] Furthermore, by conducting experiments at multiple frequencies in the range 20 kHz – 60 kHz, in Chapter 2 I will show that there is a strong correlation between skin pore radius and ultrasound frequency. This correlation scales similarly to the relationship between the resonant bubble radius and ultrasound frequency (see Section 1.2.1.1), suggesting that the direct action of cavitation bubbles collapsing onto the skin, likely as microjets (see Figure 1-5), accounts for the

observed variation in skin pore radius with ultrasound frequency.[14, 15] Other recent studies have also suggested that cavitation bubble collapses on the skin surface as microjets play a dominant role in skin permeability enhancement compared to other cavitation-related mechanisms, such as shock wave emission.[44] For example, Watanabe *et al.* have found that small pits can be observed on skin imaged with environmental scanning electron microscopy, which likely results from cavitation at the skin surface.[109]

1.3.4 Difference in the Mechanisms of LFS and HFS

It is essential to recognize that different mechanisms are responsible for skin permeability enhancement in LFS and HFS. A common erroneous practice in the sonophoresis literature is to rationalize observations made using LFS by invoking enhancement mechanisms which are only applicable using HFS. In particular, a serious mistake involves identifying the actual location of cavitation during the ultrasound treatment (compare Figures 1-4 and 1-5). In HFS, as stated earlier in Section 1.2.1.1, the linear resonant bubble radius is on the order of less than 1 μm, which is comparable to the thickness of the lipid bilayers of the stratum corneum. This suggests that it is possible for cavitation to occur within skin appendages (hair follicle shafts, sweat glands, etc.)[79] or in lacunar cavities within the skin itself.[34] Indeed, there have been numerous studies reporting that cavitation within the skin is an important factor in skin permeability enhancement using HFS, at frequencies ranging from 1-16 MHz. [28, 32-34] In fact, it was believed that cavitation outside the skin would decrease the efficiency of the HFS treatment by decreasing energy transfer between the ultrasound horn and the skin treatment site.[27] Therefore, for these applications, it was suggested that suppressing cavitation in the coupling medium would be advantageous for overall skin permeability enhancement, which

could be achieved by utilizing non-aqueous media, such as mineral oil, in the coupling solution. Unfortunately, when the switch from HFS to LFS was made,[20] it was still believed that cavitation within the skin would continue to play a dominant role. This has led to many erroneous citations and claims in the literature that transient cavitation within the skin is significant in LFS enhancement of skin permeability (e.g., [58, 64, 110, 111]). However, since that time, it has been shown conclusively through cavitation suppression experiments, chemical and acoustic dosimetry methods, and theoretical analysis, that cavitation in the coupling medium near the skin surface is, in fact, the primary mechanism of skin permeability enhancement in LFS.[14, 15, 42, 44, 59, 60] Therefore, careful attention should be paid when designing experiments and explaining observed trends, depending on the frequency of ultrasound utilized. For example, when utilizing LFS, cavitation above the skin has been shown to be the primary mechanism of enhancement, and therefore, the utilization of experimental protocols that suppress this mechanism, such as degassing of the coupling medium, placing the ultrasound horn in contact with the skin, or using a coupling medium with a high viscosity, is not recommended, unless suppression of cavitation above the skin is actually desired.

1.4 Phenomena Observed in Sonophoretic Transdermal Drug Delivery

1.4.1 Localized Transport Regions

An important discovery in the area of skin permeability enhancement by LFS was the identification of heterogeneity in the enhancement of skin perturbation. Tang *et al.*[48] and Tezel *et al.*[68] observed independently that LFS operating at 20 kHz, with a colored permeant present in the coupling medium, produced highly-stained regions of LFS-treated skin. These

regions of hypothesized high permeability were given the name localized transport regions (LTRs). Kushner *et al.* verified that these regions are indeed regions of increased permeability by using a unique masking method on LFS-treated skin.[51] Experiments using solely LFS (20 kHz, 15 W/cm^2) showed that only a single LTR formed during sonication of skin samples, directly below the ultrasound transducer.[43] However, further investigation into the phenomenon of LTR formation showed that when 1% w/v SLS was added to the LFS coupling medium (frequencies of 19.6 – 58.9 kHz), LTRs formed in stochastic patterns across the surface of the skin, ranging in coverage from 5 – 25% of the skin surface area (see Figure 1-6).[50, 51, 60, 68] In addition, Kushner *et al.* showed that the LTRs are not only highly perturbed (5000-fold decrease in skin resistivity), but that the non-LTRs are also permeabilized relative to untreated skin (170-fold decrease in skin resistivity) when SLS is present during the skin treatment.[51] This is a significant finding because it shows that two levels of skin electrical resistivity enhancement are present. In comparison, in the case of LFS alone, only the LTRs were shown to be perturbed to a significant extent, with minimal change to the skin in the non-LTRs.[43] The frequency dependence of the skin permeability enhancement in the presence of SLS was studied by Tezel *et al.* at 20-100 kHz and 1.08 W/cm^2, and the following trends were observed: (i) as the ultrasound frequency increases, the threshold ultrasound intensity for the observation of skin conductivity enhancement increases, (ii) at lower ultrasound frequencies, localized transport plays a more significant role, with LTRs observed on the surface of the skin, and (iii) at higher ultrasound frequencies, transport occurs more homogenously across the surface of the skin.[68] In another study utilizing multiple ultrasound frequencies (41 kHz, 158 kHz, and 445 kHz), Ueda *et al.* were able to show that disruption of the surface of gelatin membranes occurred only at 41 kHz, in discrete spots.[62] This suggests that localized transport

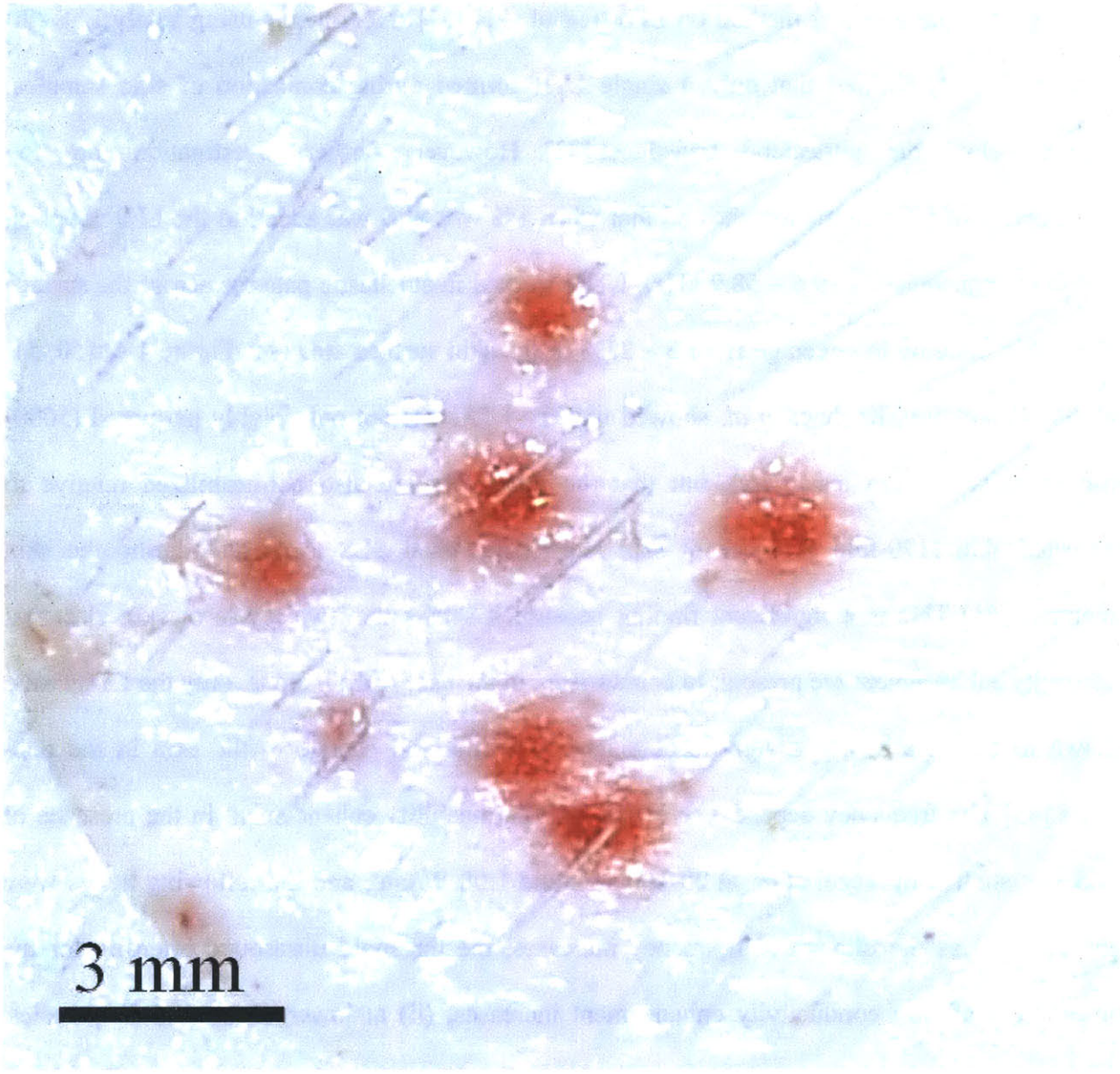

Figure 1-6. LTRs formed on the surface of pig skin treated with 20 kHz LFS and a surfactant. LTRs are stained with allura red.

is only significant when treating skin in the LFS range. Furthermore, in Chapter 2 I will show that the pore size within LTRs in skin treated with LFS/SLS is frequency dependent, while in non-LTRs no frequency dependence is observed.[14, 15] Because the size of cavitation bubbles is also frequency dependent[35], I will show that cavitation-induced microjet collapse at the skin surface is the most likely mechanism of LTR formation and of skin permeability enhancement within LTRs. Conversely, within non-LTRs, due to the frequency independence in the observed pore size, the action of SLS on the skin will be shown to be the main mechanism of non-LTR enhancement, with increased uptake of SLS into the non-LTRs taking place via a convection-related mechanism, such as boundary-layer reduction by acoustic streaming (see Section 1.2.1.3).[14, 15] It is noteworthy that there have been no reports of LTR formation with HFS, which is expected because it is known that localized transport is more significant only at lower ultrasound frequencies (interested readers are referred to Refs. [54, 68] for a more detailed discussion of LTRs).

1.4.2 Synergism of Sonophoresis and Chemical Enhancers

One of the most significant phenomena observed with sonophoresis is that its combination with chemical enhancers, such as surfactants, results in synergism in the enhancement of transdermal transport. Chemical enhancers alone are known to permeabilize skin by solubilizing or extracting skin lipids and by denaturing corneocytes.[2] However, their effect on skin permeability can be even more dramatic when combined with ultrasound. One of the first rigorous studies on the synergism between chemical enhancers and ultrasound was conducted by Johnson *et al.*, who showed that different combinations of chemical enhancers in the presence of HFS causes an increase in the permeability and flux of lipophilic permeants across *in vitro*

human cadaver skin.[112] Their major finding was that for the model permeant corticosterone, a combination of ethanol and linoleic acid, in equal proportions, enhanced the skin permeability by a factor of 8.7 and the flux by a factor of 903. However the same formulation, when combined with HFS (1 MHz, 1.4 W/cm^2), enhanced the skin permeability by a factor of 14.4 and the flux by a factor of greater than 13,000.[112] The authors explained that the observed enhancement induced by HFS/linoleic acid was caused by either an increase in the fluidity of the lipoidal domain in the stratum corneum or by the formation of a separate bulk oil phase in the skin. Another study by Meidan *et al.* demonstrated the synergism between 1.1-3.3 MHz HFS and the chemical penetration enhancer laurocapram (Azone) in delivering hydrocortisone across *in vitro* rat skin.[113] Their mechanistic findings suggested that the synergism between the two enhancers was due to accelerated laurocapram diffusion into the skin due to ultrasonic thermal effects. Furthermore, Liu *et al.* showed that the combined treatment of rat skin using LFS (20 kHz) with laurocapram or SLS exhibited synergistic topical delivery of cyclosporin A.[114] Specifically, the combination of LFS and chemical enhancers caused an increase in cyclosporin A skin concentration of over an order of magnitude compared to controls. Additional studies demonstrating synergism between chemical enhancers and ultrasound include: i) HFS (1 MHz) and d-limonene in ethanol on the percutaneous absorption of ketorolac tromethamine through *in vitro* rat skin,[115] ii) HFS (1 – 1.1 MHz) and thiazone or glycerol (among several others) to increase skin optical clearing,[116-120] iii) HFS (0.8 MHz) and laurocapram, oleic acid, or 2-propanediol on the delivery of sinomenine hydrochloride through rat skin,[121] iv) HFS (0.8 MHz) and ethanol-containing aqueous gel formulations (hydroxypropyl methylcelullose) on the delivery of ibuprofen through *in vitro* and *in vivo* rabbit skin,[95] v) ultrasound (150 kHz) and 7 different enhancers (menthol being the most thoroughly investigated) on the delivery of

aminopyrene, vi) LFS (20 kHz) and capsaicin or nonivamide on the transdermal flux of indomethacin across nude mouse skin[122], vii) LFS (20 kHz) and 14 different chemical enhancers (the best of which was 5% citral in 1:1 ethanol:PBS) on the transdermal permeation of tizanidine hydrochloride across mouse skin,[123], and viii) LFS (20 kHz) and liposomes/SLS to deliver antigens through *in vitro* and *in vivo* rat skin,[124] among others.

1.4.2.1 Synergism of LFS and Surfactants

The synergism between LFS and surfactants has been shown to be quite significant. For example, Mitragotri *et al.* showed that by adding a common anionic surfactant, SLS, to the LFS coupling medium (20 kHz), skin permeability to mannitol increased 200-fold over 90 minutes of treatment, while for LFS and SLS treatments alone, only 3-fold and 8-fold enhancements were observed, respectively.[10] Furthermore, these authors showed that the energy density threshold required to observe any skin permeability enhancement decreased by nearly an order of magnitude from 141 J/cm^2 to 18 J/cm^2, with the inclusion of SLS in the LFS coupling medium. In addition, Mitragotri *et al.* demonstrated that skin permeability enhancement is linearly proportional to SLS concentration, in the range 0 – 1 wt% SLS, and is also proportional to the LFS intensity and exposure time, but independent of duty cycle.[10] In a following study, Tezel *et al.* studied the synergism between LFS (20 kHz) and a series of eleven surfactants.[50] The study included surfactants with a variety of "head" groups (cationic, anionic, nonionic, and zwitterionic) and "tail" groups (linear alkanes containing 8-16 carbons). In 10 minutes of LFS treatment, using a surfactant concentration of 1 wt% in the coupling medium, tetradecyltrimethyl ammoniumbromide (TDAB), SLS, and hexadecyltrimethyl ammoniumbromide (HDAB) yielded the highest skin conductivity enhancement ratios of 35.4, 24.5, and 15.9, respectively, of all the

single surfactant solutions considered. However, when multiple surfactants were mixed, both synergistic and antagonistic effects were observed. For example, a 50:50 mixture of TDAD and HDAB (total concentration of 1 wt%) yielded an enhancement ratio of 42.8 (greater than using either single surfactant alone at a concentration of 1 wt%), thus exhibiting synergism. On the other hand, a 50:50 mixture of SLS and glycolic acid ethoxylate 4-tert-butyl phenyl ether (ether) only showed an enhancement ratio of 1.6, much lower than the enhancement ratio corresponding to either single surfactant solution (enhancement ratio for ether alone was 5.5), thus exhibiting extreme antagonism. No mechanism was suggested to rationalize why synergistic or antagonistic effects were observed in the binary surfactant formulations. Tezel *et al.* concluded that ionic surfactants are better than nonionic surfactants at increasing skin conductivity, and that the optimum surfactant tail length to attain synergistic skin permeability enhancement with LFS is 14 carbons, compared to 12 carbons for passive enhancement.[50]

The effects of a surfactant present in the coupling medium during sonophoretic treatment can be broadly classified into two types: (i) the effect of the surfactant on ultrasound-related phenomena, and (ii) the effect of ultrasound on surfactant penetration, dispersion, and partitioning in the skin. Although these two mechanisms are strongly coupled, for simplicity, they will be discussed separately. Surfactants can affect cavitation through several mechanisms. Because of their preferential adsorption at interfaces, surfactants tend to reduce the surface tension of aqueous solutions. Surface tension has its greatest effect on the oscillation of a cavitation bubble at the beginning of its expansion and at the end of its compression, causing an increase in the rate of expansion and a decrease in the rate of compression as the surface tension decreases.[74] In general, sonochemical activity is favored in liquids possessing higher surface

tensions because it leads to more violent collapse of bubbles, and consequently, more sonochemical related phenomena take place.[125] However, in addition to decreasing the surface tension, surfactants also play a role in stabilizing cavitation bubbles by inhibiting bubble coalescence and growth, especially in the case of charged surfactants (due to the electrostatic repulsions between charged bubbles). Therefore, the addition of surfactants to the coupling medium leads to a larger population of smaller cavitation bubbles.[84] If the ultrasound field is pulsed, some of these smaller bubbles have a tendency to dissolve back into the solution when the ultrasound is off due to the Laplace pressure of the bubble (see Section 1.2.1.2).[84] The interplay between cavitation bubble growth and coalescence inhibition depends on the surfactant concentration. Usually, in LFS-mediated transdermal drug delivery experiments, 1% w/v SLS is used in the coupling medium. At this SLS concentration, experiments have shown that shielding and stabilization effects play a more significant role than surface tension effects.[84] As a result, it is observed that when 1% w/v SLS is present in the coupling medium during LFS treatment, transient cavitation activity decreases when compared to experiments performed when SLS is not present in the coupling medium, due to the existence of a population of smaller less energetic cavitation bubbles in the presence of SLS. For example, Mitragotri *et al.* measured transient cavitation events by aluminum foil pitting and found that when 1% w/v SLS in PBS solution was used instead of just a PBS solution, the number of pits decreased from 73±20 pits, in 20 seconds, to 6±4 pits.[10] These authors also found that the average pit diameter decreased when 1% w/v SLS was present in the coupling medium. Therefore, it does not appear that a change in cavitation activity would favor synergism between LFS and surfactants, but instead, may actually inhibit it. Therefore, there must be some other mechanism to explain the synergism between surfactants and sonophoresis.

Chemical enhancers, such as surfactants, are known to increase the rate of transdermal drug delivery by: i) increasing the stratum corneum lipid fluidity, ii) changing lipid organization,[126] iii) decreasing the path length and tortuosity across the stratum corneum, iv) increasing the skin diffusion coefficient, and v) increasing the coupling medium-to-skin partition coefficient.[127, 128] However, the barrier properties of the skin inhibit the extent to which surfactants can diffuse into and perturb the skin passively in a reasonable amount of time. Therefore, it is believed that the main role of the synergism between LFS and the surfactant is the ability of LFS to increase the concentration and dispersion of the surfactant inside the stratum corneum.[46] By carrying out a series of experiments in which skin was soaked in a solution of 1% w/v SLS for various durations between 1 minute and 24 hours, followed by the application of LFS/SLS for 10 minutes, Mitragotri *et al.* found that as the skin soaking time increased, the ratio of skin conductivity after ultrasound treatment to skin conductivity prior to ultrasound treatment decreased.[10] This result shows that the effect of LFS treatment is diminished with increased passive exposure time to SLS. From these results, the authors argued that synergism between LFS and SLS is due to the increased penetration and dispersion of the surfactant in the skin induced by LFS.[10] Another study suggested that pH changes induced in the skin during LFS may explain the synergism between LFS and SLS.[63] However, it is not clear whether the pH changes in the skin are merely a consequence of the combined LFS/SLS treatment or, in fact, play a role in the observed synergism. In spite of the findings above, no convincing physical mechanism has been proposed to date to explain why LFS causes increased uptake of surfactants. Therefore, this important topic is still an area of active research (see Chapter 4).

1.4.3 Synergism of Sonophoresis with Other Physical Enhancers

Early research using HFS showed that when an injection of hydrocortisone was followed by ultrasound treatment at 1 MHz, the effects of the combined treatment were superior to those of the injection alone,[26] essentially showing synergism between the injection and the therapeutic ultrasound treatment. Later, Kost *et al.* investigated synergism between HFS and electroporation, which is the process of increasing skin permeability by applying a high-voltage pulsed electric field across the skin.[129] In this study, the transport of two model permeants, calcein and sulforhodamine, were investigated in response to 10-150 V electric pulses (1 millisecond every minute) in combination with 1 MHz HFS. Although HFS alone did not increase the skin permeability to either model permeant, the combination of HFS and electroporation increased the flux of calcein by a factor of 2 and of sulforhodamine by a factor of 3, compared to the enhancement observed by electroporation alone. In addition, the lag time to steady state was decreased by 40%, relative to the case of electroporation alone, from 15 minutes to 9 minutes. However, when 3 MHz ultrasound was applied, very little synergism was observed. This led the authors to conclude that the mechanism of synergism between HFS and electroporation was cavitation-induced disordering of the skin's lipid bilayers and convection across the skin, because cavitational effects are inversely proportional to ultrasound frequency. Furthermore, convection-induced enhancement was dependent on the properties of the permeant considered. For example, the electric field played a larger role in the flux enhancement of the more highly-charged calcein (total charge of -4) than in the transport of sulforhodamine (total charge of -1) across the skin.[129]

The most common type of physical enhancer that has been studied in combination with LFS is iontophoresis, the process of increasing skin permeability by continuously applying a low voltage electric field across the skin. Le *et al.* studied the synergism of LFS at 20 kHz, through a coupling medium containing 1 wt% SLS or dodecyl pyridinium chloride (DPC), with iontophoresis applied at an energy density of 0.45 mA/cm^2.[45] Utilizing heparin, a negatively-charged biopolymer with average molecular weight of 10 kDa, as a model drug, these authors found that the skin permeability was over two-fold higher with the combination of LFS and iontophoresis (through an SLS coupling medium) than when utilizing either physical enhancer alone. Subsequently, by utilizing the positively-charged surfactant DPC, the authors were able to show that the initial (first hour) flux of the negatively-charged heparin was nearly twice that corresponding to the SLS treatment case.[45] The authors reasoned that this was due to the fact that when the negatively-charged SLS was utilized, both SLS and heparin competed for the same current, while the opposite charges of DPC and heparin would negate this effect. However, the steady-state heparin permeability induced by SLS, in combination with LFS and iontophoresis, was still slightly higher than that attained using the same treatment with DPC. This suggests that the combined LFS treatment with SLS caused greater sustained skin perturbation than DPC. The authors concluded that the synergistic enhancement observed with LFS and iontophoresis was practically significant because it: i) allowed the delivery of a macromolecule at therapeutic levels, ii) required reduced voltage/current to achieve the desired flux, and iii) allowed for active control of transdermal transport.[45] In another study, Fang *et al.* also found that LFS (20 kHz), when combined with iontophoresis (0.5 mA/cm^2), increased permeation of sodium nonivamide acetate across nude mouse skin in a synergistic manner.[130] In a more recent study using an intermediate ultrasound frequency (270 kHz), Watanabe *et al.* demonstrated that the combined

application of iontophoresis (20 V, 0.45-1.0 mA) with ultrasound can increase the delivery of hydrophilic model compounds across hairless mouse skin in a synergistic manner.[109] Specifically, despite minimal enhancing effects when ultrasound and iontophoresis were used separately, their combination increased delivery of antipyrine and sodium salicylate 10-fold. The authors suggested that the mechanism of enhancement was loosening of the connections of the stratum corneum by ultrasound, followed by increased electroosmotic flow due to iontophoresis.[109] In another study utilizing intermediate ultrasound, Hikima *et al.* studied the mechanisms of synergistic delivery of seven model permeants, ranging in size from 122-1485 Da, utilizing 300 kHz ultrasound and iontophoresis (0.32 mA/cm^2).[131] The study found that chemicals that were non-ionized or greater than 1000 Da in molecular weight showed synergistic enhancement with the combined ultrasound and iontophoresis application, whereas ionized drugs showed similar profiles in response to the iontophoretic treatment alone. The authors also conducted simulations that showed that the synergistic effect between ultrasound and iontophoresis occurred due to increased electroosmosis in the stratum corneum. Consequently, the synergistic mechanism was a result of increased skin diffusivity due to the action of ultrasound on the skin, followed by increased electroosmotic flow induced by iontophoresis.[131] Finally, Liu *et al.* demonstrated that pretreatment of rat skin with laurocapram and LFS (20 kHz), followed by electroporation of the skin samples, increased penetration of cyclosporin A by a factor of 15.[114]

Recently, LFS has also been utilized in conjunction with other physical enhancers in a clinical setting. For example, Spierings *et al.* investigated the ability of LFS, in the form of the FDA approved SonoPrep® device (Echo Therapeutics, Franklin, MA), to act synergistically with low-

voltage iontophoresis, in the form of the FDA approved Phoresor PM700® device (Iomed Incorporated, Salt Lake City, UT), in delivering the topical anesthetic Iontocaine® (Abbot Laboratories, Chicago, IL).[19] The study showed that a pretreatment with LFS, followed by 2 minutes of low-voltage iontophoresis, provided statistically similar pain relief as 10 minutes of standard high-voltage iontophoresis. A similar study with higher ultrasound frequencies found that the combined treatment of iontophoresis (5 mA) and HFS (1 MHz) to deliver cortisol was effective in decreasing subjective pain complaints of patients with mild to intermediate stages of carpal tunnel syndrome.[132] Finally, a recent clinical study reported the use of microdermabrasion treatment, followed by the application of sonophoresis through a complex containing hyaluronic acid, retinol, and peptide.[133] The authors showed that the combination of the two physical skin penetration enhancement methods had beneficial effects in photorejuvenation of the skin, such as enhanced vascularity in the dermis and increased type I and III collagen formation.[133]

1.5 Scope of Transdermal Delivery Utilizing Sonophoresis

1.5.1 High-Frequency Sonophoresis

The use of therapeutic frequencies of ultrasound to increase the cutaneous penetration of cortisol, a topical steroid, was first demonstrated by Fellinger and Schmid in 1954.[25] Additional research on sonophoresis during the same time period showed beneficial effects of therapeutic ultrasound after injection of drugs[26, 134, 135] and the treatment of localized disorders with ultrasound treatment alone, such as in the treatment of pain, scars, arthritis, epicondylitis, keloid growth, and bursitis.[136-141] The popularity of delivering therapeutic compounds with ultrasound increased over the following decades, with at least 150 independent reports to-date

describing the use of ultrasound frequencies greater than 0.7 MHz in the delivery of permeants transdermally. These studies are summarized in Table 1-1.

Nearly all studies involving HFS have utilized the simultaneous treatment protocol, that is, the drug being delivered is included in the coupling medium (typically a gel) during ultrasound treatment. Therefore, in addition to cavitational effects within the skin[34] that can increase skin permeability, thermal and convective effects can also play a role in increasing solute partitioning into the stratum corneum of the skin and subsequent mobility therein (see Section 1.3 for more details). The additional enhancement resulting from this combination of mechanisms is beneficial, because enhancement by HFS is usually modest (1- to 10-fold) when compared to enhancements observed with LFS.[20, 27, 29, 30] However, this level of enhancement may be sufficient for the applications that HFS has been used for, which usually entail topical or regional delivery of therapeutics (for example, topical steroids for inflammatory conditions or arthritic joints, see Table 1-1). Systemic delivery is not a common goal with HFS. Furthermore, most compounds delivered by HFS are small molecules, with only a handful of drugs having molecular weights greater than 1000 Da tested (see Table 1-1). This is consistent with the assertion that HFS does not change the structure of the skin greatly, and therefore, can only operate by increasing the penetration of molecules that would likely penetrate the skin in lesser amounts under passive conditions. Nevertheless, the fact that HFS does not induce large changes to the skin barrier is also a strength of this treatment method, as it is generally considered to be a very safe technology, and is frequently utilized in other widespread applications, such as in sports and physical therapy. Furthermore, because many ultrasound devices that operate in the range 0.7 – 3.0 MHz are FDA approved, it is much easier to initiate human trials of such

Table 1-1. Molecules that have been delivered transdermally with therapeutic and high-frequency ultrasound.

Molecule	MW (Da)	Log $K_{o/w}$[a]	Freq.(MHz)	Amp.(W/cm^2)	Skin Model[b]	Ref.
Aloe vera gel	-	-	1.0	0.5	*in vivo* rat	[94]
Aminopyrine	231	1.00	3.5	0.1-2.0	*in vitro* rat FTS	[143]
Amphotericin B	924	-2.80	2.64	1.0	*in vivo* gp	[144]
Arnica montana extract	-	-	1.0	0.5	*in vivo* rat	[145]
Ascorbic acid	176	-1.85	0.88, 5	0.3-1.0	*in vivo* human	[146, 147]
Benzene	78	2.13	1.0-3.0	0-2.0	*in vitro* h FTS	[34]
Benzocaine,	165	1.86	1.1	0.25	*in vivo* human	[148]
benzethonium mixture	448	4.00				
Benzydamine	309	4.21	c	c	*in vivo* human	[149, 150]
			0.75-3.0	0-3.0	*in vivo* human	[151]
Benzyl nicotinate	213	2.40	3.0	0.2-1.0	*in vivo* human	[152]
Biomycin	451	-3.60	c	c	*in vivo* human	[153, 154]
Bufexamac	223	2.08	3.0	0.1-3.0	*in vivo* human	[155]
Butanol	74	0.88	1.0-3.0	0-2.0	*in vitro* h FTS	[34]
Caffeine	194	-0.07	1.0-3.0	0-2.0	*in vitro* h FTS	[34]
			1.0-3.0	0.01-2.0	*in vitro* m FTS	[104, 156]
Calcein	623	-	1.0-3.0	1.4	*in vitro* h FTS	[129]
Calcium	42	-0.57	1.0	0.3	*in vivo* mouse	[157]
Chymotrypsin	25k	-	c	c	*in vivo* human	[158]
Corticosterone	346	1.94	1.0-3.0	0-2.0	*in vitro* h FTS	[34, 112]
Cortisol (hydrocortisone)	362	1.61	c	c	*in vivo* human	[25, 159-180]
			0.5-1.0	0-3.0	*in vivo* human	[132, 181-186]
			0.09-3.6	1.0-3.0	*in vivo* pig	[187-190]
			c	c	*in vivo* rabbit	[191-194]

			0.87-1.0	0.5-2.75	*in vivo*	dog	[195, 196]
			1.1	1.5	*in vitro*	h FTS	[197]
			1.1-3.5	0.1-2.5	*in vitro*	rat FTS	[113, 143]
			1.0	3.0	*in vitro*	m FTS	[197]
			[c]	[c]	*in vitro*	frog	[198, 199]
Dexamethasone	392	1.83	[c]	[c]	*in vivo*	human	[200, 201]
			0.87	[c]	*in vivo*	human	[202]
			1.0-3.0	1.0	*in vivo*	human	[203, 204]
			1.0	1.5	*in vivo*	pig	[186]
			1.0	1.4	*in vitro*	h FTS	[112]
Dibucaine (cinchocaine)	343	4.40	1.1	0.25	*in vivo*	human	[148]
Diclofenac	296	4.51	1.0-3.0	0.5-1.5	*in vivo*	human	[205-209]
			0.8	0.5-3.0	*in vitro*	r FTS	[210]
Digoxin	781	1.26	3.3	1.0, 3.0	*in vitro*	h FTS	[211]
					in vitro	m FTS	
Dimethyl sulfoxide	78	-1.35	1.0	0.8	*in vivo*	rat	[142]
Ethyl nicotinate	151	1.32	3.0	1.0	*in vivo*	human	[212]
EMLA (lidocaine,	234	2.44	0.75-3.0	0.25-1.5	*in vivo*	human	[148, 213]
prilocaine mixture)	220	2.11	1.0	2.0	*in vivo*	rat	[214]
Estradiol	272	4.01	1.0-3.0	0-2.0	*in vitro*	h FTS	[34, 112, 197]
Fibrinolysin	13.8k	-	[c]	[c]	*in vivo*	human	[215]
Flufenamic acid	281	5.25	0.8, 1.0	0.0-1.5	*in vivo*	human	[216, 217]
			0.8, 1.0	0.0-1.5	*in vitro*	h FTS	[216]
Fluocinolone acetonide	452	2.48	[c]	0.2	*in vivo*	rat	[218-220]
(sinalar)			0.87	2.0	*in vivo*	human	[221]
Fluocinonide	495	3.19	1.0	1.5	*in vivo*	human	[222]
5-Fluorouracil	130	-0.89	3.5	0.1-2.0	*in vitro*	rat FTS	[143, 223]

Glucosamine	179	-4.23	1.0	0.3	*in vivo* human	[224]
Glucose	180	-3.24	10	0.2, 2.0	*in vitro* p FTS	[57]
Glycerol	92	-1.76	1.0	[f]	*in vitro* p FTS	[225]
Heparinoid	5-40k[d]	-	[c]	[c]	*in vivo* human	[226]
Hexyl nicotinate	207	3.51	3.0	1.0	*in vivo* human	[212]
Hyaluronan	1-3k	-	1.0	0.4	*in vivo* rabbit	[227]
Ibuprofen	206	3.97	1.0	1.0	*in vivo* human	[228]
			1.0	1.0	*in vitro* h HSS	[102]
			0.8	0.5-3.0	*in vitro* r FTS	[95, 210]
Indomethacin	358	4.27	1.0	0.25-2.5	*in vivo* rat	[229, 230]
Inulin	5k	-	1.0	1.5-3.0	*in vivo* gp, rat	[33]
Iodex pomade (Iodine, methyl salicylate mixture)	127 152	2.49 2.55	[c]	1.5	*in vivo* human	[231]
Ketoprofen	254	3.12	1.0-3.0	1.0-1.5	*in vivo* human	[93, 209, 232]
Ketorolac tromethamine	255	2.32	1.0	1.0-3.0	*in vitro* rat FTS	[115, 233]
Lappaconitine HBr	666	-	0.8-1.0	0.7-0.75	*in vitro* rat FTS	[234]
Lanthanum hydroxide	190	-	10, 16	0.2	*in vitro* gp FTS	[28]
Lidocaine	234	2.44	0.87	[c]	*in vivo* human	[202]
			0.5-1.0	2.0	*in vivo* human	[235, 236]
			[c]	2.0	*in vivo* rabbit	[237]
			1.0	1.4	*in vitro* h FTS	[112]
Linoleic acid	280	7.05	1.0	1.4	*in vitro* h FTS	[112]
Mannitol	182	-3.10	1.0	1.5-3.0	*in vivo* gp, rat	[33]
			1.1	1.5	*in vitro* h FTS	[197]
			3.5	0.1-2.0	*in vitro* rat FTS	[143]
			10	0.2, 2.0	*in vitro* p FTS	[57]
Menthol	156	3.40	1.0-3.0	1.5	*in vivo* human	[238]

Mepivacaine	246	1.95	[c]	[c]	*in vivo*	human	[239]
Metamizole (analgin)	333	-4.76	[c]	[c]	*in vivo*	human	[240]
Methyl nicotinate	137	0.83	3.0	1.0	*in vivo*	human	[212], [241]
Morphine	285	0.89	1.5-3.0	0.01-2.0	*in vitro*	m FTS	[156]
Niacinamide	122	-0.37	5.0	0.7	*in vivo*	human	[147]
Niflumic acid	282	4.43	3.0	0.1-3.0	*in vivo*	human	[155]
Nimesulide	308	2.60	1.0	1.0	*in vivo*	human	[92]
Oxygen gas	32	0.65	0.97	1.0-2.0	*in vitro*	frog	[242]
Panax notoginseng	-	-	1.0	0.5	*in vivo*	rat	[243]
Panthenol	205	-1.92	3.0	0.1	*in vitro*	p FTS	[244]
Paraaminohippuric acid	194	-0.89	[c]	[c]	*in vitro*	m FTS	[245]
Penicillamine (cuprenil)	149	-1.78	[c]	[c]	*in vivo*	human	[179]
Penicillin	334	1.83	[c]	[c]	*in vivo*	human	[246]
Phenylbutazone	308	3.16	3.0	0.1-3.0	*in vivo*	human	[155]
			[c]	[c]	*in vivo*	human	[158, 247]
Physostigmine	275	1.58	1.0	1.5-3.0	*in vivo*	gp, rat	[33]
Piroxicam	331	3.06	3.0	0.5	*in vivo*	human	[96]
			1.0-3.0	1.0-2.0	*in vitro*	h FTS	[248]
			0.8-0.87	0.5-3.0	*in vitro*	r FTS	[210, 249]
Prednisolone	360	1.62	1.0	1.50-4.32	*in vitro*	m FTS	[250, 251]
Prednisolone acetate	402	2.40	1.0	1.50-4.32	*in vitro*	m FTS	[250]
Progesterone	314	3.87	1.0-3.0	0-2	*in vitro*	h FTS	[34]
Radioiodine	131	2.49	[c]	[c]	*in vivo*	human	[252]
Reparil (mix of Aescin, Diethylamine salicylate)	1131 211	- -	[c]	[c]	*in vivo*	human	[253]
Salicylic acid	138	2.26	2.0-16	0.2	*in vivo*	gp	[103]
			1.0	3.0	*in vitro*	m FTS	[104]

Scopolamine	303	0.98	[c]	[c]	*in vivo*	human	[254]
Sinomenine	329	1.05	0.8	[c]	*in vitro*	r FTS	[121]
Silver Chloride	143	-	1.0-3.0	1.0, 2.2	*in vivo*	fish	[255]
Silver Nitrate	170	-	0.79-2.9	0.5	*in vivo*	rat	[256]
Streptomycin	582	-7.53	[c]	[c]	*in vivo*	rabbit	[257]
Sucrose	342	-3.70	3.5	0.1-2.0	*in vitro*	rat FTS	[143]
Sulforhodamine 101	607	-	1.0-3.0	1.4	*in vitro*	h FTS	[129]
Tannic acid	1.7k	-0.19	1.0	1.0	*in vivo*	human	[258-260]
Testosterone	288	3.32	1.0-3.0	0-2.0	*in vitro*	h FTS	[34, 112]
			1.0	0.5	*in vitro*	rat FTS	[261]
Tetracycline	444	-1.30	[c]	[c]	*in vivo*	cow	[262]
					in vivo	rabbit	[263]
Thiamin	337	-3.93	0.88	0.3-1.0	*in vivo*	human	[146]
Triamcinolone acetonide	434	2.53	1.0-3.0	1.0-2.5	*in vivo*	rat	[264, 265]
					in vitro	mouse	
Trilon B (Na_4EDTA[e])	380	-13.2	[c]	[c]	*in vitro*	frog	[266, 267]
Trolamine salicylate	287	-	1.0	0.5-1.5	*in vivo*	human	[268]
Urea	60	-2.11	1.0	1.0	*in vivo*	human	[258-260]
Zidovudine	266	0.05	1.1	1.5	*in vitro*	h FTS	[269]
					in vitro	m FTS	
Zinc Sulfate	65	-0.47	1.0	1.0	*in vivo*	human	[258-260]

[a] from Syracuse Research Corporation physical property database.[270]
[b] legend: h = human, p = pig, r = rabbit, m = mouse, gp = guinea pig, FTS = full-thickness skin, and HSS = heat-stripped skin.
[c] not available or not specified.
[d] estimated from references or other sources.
[e] ethylenediaminetetraacetate tetrasodium salt.
[f] 600 kPa, not reported in W/cm^2.

therapies, as evidenced by the large number of *in vivo* human studies presented in Table 1-1 (in comparison, far fewer *in vivo* studies are summarized in Table 1-2 in the case of LFS). Therefore, as evidenced by the nearly 90 compounds tested with HFS listed in Table 1-1, the use of therapeutic and high-frequency ultrasound for skin penetration enhancement has a rather large scope, with interest in the technology continuing to the present day.[92-96, 142]

1.5.2 Low-Frequency Sonophoresis

LFS is at a disadvantage relative to HFS in that it has been studied extensively only over the past two decades. Therefore, LFS has been investigated in fewer studies and currently lacks the historical track record of safety that HFS enjoys. The first investigations devoted *solely* to the use of LFS for transdermal delivery were conducted by Tachibana and Tachibana in the early 1990s,[100, 271, 272] and involved the use of 48 kHz and 105 kHz ultrasound for the delivery of insulin and lidocaine to mice and rabbits. Surprisingly, a review of the literature shows that Griffen *et al.* used LFS at 90 kHz, *in 1965*,[190] and demonstrated that the penetration of cortisol into subcutaneous pig nerves was higher for the 90 kHz treatments than those at 1MHz. However, frequencies in the range 20 – 100 kHz were seemingly forgotten for the next 25 years, until the aforementioned publications by Tachibana and Tachibana.[100, 271, 272] These studies were followed by work done by Mitragotri *et al.*, who showed that macromolecules even larger than insulin could be delivered transdermally at therapeutic levels, including interferon-γ (17 kDa) and erythropoietin (48 kDa).[20] A subsequent investigation demonstrated that LFS is up to three orders of magnitude more effective at increasing skin penetration enhancement of compounds transdermally than HFS.[30] From these beginnings, research on low-frequency

Table 1-2. Molecules that have been delivered transdermally by low-frequency ultrasound.

Molecule	MW (Da)	Log $K_{o/w}$[a]	Freq. (kHz)	Amp. (W/cm^2)	Skin Model[b]		Ref.
Acetic acid	60	-0.17	58	1.08	*in vitro*	p FTS	[273]
Aldosterone	360	1.08	20	0.125	*in vitro*	h HSS	[30]
Aminopyrine	231	1.00	150	0.111	*in vitro*	rat FTS	[105, 274]
Antipyrine	188	0.38	150	0.111	*in vitro*	rat FTS	[105]
Ascorbic acid	176	-1.85	25	0.05-0.1	*in vivo*	human	[275]
Azelaic acid	188	1.57	25	0.05-0.1	*in vivo*	human	[275]
Benzoate ion	121	-2.27	150	0.111	*in vitro*	rat FTS	[276]
Betamethasone valerate	477	3.60	36	2.72	*in vivo*	human	[277]
Bovine serum albumin	66k	-	20	[g]	*in vitro*	rat FTS	[124]
					in vivo	rat	
Butanol	74	0.88	20	0.125	*in vitro*	h HSS	[30]
Caffeine	194	-0.07	20	2.5	*in vitro*	rat FTS	[278]
			40	0.13-0.44	*in vitro*	m FTS	[156]
Calcein	623	-	20	1-15	*in vitro*	p FTS	[14, 15, 43, 51]
			41 - 445	0.06-0.30	*in vitro*	rat FTS	[62, 69, 279]
Clobetasol propionate	467	3.50	20	[d]	*in vitro*	m FTS	[280]
Corticosterone	346	1.94	20	0.125	*in vitro*	h HSS	[30]
			58	1.08	*in vitro*	p FTS	[273]
Cortisol	362	1.61	90	1.0	*in vivo*	pig	[190]
Cyclobarbital	236	1.77	150	0.111	*in vitro*	rat FTS	[105, 274]
Cyclosporin	1.2k	2.92	25	0.05-0.1	*in vivo*	human	[275]
			20	0.4-1.2	*in vitro*	rat FTS	[114]
Daniplestim	13k	-	55	≤15	*in vivo*	rat	[281]
Dextran	70k	-	58, 20	1.08, 7.0	*in vitro*	p FTS	[61, 65]
Deuterium oxide	20	-1.38	41 – 445	0.06-0.24	*in vitro*	rat FTS	[105, 274, 279]
Epinephrine	183	-1.37	55	≤15	*in vivo*	human	[19]

Erythropoeitin	48k	-	20	0-0.225	*in vitro*	h HSS	[20]
Estradiol	272	4.01	20	0.125	*in vitro*	h HSS	[30]
Fentanyl	336	4.05	20	2.5	*in vitro*	rat FTS	[278]
FITC-dextran[c]	4.4k, 38k	-	20	4.4	*in vitro*	p FTS	[44]
			41, 150	0.06-0.30	*in vitro*	rat FTS	[69, 105]
Fluorescein	332	3.35	20	0.008-0.024	*in vitro*	h FTS	[282]
5-Fluorouracil	130	-0.89	150	0.111	*in vitro*	rat FTS	[105]
Flurbiprofen	244	4.16	150	0.111	*in vitro*	rat FTS	[105]
Glucose	180	-3.24	20	[g]	*in vitro*	p FTS	[57]
Gold nanoparticles	5 nm	-	20	7.5	*in vitro*	p FTS	[56]
					in vitro	p 700	
Heparin	10k – 19k[f]	-	20	7.0, 7.4	*in vitro*	p FTS	[45, 65]
					in vivo	rat	[65]
Heparin (Low-Molecular	3.0k – 8.0k[f]	-	20	7.0	*in vivo*	rat	[65]
Weight)			20	7.0	*in vitro*	p FTS	[65]
			55	≤15	*in vitro*	rat FTS	[283]
Histamine	111	-0.70	36	2.72-3.5	*in vivo*	human	[284]
Ibuprofen	206	3.97	150	0.111	*in vitro*	rat FTS	[105]
Indomethacin	358	4.27	20	0.2	*in vitro*	m FTS	[122]
Interferon - γ	17k	-	20	0.0125-0.225	*in vitro*	h HSS	[20]
Insulin	5.8k	-	48	[e]	*in vivo*	mouse	[272]
			20	0-10.0	*in vivo*	rat	[20, 285-287]
			20, 32, 105	0.05-0.1, [e]	*in vivo*	rabbit	[271, 288, 289]
			20	0.1, 2.5	*in vivo*	pig	[287, 290]
			20	0.0125-1.0	*in vitro*	h HSS	[20, 291]
			20	0.173	*in vitro*	h FTS	[292]

Inulin	5.0k	-	20	1.6	*in vivo*	rat	[47]
			58, 20	1.08, 7.0	*in vitro*	p FTS	[61, 65]
			20	7.2	*in vitro*	h FTS	[53, 55]
Iron oxide particles	5 - 10 nm	-	25	0.8	*in vivo*	mouse	[58]
Isosorbide dinitrate	236	1.31	150	0.111	*in vitro*	rat FTS	[105]
Ketoprofen	254	3.12	150	0.111	*in vitro*	rat FTS	[105]
Kojic acid	142	-0.64	25	0.05-0.1	*in vivo*	human	[275]
Lanthanum nitrate	433	-	35	0.80	*in vivo*	mouse	[58]
LHRH	1.3k	-	58	1.08	*in vitro*	p FTS	[61]
Lidocaine	234	2.44	55	≤15	*in vivo*	human	[17-19, 293-295]
			48	0.17	*in vivo*	mouse	[100]
			150	0.111	*in vitro*	rat FTS	[105]
Lipid particles	~100 nm[f]	-	20	2.5-5.0	*in vitro*	rat FTS	[261]
Liposomes	0.08 µm,	-	20	[g]	*in vitro*	rat FTS	[124]
	4.6 µm				*in vivo*	rat	
Mannitol	182	-3.10	20	1.6	*in vivo*	rat	[47]
			20	6.5	*in vivo*	pig	[48]
			20	1.6, 6.5	*in vitro*	h HSS	[21, 48]
			20	7.2	*in vitro*	h FTS	[53, 55]
			20	6.5	*in vitro*	p 700	[48]
			19 - 93	1.08-14	*in vitro*	p FTS	[10, 12, 21, 48, 49, 61, 273]
Methylprednisolone	374	1.82	55	≤15	*in vivo*	human	[275]
Microparticles	1.5-173 µm[h]	-	20	19	*in vitro*	h HSS	[296]
					in vitro	h FTS	
Morphine	285	0.89	40	0.13-0.44	*in vitro*	m FTS	[156]
Nile red	318	-	20	15	*in vitro*	p FTS	[43]
Oligonucleotides	7k – 10k[f]	-	20	2.4	*in vitro*	p FTS	[66]
poly-l-lysine-FITC[c]	51k	-	20	2-50	*in vitro*	h HSS	[296]

Quantum dots	10-22 nm	-	20	7.5	*in vitro*	p700	[56, 297]
			20	7.5, 2.4	*in vitro*	p FTS	[52, 56]
Octa-l-lysine-4-FITC[c]	2.5k	-	20	2-50	*in vitro*	h HSS	[296]
Polymer nanoparticles	200 nm	-	28	8	*in vivo*	rat	[298]
Prilocaine	220	2.11	55	≤15	*in vivo*	human	[18]
Raffinose	504	-6.76	20	7.2	*in vitro*	h FTS	[53, 55]
Rhodamine B	479	1.95	41	0.06-0.30	*in vitro*	rat FTS	[62, 69]
Rhod. B hexyl ester	627	-	20	7.2	*in vitro*	h FTS	[13]
Salicylic acid	138	2.26	20	0.125	*in vivo*	mouse	[30]
					in vitro	h HSS	
siRNA-liposomes	50 nm	-	20	0.05	*in vivo*	mouse	[299]
Sodium nonivamide acet.	373	-	20	0.20	*in vitro*	m FTS	[130]
Sucrose	342	-3.70	20	0.125, 1.6	*in vitro*	h HSS	[21, 30]
			20	7.5	*in vitro*	p 700	[14, 56]
			20	1.6, 7.5	*in vitro*	p FTS	[14, 21, 56]
Sulforhodamine B	559	-0.01	20, 58	0-7.5	*in vitro*	p FTS	[13]
Testosterone	288	3.32	20	2.5-5.0	*in vitro*	rat FTS	[261]
Tetanus Toxoid	150k	-	20	2.4, [g]	*in vivo*	mouse	[67, 300]
Tizanidine	254	-	20	10	*in vitro*	mouse	[123]
Urea	60	-2.11	20	7.2	*in vitro*	h FTS	[53, 55]
Vasopressin	1.1k	-8.37	20	0.1-1.0	*in vitro*	h HSS	[291]
Water	18	-1.38	20	0.125	*in vitro*	h HSS	[30]
			41	0.06-0.30	*in vitro*	rat FTS	[69]
			58	1.08	*in vitro*	p FTS	[273]

[a] from Syracuse Research Corporation physical property database.[270]
[b] Legend: h = human, p = pig, r = rabbit, m = mouse, gp = guinea pig, FTS = full-thickness skin, 700 = dermatomed 700 μm skin, and HSS = heat-stripped skin.
[c] FITC = Fluorescein isothiocyanate.
[d] estimated from references or other sources.
[e] Intensity was reported as 3000 - 8000 Pa.
[f] Molecular weight or size were estimated from references.
[g] A setting of 10-70% was reported (VCX 400 or 500, Sonics and Materials, USA).
[h] Particles larger than 25 μm in diameter were not observed to penetrate the skin.

ultrasound-mediated transdermal drug delivery has exploded, with dozens of different groups working on applications of this technology (see Table 1-2). All types of permeants, from small hydrophobic compounds, such as salicylic acid, to highly hydrophilic compounds, such as vasopressin, to proteins, such as insulin, and even vaccines or nanoparticles, have been delivered transdermally with LFS. All the permeants that have been delivered by LFS through varying skin models, to-date, are listed in Table 1-2. Note the wide range of molecules that have been delivered by LFS, including those that are either hydrophilic (negative octanol-water partition coefficient, log $K_{o/w}$) or hydrophobic (positive log $K_{o/w}$), and those that are low-molecular weight (< 1000 Da molecular weight, MW) or high-molecular weight (≥ 1000 Da MW). LFS has truly increased both the type and the extent to which molecules can be delivered through the skin at therapeutic levels, compared to HFS, which is typically limited to lower molecular weight compounds. Therefore, the scope of LFS may be even greater than that of HFS, although LFS faces more regulatory hurdles than HFS treatments, due to the current lack of historical precedence of safety.

1.6 Delivery of Hydrophilic Permeants and Macromolecules with LFS

1.6.1 Delivery of Hydrophilic Permeants

1.6.1.1 The Aqueous Porous Pathway Model

Although traditional transdermal transport models have typically utilized molecular weight and octanol-water partition coefficients ($\log K_{o/w}$) to describe solute transport through the skin, including transport of hydrophilic permeants,[312, 313] an improved mechanistic understanding of hydrophilic permeant transport through LFS-treated skin was made possible by the

development of the aqueous porous pathway model (APPM).[21] By assuming that hydrophilic permeants traverse the stratum corneum along the same pathways as the current carrying ions, the APPM derives a quantitative relationship between the skin permeability of hydrophilic permeants, P, and the skin electrical resistivity, R. Specifically, by utilizing relations from hindered-transport theory for the diffusion of permeants through confined pores,[314] the APPM demonstrates that a linear regression of log P versus log R should yield a slope of -1.[21] Moreover, by substituting the values of known parameters associated with the bulk solution, the skin membrane, and the diffusing permeant (hydrodynamic radius), one can calculate important structural parameters of the skin utilizing the APPM, including the average skin aqueous pore radius and the skin porosity to tortuosity ratio. The APPM has been applied to a broad class of hydrophilic permeants (see Table 1-3), for both small molecules and macromolecules, diffusing through LFS-treated skin.[12, 14, 15, 21, 51, 53, 55, 56, 61] Although the APPM assumes a single average pore radius, it can be extended to include: (i) a distribution of aqueous pore radii,[61] and (ii) lipophilic pathways.[273] There is strong evidence that there is a distribution of skin pore radii, as reflected by the fact that the size of the permeant used in the context of the APPM affects the average pore radius calculated.[53, 61] In other words, larger permeants can only travel through aqueous pores that are larger than their hydrodynamic radius. Therefore, macromolecules can only sample the upper tail of the aqueous pore radius distribution, while smaller permeants have access to a wider range of pore radii. In addition to the apparent pore radius depending on the size of the permeant used, the ultrasound amplitude also plays an important role. An examination of Table 1-3 shows that most studies conducted in the range 7.2 – 7.5 W/cm^2 at 20 kHz calculated the average skin aqueous pore radius to be close to 100 Å. On the other hand, studies which utilized 1.0 – 1.6 W/cm^2 at 20 kHz generally calculated average

skin aqueous pore radii which are smaller than 35 Å (comparable to the radius of native skin pores). It is also worth noting that at lower LFS intensities (1.08 W/cm^2), no frequency dependence of the pore radii was observed.[61] On the other hand, at higher LFS intensities (7.5 W/cm^2), pore radii were affected significantly by the applied ultrasound frequency (see Chapter 2).[14, 15] The observed intensity and frequency dependence of pore radii are both likely due to the formation of larger LTRs at higher ultrasound intensities. Indeed, it is known that large aqueous pores are formed almost exclusively within LTRs due to cavitational processes,[14, 15, 51, 273] and that LTR area is inversely proportional to skin resistivity (skin samples with lower skin resistivities generally possess larger LTRs).[14, 15, 51] Therefore, given that the log R values in Table 1-3 are lower for the samples treated at higher LFS intensities (7.2 – 7.5 W/cm^2), the larger pores and the observed frequency dependence of pore radii in these skin samples is due to an increase in LTR area and to a higher level of skin perturbation in these samples, with respect to samples treated at LFS intensities of 1.0 – 1.6 W/cm^2.

The APPM has been very useful to extract information about how various LFS treatment regimens, both in the presence and absence of chemical enhancers, affects the structural state of the skin. For example, the mechanistic investigation presented in Chapter 2 will investigate the pore radii within LTRs and non-LTRs of LFS-treated skin.[14, 15] It will be shown that the pore radii within LTRs correlate strongly with the applied LFS frequency, while the pore radii within non-LTRs are frequency independent, useful conclusions about the enhancement mechanisms operating within each skin region will be drawn (see Section 2.4.1).[14, 15] In addition, utilizing the APPM, Seto *et al.* have recently shown that the response of different skin models to the LFS/SLS treatment is not necessarily the same. Specifically, it was demonstrated that, although

Table 1-3. Hydrophilic molecules that have been investigated in the context of the aqueous porous pathway model (APPM) for LFS-treated skin.

		Ultrasound Parameters							APPM Results			
Molecule	MW (Da)	Freq. (kHz)	Amplitude (W/cm^2)	Skin-to-Horn Distance (mm)	log *R* Range	Duty Cycle	Co-Enhancer	Skin Model[a]	Slope	log C[b]	Pore Radius (Å)[c]	Ref.
Mannitol	182	19	1.08	3	0.3 to 1.7	100%	1% SLS	p FTS	-	-2.92	28 ± 10	[12]
Mannitol	182	58	1.08	3	0.2 to 1.6	100%	1% SLS	p FTS	-0.85	-2.93	23 ± 13	[61]
Mannitol	182	58	1.08	3	0.1 to 1.9	100%	1% SLS	p FTS	-	-2.91	29 ± 9	[12]
Mannitol	182	76	1.08	3	0.6 to 1.9	100%	1% SLS	p FTS	-	-2.92	28 ± 12	[12]
Mannitol	182	93	1.08	3	0.6 to 1.9	100%	1% SLS	p FTS	-	-2.94	26 ± 8	[12]
Mannitol	182	20	1.6	8	-1.0 to 0.4	10%	none	h HSS	-0.95	-2.50	> 92	[21]
Mannitol	182	20	1.6	8	-0.4 to 1.6	10%	none	p FTS	-0.87	-2.98	22 ± 20	[21]
Mannitol	182	20	7.2	3	0.6 to 0.8	50%	1% SLS	h FTS	-	-	41[d]	[53]
Mannitol	182	20	7.2	3	-1.1 to -0.9	50%	1% SLS	h FTS	-	-	57[d]	[53]
Sucrose	342	20	1.6	8	-1.0 to 0.1	10%	none	h HSS	-0.88	2.61	> 125	[21]
Sucrose	342	20	1.6	8	-0.2 to 1.7	10%	none	p FTS	-1.05	-3.21	23 ± 10	[21]
Sucrose	342	20	7.5	3	0.0 to 1.6	50%	1% SLS	h FTS	-1.08	-3.05	39	[56]
Sucrose	342	20	7.5	3	-0.4 to 1.6	50%	1% SLS	h 700	-1.04	-2.91	>120	[46]
Sucrose	342	20	7.5	3	-0.2 to 1.6	50%	1% SLS	h 250	-1.09	-2.69	>120	[46]
Sucrose	342	20	7.5	3	-0.3 to 1.4	50%	1% SLS	p FTS	-1.07	-2.95	113	[56]
Sucrose	342	20	7.5	3	-0.2 to 1.4	50%	1% SLS	p 700	-1.07	-2.89	113	[56]
Sucrose	342	20	7.5	3	-0.3 to 1.5	50%	1% SLS	p FTS	-1.08	-2.96	>120	[14]
Sucrose	342	20	7.5	3	-0.1 to 1.3	50%	1% SLS	p 700	-1.07	-2.90	>120	[14]
Sucrose	342	20	7.5	3	0.0 to 1.3	50%	none	p FTS	-0.98	-2.96	>120	[14]
Sucrose	342	20	7.5	3	0.0 to 1.3	50%	none	p 700	-1.02	-2.68	>120	[14]
Raffinose	504	20	7.2	3	0.6 to 0.8	50%	1% SLS	h FTS	-	-	88[d]	[53]
Raffinose	504	20	7.2	3	-1.1 to -0.9	50%	1% SLS	h FTS	-	-	98[d]	[53]
Calcein	623	20	7.5	3	-0.2 to -0.8	50%	1% SLS	p FTS	-0.92	-3.14	105	[15]
Calcein	623	40	7.5	3	-0.2 to -0.8	50%	1% SLS	p FTS	-1.02	-3.19	73.9	[15]
Calcein	623	60	7.5	3	-0.2 to -0.9	50%	1% SLS	p FTS	-1.08	-3.26	50.7	[15]
LHRH[e]	1311	58	1.08	3	0.0 to 1.7	100%	1% SLS	p FTS	-0.74	-3.42	28 ± 4	[61]
Inulin	5000	58	1.08	3	0.1 to 1.8	100%	1% SLS	p FTS	-0.65	-3.86	34 ± 4	[61]
Inulin	5000	20	7.2	3	0.6 to 0.8	50%	1% SLS	h FTS	-	-	111[d]	[53]
Inulin	5000	20	7.2	3	-1.1 to -0.9	50%	1% SLS	h FTS	-	-	95[d]	[53]
Dextran	70000	58	1.08	3	0.2 to 1.6	100%	1% SLS	p FTS	-0.44	-4.40	58 ± 3	[61]

[a] All skin models are *in-vitro*. Legend: p = pig, h = human, FTS = full-thickness skin, HSS = heat-stripped skin, 700 = 700-μm dermatomed skin, and 250 = 250-μm dermatomed skin.

[b] log C is equivalent to the y-intercept in a plot of log *P* vs. log *R*, where the slope is required to be equal to the APPM theoretical value of -1.

[c] Publications after 2008 utilized an updated form of the hindrance-factor expression in pore radius calculations.

[d] Pore radii were calculated by comparing permeant permeability to urea permeability, rather than to ion permeability (*R*).

[e] LHRH = luteinizing-hormone-releasing hormone.

full-thickness and split-thickness pig skin models respond in an equivalent manner to the LFS/SLS treatment, human skin models of varying thickness do not respond in an identical fashion.[56] In general, the APPM provides a useful tool to understand and analyze the transport of hydrophilic permeants across the skin, as well as to analyze the structural state of the skin following LFS treatment.

1.6.1.2 LFS-Mediated Transdermal Transport of Hydrophilic Permeants

The ability of LFS to increase skin permeability to hydrophilic permeants has been well established through research done with the APPM. Simple sugars, such as sucrose and raffinose (see Table 1-3), having log octanol-water partition coefficients (log $K_{o/w}$) less than -3,[270] and even larger water soluble fibers, such as inulin, have been shown to penetrate through skin in appreciable amounts following LFS treatment.[14, 15, 21, 53, 56, 61] In addition to allowing the delivery of hydrophilic permeants, LFS skin treatment has also been shown to allow the extraction of hydrophilic analytes, such as blood glucose (log $K_{o/w}$ = -3.24[270]).[22, 23, 310, 315] Strict glycemic control is critical for proper care of diabetic patients. By increasing the permeability of the skin using LFS, followed by the application of a transdermal glucose sensor, it has been shown that blood-glucose levels can be monitored continuously for up to 24 hours.[16, 309] The delivery and extraction of hydrophilic permeants in clinical use will be discussed further in Section 1.6.3.

1.6.2 Delivery of Macromolecules Utilizing LFS

The delivery of proteins, biopolymers, nanoparticles, and other high-molecular weight drugs or particles has received considerable attention during the past few years. However, this application of LFS is not just a recent trend, but dates back to some of the earliest studies with LFS.[20, 271] The benefit of transdermal protein delivery is that it bypasses the harsh environment of the gastro-intestinal tract, which can induce protein denaturation, enzymatic degradation, and loss of therapeutic activity. Moreover, compared to injections, it allows for controlled release profiles (not just a bolus), and displays possible compliance and safety benefits due to the elimination of needles from the delivery process.[1, 2] Therefore, it is not surprising that when LFS was established as a feasible means of delivering high-molecular weight proteins, some of the first molecules that were tested included proteins, such as insulin and interferon-γ.[20, 271] However, delivery of high-molecular weight molecules by LFS is not only limited to proteins, but includes high-molecular weight drugs, hormones, fibers, biopolymers, oligonucleotides, liposomes, nanoparticles, and even vaccines (see Table 1-4).

The most widely studied protein, with respect to transdermal delivery by LFS, is insulin (see Table 1-4), because of its implications in the treatment of diabetes. After Tachibana *et al.* showed the feasibility of transdermal insulin delivery with LFS,[271] Mitragotri *et al.* conducted the first comprehensive study comparing LFS-mediated insulin delivery with subcutaneous injection.[20] These authors showed that, above a threshold ultrasound intensity and treatment time, LFS-mediated insulin delivery was as effective at lowering blood glucose levels as subcutaneous injection, including lowering blood glucose levels of diabetic rats to normal levels.[20] More recently, there has been extensive research on insulin delivery using a light,

Table 1-4. High molecular weight molecules (>1000 g/mol) and particles that have been delivered transdermally with LFS.

		Ultrasound Parameters							
Molecule	MW (kDA)	Frequency (kHz)	Amplitude (W/cm^2)	Skin-to-Horn Distance (m)	US ON Time (min)	Duty Cycle	Co-Enhancer	Skin Model[a]	Ref.
Vasopressin	1.1	20	0.1 - 1.0	10	12 - 30	10%	hydrogel	*in vitro* h HSS	[291]
Cyclosporin A	1.2	20	0.4 -1.2	5	5 - 30	50%	various	*in vitro* rat FTS	[114]
LHRH	1.3	58	1.08	3	[b]	100%	1% SLS	*in vitro* p FTS	[61]
Octa-l-lysine-4-FITC[c]	2.5	20	2 - 50	2 – 4	0.05 - 3	5%	none	*in vitro* h HSS	[317]
FITC-dextran[c]	4.4	41	0.06 - 0.30	3	120	100%	none	*in vitro* rat FTS	[69]
Inulin	5.0	58	1.08	3	[b]	100%	1% SLS	*in vitro* p FTS	[61]
Inulin	5.0	20	7.2	3	[b]	50%	1% SLS	*in vitro* h FTS	[53]
Inulin	5.0	20	7.0	10	[d]	50%	1% SLS	*in vitro* p FTS	[65]
Dextran	5.0	20	7.0	10	[d]	50%	1% SLS	*in vitro* p FTS	[65]
Insulin	5.8	20	0.0125 - 0.225	10	1 - 24	10%	none	*in vitro* h HSS *in vivo* rat	[20]
Insulin	5.8	20	2.5 - 10.0	10	6 - 18	10 - 30%	none	*in vivo* rat	[286]
Insulin	5.8	20	0.173	5	60.0	20%	none	*in vitro* h FTS	[292]
Insulin	5.8	20	0.1	1	12	20%	none	*in vivo* pig	[290]
Insulin	5.8	20	0.1	1	12	20%	none	*in vivo* rabbit	[288]
Insulin	5.8	20, 32	0.05	1	12	20%	none	*in vivo* rabbit	[289]
Insulin	5.8	20	0.1	1	12	20%	none	*in vivo* rat	[285]
Insulin	5.8	20	0.1 - 1.0	10	12 - 30	10%	hydrogel	*in vitro* h HSS	[291]
Insulin	5.8	48	[e]	2	5	100%	none	*in vivo* mouse	[272]
Insulin	5.8	105	[e]	2	45	50%	none	*in vivo* rabbit	[271]
Low-Molecular Weight Heparin	< 8.0[f]	20	7.0	10	[d]	50%	1% SLS	*in vitro* p FTS *in vivo* rat	[65]
Oligonucleotides	7 - 10[f]	20	2.4	33	10	50%	1% SLS	*in vitro* P FTS	[66]
Daniplestim	13	55	15	7.5	1.5	100%	1% SLS	*in vivo* rat	[281]
Interferon - γ	17	20	0.0125 – 0.225	10	24	10%	none	*in vitro* h HSS	[20]
Heparin	10 - 19[f]	20	7.0	10	[d]	50%	1% SLS	*in vitro* p FTS *in vivo* rat	[65]
FITC-dextran[c]	38	41	0.06 – 0.30	3	120	100%	none	*in vitro* rat FTS	[69]
Erythropoeitin	48	20	0.0125 – 0.225	10	24.0	10%	none	*in vitro* h HSS	[20]
poly-l-lysine-FITC[c]	51	20	2 – 50	2 – 4	0.05 - 0.5	5%	none	*in vitro* h HSS	[317]
Bovine serum albumin	66	20	[g]	5	2	50%	0 - 1% SLS	*in vitro* rat FTS *in vivo* rat	[124]
Dextran	70	58	1.08	3	[b]	100%	1% SLS	*in vitro* p FTS	[61]
Dextran	70	20	7.0	10	[d]	50%	1% SLS	*in vitro* p FTS	[65]
Tetanus Toxoid	150	20	2.4	5	1.3	50%	1% SLS	*in vivo* mouse	[67]
Tetanus Toxoid	150	20	[g]	7.5	0.75	10 – 20%	0 - 1% SLS	*In vivo* mouse	[300]

Particles	Diameter	Ultrasound Parameters: Frequency (kHz)	Amplitude (W/cm^2)	Skin-to-Horn distance (mm)	US ON Time (min)	Duty Cycle	Co-Enhancer	Skin Model[a]	Ref.
Gold nanoparticles	5 nm	20	7.5	3	~3[h]	50%	1% SLS	*in vitro* p FTS *in vitro* p 700	[56]
Iron oxide particles	5 - 10 nm	25	0.8	0	5	100%	0.3 M oleic acid	*in vivo* mice	[58]
Quantum dots	10 - 22 nm	20	7.5	3	~3[h]	50%	1% SLS	*in vitro* p 700	[297]
Quantum dots	20 nm	20	7.5	3	~3[h]	50%	1% SLS	*in vitro* p FTS *in vitro* p 700	[56]
Quantum dots	20 nm	20	2.4	5	3	50%	0 - 1% SLS	*in vitro* p FTS	[52]
siRNA-liposome complex	50 nm	20	0.05	1	3	20%	none	*in vitro* cell lines *in vivo* mouse	[299]
Testosterone in solid lipid microparticles	~100 nm[f]	20	2.5 – 5.0	5	6 - 15	20 - 50%	1% dodecyl-amine	*in vitro* rat FTS	[261]
Lidocaine in polymer nanoparticles	200 nm	28	8	1	10	100%	none	*in vivo* rats	[298]
Liposomes	0.08 µm, 4.6 µm	20	[g]	5	2	50%	0 - 1% SLS	*in vitro* rat FTS *in vivo* rat	[124]
Microparticles	1 - 173 µm[i]	20	19	6	0.25 - 1.5	20-100%	none	*in vitro* h HSS *in vitro* h FTS	[317]

[a] Legend: p = pig, h = human, FTS = full-thickness skin, HSS = heat-stripped skin, and 700 = 700-µm dermatomed skin.
[b] No treatment times were specified, see log *R* values in Table 1 for relative extents of skin perturbation.
[c] FITC = fluorescein isothiocyanate.
[d] No treatment times were specified; skin was treated to a skin conductivity of 0.6 $(kohm\text{-}cm^2)^{-1}$.
[e] Amplitude was not reported in W/cm^2; reported intensity was 3000-8000 Pa.
[f] Molecular weight or size were not reported, but was instead estimated from the paper's references.
[g] Amplitude was not reported in W/cm^2; a setting of 20-30% on the machine was reported (VCX 500, Sonics and Materials, USA).
[h] Approximate treatment time, skin was treated to attain a specified range of skin resistivity values.
[i] Particles as large as 25 µm in diameter were observed to penetrate the skin, but larger particles did not.

portable cymbal array device, which operates at 20 kHz and intensities between 50 – 100 mW/cm^2.[285, 289, 290, 292] The novelty of the cymbal array is in its compact size, being only 3 mm in thickness and varying in surface dimensions between 3 cm × 3 cm and 6 cm × 6 cm, which allows the device to be worn during treatment. This could potentially lead to a closed-loop system, where one wearable device could house both a glucose sensor and the ultrasound transducer, allowing the delivery of insulin on demand in response to glucose readings. The feasibility of both insulin delivery[285, 289, 290, 292] and glucose sensing[310] using the cymbal array device has been tested and validated.

1.6.2.1 Transdermal Vaccination

In addition to insulin, another research area that is gaining increased attention is transdermal vaccination. Transdermal vaccination would provide many advantages over current injection-based methods of vaccination, because it would completely eliminate safety concerns involving the use of needles, especially with regards to misuse and improper re-use in lower-income areas and nations. Furthermore, using a patch vaccine formulation, it may be possible to expose the body to a lower concentration of antigens for a longer period of time, which could provide a similar, or stronger, immune response by targeting the Langerhans cells within the skin, while having the added safety benefit associated with lower concentrations of antigen encountered by the immune system.[306, 316] The first study of LFS-mediated vaccine delivery was conducted by Tezel *et al.*, and involved the delivery of tetanus toxoid (TT) into an *in vivo* mouse model following pretreatment with 20 kHz LFS and 1% SLS.[67] The study found that TT IgG titers increased with increasing LFS energy density (LFS energy density = LFS amplitude x LFS treatment time), and that the titers obtained with 1.3 μg of TT delivered by LFS were similar to

those obtained by subcutaneous injection of 10 μg of TT (note that subcutaneous injection of 5 μg of TT is sufficient for immunity to tetanus toxin). Therefore, the authors concluded that LFS not only elicits an enhanced immune response because of the increased delivery of TT to the Langerhans cells, but also through LFS-induced activation of Langerhans cells. In fact, LFS alone, in the absence of antigen, was found to induce activation of Langerhans cells in these studies.[67] Other studies have also shown the ability of high-amplitude LFS (5-7 W/cm^2) to induce an increased immune response, when compared to low-amplitude LFS (0.15 W/cm^2) and negative controls.[308] These findings demonstrate the significant potential of LFS to act as a physical adjuvant, and motivate further investigation of LFS-mediated transdermal immunization. A more recent study investigated the level of TT antibody titers in mice treated with LFS, while varying SLS concentrations and ultrasound parameters.[300] This study found that 0.5% SLS provided an immune response superior to that of 1% SLS, despite causing less skin perturbation. Similarly, a 10% duty cycle produced higher antibody titers than a 20% duty cycle, in spite of again causing less skin damage.[300] Therefore, it is clear that the mechanisms of immune response by LFS are not well understood, and more research is needed in order to optimize protocols for transdermal vaccination using LFS.

1.6.2.2 Delivery of Nanoparticles

In addition to the delivery of simple molecules, the delivery of nanoparticles and molecules in liposomal formulations have also been tested with LFS (see Table 1-4). With respect to mechanistic investigations, quantum dots (QDs) have been utilized in several studies, because it is possible to tune their size and surface chemistry in a controlled fashion.[52, 56, 297] A recent study by Lopez *et al.* investigated the delivery of QDs (10-22 nm in diameter), with varying

surface charge (cationic, neutral, and anionic), in order to evaluate LFS treatment to enhance skin penetration of transdermal carriers.[297] Lopez *et al.* found that the LFS treatment increased the amount of QDs penetrating past the epidermis by 500-1300%. Interestingly, however, the highest charged cationic QD did not penetrate the most, as originally expected, suggesting that there is an optimal cationic surface charge for designing transdermal carriers.[297] Other studies have considered the delivery of metallic nanoparticles into LFS-treated skin, including gold nanoparticles[56] and iron oxide nanoparticles.[58] The latter study, utilizing iron oxide nanoparticles, was conducted using zero clearance between the skin surface and the ultrasound horn, which is not typical of treatment protocols involving LFS. In general, it is advisable to leave some clearance between the skin and the ultrasound horn, even if it is a small distance (2-3 mm), to avoid the creation of pockets of air/coupling solution between the skin and the ultrasound horn. Without any clearance, small solution volumes trapped between the skin and the ultrasound horn, which are restricted from mixing with the bulk solution, could heat rapidly. This heating can cause thermal effects that are unaccounted for and could lead to difficulty in the interpretation of the mechanisms of enhancement.

Larger particles have also been delivered through LFS-treated skin, the majority of which are liposomal formulations. Liposomal formulations are a natural delivery vehicle in the context of LFS-mediated transdermal delivery, because formulations of lidocaine within liposomes are already clinically used for topical anesthesia, which will be discussed further in Section 1.6.3 (see Table 1-5). An interesting application of liposomal formulations has been reported by Tran *et al.* for the delivery of siRNA-liposome complexes for treatment of melanoma.[299] The study showed that the application of LFS enabled the delivery of loaded cationic liposomes throughout

the epidermis and the dermis of skin reconstructs, as well as in an *in vivo* mouse model, which led to a decrease of melanoma by a statistically significant amount.[299] Other studies have examined the delivery of liposomes or microparticles as large as 173 μm in diameter,[124, 317] and have shown that particles as large as 25 μm in diameter can penetrate the skin.[317] However, the study involving the delivery of microparticles as large as 173 μm was conducted at extremely high amplitudes, approximately 3 – 7-fold higher (19 – 49 W/cm^2) than the highest amplitudes commonly used for LFS-mediated transdermal delivery (7 – 8 W/cm^2). Therefore, although particles as large as 25 μm in diameter were delivered through heat-stripped skin, microscopy showed macroscopic holes in the skin,[317] which casts significant concern with regards to the safety of this treatment protocol. Under typical LFS conditions, which have been tested for safety, it is generally believed that particles no larger than ~100 nm can penetrate LFS-treated skin as intact entities (see Table 1-4).

1.6.3 Clinical Applications of LFS

LFS has been utilized in many clinical applications for the delivery and extraction of different types of drugs and analytes (see Table 1-5), in addition to being used for cosmetic purposes in skin rejuvenation and cellulite remediation. Here, I will focus solely on clinical applications relevant to drug delivery and analyte extraction. The first clinical application of LFS involved the delivery of liposomal lidocaine, or lidocaine/prilocaine (both are small, hydrophobic molecules), to decrease the time of onset for local anesthesia.[18] This application has been well documented, with multiple pilot and clinical trials showing that LFS decreases the onset to anesthesia with lidocaine, from 30-60 minutes passively, to less than 5 minutes with LFS pretreatment. This technology is FDA approved for use in both adults and children for local

Figure 1-7. Low-frequency ultrasound treatment in a clinical setting with the SonoPrep® device (Echo Therapeutics, Franklin, MA). The patient holds a conductive polymer hand-piece and the device automatically stops when the skin impedance is decreased to the desired treatment level. Usual treatment times are on the order of 10 seconds.

anesthesia prior to hypodermic injection, IV cannulation, and blood donation (SonoPrep®, Echo Therapeutics, Franklin, MA, see Figure 1-7).[17, 18, 293-295] The device has also been tested for use in combination with iontophoresis, which results in an even shorter time to onset of anesthesia (2 minutes).[19] Other applications of the device involve the extraction of interstitial fluid for blood-glucose and lactate monitoring, which is currently in the process of attaining FDA approval.[16, 309]

Other studies have investigated the delivery of hydrophilic molecules in clinical applications (see log $K_{o/w}$ values in Table 1-5), including the delivery of histamine,[284] kojic acid,[275] ascorbic acid,[275] and epinephrine.[19] Additionally, cyclosporine solution (MW = 1203 kDa) has been utilized in combination with LFS for the treatment of alopecia areata.[275] In all cases, the drugs delivered were reported to have the desired effect. For complete experimental details of clinical trials, refer to Table 1-5.

1.6.4 Safety of LFS

The safety of LFS for use in animals and humans has been evaluated rather rigorously for single dose applications. Clinical studies with the SonoPrep® device have shown that, following a single treatment (~10 seconds), there are usually minimal or no adverse reactions, with the most common side effect being mild erythema.[17, 18, 293-295] As stated above, the SonoPrep® has therefore been FDA approved for use in children and adults for decreasing the onset time to local anesthesia. The effect of LFS on animal models and cultured cell lines has also shown that the use of low ultrasound intensities is safe, causing no changes in skin pathology and cell viability.[20, 23, 30, 308, 318] In general, for single application treatments, thermal effects

Table 1-5. Drugs that have been tested in clinical (*in vivo* human) settings, including experimental details.

Drug	MW (Da)	log Ko/w[a]	Equipment: Device	Equipment: Manufacturer	Experimental Details: Purpose	Metric Utilized	Method: Randomized	Method: Blinded	Participants: Total	Participants: with LFS	Results: Benefit	Results: Conclusion	Ref.
Electrical current	-	-	SonoPrep[b]	Echo/ Sontra[c]	Skin resistivity reduction	Increase in skin impedance	No	No	10	10	Yes	LFS led to an immediate decrease in skin impedence, which lasted for 24 hours.	[318]
Electrical current)	-	-	SonoPrep[b]	Echo/ Sontra[c]	Recovery time of skin barrier properties	Increase in skin impedance	No	No	10	10	Yes	LFS caused increased and sustained skin permeability for up to 48 hours under occlusion. Skin barrier properties recovered rapidly after occlusion removal.	[319]
Histamine	111	-0.70	Mésothérapie Ultrasonore[d]	Trans-derma[e]	Transdermal histamine delivery with LFS	Papule formation caused by histamine, patient pain score	Yes	Yes	10	10	Yes	90% of patients showed papule formation with LFS, compared to none without LFS. Pain scores with LFS were similar to pain scores for pin prick tests.	[284]
Glucose extraction	180	-3.24	SonoPrep[b]	Echo/ Sontra[c]	Accurately monitor blood glucose through LFS-treated skin	Comparison of transdermal blood glucose readings to controls	No	No	10	10	Yes	Transdermal glucose monitoring was found to be safe and effective, with a correlation coefficient of 0.84 between the transdermal and control blood glucose measurements.	[16]
Glucose extraction	180	-3.24	SonoPrep[b]	Echo/ Sontra[c]	Accurately monitor blood glucose through LFS and abraded skin	Comparison of transdermal blood glucose readings to controls	Yes	Yes	24	24	Yes	Good agreement was observed between the transdermal (both LFS and abraded skin) and control blood glucose measurements.	[309]
Azelaic acid, ascorbic acid, and kojic acid (emulsion)	188, 176, 142	1.57, -1.85, -0.64	25 kHz, 50 -100 mW/cm^2	NS	Treatment of melasma and solar lentigo	Skin color and luminosity index	NS	NS	48	32	Yes	Treatment with emulsion and LFS resulted in complete depigmentation in 75% of melasma cases and 43% total remission in solar lentigo cases.	[275]
Liposomal lidocaine cream[f]	234	2.44	SonoPrep[b]	Echo/ Sontra[c]	Ability of LFS to decrease onset of lidocaine to 5 minutes	Patients' pain scores during IV cannulation, skin irritation	Yes	Yes	94	45	Yes	91% of LFS-treated patients reported pain scores less than 5, compared to 43% in the controls. Skin Irritation was similar in both.	[17]
Liposomal lidocaine cream[f]	234	2.44	SonoPrep[b]	Echo/ Sontra[c]	Ability of LFS to decrease onset of lidocaine to 5 minutes in children	Children's and parents' pain scores with IV placement	Yes	Yes	77	38	Yes	Both children's (2.29 vs. 3.23) and parents' (2.47 vs. 3.39) pain scores decreased significantly with LFS/lidocaine treatment, compared to controls.	[293]

Liposomal lidocaine cream[f]	234	2.44	SonoPrep[b]	Echo/ Sontra[c]	Ability of LFS to decrease pain associated with venipuncture in children	Children's' and parents' pain scores with IV placement	Yes	Yes	70	39	Yes	Compared to passive lidocaine for 30 minutes, 5 minutes of lidocaine post LFS resulted in statistically similar anesthetic effect for venipuncture.	[295]
Liposomal lidocaine cream[f]	**234**	**2.44**	**SonoPrep[b]**	**Echo/ Sontra[c]**	**Ability of LFS to decrease pain associated with blood donation**	**Patients' pain scores) during blood donation, skin irritation**	**Yes**	**Yes**	**100**	**49**	**Yes**	**LFS was shown to decrease onset of anesthesia to 5 minutes in a safe manner for use with blood donation.**	**[294]**
Lidocaine, epinephrine[g]	234, 183	2.44, -1.37	SonoPrep[b]	Echo/ Sontra[c]	Ability of LFS, in combination with iontophoresis, to decrease onset to 2 minutes	Patients' pain scores upon needle prick	Yes	Yes	30	10	Yes	Pain scores for 10 minute iontophoresis and 2 minute iontophoresis, following LFS, were statistically similar, showing that LFS decreases onset time to 2 minutes.	[19]
Lidocaine, Prilocaine (EMLA cream[h])	**234, 220**	**2.44, 2.11**	**SonoPrep[b]**	**Echo/ Sontra[c]**	**Ability of LFS to decrease onset of EMLA cream to 5 minutes**	**Patients' pain scores upon needle prick**	**Yes**	**Yes**	**42**	**42**	**Yes**	**Onset of cutaneous anesthesia was decreased from 60 minutes (without LFS) to 5 minutes with LFS, as evidenced by statistically similar pain scores.**	**[18]**
Methylpred-nisolone ointment	374	1.82	25 kHz, 50 - 100 mW/cm^2	NS	Treatment of alopecia areata	Hair re-growth (total, partial, none)	NS	NS	15	15	Yes	29% of patients had total re-growth and 57% of patients showed partial re-growth of hair within 3 months.	[275]
Beta-methasone-17-valerate cream	**477**	**3.60**	**Mésothérapie Ultrasonore[d]**	**Trans-derma[e]**	**Efficacy of topical steroids for vasoconstriction**	**Color of skin evaluated by chromometer and visual inspection**	**Yes**	**Yes**	**15**	**15**	**Yes**	**Vasconstriction increased after LFS and persisted for 6 hours, but disappeared by 24 hours. Occlusion increased the effect of LFS on vasoconstriction.**	**[277]**
Cyclosporine solution	1203	2.92	25 kHz, 50 - 100 mW/cm^2	NS	Treatment of alopecia areata	Hair re-growth (total, partial, none)	NS	NS	15	15	Yes	34% of patients had total re-growth and 33% of patients showed partial re-growth of hair within 3 months.	[275]

NS = not specified

[a] Log octanol-water partition coefficients reported from Ref 270 (Syracuse Research Corporation Physical Property Database).

[b] Operating frequency = 55 kHz, Amplitude ≤15 W/cm^2, transduce-to-skin distance = 0.5 cm, duty cycle = 100%, coupling medium = 1.0% SLS, and treatment times = ~10 seconds.

[c] Echo Therapeutics (Franklin, MA) merged with Sontra in 2007.

[d] Operating frequency = 36 kHz, Amplitude =2.72-3.5 W/cm^2, transducer-to-skin distance = 0.5 cm, duty cycle = 29-38% coupling medium = saline, and treatment time = 5 minutes.

[e] Transderma Systems (Tours, France).

[f] Ferndale Laboratories (Ferndale, MI).

[g] Iontocaine (Abbot Laboratories, Chicago, IL).

[h] EMLA = Eutectic mixture of local anesthetics.

caused by LFS are of most consequence to the skin if not monitored properly, causing potentially serious side effects such as burns, epidermal detachment, epidermal or dermal necrosis, and, on a cellular level, keratinocyte apoptosis.[308, 318] However, these types of side effects are easily mitigated by minimizing the duration and intensity of the LFS treatment utilized.

Although LFS has been generally accepted as safe for single dose uses, there have been no significant studies of the prolonged or repeated use of such treatments. These types of studies will need to be conducted to establish the safety of LFS in the treatment of chronic diseases. For example, the current application of non-invasive blood glucose monitoring would require daily LFS treatment, as would other drug delivery applications. Therefore, sustained *in vivo* safety studies are needed to understand the potential skin toxicities involved with repeated LFS treatment.

1.7 Emerging Trends in Sonophoresis

1.7.1 High-Frequency Sonophoresis

The future of HFS appears to be very similar to its past, that is, in its utilization for the treatment of topical or regional disorders. A review of publications in the last two years reveals that the most common types of drugs delivered with HFS are anti-inflammatory medications for joint and muscle pain, as well as ointments for local skin or muscle conditions. However, while historically the most common types of anti-inflammatory medications used with HFS have been topical steroids, such as cortisol, dexamethasone, or prednisolone (see Table 1-1), a shift has been seen in recent years to non-steroidal anti-inflammatory drugs (NSAIDs). These include: i) diclofenac, used to alleviate knee pain or arthritis,[209, 210], ii) ibuprofen, used to treat pain and

inflammation in arthritis and other ailments,[95, 210] iii) ketoprofen, used in treating pain of the knee and temporomandibular joints,[93], iv) ketorolac, used for post-operative pain and inflammation,[233] v) nimesulide, used for acute pain, such as that associated with osteoarthritis,[92] and vi) piroxicam, used to treat symptoms of arthritis.[96, 210, 249] This trend is likely due to the fact that oral NSAIDs commonly cause gastrointestinal (GI) side-effects, such as nausea, heartburn, GI ulcers, GI inflammation, nonspecific colitis, relapse of inflammatory bowel disease, and GI bleeding, among others.[301, 302] Meanwhile, common uses of oral NSAIDs include local joint conditions such as arthritis, that may be equally, or more, effective if administered topically, while greatly mitigating systemic side-effects.[303] In fact, it has been shown that treating GI-related side-effects of NSAID usage adds, on average, nearly 46% to the total cost of patient care.[304, 305] Therefore, creating a dependable and usable topical NSAID treatment method is clearly an area of need, and is a current and emerging trend with HFS.

Other recent studies that have utilized HFS for increased percutaneous absorption to treat local ailments include: i) aloe vera, a common skin moisturizer or skin healing agent,[94] ii) *Arnica montana*, a plant extract used to treat inflammatory muscle lesions,[145] iii) dimethylsulfoxide, for the treatment of local muscle damage and oxidative stress,[142] panax notoginseng, an herbal extract used to increase strength of local ligament repair,[243] and v) sinomenine, a morphinan derivative used in the treatment of rheumatism and arthritis.[121] In nearly all of these studies, the combination of HFS treatment with the active agent showed increased benefit over passive treatment with the drug alone. Therefore, because of its track-record of safety and its ability to increase the epidermal penetration of topical ointments, it is likely that HFS will continue to

emerge as a viable method for the delivery of low-molecular weight drugs (<1000 Da) for local and regional ailments.

1.7.2 Low-Frequency Sonophoresis

Unlike HFS, LFS is not restricted as severely by the size of the molecules that it can deliver, since proteins, vaccines, and even nanoparticles have been demonstrated to be deliverable by LFS (see Table 1-2). Therefore, emerging trends with LFS include the delivery of therapeutics for systemic, regional, or local conditions. Arguably the most exciting application is the use of LFS for transdermal vaccination. Transcutaneous administration of vaccines is already known to act as an immunization adjuvant, by targeting the Langerhans cells of the viable epidermis.[306, 307] Even ultrasound itself, without exposure to an antigen, has been shown to elicit an immune response and to activate Langerhans cells.[67, 308] Furthermore, it has been demonstrated that LFS can be utilized to deliver high-molecular weight vaccines, such as tetanus toxoid, and can offer equal protection as intramuscular injection.[67, 300] Therefore, it is of no surprise that transdermal vaccination by LFS is an area of increased research interest. Transdermal vaccination has the added safety benefits of decreased risk of needle misuse, abuse, or re-use, especially in lower income areas and nations where these types of issues can be a problem.[1, 2] Moreover, an equal immune response can be achieved by transdermal application of antigens, as injection, but with the body being exposed to a far smaller concentration of antigen. For example, Tezel *et al.* have shown that just 1.3 μg of tetanus toxoid delivered to the Langerhans cells after LFS treatment elicited an immune response equivalent to that of 10 μg injected subcutaneously in mouse models.[67] This clearly demonstrates the ability of LFS to deliver vaccines effectively.

Another interesting area of research is the use of LFS to transdermally deliver drug carriers, which could be used for targeted or systemic delivery of agents. For example, several groups have recently shown the ability of LFS to deliver nanoparticles as large as ~100 nm through the stratum corneum, the primary barrier of the skin, into the viable epidermal and dermal skin layers.[52, 56, 58, 297] Specifically, Lopez *et al.* have utilized functionalized quantum dots (QDs), to mimic drug delivery vehicles, in order to understand optimum surface chemistry for the delivery of nano-carriers through LFS-treated skin.[297] Their findings showed that cationic, neutral, and anionic QDs, ranging in size from 10 – 22 nm, could be delivered into the dermal layers of LFS-treated skin. They found that, unexpectedly, the cationic-functionalized QD with the highest charge did not penetrate to the greatest extent through LFS-treated skin. Therefore, it is likely that an optimal cationic surface charge exists when designing transdermal drug delivery vehicles.[297] Therefore, with further research in this area, one could design drug delivery carriers that could be administered through LFS-treated skin for applications such as transdermal vaccination, the delivery of drugs for treatment of skin disorders, or even for systemic delivery.

Other areas in which LFS has been utilized in emerging technologies include: i) blood glucose monitoring,[16, 22, 23, 47, 309-311], protein delivery,[235, 281, 285, 288, 289], and in clinical allergy testing.[284] Glucose-monitoring, coupled with transdermal insulin delivery,[235, 285, 288, 289] is especially exciting because it may permit the creation of a closed-loop system that allows for on-demand delivery of insulin, based on a patient's continuous blood-glucose measurements.[311] The miniaturization of LFS horns, to the size of 3 – 6 cm wearable devices, has brought this goal even closer to reality. [285, 288-290, 292, 299, 310, 311] Needless to say,

there are many emerging LFS technologies on the horizon that may change how doctors administer, and patients receive, drug therapies in the future.

1.8 Thesis Objectives

Although the field of low-frequency sonophoresis has progressed considerably over the past decade, there are still many unanswered questions concerning phenomena that occur in response to LFS treatment (see Sections 1.4.1 and 1.4.2). In order to address these unanswered questions and advance current understanding of the field of LFS, the following three research areas will be investigated in this thesis: i) understanding the role of cavitation in low-frequency sonophoresis (LFS), with specific emphasis to its role in inducing heterogeneous skin perturbation, ii) the role of chemical penetration enhancers (CPEs), primarily surfactants, in causing skin perturbation with LFS, and iii) the synergism between CPEs and cavitation in LFS treatment.

The first research area investigates the role of cavitation, particularly acoustic cavitation microjets, in the heterogeneous transport observed in LFS-treated skin (see Figure 1-6). In general, it is not well understood why highly-perturbed regions, LTRs, and less-perturbed regions, non-LTRs, are formed on skin samples treated with LFS. Therefore, it is not known what role cavitation, or other enhancement mechanisms, may be playing in the formation of each of these discrete skin regions. A deeper understanding of the transport pathways within these regions could lead to a deeper mechanistic understanding of the formation of LTRs and, therefore, allow for the exploitation of this mechanism to create larger LTR areas, which would permit not only achieving greater skin permeabilities but also more control of the extent of skin perturbation with LFS-treatment. Specifically, the research objectives in this area are to: i) better

characterize the transport pathways through LTRs and non-LTRs by independently determining the permeabilities and the effective aqueous pore radii in LTRs and non-LTRs, and ii) explain mechanisms of enhancement within LTRs and non-LTRs.

The second research area explores the role of surfactants in inducing skin perturbation when applied simultaneously with LFS. In particular, the role of traditional and non-traditional surfactants in causing skin perturbation with LFS is not well understood, especially with regards to their role in causing permeability enhancement within LTRs and non-LTRs of LFS-treated skin. In addition, non-traditional surfactants, such as dyes, are often utilized in LFS coupling solutions, with little known about how their inclusion affects the resulting skin permeability enhancement. Therefore, it is very important to understand how these additives affect LFS treatment protocols. This motivates the following important goals of this research area: i) understanding the role of surfactants in skin perturbation in LTRs and non-LTRs, and ii) elucidating the role of non-traditional surfactants, such as dyes that are added to typical LFS coupling solutions, on skin permeability enhancement.

The third research area ties together the first two research areas, by investigating the synergism between chemical penetration enhancers (CPEs), such as surfactants, and LFS. Specifically, in spite of previous work showing that LFS increases the penetration and dispersion of CPEs in the skin, no mechanism for this increased penetration has previously been proposed. Furthermore, the effect of a simultaneous treatment of skin with LFS and surfactants is not understood from the perspective of the structural changes which result from combined LFS/surfactant treatment. Therefore, little is known about how simultaneous skin treatment with LFS and surfactants can

affect important characteristics associated with LFS treatment, including reproducibility and predictability of permeability enhancement. Accordingly, the significant aims of this research area involve: i) explaining the mechanism of increased penetration and dispersion of CPEs, and specifically surfactants, in LFS-treated skin, ii) elucidating how the extent of skin perturbation differs between skin samples treated with LFS/surfactants and LFS, iii) understanding how skin structural parameters differ between skin samples treated with LFS/surfactants and LFS, iv) explaining how the extent of mechanical support (i.e., the thickness of the dermis in the skin model considered) affects the extent of skin perturbation in samples treated with LFS/surfactants and LFS, and v) elucidating how the reproducibility and predictability of skin permeability enhancement and treatment times of skin samples treated with LFS/surfactants compares to those of skin samples treated solely with LFS.

Investigating the three research areas discussed above will have a significant impact in furthering the current mechanistic understanding of low-frequency ultrasound-mediated transdermal drug delivery. Additionally, the insights provided by the proposed research could lead to the development of optimized LFS treatment protocols and improved LFS coupling solution formulations. This would permit attaining the desired skin permeability using milder LFS treatment conditions and smaller skin treatment areas. This could also lead to lower power requirements of LFS devices, thereby leading to miniaturization of devices and the creation of more commercially-viable LFS equipment.

1.9 Thesis Overview

The remainder of this thesis is devoted to an in-depth investigation of the role of cavitation, ultrasound, and their synergism in ultrasound-mediated transdermal drug delivery, especially with respect to previously poorly understood phenomena outlined in Section 1.8.

Chapter 2 provides a detailed study of the transport pathways present in the LTRs and non-LTRs of LFS-treated skin and elucidates the mechanisms that lead to these differences. Specifically, by utilizing the APPM and by treating skin at three LFS frequencies (20, 40, and 60 kHz), average pore radii for LTRs, non-LTRs, and total skin samples are calculated as a function of ultrasound frequency. This allows one to understand the role of cavitation, which is known to be a frequency-dependent process, as well as of other enhancement mechanisms, on skin perturbation within each skin region. In addition, the role of CPEs, such as the surfactant sodium lauryl sulfate (SLS), in causing skin perturbation within non-LTRs is examined.

Chapter 3 investigates the role of traditional and non-traditional surfactants in causing skin perturbation when applied simultaneously with LFS. In this chapter, the role of a commonly utilized fluorescent dye, sulforhodamine B (SRB), in affecting bulk and interfacial solution properties is investigated. SRB has been commonly used in the past as a colorimetric dye with LFS treatment in order to visualize LTRs, without investigating whether the dye itself could play a role in skin perturbation. These studies investigate explicitly the role of SRB in causing skin perturbation both passively and when combined with LFS. Additionally, I investigate how the combination of SRB with other CPEs, such as SLS, can have unintended consequences on the extent of skin perturbation produced.

Chapters 4 and 5 investigate the synergism between LFS and CPEs. Chapter 4 ties together many of the elements of the previous chapters of this thesis, especially Chapter 2, by proposing a physical mechanism by which LFS induces increased penetration of all CPEs into the LTRs of LFS-treated skin. In addition, a physical mechanism is proposed to explain why amphiphilic CPEs, specifically, should exhibit even greater synergism with LFS. These studies answer the important question of *how* the synergism between LFS and CPEs actually occurs, and specifically why this synergism is so pronounced with amphiphilic CPEs. Chapter 5 builds upon current understanding of the synergism between LFS and CPEs, specifically SLS, by investigating how skin treated solely with LFS compares to that treated with LFS/SLS from the viewpoint of skin structural perturbation. In Chapter 5, I investigate how the skin responds to treatment with LFS and LFS/SLS, including its implications on important metrics for transdermal delivery, such as reproducibility and predictability of the skin permeability enhancement.

Chapter 6 concludes this thesis by: (i) providing a summary of the important findings and conclusions of the research presented, (ii) presenting a critical analysis of the current and future prospects of LFS, and (iii) proposing future research directions in this area.

1.10 References

[1] M. Prausnitz, R. Langer, Transdermal drug delivery. Nat Biotechnol 26(11) (2008) 1261-1268.

[2] M. Prausnitz, S. Mitragotri, R. Langer, Current status and future potential of transdermal drug delivery. Nat Rev Drug Discov 3(2) (2004) 115-124.

[3] J. Bos, M. Meinardi, The 500 Dalton rule for the skin penetration of chemical compounds and drugs. Exp Dermatol 9(3) (2000) 165-169.

[4] R. Langer, New methods of drug delivery. Science 249(4976) (1990) 1527.

[5] B.W. Barry, Novel mechanisms and devices to enable successful transdermal drug delivery. Eur J Pharm Sci 14(2) (2001) 101-114.

[6] M.R. Prausnitz, The effects of electric current applied to skin: A review for transdermal drug delivery. Adv Drug Deliver Rev 18(3) (1996) 395-425.

[7] S. Jacques, D. McAuliffe, I. Blank, J. Parrish, Controlled removal of human stratum corneum by pulsed laser. J Invest Dermatol 88(1) (1987) 88-93.

[8] A. Arora, M.R. Prausnitz, S. Mitragotri, Micro-scale devices for transdermal drug delivery. Int J Pharm 364(2) (2008) 227-236.

[9] S. Mitragotri, J. Farrell, H. Tang, T. Terahara, J. Kost, R. Langer, Determination of threshold energy dose for ultrasound-induced transdermal drug transport. J Control Release 63(1-2) (2000) 41-52.

[10] S. Mitragotri, D. Ray, J. Farrell, H. Tang, B. Yu, J. Kost, D. Blankschtein, R. Langer, Synergistic effect of low-frequency ultrasound and sodium lauryl sulfate on transdermal transport. J Pharm Sci 89(7) (2000) 892-900.

[11] T. Terahara, S. Mitragotri, J. Kost, R. Langer, Dependence of low-frequency sonophoresis on ultrasound parameters; distance of the horn and intensity. Int J Pharm 235(1-2) (2002) 35-42.

[12] A. Tezel, A. Sens, S. Mitragotri, A theoretical analysis of low-frequency sonophoresis: dependence of transdermal transport pathways on frequency and energy density. Pharm Res 19(12) (2002) 1841-1846.

[13] J. Kushner, D. Kim, P. So, D. Blankschtein, R. Langer, Dual-channel two-photon microscopy study of transdermal transport in skin treated with low-frequency ultrasound and a chemical enhancer. J Invest Dermatol 127(12) (2007) 2832-2846.

[14] B.E. Polat, J.E. Seto, D. Blankschtein, R. Langer, Application of the aqueous porous pathway model to quantify the effect of sodium lauryl sulfate on ultrasound-induced skin structural perturbation. J Pharm Sci 100(4) (2011) 1387-1397.

[15] B.E. Polat, P.L. Figueroa, D. Blankschtein, R. Langer, Transport pathways and enhancement mechanisms within localized and non-localized transport regions in skin treated with low-frequency sonophoresis and sodium lauryl sulfate. J Pharm Sci 100(2) (2011) 512-529.

[16] H. Chuang, E. Taylor, T. Davison, Clinical evaluation of a continuous minimally invasive glucose flux sensor placed over ultrasonically permeated skin. Diabetes Technol The 6(1) (2004) 21-30.

[17] B. Becker, S. Helfrich, E. Baker, K. Lovgren, P. Minugh, J. Machan, Ultrasound with topical anesthetic rapidly decreases pain of intravenous cannulation. Acad Emerg Med 12(4) (2005) 289-295.

[18] N. Katz, D. Shapiro, T. Herrmann, J. Kost, L. Custer, Rapid onset of cutaneous anesthesia with EMLA cream after pretreatment with a new ultrasound-emitting device. Anesth Analg 98(2) (2004) 371.

[19] E. Spierings, J. Brevard, N. Katz, Two-minute skin anesthesia through ultrasound pretreatment and iontophoretic delivery of a topical anesthetic: A feasibility study. Pain Med 9(1) (2008) 55-59.

[20] S. Mitragotri, D. Blankschtein, R. Langer, Ultrasound-mediated transdermal protein delivery. Science 269(5225) (1995) 850-853.

[21] H. Tang, S. Mitragotri, D. Blankschtein, R. Langer, Theoretical description of transdermal transport of hydrophilic permeants: application to low-frequency sonophoresis. J Pharm Sci 90(5) (2001) 545-568.

[22] J. Kost, S. Mitragotri, R. Gabbay, M. Pishko, R. Langer, Transdermal monitoring of glucose and other analytes using ultrasound. Nat Med 6(3) (2000) 347-350.

[23] S. Mitragotri, M. Coleman, J. Kost, R. Langer, Transdermal extraction of analytes using low-frequency ultrasound. Pharm Res 17(4) (2000) 466-470.

[24] S. Mitragotri, Sonophoresis: a 50-year journey. Drug Discov Today 9(17) (2004) 735-736.

[25] K. Fellinger, J. Schmid, Klinik und Therapie des chronischen Gelenkrheumatismus, Maudrich, Vienna, Austria, 1954.

[26] M. Newman, M. Kill, G. Frampton, Effects of ultrasound alone and combined with hydrocortisone injections by needle or hypo-spray. Amer J Physical Med 37(4) (1958) 206 - 209.

[27] P. Tyle, P. Agrawala, Drug delivery by phonophoresis. Pharm Res 6(5) (1989) 355-361.

[28] D. Bommannan, G. Menon, H. Okuyama, P. Elias, R. Guy, Sonophoresis. II. Examination of the mechanism (s) of ultrasound-enhanced transdermal drug delivery. Pharm Res 9(8) (1992) 1043-1047.

[29] N. Byl, The use of ultrasound as an enhancer for transcutaneous drug delivery: phonophoresis. Phys Ther 75(6) (1995) 539.

[30] S. Mitragotri, D. Blankschtein, R. Langer, Transdermal drug delivery using low-frequency sonophoresis. Pharm Res 13(3) (1996) 411-420.

[31] R. Apfel, Acoustic cavitation: a possible consequence of biomedical uses of ultrasound. Br J Cancer Suppl 5 (1982) 140-146.

[32] J. Kost, D. Levy, R. Langer, Ultrasound effect on transdermal drug delivery. International Symposium Controlled Release 1986, pp. 177-178.

[33] D. Levy, J. Kost, Y. Meshulam, R. Langer, Effect of ultrasound on transdermal drug delivery to rats and guinea pigs. J Clin Invest 83(6) (1989) 2074.

[34] S. Mitragotri, D. Edwards, D. Blankschtein, R. Langer, A mechanistic study of ultrasonically-enhanced transdermal drug delivery. J Pharm Sci 84(6) (1995) 697-706.

[35] W. Gaertner, Frequency Dependence of Ultrasonic Cavitation. J Acoust Soc Am 26(6) (1954) 977-980.

[36] B. Baroli, Penetration of nanoparticles and nanomaterials in the skin: Fiction or reality? J Pharm Sci 99(1) (2010) 21-50.

[37] G. Cevc, U. Vierl, Nanotechnology and the transdermal route:: A state of the art review and critical appraisal. J Control Release 141(3) (2010) 277-299.

[38] B.E. Polat, D. Blankschtein, R. Langer, Low-frequency sonophoresis: application to the transdermal delivery of macromolecules and hydrophilic drugs. Expert Opin Drug Del 7(12) (2010) 1415-1432.

[39] T. Leighton, What is ultrasound? Prog Biophys Mol Bio 93(1-3) (2007) 3-83.

[40] A. Pointon, Piezoelectric devices. IEE Proc-A 129(5) (1982) 285-307.

[41] A. Boucaud, J. Montharu, L. Machet, B. Arbeille, M. Machet, F. Patat, L. Vaillant, Clinical, histologic, and electron microscopy study of skin exposed to low-frequency ultrasound. Anat Rec Part A 264(1) (2001) 114-119.

[42] H. Tang, C. Wang, D. Blankschtein, R. Langer, An investigation of the role of cavitation in low-frequency ultrasound-mediated transdermal drug transport. Pharm Res 19(8) (2002) 1160-1169.

[43] R. Alvarez-Román, G. Merino, Y. Kalia, A. Naik, R. Guy, Skin permeability enhancement by low frequency sonophoresis: lipid extraction and transport pathways. J Pharm Sci 92(6) (2003) 1138-1146.

[44] L. Wolloch, J. Kost, The importance of microjet vs shock wave formation in sonophoresis. J Control Release (in press) (2010).

[45] L. Le, J. Kost, S. Mitragotri, Combined effect of low-frequency ultrasound and iontophoresis: applications for transdermal heparin delivery. Pharm Res 17(9) (2000) 1151-1154.

[46] S. Mitragotri, Synergistic effect of enhancers for transdermal drug delivery. Pharm Res 17(11) (2000) 1354-1359.

[47] S. Mitragotri, J. Kost, Low-frequency sonophoresis: a noninvasive method of drug delivery and diagnostics. Biotechnol Prog 16(3) (2000) 488-492.

[48] H. Tang, D. Blankschtein, R. Langer, Effects of low-frequency ultrasound on the transdermal permeation of mannitol: comparative studies with in vivo and in vitro skin. J Pharm Sci 91(8) (2002) 1776-1794.

[49] T. Terahara, S. Mitragotri, R. Langer, Porous resins as a cavitation enhancer for low-frequency sonophoresis. J Pharm Sci 91(3) (2002) 753-759.

[50] A. Tezel, A. Sens, J. Tuchscherer, S. Mitragotri, Synergistic effect of low-frequency ultrasound and surfactants on skin permeability. J Pharm Sci 91(1) (2002) 91-100.

[51] J. Kushner, D. Blankschtein, R. Langer, Experimental demonstration of the existence of highly permeable localized transport regions in low-frequency sonophoresis. J Pharm Sci 93(11) (2004) 2733-2745.

[52] S. Paliwal, G. Menon, S. Mitragotri, Low-frequency sonophoresis: ultrastructural basis for stratum corneum permeability assessed using quantum dots. J Invest Dermatol 126(5) (2006) 1095-1101.

[53] J. Kushner, D. Blankschtein, R. Langer, Evaluation of the porosity, the tortuosity, and the hindrance factor for the transdermal delivery of hydrophilic permeants in the context of the aqueous pore pathway hypothesis using dual-radiolabeled permeability experiments. J Pharm Sci 96(12) (2007) 3263-3282.

[54] J. Kushner, D. Blankschtein, R. Langer, Heterogeneity in skin treated with low-frequency ultrasound. J Pharm Sci 97(10) (2008) 4119-4128.

[55] J. Kushner, D. Blankschtein, R. Langer, Evaluation of hydrophilic permeant transport parameters in the localized and non-localized transport regions of skin treated simultaneously with low-frequency ultrasound and sodium lauryl sulfate. J Pharm Sci 97(2) (2008) 906-918.

[56] J. Seto, B. Polat, R. Lopez, D. Blankschtein, R. Langer, Effects of ultrasound and sodium lauryl sulfate on the transdermal delivery of hydrophilic permeants: Comparative in vitro studies with full-thickness and split-thickness pig and human skin. J Control Release 145(1) (2010) 26-32.

[57] G. Merino, Y. Kalia, M. Delgado-Charro, R. Potts, R. Guy, Frequency and thermal effects on the enhancement of transdermal transport by sonophoresis. J Control Release 88(1) (2003) 85-94.

[58] S. Lee, K. Choi, G. Menon, H. Kim, E. Choi, S. Ahn, S. Lee, Penetration Pathways Induced by Low-Frequency Sonophoresis with Physical and Chemical Enhancers: Iron Oxide Nanoparticles versus Lanthanum Nitrates. J Invest Dermatol 130(4) (2010) 1063-1072.

[59] A. Tezel, S. Mitragotri, Interactions of inertial cavitation bubbles with stratum corneum lipid bilayers during low-frequency sonophoresis. Biophys J 85(6) (2003) 3502-3512.

[60] A. Tezel, A. Sens, S. Mitragotri, Investigations of the role of cavitation in low-frequency sonophoresis using acoustic spectroscopy. J Pharm Sci 91(2) (2002) 444-453.

[61] A. Tezel, A. Sens, S. Mitragotri, Description of transdermal transport of hydrophilic solutes during low-frequency sonophoresis based on a modified porous pathway model. J Pharm Sci 92(2) (2003) 381-393.

[62] H. Ueda, M. Mutoh, T. Seki, D. Kobayashi, Y. Morimoto, Acoustic Cavitation as an Enhancing Mechanism of Low-Frequency Sonophoresis for Transdermal Drug Delivery. Biol Pharm Bull 32(5) (2009) 916-920.

[63] I. Lavon, N. Grossman, J. Kost, The nature of ultrasound-SLS synergism during enhanced transdermal transport. J Control Release 107(3) (2005) 484-494.

[64] I. Lavon, N. Grossman, J. Kost, E. Kimmel, G. Enden, Bubble growth within the skin by rectified diffusion might play a significant role in sonophoresis. J Control Release 117(2) (2007) 246-255.

[65] S. Mitragotri, J. Kost, Transdermal delivery of heparin and low-molecular weight heparin using low-frequency ultrasound. Pharm Res 18(8) (2001) 1151-1156.

[66] A. Tezel, S. Dokka, S. Kelly, G. Hardee, S. Mitragotri, Topical delivery of anti-sense oligonucleotides using low-frequency sonophoresis. Pharm Res 21(12) (2004) 2219-2225.

[67] A. Tezel, S. Paliwal, Z. Shen, S. Mitragotri, Low-frequency ultrasound as a transcutaneous immunization adjuvant. Vaccine 23(29) (2005) 3800-3807.

[68] A. Tezel, A. Sens, J. Tuchscherer, S. Mitragotri, Frequency dependence of sonophoresis. Pharm Res 18(12) (2001) 1694-1700.

[69] Y. Morimoto, M. Mutoh, H. Ueda, L. Fang, K. Hirayama, M. Atobe, D. Kobayashi, Elucidation of the transport pathway in hairless rat skin enhanced by low-frequency sonophoresis based on the solute-water transport relationship and confocal microscopy. J Control Release 103(3) (2005) 587-597.

[70] M. Brown, G. Martin, S. Jones, F. Akomeah, Dermal and transdermal drug delivery systems: current and future prospects. Drug Deliv 13(3) (2006) 175-187.

[71] H. Tang, D. Blankschtein, R. Langer, Prediction of steady-state skin permeabilities of polar and nonpolar permeants across excised pig skin based on measurements of transient diffusion: Characterization of hydration effects on the skin porous pathway. J Pharm Sci 91(8) (2002) 1891-1907.

[72] S. Ghosh, D. Blankschtein, The role of sodium dodecyl sulfate (SDS) micelles in inducing skin barrier perturbation in the presence of glycerol. Int J Cosmetic Sci 30 (2007) 73.

[73] C. Brennen, Cavitation and bubble dynamics, Oxford University Press, USA, 1995.

[74] M. Margulis, Sonochemistry and Cavitation, Taylor & Francis, 1995.

[75] L. Crum, Sonochemistry and sonoluminescence, Springer Netherlands, 1999.

[76] S. Fong, E. Klaseboer, C. Turangan, B. Khoo, K. Hung, Numerical analysis of a gas bubble near bio-materials in an ultrasound field. Ultrasound Med Biol 32(6) (2006) 925-942.

[77] T. Leighton, A. Walton, M. Pickworth, Primary Bjerknes forces. Eur J Phys(1) (1990) 47.

[78] T. Leighton, An introduction to acoustic cavitation. Med Sci Ser (1998) 199–223.

[79] J. Simonin, On the mechanisms of in vitro and in vivo phonophoresis. J Control Release 33(1) (1995) 125-141.

[80] D. Hsieh, M. Plesset, Theory of Rectified Diffusion of Mass into Gas Bubbles. J Acoust Soc Am 33(2) (1961) 206-215.

[81] A. Eller, H. Flynn, Rectified diffusion during nonlinear pulsations of cavitation bubbles. J Acoust Soc Am 37 (1965) 493.

[82] A. Naji Meidani, M. Hasan, Mathematical and physical modelling of bubble growth due to ultrasound. Appl Math Model 28(4) (2004) 333-351.

[83] S. Jones, G. Evans, K. Galvin, Bubble nucleation from gas cavities -- a review. Adv Colloid Interfac 80(1) (1999) 27-50.

[84] J. Lee, S. Kentish, T. Matula, M. Ashokkumar, Effect of surfactants on inertial cavitation activity in a pulsed acoustic field. J. Phys. Chem. B 109(35) (2005) 16860-16865.

[85] T. Mason, D. Peters, Practical sonochemistry: Uses and applications of ultrasound, Horwood Publishing Limited, 2002.

[86] N. Pelekasis, A. Gaki, A. Doinikov, J. Tsamopoulos, Secondary Bjerknes forces between two bubbles and the phenomenon of acoustic streamers. J Fluid Mech 500 (2004) 313-347.

[87] R. Mettin, I. Akhatov, U. Parlitz, C.D. Ohl, W. Lauterborn, Bjerknes forces between small cavitation bubbles in a strong acoustic field. Phys Rev E 56(3) (1997) 2924.

[88] R. Mettin, P. Koch, W. Lauterborn, D. Krefting, Modeling acoustic cavitation with bubble redistribution. Sixth International Symposium on Cavitation, Wageningen, The Netherlands, 2006.

[89] R. Mettin, D. Krefting, J. Appel, P. Koch, W. Lauterborn, Stereoscopic high- speed recording of bubble structures. Proceedings of the 3rd Conference on Ultrasound in Processing, Paris, France, 2001, pp. 199-203.

[90] J. Appel, P. Koch, R. Mettin, D. Krefting, W. Lauterborn, Stereoscopic high-speed recording of bubble filaments. Ultrason Sonochem 11(1) (2004) 39-42.

[91] M. Ogura, S. Paliwal, S. Mitragotri, Low-frequency sonophoresis: current status and future prospects. Adv Drug Deliv Rev 60(10) (2008) 1218-1223.

[92] P. Barja, D. Veloso, Photoacoustic study of the penetration kinetics of nimesulid into human skin. International Conference on Photoacoustic and Photothermal Phenomena, IOP Publishing, 2010, p. (214) 012017.

[93] K. Kaya, S. Delialouglu, M. Babadag, D. Duleroglu, S. Ozel, C. Culha, S. Gorgun, Combined Physiotherapy in Patients with Arthrogenous Pain of Temporomandibular Joint. J PMR Sci 13 (2010) 6-14.

[94] A.L.M. Maia Filho, A.B. Villaverde, E. Munin, F. Aimbire, R. Albertini, Comparative Study of the Topical Application of Aloe Vera Gel, Therapeutic Ultrasound and Phonophoresis on the Tissue Repair in Collagenase-Induced Rat Tendinitis. Ultrasound Med Biol 36(10) (2010) 1682-1690.

[95] M. Meshali, H. Abdel-Aleem, F. Sakr, S. Nazzal, Y. El-Malah, Effect of gel composition and phonophoresis on the transdermal delivery of ibuprofen: In vitro and in vivo evaluation. Pharm Dev Technol (in press) (2010).

[96] F. Silveira, P. Barja, D. Acosta-Avalos, Photoacoustic evaluation of the penetration of piroxicam gel applied with phonophoresis into human skin. International Conference on Photoacoustic and Photothermal Phenomena, IOP Publishing, 2010, p. (214) 012022.

[97] P. Riesz, T. Kondo, Free radical formation induced by ultrasound and its biological implications. Free Radical Bio Med 13(3) (1992) 247-270.

[98] V. Meidan, A. Walmsley, W. Irwin, Phonophoresis is it a reality? Int J Pharm 118(2) (1995) 129-149.

[99] T. Julian, G. Zentner, Mechanism for ultrasonically enhanced transmembrane solute permeation. J Control Release 12(1) (1990) 77-85.

[100] K. Tachibana, S. Tachibana, Use of ultrasound to enhance the local anesthetic effect of topically applied aqueous lidocaine. Anesthesiology 78(6) (1993) 1091.

[101] I. Lenart, D. Ausländer, The effect of ultrasound on diffusion through membranes. Ultrasonics 18(5) (1980) 216-218.

[102] R. Brucks, M. Nanavaty, D. Jung, F. Siegel, The effect of ultrasound on the in vitro penetration of ibuprofen through human epidermis. Pharm Res 6(8) (1989) 697-701.

[103] D. Bommannan, H. Okuyama, P. Stauffer, R. Guy, Sonophoresis. I. The use of high-frequency ultrasound to enhance transdermal drug delivery. Pharm Res 9(4) (1992) 559-564.

[104] M. Machluf, J. Kost, Ultrasonically enhanced transdermal drug delivery. Experimental approaches to elucidate the mechanism. J Biomat Sci-Polym E 5(1-2) (1993) 147-156.

[105] H. Ueda, K. Sugibayashi, Y. Morimoto, Skin penetration-enhancing effect of drugs by phonophoresis. J Control Release 37(3) (1995) 291-297.

[106] D. Skauen, G. Zentner, Phonophoresis. Int J Pharm 20(3) (1984) 235-245.

[107] J. Sundaram, B. Mellein, S. Mitragotri, An experimental and theoretical analysis of ultrasound-induced permeabilization of cell membranes. Biophys J 84(5) (2003) 3087-3101.

[108] J. Isselin, A. Alloncle, M. Autric, On laser induced single bubble near a solid boundary: Contribution to the understanding of erosion phenomena. J Appl Phys 84 (1998) 5766.

[109] S. Watanabe, S. Takagi, K. Ga, K. Yamamoto, T. Aoyagi, Enhanced transdermal drug penetration by the simultaneous application of iontophoresis and sonophoresis. Drug Del Sci Tech 19(3) (2009) 185-189.

[110] A. Joshi, J. Raje, Sonicated transdermal drug transport. J Control Release 83(1) (2002) 13-22.

[111] M. Pahade, M. Jadhav, M. Kadam, Sonophoresis: An Overview. Int J Pharm Sci Res 3(2) (2010) 24-32.

[112] M. Johnson, S. Mitragotri, A. Patel, D. Blankschtein, R. Langer, Synergistic effects of chemical enhancers and therapeutic ultrasound on transdermal drug delivery. J Pharm Sci 85(7) (1996) 670-679.

[113] V. Meidan, M. Docker, A. Walmsley, W. Irwin, Phonophoresis of hydrocortisone with enhancers: an acoustically defined model. Int J Pharm 170(2) (1998) 157-168.

[114] H. Liu, S. Li, W. Pan, Y. Wang, F. Han, H. Yao, Investigation into the potential of low-frequency ultrasound facilitated topical delivery of Cyclosporin A. Int J Pharm 326(1-2) (2006) 32-38.

[115] S. Tiwari, R. Pai, N. Udupa, Influence of ultrasound on the percutaneous absorption of ketorolac tromethamine in vitro across rat skin. Drug Deliv 11(1) (2004) 47-51.

[116] X. Xu, Q. Zhu, C. Sun, Combined effect of ultrasound-SLS on skin optical clearing. IEEE Photonic Tech L 20(24) (2008) 2117-2119.

[117] X. Xu, Q. Zhu, C. Sun, Assessment of the effects of ultrasound-mediated alcohols on skin optical clearing. J Biomed Opt 14(3) (2009) 034042.

[118] X. Xu, Q. Zhu, C. Sun, Assessment of the effects of ultrasound-mediated alcohols on skin optical clearing. J Biomed Opt 14 (2009) 034042.

[119] H. Zhong, Z. Guo, H. Wei, L. Guo, C. Wang, Y. He, H. Xiong, S. Liu, Synergistic Effect of Ultrasound and Thiazone–PEG 400 on Human Skin Optical Clearing In Vivo. Photochem Photobiol 86(3) (2010) 732-737.

[120] H. Zhong, Z. Guo, H. Wei, C. Zeng, H. Xiong, Y. He, S. Liu, In vitro study of ultrasound and different-concentration glycerol--induced changes in human skin optical attenuation assessed with optical coherence tomography. J Biomed Opt 15(3) (2010) 036012.

[121] L. Li-an, W. Hong, L. Xin-Ping, G. Jian-Qing, Effect of Sonophoresis Combined with Chemical Enhancer on Transdermal Delivery of Sinomenine Hydrochloride Gel in Vitro. Chin Arch Trad Chin Med (2009).

[122] J. Fang, C. Fang, C. Hong, H. Chen, T. Lin, H. Wei, Capsaicin and nonivamide as novel skin permeation enhancers for indomethacin. Eur J Pharm Sci 12(3) (2001) 195-203.

[123] S. Mutalik, H. Parekh, N. Davies, N. Udupa, A combined approach of chemical enhancers and sonophoresis for the transdermal delivery of tizanidine hydrochloride. Drug Deliv 16(2) (2009) 82-91.

[124] A. Dahlan, H. Alpar, S. Murdan, An investigation into the combination of low frequency ultrasound and liposomes on skin permeability. Int J Pharm 379(1) (2009) 139-142.

[125] Y. Shah, A. Pandit, V. Moholkar, Cavitation reaction engineering, Plenum Pub Corp, 1999.

[126] G. Golden, J. McKie, R. Potts, Role of stratum corneum lipid fluidity in transdermal drug flux. J Pharm Sci 76(1) (1987) 25-28.

[127] B. Yu, C. Dong, P. So, D. Blankschtein, R. Langer, In vitro visualization and quantification of oleic acid induced changes in transdermal transport using two-photon fluorescence microscopy. J Invest Dermatol 117(1) (2001) 16-25.

[128] B. Yu, K. Kim, P. So, D. Blankschtein, R. Langer, Visualization of oleic acid-induced transdermal diffusion pathways using two-photon fluorescence microscopy. J Invest Dermatol 120(3) (2003) 448-455.

[129] J. Kost, U. Pliquett, S. Mitragotri, A. Yamamoto, R. Langer, J. Weaver, Synergistic effect of electric field and ultrasound on transdermal transport. Pharm Res 13(4) (1996) 633-638.

[130] J. Fang, T. Hwang, Y. Huang, Y. Tsai, Transdermal iontophoresis of sodium nonivamide acetate: V. Combined effect of physical enhancement methods. Int J Pharm 235(1-2) (2002) 95-105.

[131] T. Hikima, S. Ohsumi, K. Shirouzu, K. Tojo, Mechanisms of Synergistic Skin Penetration by Sonophoresis and Iontophoresis. Biol Pharm Bull 32(5) (2009) 905-909.

[132] A. Dakowicz, R. Latosiewicz, The value of iontophoresis combined with ultrasound in patients with the carpal tunnel syndrome. Rocz Akad Med Bialymst 50 (2005) 196-198.

[133] J. Dudelzak, M. Hussain, R. Phelps, G. Gottlieb, D. Goldberg, Evaluation of histologic and electron microscopic changes after novel treatment using combined microdermabrasion and ultrasound induced phonophoresis of human skin. J Cosmet Laser Ther 10(4) (2008) 187-192.

[134] E. Coodley, Bursitis and post-traumatic lesions: management with combined use of ultrasound and intra-articular hydrocortisone. Am Pract 11 (1960) 181 -187.

[135] O. Mune, K. Thorseth, Ultrasonic treatment of subcutaneous infiltrations after injections. Acta Orthop Scand 33(1-4) (1963) 347-349.

[136] J. Aldes, Ultrasonic radiation in the treatment of epicondylitis. GP 13(6) (1956) 89.

[137] J. Aldes, W. Jadeson, Ultrasonic therapy in the treatment of hypertrophic arthritis in elderly patients. Ann West Med Surg 6(9) (1952) 545.

[138] J. Aldes, T. Klaras, Use of ultrasonic radiation in the treatment of subdeltoid bursitis with and without calcareous deposits. West J Surg Obstet Gynecol 62(7) (1954) 369-376.

[139] W. Bierman, Ultrasound in the treatment of scars. Arch Phys Med Rehabil 35(4) (1954) 209-214.

[140] J. Kuitert, M. Davis, A. Brittis, J. Aldes, Control of keloid growth with ultrasonic energy; a report of two cases. Am J Phys Med 34(3) (1955) 408-412.

[141] O. Mune, K. Thorseth, Ultrasonic Treatment of Cicatricalgia. Acta Orthop Scand 33(1-4) (1963) 342-346.

[142] P. Silveira, E. Victor, D. Schefer, L. Silva, E. Streck, M. Paula, R. Pinho, Effects of Therapeutic Pulsed Ultrasound and Dimethylsulfoxide (DMSO) Phonophoresis on Parameters of Oxidative Stress in Traumatized Muscle. Ultrasound Med Biol 36(1) (2010) 44-50.

[143] V. Meidan, M. Docker, A. Walmsley, W. Irwin, Low intensity ultrasound as a probe to elucidate the relative follicular contribution to total transdermal absorption. Pharm Res 15(1) (1998) 85-92.

[144] I. Romanenko, R. Aravi ski Comparative levels of amphotericin B in the skin and subcutaneous fatty tissue after cutaneous application of amphotericin ointment by phonophoresis and with preliminary treatment by dimethyl sulfoxide. Antibiot Khimioter 36(9) (1991) 29.

[145] P. Alfredo, C. Anaruma, A. Pião, S. João, R. Casarotto, Effects of phonophoresis with Arnica montana onto acute inflammatory process in rat skeletal muscles: An experimental study. Ultrasonics 49(4-5) (2009) 466-471.

[146] L. Glushchenko, Phonophoresis of thiamin and ascorbic acid. Zdravookhr Beloruss 11 (1977) 80-81.

[147] T. Hakozaki, H. Takiwaki, K. Miyamoto, Y. Sato, S. Arase, Ultrasound enhanced skin-lightening effect of vitamin C and niacinamide. Skin Res Technol 12(2) (2006) 105-113.

[148] A.R. Williams, Phonophoresis: An in vivo evaluation using three topical anaesthetic preparations. Ultrasonics 28(3) (1990) 137-141.

[149] D. Chatterjee, A double-blind clinical study with benzydamine 3% cream on soft tissue injuries in an occupational health centre. J Int Med Res 5(6) (1977) 450 - 458.

[150] H. Benson, J. McElnay, J. Whiteman, R. Harland, Lack of effect of ultrasound on the percutaneous absorption of benzydamine. J Pharm Pharmacol 38 (1986).

[151] H. Benson, J. McElnay, R. Harland, Use of ultrasound to enhance percutaneous absorption of benzydamine. Phys Ther 69(2) (1989) 113.

[152] D. Hofmann, F. Moll, The effect of ultrasound on in vitro liberation and in vivo penetration of benzyl nicotinate. J Control Release 27(3) (1993) 185-192.

[153] P. Indkevich, Experience in the treatment of hidradenitis with biomycin phonophoresis. Vestn Dermatol Venerol(44) (1971) 75 - 77.

[154] P. Indkevich, Use of biomycin phonophoresis in the treatment of suppurative skin diseases. Vestn Dermatol Venerol(37) (1972) 266 - 267.

[155] J. Famaey, Sonophoresis with non-steroidal antiinflammatory drugs. A survey of the problem (author's transl). J Belge Rhumatol Med Phys 30(3) (1975) 129 - 141.

[156] D. Monti, R. Giannelli, P. Chetoni, S. Burgalassi, Comparison of the effect of ultrasound and of chemical enhancers on transdermal permeation of caffeine and morphine through hairless mouse skin in vitro. Int J Pharm 229(1-2) (2001) 131-137.

[157] E.H. Choi, M.J. Kim, B.-I. Yeh, S.K. Ahn, S.H. Lee, Iontophoresis and Sonophoresis Stimulate Epidermal Cytokine Expression at Energies That Do Not Provoke a Barrier Abnormality: Lamellar Body Secretion and Cytokine Expression Are Linked to Altered Epidermal Calcium Levels. J Invest Dermatol 121(5) (2003) 1138-1144.

[158] G. Wanet, N. Dehon, Clinical study of ultrasonophoresis with a topical preparation combining phenylbutazone and alpha-chymotrypsin. J Belge Rhumatol Med Phys 31(2) (1976) 49 - 58.

[159] S. Gatev, E. Vatsov, Attempt to treat essential pruritus vulvae and some inflammatory gynecologic diseases with hydrocortisone phonophoresis. Akush Ginekol 5(2) (1966) 123.

[160] S. Safiulina, A. Pushkareva, Experience in the phonophoresis treatment with hydrocortisone of patients with diseases of the musculoskeletal system. Vopr Kurortol Fizioter Lech Fiz Kult 32(6) (1967) 485 - 488.

[161] E. Nagovitsyn, Comparative evaluation of the effectiveness of hydrocortisone injections and phonophoresis in the treatment of diseases of the support-motor apparatus. Vestn Khir Im I I Grek 104(3) (1970) 54 - 55.

[162] E. Nagovitsyn, I. Vakhatova, Hydrocortisone phonophoresis for various diseases of the locomotor apparatus. Vopr Kurortol Fizioter Lech Fiz Kult 36(2) (1971) 180.

[163] E. Bel'ts, M. Bondarenko, The use of ultrasound and phonophoresis with hydrocortisone in chronic psoriasis. Vestn Dermatol Venerol(45) (1971) 70-72.

[164] T. Burgudzhieva, The treatment of pruritus vulvae essentialis with ultrasound and hydrocortisone ointment as well as phonophoresis with hydrocortisone ointment. Akush Ginekol 10(3) (1971) 231 - 234.

[165] T. Burgudzhieva, Comparative data on histological changes in the external genitalia in patients with pruritus vulvae essentialis before and after treatment by phonophoresis with unguentum hydrocortisone. Akush Ginekol 10(16) (1971) 477 - 482.

[166] T. Burgudzhieva, Histological changes in external genital organs in patients with kraurosis vulvae, treated by phonophoresis and hydrocortisone ointment. Akush Ginekol 10(4) (1971) 287 - 291.

[167] T. Burgudzhieva, Comparative study of treatment of kraurosis vulvae (lichen scleroatrophicus vulvae) with ultrasound, hydrocortisone ointment and phonophoresis with hydrocortisone ointment. Akush Ginekol 11(3) (1972) 246 - 251.

[168] T. Burgudzhieva, Effect of ultrasonics, hydrocortisone ointment and phonophoresis of hydrocortisone ointment on indices of sensory chronaximetry of kraurosis vulvae, lichen scleroatrophicus vulvae and pruritis vulvae essentialis. Vopr Kurortol Fizioter Lech Fiz Kult(3) (1974) 267 - 269.

[169] A. Grinshtein, S. Shevchenko, Rheoencephalographic studies of facial neuritis in treatment by ultrasonics and hydrocortisone phonophoresis. Vopr Kurortol Fizioter Lech Fiz Kult 38(3) (1973) 230.

[170] A. Grinshtein, A. Tolmacheva, V. Khriptulov, The effectiveness of hydrocortisone phonophoresis in facial nerve neuritis according to strength-duration findings. Vopr Kurortol Fizioter Lech Fiz Kult 36(6) (1971) 528 - 530.

[171] T. Bioarintseva, I. Grushlavski, Hydrocortisone phonophoresis treatment of various diseases of the weight bearing-locomoter apparatus. Vrach Delo(11) (1972) 119-120.

[172] N. Blinova, M. Ishchenko, The effect of hydrocortisone phonophoresis in the androgenic and glucocorticoid function of the adrenal cortex in patients with lumbosacral radiculitis. Vopr Kurortol Fizioter Lech Fiz Kult(37) (1972) 220-223.

[173] M. Antropova, Use of hydrocortisone phonophoresis in the treatment of facial nerve neuritis. Zh Nevropatol Psikhiatr Im S S Korsakova(7) (1974) 506 - 511.

[174] A. Kornienko, Use of hydrocortisone phonophoresis in the treatment of allergic rhinitis. Vestn Otolorinolaringol(1) (1974) 55 - 57.

[175] M. Braginski Treatment of certain dermatoses by hydrocortisone phonophoresis. Sov Med(7) (1975) 145.

[176] E. Bratslavskaia, S. Vitushkina, Hydrocortisone phonophoresis in trauma and diseases of the locomotor system in athletes. Med Sestra 34 (1975) 34 - 36.

[177] R. Kharitonov, V. Gol'dblat, A. Anisimov, Hydrocortisone phonophoresis in complex conservative treatment of arthrosis deformans of the knee joint. Ortop Traumatol Protez(2) (1975) 22 - 26.

[178] V. Artamonova, T. Nikitana, Use of ultrasound and hydrocortisone phonophoresis in the complex treatment of children with rheumatoid arthritis. Vopr Kurortol Fizioter Lech Fiz Kult(42) (1977) 29 - 33.

[179] V. Dozhanskaia, Hydrocortisone and cuprenil phonophoresis in the therapy of scleroderma. Vestn Dermatol Venerol.(10) (1980) 50 - 51.

[180] F. Pottenger, B. Karalfa, Utilization of hydrocortisone phonophoresis in United States Army Physical Therapy Clinics. Mil Med 154(7) (1989) 355.

[181] J. Griffin, J. Echternach, R. Price, J. Touchstone, Patients treated with ultrasonic driven hydrocortisone and with ultrasound alone. Phys Ther 47(7) (1967) 595 - 601.

[182] A. Bare, M. McAnaw, A. Pritchard, J. Struebing, M. Smutok, D. Christie, M. Domenech, M. Bare, M. Bloodworth, L. Seal, Phonophoretic delivery of 10% hydrocortisone through the epidermis of humans as determined by serum cortisol concentrations. Phys Ther 76(7) (1996) 738.

[183] P. Koeke, N. Parizotto, P. Carrinho, A. Salate, Comparative study of the efficacy of the topical application of hydrocortisone, therapeutic ultrasound and phonophoresis on the tissue repair process in rat tendons. Ultrasound Med Biol 31(3) (2005) 345-350.

[184] J. Kleinkort, F. Wood, Phonophoresis with 1 percent versus 10 percent hydrocortisone. Phys Ther 55(12) (1975) 1320 - 1324.

[185] A. Kuntz, C. Griffiths, J. Rankin, C. Armstrong, T. McLoughlin, Cortisol concentrations in human skeletal muscle tissue after phonophoresis with 10% hydrocortisone gel. J Athl Training 41(3) (2006) 321.

[186] N. Byl, A. McKenzie, B. Halliday, T. Wong, J. O'Connell, The effects of phonophoresis with corticosteroids: a controlled pilot study. J Orthop Sports Phys Ther 18(5) (1993) 590.

[187] J. Griffin, J. Touchstone, Ultrasonic movement of cortisol into pig tissues. I. Movement into skeletal muscle. Amer J Physical Med 42 (1963) 77 - 85.

[188] J. Griffin, J. Touchstone, Low-intensity phonophoresis of cortisol in swine. Phys Ther 48(12) (1968) 1336.

[189] J. Griffin, J. Touchstone, Effects of ultrasonic frequency on phonophoresis of cortisol into swine tissues. Amer J Physical Med 51(2) (1972) 62 - 78.

[190] J. Griffin, J. Touchstone, A. Liu, Ultrasonic movement of cortisol into pig tissue. II. Movement into the paravertebral nerve. Amer J Physical Med 44 (1965) 20 - 25.

[191] N. Popov, V. Kudriashov, L. Pristupa, 17-oxycorticosteroids in levels in blood and skin of rabbits after hydrocortisone phonophoresis. Voprosy kurortologii, fizioterapii, i lechebnoÄ fizicheskoÄ kultury 35(4) (1970) 295 - 297.

[192] V. Tsitlanadze, Changes in the metabolism of trace elements and the comparative effectiveness of treating infectious non-specific polyarthritis with ultrasound and hydrocortisone phonophoresis. Vopr Kurortol Fizioter Lech Fiz Kult 36(2) (1971) 158 - 161.

[193] V. Tsitlanadze, Morphohistochemical changes during experimental arthritis in rabbits caused by hydrocortisone phonophoresis. Soobshch Akad Nauk Gruz SSR(63) (1971) 237 - 240.

[194] V. Tsitlanadze, The mechanism of action of hydrocortisone phonophoresis in rabbits with adjuvant arthritis. Voprosy revmatizma 12(4) (1973) 19 - 22.

[195] J.P. Davick, R.K. Martin, J.P. Albright, Distribution and Deposition of Tritiated Cortisol Using Phonophoresis. Phys Ther 68(11) (1988) 1672-1675.

[196] W. Muir, F. Magee, J. Longo, R. Karpman, P. Finley, Comparison of ultrasonically applied vs. intra-articular injected hydrocortisone levels in canine knees. Orthop Rev 19(4) (1990) 351.

[197] L. Machet, N. Cochelin, F. Patat, B. Arbeille, M. Machet, G. Lorette, L. Vaillant, In vitro phonophoresis of mannitol, oestradiol and hydrocortisone across human and hairless mouse skin. Int J Pharm 165(2) (1998) 169-174.

[198] S. Safiulina, G. Proskurova, Phonophoresis of hydrocortisone. Vopr Kurortol Fizioter Lech Fiz Kult 35(4) (1970) 293 - 295.

[199] S. Gatev, Effect of ultrasonic phonophoresis on passage of hydrocortisone through the skin of Rana ridibunda. Eksp Med Morfol 11(4) (1972) 231 - 236.

[200] W. Quillin, Ultrasonic phonophoresis. Phys Sportsmed 10 (1982) 211.

[201] T. Conner-Kerr, M. Franklin, J. Kerr, S. Smith, R. Franklin, Phonophoretic delivery of dexamethasone to human transdermal tissues: a controlled pilot study. Eur J Phys Rehab Med 8(1) (1998) 19-23.

[202] M. Moll, A new approach to pain: lidocaine and decadron with ultrasound. USAF Med Serv Dig 30 (1979) 8-11.

[203] H. Darrow, S. Schulthies, D. Draper, M. Ricard, G. Measom, Serum dexamethasone levels after Decadron phonophoresis. J Athl Training 34(4) (1999) 338.

[204] S. Saliba, D. Mistry, D. Perrin, J. Gieck, A. Weltman, Phonophoresis and the Absorption of Dexamethasone in the Presence of an Occlusive Dressing. J Athl Training 42(3) (2007) 349.

[205] S. Alballa, Effect of phonophoretic application of diclofenac gel on localized musculoskeletal disorders. Curr Ther Res 55(11) (1994) 1382-1390.

[206] P. Barja, D. Acosta-Avalos, P. Rompe, F. Dos Anjos, F. Marciano, M. da Silva, In vivo evaluation of drug delivery after ultrasound application: A new use for the photoacoustic technique. J. Phys. IV France 125 (2005) 789-791.

[207] G. Rosim, C. Barbieri, F. Lanças, N. Mazzer, Diclofenac phonophoresis in human volunteers. Ultrasound Med Biol 31(3) (2005) 337-343.

[208] Y.-L. Hsieh, Effects of Ultrasound and Diclofenac Phonophoresis on Inflammatory Pain Relief: Suppression of Inducible Nitric Oxide Synthase in Arthritic Rats. Phys Ther 86(1) (2006) 39-49.

[209] D. Sharma, M. Hanesh, A. Yahya, M. Mohamed, Phonophoresis with Diclofenac versus Ketoprofen for Knee Joint

Injuries. Middle East J Int Med 2(2) (2009) 9 - 12.

[210] M. Meshali, H. Abdel-Aleem, F. Sakr, S. Nazzal, Y. El-Malah, In vitro phonophoresis: effect of ultrasound intensity and mode at high frequency on NSAIDs transport across cellulose and rabbit skin membranes. Pharmazie 63(1) (2008) 49-53.

[211] L. Machet, J. Pinton, F. Patat, B. Arbeille, L. Pourcelot, L. Vaillant, In vitro phonophoresis of digoxin across hairless mice and human skin: Thermal effect of ultrasound. International Journal of Pharmaceutics 133(1-2) (1996) 39-45.

[212] H.A.E. Benson, J.C. McElnay, R. Harland, J. Hadgraft, Influence of Ultrasound on the Percutaneous Absorption of Nicotinate Esters. Pharm Res 8(2) (1991) 204-209.

[213] H.A.E. Benson, J.C. McElnay, R. Harland, Phonophoresis of lignocaine and prilocaine from Emla cream. Int J Pharm 44(1-3) (1988) 65-69.

[214] Y. Wu, W. Chen, J. Luh, F. Chong, Thermal Effect of Sonophoresis for Accelerating the Analgesic Effect of Local Anesthetics on Rat Tail Nerve. International IEEE EMBS Conference, Vancouver, BC, 2008, pp. 2504-2507.

[215] E. Vainshtein, L. Lutsker, L. Zobina, A. Tartakovskaia, Electro-and phonophoresis of fibrinolysin. Vestn Oftalnol(4) (1975) 74 - 76.

[216] M. Hippius, C. Uhlemann, U. Smolenski, U. Schreiber, S. Reissig, A. Hoffmann, In vitro investigations of drug release and penetration: enhancing effect of ultrasound on transmembrane transport of flufenamic acid. Int J Clin Pharm Th 36(2) (1998) 107-111.

[217] C. Uhlemann, S. Reißig, M. Hippius, U. Smolenski, T. Schreiber, Phonophorese mit Flufenaminsäure in Abhängigkeit von Parametern der Ultraschalldosis Phonophoresis of flufenamin acid dependent on parameters of dose of ultrasound. Phys Rehab Kur Med 10 (2000) 86-93.

[218] A. Chirkin, V. Kozin, Enzymatic activity of the pentosephosphate pathway of carbohydrate conversion in the experimental therapy of dermatitis in rats. Vopr Med Khim 22(4) (1976) 448 - 451.

[219] V. Kozin, Morphological changes in the skin of rats under experimental therapy for dermatitis. Zdravookhr Beloruss(4) (1976) 81 - 82.

[220] V. Kozin, A. Chirkin, I. Griaditski Histamine and serotonin content in the blood and skin in experimental therapy of dermatitis in rats. Fiziol Zh 22(3) (1976) 390 - 394.

[221] J.C. McElnay, T.A. Kennedy, R. Harland, The influence of ultrasound on the percutaneous absorption of fluocinolone acetonide. International Journal of Pharmaceutics 40(1-2) (1987) 105-110.

[222] M. Klaiman, J. Shrader, J. Danoff, J. Hicks, W. Pesce, J. Ferland, Phonophoresis versus ultrasound in the treatment of common musculoskeletal conditions. Med Sci Sport Exer 30(9) (1998) 1349.

[223] V. Meidan, A. Walmsley, M. Docker, W. Irwin, Ultrasound-enhanced diffusion into coupling gel during phonophoresis of 5-fluorouracil. Int J Pharm 185(2) (1999) 205-213.

[224] P. Kafas, Ghicosaminoglycan Phonophoresis of the TMJ in the Symptomatic Treatment of Internal Derangement. J Med Sci 7(1) (2007) 158-160.

[225] D. Park, J. Yoon, J. Park, B. Jung, H. Park, J. Seo, Transdermal Drug Delivery Aided by an Ultrasound Contrast Agent: An In Vitro Experimental Study. Open Biomed Eng J 4 (2010) 56-62.

[226] V. Klare, W. KURY, On phonophoresis treatment with hirudoid. Wien Med Wschr 110 (1960) 701 - 702.

[227] S.R. Park, K.W. Jang, S.-H. Park, H.S. Cho, C.Z. Jin, M.J. Choi, S.I. Chung, B.-H. Min, The effect of sonication on simulated osteoarthritis. Part I: Effects of 1 MHz ultrasound on uptake of hyaluronan into the rabbit synovium. Ultrasound Med Biol 31(11) (2005) 1551-1558.

[228] E. Kozanoglu, S. Basaran, R. Guzel, F. Guler-Uysal, Short term efficacy of ibuprofen phonophoresis versus continuous ultrasound therapy in knee osteoarthritis. Swiss Med Wkly 133(23-24) (2003) 333-338.

[229] J. Asano, F. Suisha, M. Takada, N. Kawasaki, S. Miyazaki, Effect of pulsed output ultrasound on the transdermal absorption of indomethacin from an ointment in rats. Biol Pharm Bull 20(3) (1997) 288-291.

[230] S. Miyazaki, H. Mizuoka, Y. Kohata, M. Takada, External control of drug release and penetration. VI. Enhancing effect of ultrasound on the transdermal absorption of indomethacin from an ointment in rats. Chem Pharm Bull 40(10) (1992) 2826.

[231] G. Bumin, F. Can, Effects of iontophoresis and phonophoresis methods on pain in cases with shoulder periarthritis. Pain Clinic 13(2) (2001) 159-162.

[232] B. Cagnie, E. Vinck, S. Rimbaut, G. Vanderstraeten, Phonophoresis Versus Topical Application of Ketoprofen: Comparison Between Tissue and Plasma Levels. Phys Ther 83(8) (2003) 707-712.

[233] J.-H. Yang, T.-Y. Kim, J.-H. Lee, S.-W. Yoon, K.-H. Yang, S.-C. Shin, Anti-hyperalgesic and anti-inflammatory effects of Ketorolac Tromethamine gel using pulsed ultrasound in inflamed rats. Arch Pharm Res 31(4) (2008) 511-517.

[234] L. Wei, L. Xinping, W. Gang, Sonophoresis Induces the Enhanced Permeation of Drug and Its Effect on Stratum Corneum. Chin JMAP 26(6) (2009) 510 - 513.

[235] J. McElnay, M. Matthews, R. Harland, D. McCafferty, The effect of ultrasound on the percutaneous absorption of lignocaine. Brit J Clin Pharmaco 20(4) (1985) 421.

[236] T. Kim, D. Jung, Y. Kim, J. Yang, S. Shin, Anesthetic effects of lidocaine hydrochloride gel using low frequency ultrasound of 0.5 MHz. J Pharm Pharm Sci 10(1) (2007) 1-8.

[237] E. Novak, Experimental Transmission of lidocaine through intact skin by ultrasound. Arch Phys Med Rehab 45 (1964) 231 - 232.

[238] D. Ashton, D. Draper, J. Myrer, Temperature rise in human muscle during ultrasound treatments using Flex-All as a coupling agent. J Athl Training 33(2) (1998) 136.

[239] B. Cameroy, Ultrasound enhanced local anesthesia. Am J Orthaped 8(47) (1966).

[240] L. Glushchenko, Quantitative study of analgin phonophoresis. Vopr Kurortol Fizioter Lech Fiz Kult(41) (1976) 20 - 23.

[241] J.C. McElnay, H.A.E. Benson, R. Harland, J. Hadgraft, Phonophoresis of Methyl Nicotinate: A Preliminary Study to Elucidate the Mechanism of Action. Pharmaceutical research 10(12) (1993) 1726-1731.

[242] A. Mortimer, B. Trollope, E. Villeneuve, O. Roy, Ultrasound-enhanced diffusion through isolated frog skin. Ultrasonics 26(6) (1988) 348-351.

[243] G.Y.F. Ng, R.Y.F. Wong, Ultrasound Phonophoresis of Panax Notoginseng Improves the Strength of Repairing Ligament: A Rat Model. Ultrasound Med Biol 34(12) (2008) 1919-1923.

[244] V. Zague, M. Polacow, M. Pires-de-Campos, G. Leonardi, Evaluation of the ultrasound influence in the cutaneous penetration of d-panthenol: test in vitro. J Cosmet Dermatol 4(1) (2005) 29-33.

[245] J. Kost, K. Leong, R. Langer, Ultrasonically controlled drug delivery in vivo. Proc. Int. Symp. Controlled Release Bioact. Mater, Vol. 14, Controlled Release Society, 1987, pp. 186-187.

[246] T. Dynnik, A. Garbar, Use of antibiotic phonophoresis in purulent inflammatory skin diseases. Vrach Delo(8) (1977) 115 -116.

[247] W. Brondolo, Phenylbutazone with ultrasonics in some cases of arthrosynovitis of the knee. Arch Orthoped(73) (1960) 532 - 540.

[248] K. Chung, Y. Kim, J. Yang, Phonophoretic delivery of piroxicam. J Korean Pharm Sci 32(4) (2002) 259-266.

[249] M. Shiran, M. Motevalian, R. Ravanfar, S. Bohlouli, The effect of bubble surface charge on phonophoresis: implications in transderaml piroxicam delivery. Iran J Pharm Ther 7(1) (2008) 15-19.

[250] T. Hikima, Y. Hirai, K. Tojo, Effect of Ultrasound Application on Skin Metabolism of Prednisolone 21-Acetate. Pharmaceutical research 15(11) (1998) 1680-1683.

[251] A. Yamashita, Y. Hirai, K. Tojo, Effect of ultrasound on rate of drug absorption through skin. j Chem Eng Jpn 29(5) (1996) 812-816.

[252] J. Dohnalek, I. Hrazdira, J. Cecava, F. Novak, J. Svoboda, Penetration of radioiodine through the skin enhanced by ultrasonics. Cesk Derm 40 (1965) 173 - 178.

[253] V. Klare, Experiences with Reparil. Iontophoretic, phonophoretic and oral application. Ther Ggw 107(2) (1968) 240.

[254] I. Doweck, Z. Nachum, S. Dachir, O. Spitzer, C. Gordon, A. Gonen, A. Levy, A. Shupak, Enhancement of transdermal scopolamine absorption using sonophoresis. International Congress of Aviation and Space Medicine, Jerusalem, Israel, 1996.

[255] V. Frenkel, E. Kimmel, Y. Iger, Ultrasound-facilitated transport of silver chloride (AgCl) particles in fish skin. Journal of Controlled Release 68(2) (2000) 251-261.

[256] M.C. Fyfe, L.A. Chahl, The effect of ultrasound on experimental oedema in rats. Ultrasound Med Biol 6(2) (1980) 107-111.

[257] S. Ragelis, Penicillin and streptomycin penetration into tissue by a modified electrophoretic method. Antibiotiki 26(9) (1981) 699 - 703.

[258] T. Brawner, J. Senne, M. Fahim, A combined chemical-physical treatment for herpes simplex lesions in guinea pigs. Arch Dermatol Res 265(1) (1979) 71-77.

[259] M. Fahim, T. Brawner, D. Hall, New treatment for herpes simplex virus type 2 [ultrasound and zinc, urea and tannic acid ointment]. Part II: Female patients. J Med 11(2-3) (1980) 143 - 167.

[260] M. Fahim, T. Brawner, L. Millikan, M. Nickell, D. Hall, New treatment for herpes simplex virus type 2 [ultrasound and zinc, urea, and tannic acid ointment]. Part I--Male patients. J Med 9(3) (1978) 245 - 264.

[261] A. El-Kamel, I. Al-Fagih, I. Alsarra, Effect of sonophoresis and chemical enhancers on testosterone transdermal delivery from solid lipid microparticles: an in vitro study. Curr Drug Deliv 5(1) (2008) 20-26.

[262] V. Parikov, Injection of tetracyline into the tissues of cow udders by ultrasonics. Veterinariia 43(6) (1966) 88 - 91.

[263] S. Ragelis, Tetracycline penetration into tissue by modified electro-and phonophoretic methods. Antibiotiki 26(9) (1981) 699.

[264] J. Yang, D. Kim, T. Kim, G. Kim, S. Shin, Anti-inflammatory effects by transdermal application of triamcinolone acetonide gel using phonophoresis in rats. Int J Pharm 302(1-2) (2005) 39-46.

[265] J. Yang, D. Kim, M. Yun, T. Kim, S. Shin, Transdermal delivery system of triamcinolone acetonide from a gel using phonophoresis. Arch Pharm Res 29(5) (2006) 412-417.

[266] A. Grinshtein, A. Tolmacheva, V. Khriptulov, Phonophoresis of Trilon B. Vopr Kurortol Fizioter Lech Fiz Kult 37(3) (1972) 223 - 225.

[267] L. Kamrash, M. Mal'tseva, V. Tigeev, Trylon B phonophoresis in the rehabilitation of patients with stable contractures of extremity joints. Ortop Traumatol Protez(9) (1974) 79 - 80.

[268] C.D. Ciccone, B.G. Leggin, J.J. Callamaro, Effects of Ultrasound and Trolamine Salicylate Phonophoresis on Delayed-Onset Muscle Soreness. Phys Ther 71(9) (1991) 666-675.

[269] C. Pelucio-Lopes, L. Machet, L. Vaillant, F. Patat, M. Lethiecq, Y. Furet, L. Pourcelot, G. Lorette, Phonophoresis of azidothymidine (AZT). Int J Pharm 96(1-3) (1993) 249-252.

[270] SyracuseResearchCorporation, Interactive PhysProp Database Demo. http://www.syrres.com/what-we-do/databaseforms.aspx?id=386.

[271] K. Tachibana, Transdermal Delivery of Insulin to Alloxan-Diabetic Rabbits by Ultrasound Exposure. Pharm Res 9(7) (1992) 952-954.

[272] K. Tachibana, S. Tachibana, Transdermal delivery of insulin by ultrasonic vibration. J Pharm Pharmacol 43(4) (1991) 270-271.

[273] A. Tezel, A. Sens, S. Mitragotri, Incorporation of lipophilic pathways into the porous pathway model for describing skin permeabilization during low-frequency sonophoresis. J Control Release 83(1) (2002) 183-188.

[274] H. Ueda, R. Isshiki, M. Ogihara, K. Sugibayashi, Y. Morimoto, Combined effect of ultrasound and chemical enhancers on the skin permeation of aminopyrine. Int J Pharm 143(1) (1996) 37-45.

[275] P. Santoianni, M. Nino, G. Calabro, Intradermal drug delivery by low-frequency sonophoresis (25 kHz). Dermatol Online J 10(2) (2004) 24.

[276] H. Ueda, M. Ogihara, K. Sugibayashi, Y. Morimoto, Change in the electrochemical properties of skin and the lipid packing in stratum corneum by ultrasonic irradiation. Int J Pharm 137(2) (1996) 217-224.

[277] A. Maruani, A. Boucaud, E. Perrodeau, D. Gendre, B. Giraudeau, L. Machet, Low-frequency ultrasound sonophoresis to increase the efficiency of topical steroids: A pilot randomized study of humans. Int J Pharm 395 (2010) 84-90.

[278] A. Boucaud, L. Machet, B. Arbeille, M. Machet, M. Sournac, A. Mavon, F. Patat, L. Vaillant, In vitro study of low-frequency ultrasound-enhanced transdermal transport of fentanyl and caffeine across human and hairless rat skin. Int J Pharm 228(1-2) (2001) 69-77.

[279] M. Mutoh, H. Ueda, Y. Nakamura, K. Hirayama, M. Atobe, D. Kobayashi, Y. Morimoto, Characterization of transdermal solute transport induced by low-frequency ultrasound in the hairless rat skin. J Control Release 92(1-2) (2003) 137-146.

[280] J.-Y. Fang, C.-L. Fang, K.C. Sung, H.-Y. Chen, Effect of low frequency ultrasound on the in vitro percutaneous absorption of clobetasol 17-propionate. Int J Pharm 191(1) (1999) 33-42.

[281] S. Katikaneni, G. Li, A. Badkar, A. Banga, Transdermal delivery of a~ 13 kDa protein—an in vivo comparison of physical enhancement methods. J Drug Target 18(2) (2010) 141-147.

[282] L. Cancel, J. Tarbell, A. Ben-Jebria, Fluorescein permeability and electrical resistance of human skin during low frequency ultrasound application. J Pharm Pharmacol 56(9) (2004) 1109-1118.

[283] S. Lanke, C. Kolli, J. Strom, A. Banga, Enhanced transdermal delivery of low molecular weight heparin by barrier perturbation. Int J Pharm 365(1-2) (2009) 26-33.

[284] A. Maruani, E. Vierron, L. Machet, B. Giraudeau, A. Boucaud, Efficiency of low-frequency ultrasound sonophoresis in skin penetration of histamine: A randomized study in humans. Int J Pharm 385(37-41) (2010).

[285] E. Park, J. Dodds, N. Smith, Dose comparison of ultrasonic transdermal insulin delivery to subcutaneous insulin injection. Int J Nanomed 3(3) (2008) 335.

[286] A. Boucaud, M. Garrigue, L. Machet, L. Vaillant, F. Patat, Effect of sonication parameters on transdermal delivery of insulin to hairless rats. J Control Release 81(1-2) (2002) 113-119.

[287] A. Boucaud, L. Machet, M. Garrigue, L. Vaillant, F. Patat, A Practical Use of Low Frequency Ultrasound For Rapid and Reproducible Transdermal Delivery of Insulin. IEEE Ultrasonics Symposium, Vol. 2, Atlanta, GA, 2001, pp. 1327 - 1330.

[288] S. Lee, B. Snyder, R. Newnham, N. Barrie Smith, Noninvasive ultrasonic transdermal insulin delivery in rabbits using the light-weight cymbal array. Diabetes Technol The 6(6) (2004) 808-815.

[289] J. Luis, E.J. Park, J.R.J. Meyer, N.B. Smith, Rectangular cymbal arrays for improved ultrasonic transdermal insulin delivery. J Acoust Soc Am 122(4) (2007) 2022-2030.

[290] E. Park, J. Werner, N. Smith, Ultrasound mediated transdermal insulin delivery in pigs using a lightweight transducer. Pharm Res
24(7) (2007) 1396-1401.

[291] I. Zhang, K. Shung, D. Edwards, Hydrogels with enhanced mass transfer for transdermal drug delivery. J Pharm Sci 85(12) (1996) 1312-1316.

[292] N. Smith, S. Lee, E. Maione, R. Roy, S. McElligott, K. Shung, Ultrasound-mediated transdermal transport of insulin in vitro through human skin using novel transducer designs. Ultrasound Med Biol 29(2) (2003) 311-317.

[293] S. Skarbek-Borowska, B.M. Becker, K. Lovgren, A. Bates, P.A. Minugh, Brief Focal Ultrasound With Topical Anesthetic Decreases the Pain of Intravenous Placement in Children. Pediatr Emerg Care 22(5) (2006) 339-345.

[294] C.P. Stowell, M.Q. Trieu, H. Chuang, N. Katz, C. Quarrington, Ultrasound-enabled topical anesthesia for pain reduction of phlebotomy for whole blood donation. Transfusion 49(1) (2009) 146-153.

[295] W. Zempsky, B. Robbins, K. McKay, Reduction of topical anesthetic onset time using ultrasound: a randomized controlled trial prior to venipuncture in young children. Pain Med 9(7) (2008) 795-802.

[296] L. Weimann Jr, J. Wu, Ultrasound induced enhancement of skin permeability to Octa L Lysine. J Acoust Soc Am 106 (1999) 2230.

[297] R.F.V. Lopez, J.E. Seto, D. Blankschtein, R. Langer, Enhancing the transdermal delivery of rigid nanoparticles using the simultaneous application of ultrasound and sodium lauryl sulfate. Biomaterials 32(3) (2011) 933-941.

[298] M. Gou, L. Wu, Q. Yin, Q. Guo, G. Guo, J. Liu, X. Zhao, Y. Wei, Z. Qian, Transdermal Anaesthesia with Lidocaine Nano-Formulation Pretreated with Low-Frequency Ultrasound in Rats Model. J Nanosci Nanotechno 9(11) (2009) 6360-6365.

[299] M. Tran, R. Gowda, A. Sharma, E. Park, J. Adair, M. Kester, N. Smith, G. Robertson, Targeting V600EB-Raf and Akt3 using nanoliposomal-small interfering RNA inhibits cutaneous melanocytic lesion development. Cancer Res 68(18) (2008) 7638.

[300] A. Dahlan, H. Alpar, P. Stickings, D. Sesardic, S. Murdan, Transcutaneous immunisation assisted by low-frequency ultrasound. Int J Pharm 368(1-2) (2009) 123-128.

[301] I. Bjarnason, J. Hayllar, A. MacPherson, A. Russell, Side effects of nonsteroidal anti-inflammatory drugs on the small and large intestine in humans. Gastroenterology 104(6) (1993) 1832.

[302] K.D. Rainsford, Profile and mechanisms of gastrointestinal and other side effects of nonsteroidal anti-inflammatory drugs (NSAIDs). Am J Med 107(6, Supplement 1) (1999) 27-35.

[303] C. Heyneman, C. Lawless-Liday, G. Wall, Oral versus topical NSAIDs in rheumatic diseases: a comparison. Drugs 60(3) (2000) 555-574.

[304] B. Bloom, Risk and cost of gastrointestinal side effects associated with nonsteroidal anti-inflammatory drugs. Arch Intern Med 149(5) (1989) 1019-1022.

[305] B.S. Bloom, Direct medical costs of disease and gastrointestinal side effects during treatment for arthritis. Am J Med 84(2, Supplement 1) (1988) 20-24.

[306] P. Karande, S. Mitragotri, Transcutaneous immunization: an overview of advantages, disease targets, vaccines, and delivery technologies. Annu Rev Chem Biomol Eng 1 (2010) 175-201.

[307] J. Mikszta, J. Alarcon, J. Brittingham, D. Sutter, R. Pettis, N. Harvey, Improved genetic immunization via micromechanical disruption of skin-barrier function and targeted epidermal delivery. Nat Med 8(4) (2002) 415-419.

[308] C. Scarponi, F. Nasorri, F. Pavani, S. Madonna, R. Sestito, M. Simonacci, O. De Pità, A. Cavani, C. Albanesi, Low-Frequency Low-Intensity Ultrasounds Do Not Influence the Survival and Immune Functions of Cultured Keratinocytes and Dendritic Cells. J Biomed Biotechnol (2009).

[309] H. Chuang, M. Trieu, J. Hurley, E. Taylor, M. England, S. Nasraway Jr, Pilot Studies of Transdermal Continuous Glucose Measurement in Outpatient Diabetic Patients and in Patients during and after Cardiac Surgery. J Diabetes Sci Technol 2(5) (2008) 595-602.

[310] E. Park, J. Werner, J. Beebe, S. Chan, N. Smith, Noninvasive Ultrasonic Glucose Sensing with Large Pigs (200 Pounds) Using a Lightweight Cymbal Transducer Array and Biosensors. J Diabetes Sci Technol 3(3) (2009) 517 - 523.

[311] M. Pishko, N. Smith, R. Gabbay, J. Werner, Closed-Loop Noninvasive Ultrasound Glucose Sensing and Insulin Delivery. Storming Media, 2006.

[312] S. Mitragotri, Modeling skin permeability to hydrophilic and hydrophobic solutes based on four permeation pathways. J Control Release 86(1) (2003) 69-92.

[313] G. Moss, J. Dearden, H. Patel, M. Cronin, Quantitative structure-permeability relationships (QSPRs) for percutaneous absorption. Toxicol In Vitro 16(3) (2002) 299-317.

[314] P. Dechadilok, W. Deen, Hindrance factors for diffusion and convection in pores. Ind Eng Chem Res 45(21) (2006) 6953-6959.

[315] D. Li, X. Huang, H. Yu, Z. Zhang, F. Huang, K. Xu, X. Hu, A Novel Minimally Invasive Method to Detect Glucose Concentration without Blood Extraction. 1st IEEE International Conference on Nano/Micro Engineered and Molecular Systems, Zhuhai 2006, pp. 1185-1189.

[316] S. Naito, J. Maeyama, T. Mizukami, M. Takahashi, I. Hamaguchi, K. Yamaguchi, Transcutaneous immunization by merely prolonging the duration of antigen presence on the skin of mice induces a potent antigen-specific antibody response even in the absence of an adjuvant. Vaccine 25(52) (2007) 8762-8770.

[317] L. Weimann, J. Wu, Transdermal delivery of poly-l-lysine by sonomacroporation. Ultrasound Med Biol 28(9) (2002) 1173-1180.

[318] A.J. Singer, C.S. Homan, A.L. Church, S.A. McClain, Low-frequency Sonophoresis: Pathologic and Thermal Effects in Dogs. Acad Emerg Med 5(1) (1998) 35-40.

[319] A. Farinha, S. Kellogg, K. Dickinson, T. Davison, Skin impedance reduction for electrophysiology measurements using ultrasonic skin permeation: initial report and comparison to current methods. Biomed Instrum Techn 40(1) (2006) 72-77.

[320] J. Gupta, M. Prausnitz, Recovery of skin barrier properties after sonication in human subjects. Ultrasound Med Biol 35(8) (2009) 1405-1408.

Chapter 2

Transport Pathways and Enhancement Mechanisms within Localized and Non-Localized Transport Regions in Skin Treated with Low-Frequency Sonophoresis and Sodium Lauryl Sulfate

2.1 Introduction

The use of ultrasound to increase skin permeability, referred to as sonophoresis, has generated considerable interest and gained much use over the past few decades.[1] Initial research in the field was conducted at therapeutic frequencies, 1-3 MHz,[2-4] while more recent research efforts have focused on low-frequency sonophoresis (LFS), in the range 20-100 kHz. This shift in frequencies was prompted by the discovery that cavitation is the primary mechanism responsible for skin permeability enhancement.[5-9] The observed frequency dependence of cavitation occurs because of the inverse relationship between the ultrasound frequency and the radii of the

cavitation bubbles generated in the coupling medium between the ultrasound horn and the skin.[10-12] As the ultrasound frequency decreases, the radii of the cavitation bubbles tend to grow on average, resulting in more forceful collapses when cavitation bubbles approach the surface of the skin. These transient cavitation events near the skin surface have been identified as the primary mechanism of skin permeability enhancement in response to LFS treatment.[5, 6, 8]

In addition to uncovering the connection between cavitation and skin permeability enhancement, recent research has revealed many additional interesting phenomena. First, it has been demonstrated that when LFS and chemical enhancers, especially surfactants, are applied simultaneously during skin treatment, a synergistic enhancement is observed.[6, 13] This synergism can lead to an increase in skin conductivity or permeability by orders-of-magnitude when compared to skin treated separately with LFS or chemical enhancers.[13-15] Second, it has been shown that skin permeability enhancement by LFS and by LFS/SLS at 20 kHz is not homogenous.[15-21] Instead, the LFS treatment generates discrete regions within the skin, referred to as localized transport regions (LTRs), which are orders-of-magnitude more permeable than the surrounding skin regions (non-LTRs) and native skin samples.[14] Furthermore, it has been shown that the non-LTRs also exhibit increased skin permeability, with respect to native skin, when treated with 20 kHz LFS in combination with the surfactant sodium lauryl sulfate (SLS).[14, 17, 21] Accordingly, it was proposed that two levels of enhancement are present in skin samples that are treated simultaneously with LFS at 20 kHz and a chemical enhancer, such as SLS. The proposed existence of two levels of enhancement on a single skin sample in response to LFS/SLS at 20 kHz suggests that separate mechanisms of enhancement may operate within the LTRs and the non-LTRs, or that an enhancement mechanism that is significant within

the LTRs does not play a role within the non-LTRs. This possibility motivates the need for a deeper understanding of the transport pathways within LTRs and non-LTRs. In addition to quantifying the relative extents of skin perturbation by measuring skin permeability and skin resistivity, it is possible to utilize the aqueous porous pathway model (APPM)[22] and previously published masking techniques[14] to independently probe the effective pore radii in the LTRs and the non-LTRs. In doing so, one may be able to provide deeper insight into the nature of the aqueous transdermal pathways that exist within LTRs and non-LTRs, including the permeability enhancement mechanisms that are most significant in each of these skin regions. Moreover, because acoustic cavitation bubble collapse on the skin surface is a frequency-dependent process,[10-12] with the average cavitation bubble radius increasing with decreasing ultrasound frequency, one would expect that the average pore radii in the skin regions where such collapses occur would also increase with decreasing ultrasound frequency, if this mechanism was present.

It is important to note that a previous study investigated the average pore radius of skin treated with a range of LFS frequencies, in the context of the APPM.[19] However, because that study did not independently study LTRs and non-LTRs, it is significantly different than the study presented here. First, because the pore radii within LTRs and non-LTRs were not studied separately, no direct conclusions could be reached about the nature of the transport pathways or enhancement mechanisms within LTRs and non-LTRs. Second, the ultrasound intensity used in the previous study was 1.08 W/cm^2, which is significantly lower than the 7.5 W/cm^2 ultrasound intensity used in the experiments reported here. Note that the ultrasound intensity used here is similar to those used in other recent papers discussing LTR formation using LFS/SLS.[14-17,

23] Third, the range of skin electrical resistivities investigated here is lower than that of the previous study, indicating that the skin samples considered here are perturbed to a greater extent by the LFS/SLS treatment than those considered in the prior study. In fact, because LTR size is closely related to the extent of skin perturbation, as measured by skin resistivity,[14] it is likely that any LTRs that were formed would be much smaller than those observed in the study reported here. Because the effects of the enhancement mechanisms are expected to be magnified under the ultrasound skin treatment conditions used in this study, relative to those used previously, the combination of a higher ultrasound intensity and a greater extent of skin perturbation by the LFS/SLS treatment utilized here should facilitate gaining insight into the enhancement mechanisms at play within LTRs and non-LTRs, including the effect of the ultrasound frequency on the resulting transdermal pathways in each skin region.

With all of the above in mind, the goals of this study are four-fold: i) to demonstrate that at the three ultrasound frequencies tested (20 kHz, 40 kHz, and 60 kHz), LTRs form on the surface of the skin and exhibit increased permeability relative to both the non-LTRs and native skin, ii) to demonstrate that at the three frequencies considered here there are two levels of skin permeability enhancement relative to native skin when LFS and SLS are used simultaneously, indicating that the non-LTRs also exhibit increased permeability relative to native skin, iii) to better characterize the transport pathways through LTRs and non-LTRs by independently determining the permeabilities and the effective aqueous pore radii in LTRs, non-LTRs, and total skin samples in the context of the APPM, and iv) to propose mechanisms of enhancement within LTRs and non-LTRs.

2.2 Materials and Methods

2.2.1 Materials

Phosphate buffer saline (PBS; 0.01 M phosphate, 0.137 M NaCl), calcein, and SLS were obtained from Sigma Chemical Company (St. Louis, MO). The dye allura red (molecular weight = 496 g/mol, water solubility = 225 g/L = 22.5 wt% at 25 °C, log $K_{O/W}$=-0.550 [24]) was obtained from TCI America (Portland, OR). C_{14}-labeled SLS (specific activity of 55 mCi/mmol) was obtained from American Radiolabeled Chemicals (St. Louis, MO). Soluene-350, a tissue solubilizer, and Hionic-Fluor, a scintillation cocktail, were obtained from Perkin-Elmer (Waltham, MA). All chemicals were used as received.

2.2.2 Skin Preparation

Previously published protocols were utilized for the storage and preparation of skin samples.[22] A brief summary of these protocols follows. This procedure has been approved by the MIT Committee on Animal Care. Skin was harvested from the back and flank of Female Yorkshire pigs within 1 hour of sacrificing the animal. Subcutaneous fat was removed from the skin using a razor blade and then sectioned into one-inch strips prior to storage at -85 °C for up to 6 months. Before use in experiments, the skin was thawed for 1 hour in PBS and then excess hair was trimmed using surgical scissors. The thawed skin was then cut into 25 mm by 25 mm samples. Before mounting of the skin samples into the 15-mm inner diameter diffusion cells (PermeGear, Hellertown, PA), high vacuum grease (Dow Corning, Midland, MI) was applied to the inner flange of the donor and the receiver compartments in order to provide a water-tight seal between the skin and the diffusion cell. For additional mechanical support, a 150-μm opening nylon

mesh (Sefar Filtration, Depew, NY) was placed onto the top of the receiver chamber of the diffusion cell. The receiver chamber was then filled with PBS, the skin sample was mounted into the diffusion cell, and the diffusion cell was clamped tightly. The donor chamber was then filled with the appropriate solution for treatment or permeation experiments.

2.2.3 Skin Electrical Resistivity Measurements

The skin electrical resistivity, *R*, has been shown to be an accurate and instantaneous indicator of the structural state of the skin.[25, 26] Previously published methods were followed to measure *R*[16, 23, 26] and are summarized next. A signal generator (Hewlett-Packard, model HP 33120A) was used to generate an AC voltage at 100 mV and 10 Hz. The voltage was applied across the skin using two Ag/AgCl electrodes (In Vivo Metrics, Healdsburgh, CA). The skin electrical current was measured using a multimeter (Fluke Corporation, Model 189) and the skin electrical resistance was calculated using Ohm's Law. The background resistance of the system was accounted for by removing the skin sample from the diffusion cell and measuring the resistance of the system (note that this resistance is a function of the area available for diffusion, therefore the background resistances for the LTRs and the non-LTRs are not necessarily the same as that for the total skin samples). Subsequently, the background resistance was subtracted from the resistance measured for the total system, including the skin. *R* was then calculated by multiplying the skin electrical resistance by the area of the skin sample. In order to ensure that the skin was intact prior to experimentation, the initial *R* value of a skin sample was required to be above 50 kOhm·cm^2.[27-29] The electrical current measured, and the resulting resistivity values, were calibrated by testing the electrical equipment with resistors of known resistance.

2.2.4 Determination of Steady-State Calcein Permeability through Skin

Calcein was chosen as a model aqueous permeant because its concentration in aqueous solution can be determined with relative ease using simple spectrophotometric methods, which minimizes sample preparation time and the cost of sample analysis. Calcein has also been used in the past to determine skin permeabilities in the context of the APPM.[14] The procedures described in the following sub-sections were carried out on LTRs, non-LTRs, and total skin samples, as well as on native skin and skin dermis.

2.2.4.1 Pre-Treatment of Skin Samples by LFS/SLS

LFS/SLS pre-treatment of skin samples was carried out according to previously published methods, which are summarized next.[14-17, 22] Three separate ultrasound systems (Sonics and Materials, Inc., Newtown, CT) were used in this study, each operating at a different frequency: 20 kHz (VCX 500), 40 kHz (VCX 130), and 60 kHz (custom order). The intensity of each horn was calibrated using calorimetry, and the skin treatment with each system was carried out under identical experimental conditions: intensity - 7.5 W/cm^2, duty cycle - 50% (5 s on, 5 s off), tip displacement - 3 mm, and a coupling medium containing 1% (w/v) SLS and 0.025% (w/v) allura red in PBS. Samples were treated with LFS until they reached pre-determined electrical current thresholds of 225, 275, or 335 μA (±10%), which are similar to previously published thresholds used when studying LTR formation.[14, 23] These thresholds were chosen in order to: i) create LTRs that are sufficiently large to be quantifiable on a macroscopic scale (at least 5% coverage of LTRs on the skin surface), and ii) study different levels of skin perturbation. After each

minute of LFS treatment, the coupling medium was changed in order to minimize thermal effects (maintain the temperature within 10 °C of room temperature), and the electrical current of the skin samples was measured to determine if the target threshold had been reached. Upon completion of the LFS treatment, samples were rinsed thoroughly with PBS, in order to remove all excess SLS from the skin surface, and then the donor solution was replaced with 0.025% (w/v) allura red in PBS for 1 hour. Because of the significantly higher permeability of LTRs, relative to non-LTRs (see Results section), increased uptake of allura red occurs significantly only within LTRs during the additional 1 hour soak, which aids in the subsequent digital imaging of the LTRs.

2.2.4.2 Digital Imaging and Analysis of LTR Areas

Digital imaging and analysis of LTRs was conducted according to previously published protocols, which are summarized next.[14] After the 1-hour soak in the allura red solution, the skin samples were thoroughly rinsed with PBS and blotted dry. The skin samples were then imaged in triplicate using a digital camera (HP Photosmart R967, 10 Megapixels, auto macro setting) at a distance of approximately 8 inches above the sample. In order to correct for fluctuations in laboratory lighting and infidelity of the charged coupled device, a red-colored strip was included in each image as a standard (VWR, general-purpose laboratory labeling tape, color "red"). Images were then analyzed using the Corel Photo-Paint 11 Software Package (Corel Corporation, Ontario, Canada) according to the method published by Kushner *et al.*[14] Briefly, first the red-colored tape strip in each image was isolated in order to measure the average blue-channel levels for all of the isolated strips. Then, the blue level for each image was shifted using the "Contrast Enhancement" function to the average blue level for all samples.

After this standardization, the images were cropped to the size of the skin sample treated by LFS (15 mm by 15 mm image size). Subsequently, the total number of pixels in the image was noted using the "Histogram" function. In order to determine the size of the LTRs, the "Threshold" function was used to tabulate the number of pixels having a blue-channel level below 50. The reasons for the selection of these criteria are discussed further in Kushner *et al.*[14] It is important to note that the blue level threshold used in the current study is different than that used by Kushner *et al.*, because allura red was utilized to visualize the LTRs instead of sulforhodamine B (SRB).[14] SRB was not used in the present study because a fluorescent dye was not required. It is then straightforward to calculate the area of the LTRs on the skin surface, A_{LTR}, in terms of the number of LTR pixels, the total number of pixels in the image, and the total area of the image (A_{total} =1.5 cm by 1.5 cm = 2.25 cm^2). Specifically,

$$A_{LTR} = \frac{(\text{LTR Pixels})}{(\text{Total Pixels})} \cdot A_{total} \tag{2.1}$$

2.2.4.3 Diffusion Masking Experiments

Diffusion masking is a previously published method[14] that allows one to probe the transport properties of the LTRs and the non-LTRs separately. Use of this method allowed us to test three groups of samples at each ultrasound frequency following pre-treatment with LFS/SLS: total, LTR, and non-LTR samples. Skin samples in the total group were not masked (indicating that the entire skin surface was available for calcein permeation). Skin samples in the LTR group had the non-LTR regions masked in order to leave the LTR regions accessible for permeation of calcein (see Figure 2-1 for an image of a skin sample showing LTRs and non-LTRs). Similarly,

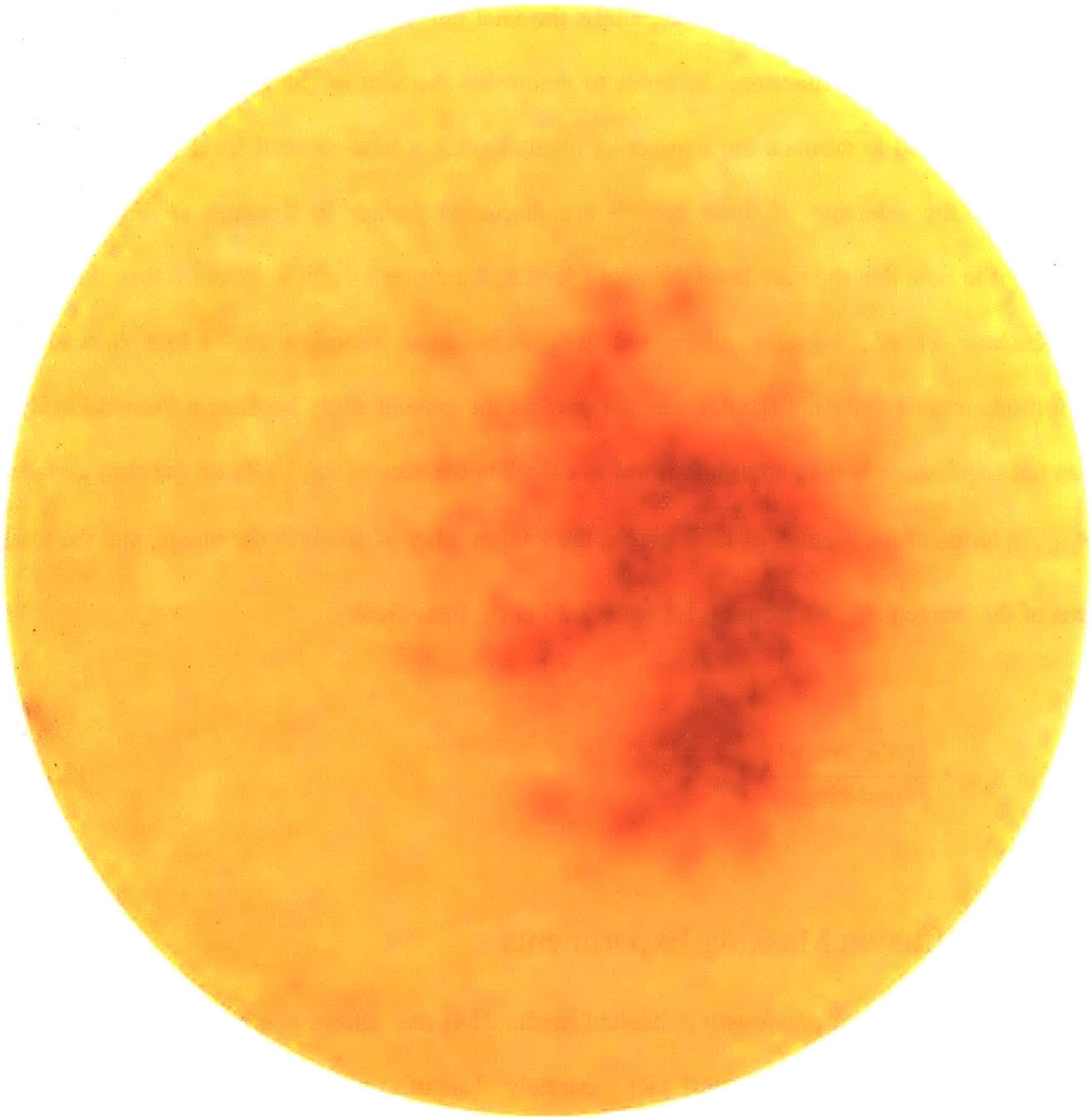

Figure 2-1. Porcine skin sample treated with LFS/SLS at 40 kHz. Regions of the skin dyed red are LTRs, regions of the skin that are not dyed red are non-LTRs. The diameter of the circular sample is 15 mm.

skin samples in the non-LTR group had the LTR regions masked in order to leave the non-LTR regions accessible for permeation of calcein. The masking technique involves applying vacuum grease to either the LTR or the non-LTR regions, respectively. The vacuum grease does not allow diffusion of hydrophilic permeants through the skin regions that are masked with vacuum grease. This method has been validated previously by Kushner *et al.*[14]

2.2.4.4 Calculating Steady-State Calcein Permeability through the Skin

Following imaging and masking, all skin samples were remounted into clean, dry diffusion cells. The receiver chamber of each sample was filled with PBS (12 mL) and the donor chamber was filled with 2.5 mL of 0.2% (w/v) calcein in PBS solution. These experiments were conducted at room temperature (25 °C), and the receiver chambers were magnetically stirred at 400 rotations per minute. Samples were allowed sufficient time to reach steady-state (which has previously been established for calcein through porcine skin[14]), and then were sampled at two-hour intervals between 18 – 26 hours after initiation of the experiments. For each sample, a 1 mL aliquot was withdrawn from the receiver chamber and immediately replaced with an equal volume of PBS. In addition, at each time interval, a 20 μL aliquot was withdrawn from the donor chamber and diluted to 2 mL (in order for the absorbance to be in the linear regime for calcein). The concentration of calcein in each aliquot was determined using a UV/VIS spectrophotometer (Beckman Coulter DU 800) to measure absorbance at λ = 494 nm and, subsequently, was converted to units of % (w/v) using a standard curve generated from known concentrations of calcein.

Finally, the permeability of calcein through the skin, P, was calculated at steady-state, infinite sink conditions using the following equation:

$$P = \frac{V}{AC_d}\left(\frac{\Delta C}{\Delta t}\right) \tag{2.2}$$

where A is the area of skin available for permeation (which can vary with LTR area for the masked samples, with A = 1.77 cm^2 for the total skin samples), V is the volume of PBS in the receiver chamber, C_d is the average calcein concentration in the donor chamber over the sampling period, and $(\Delta C/\Delta t)$ is the rate of change of calcein concentration in the receiver chamber (where replacement of the sampled aliquots by PBS is taken into account).

As previously noted, three main skin sample groups were studied: total samples, LTR samples, and non-LTR samples. In addition, passive samples were also tested, which involved no LFS/SLS pre-treatment, in order to compare the permeabilities of LTRs and non-LTRs to that of native skin. Note that in the non-LTR and passive sample groups, it was necessary to account for the background absorption of lipids in the receiver chamber in the spectrophotometric analysis. It is well established that many epidermal and dermal components have broad range absorption in the visible light range,[30-34] which justifies the need for this correction when the absorption of calcein is of similar, or of lower, magnitude than the absorption of the skin components in solution at the wavelength of interest. This procedure is described in Section 2.A. Because there is a higher concentration of calcein present in the receiver chambers of LTR samples, background absorption was found to be insignificant within these samples and, therefore, there was no need to implement the procedure described in Section 2.A.

2.2.4.5 Calcein Permeability through the Skin Dermis

The final group of samples consisted of skin that was first dermatomed (Zimmer Electric Dermatome, Model 8821, Dover, OH) at a depth of 300 μm to completely remove the entirety of the epidermis from the dermis. The epidermis was then discarded, and the calcein permeability and skin electrical resistivity of the dermis were measured. Note that the calcein permeability and skin electrical resistivity of the dermis are necessary in order to find the effective aqueous pore radius of the dermis in the context of the APPM (see Section 2.3).[22]

2.2.5 Experiments with C_{14}-Labeled SLS

In order to quantify the amount of SLS partitioning into the LTRs, the non-LTRs, and the passive samples, the skin was pre-treated as described in the Section 2.2.4.1, but the coupling medium also contained 0.5 μCi/mL C_{14}-labeled SLS, in addition to the 1% (w/v) SLS, and 0.025% (w/v) allura red in PBS. Skin samples were treated with 20 kHz ultrasound for a total ON time of 10 minutes (20 minutes at 50% duty cycle), resulting in skin samples with an average current of 330 μA (within the range of currents tested in the experiments used when calculating calcein permeabilities). Following treatment, skin samples were rinsed with PBS, blotted dry with lab tissue, and then LTRs (that were dyed red, see Figure 2-1) and non-LTRs (the undyed skin regions, see Figure 2-1) were sampled using a circular cutting tool with an area of 7.9 mm^2. On each skin sample, it was typically possible to sample 2-3 LTR samples and 4-7 non-LTR samples (since the non-LTRs occupy larger areas on the skin). The skin samples were then solubilized using Soluene-350 (1.5 mL), and the amount of SLS was quantified using a Tri-Carb Liquid Scintillation Counter (Perkin-Elmer), utilizing the scintillation cocktail Hionic-Fluor (5 mL). This process was repeated for ten skin samples. Passive samples were contacted with the C_{14}-

labeled SLS-containing coupling medium for 20 minutes. For passive samples, the entire skin sample that contacted the solution (with area of 1.77 cm^2) was used to quantify the amount of SLS in the skin. For the case of the larger passive samples, 5 mL of Soluene-350 and 15 mL of Hionic-Fluor were utilized in the analysis of each sample. This process was repeated for 20 skin samples. For all samples, the concentration of SLS in the skin was normalized by the surface area of that sample.

In addition, to further test the mechanism of SLS penetration into non-LTRs, experiments were conducted to quantify the penetration of SLS into the skin for two additional cases: i) with increased temperature of the donor solution, and ii) with vigorous stirring in the donor compartment of the diffusion cell. During ultrasound application, the temperature of the donor solution increases linearly from room temperature (25 °C) by no more than 10 °C during a two-minute treatment (with 50% duty cycle, 5 s ON: 5 s OFF, and 1-minute ultrasound ON time). Therefore, to quantify the effect of just the temperature increase on SLS penetration into the skin, an identical donor solution to that described above was initially heated to 37 °C (body temperature and approximately 10 °C higher than room temperature) and was contacted with the skin in two-minute increments (the same time interval corresponding to the ultrasound experiments). The solution was replaced 10 times, with the 37 °C donor solution, for a total contact time of 20 minutes. To test the effect of decreasing the concentration boundary layer above the skin, an experimental setup was designed to allow for rapid stirring of the donor solution above the skin. Samples were prepared by: i) placing a 12.5 mm stir bar (VWR) in the donor compartment (having a diameter of 15 mm), ii) filling the donor compartment with ~1.5 mL of C_{14}-labeled SLS-containing coupling medium, and iii) capping the diffusion cell with a

plastic stopper (Chemglass, Vineland, NJ, part# CG-3021-01). Once the samples were capped, the distance between the skin surface and the bottom of the stopper was 5 mm. The diffusion cells were placed underneath a ¼" thick acrylic platform (fabricated in-house) with a magnetic stir plate inverted on top of it (Corning, Lowell, MA, model PC-410). Once the samples were placed under the magnetic stir plate, and the height of the platform was adjusted so that it was resting on top of the diffusion cell, the magnetic stir bar was attracted to the stir plate and therefore rested at the bottom of the plastic stopper (5 mm above the skin surface). It was necessary that the stir bar not contact the skin during mixing, because if the stir bar had rested on the skin surface, it could cause mechanical abrasion of the skin due to friction. The stir plate was then set to its maximum speed, a setting of "10", and the experiment was allowed to proceed for 20 minutes. Although the LFS/SLS experiments have an LFS ON time of 10 minutes (50% duty cycle), it was observed that fluid flow persisted in the donor compartment of the diffusion cell during the LFS OFF time (that is, fluid flow did not cease immediately after LFS was turned off). Accordingly, to better reproduce the environment above non-LTRs in the LFS/SLS experiments, the vigorously-stirred experiments were conducted for 20 minutes (the full contact time of the SLS donor solution with the skin during the LFS/SLS treatment). Both sets of samples were prepared, and the amount of SLS quantified, in the same manner as described earlier in this section for the passive samples contacted with C_{14}-labeled SLS.

2.3 Theory

2.3.1 Calculating the Effective Aqueous Pore Radius of the Skin

In order to calculate the effective aqueous pore radius (r_{pore}) of the skin samples tested, the APPM was utilized.[22] The main assumption of this model is that aqueous permeants (in this

case, calcein) traverse the skin along the same paths as the current carrying ions of the electrolyte solution that the skin is immersed in (for PBS, the dominant ions are Na^+ and Cl^-). This model utilizes hindered transport theory[35] in order to quantify the steric hindrance exerted by the finite-size skin pores on the flux of the aqueous permeant and the current carrying ions through the skin. The hindrance factors corresponding to both species are related solely to the radius of each permeant and r_{pore}. Therefore, by equating the diffusion of the aqueous permeant, which is related to P, and of the current carrying ions, which is related to R, one can determine r_{pore}.

The relation between permeability, P, and skin electrical resistivity, R, in the context of the APPM, is given by:[22]

$$\log P = \log C - \log R \tag{2.3}$$

where C is defined as follows:

$$C = \frac{kT}{2z^2 F c_{ion} e_0} \cdot \frac{D_p^{\infty} H(\lambda_p)}{D_{ion}^{\infty} H(\lambda_{ion})} \tag{2.4}$$

where z is the electrolyte valence, F is Faraday's constant, c_{ion} is the electrolyte molar concentration, e_0 is the electronic charge, k is the Boltzmann constant, T is the absolute temperature, D_i^{∞} is the infinite-dilution diffusion coefficient of solute i, $H(\lambda_i)$ is the hindrance factor for solute i, and λ_i is defined as the ratio of the radius of solute i, r_i, to the radius of the aqueous skin pores, r_{pore}.[14] Although previous work has utilized older expressions for the hindrance factor, $H(\lambda_i)$,[14, 19, 22, 23, 26, 36, 37] the most advanced expression for $H(\lambda_i)$, which has been used recently in the context of the APPM[38] and is valid for $\lambda_i \leq 0.95$, is given by:[35]

$$H(\lambda_i) = 1 + \frac{9}{8}\lambda_i \ln \lambda_i - 1.56034\lambda_i + 0.528155\lambda_i^2 + 1.91521\lambda_i^3 \tag{2.5}$$

$$-2.81903\lambda_i^4 + 0.270788\lambda_i^5 + 1.10115\lambda_i^6 - 0.435933\lambda_i^7$$

It is important to note that the only variable in Eq. (2.4) that depends on the intrinsic properties of the skin is r_{pore}. All the other variables are either constants or are properties of the permeants used. Therefore, once an experimental C value is determined using Eq. (2.3), r_{pore} can be determined by iteratively solving Eq. (2.4) until C converges.

It is important to stress that, for any given aqueous permeant used (with given hydrodynamic radius, which is 8 Å for calcein[39]), only a certain range of r_{pore} values can be probed in the context of the APPM. In fact, for any permeant, there will be an upper bound on the r_{pore} values that can be determined depending on the hydrodynamic radius of the permeant. This is due to the fact that, as the pores become increasingly large, the extent of hindrance exerted by the pores on the diffusing permeant becomes increasingly small as the hindrance factor approaches unity (recall that hindrance factors range from 0 to 1, where a hindrance factor of 1 corresponds to no hindrance and a hindrance factor of 0 corresponds to infinite hindrance). Beyond a certain r_{pore} value, the hindrance exerted by the pores on the permeant becomes statistically indistinguishable from the diffusion of the permeant at infinite dilution, which corresponds to the upper bound of r_{pore} that can be probed with that permeant. This infinite-dilution limit (also known as an infinite-pore limit) will be attained at lower r_{pore} values for smaller permeants and will be higher for larger permeants. This limit can be estimated in one of two ways: i) assuming that, beyond a certain r_{pore} value, the hindrance factor calculated for calcein cannot be differentiated from a

hindrance factor of unity. In past publications, the level of uncertainty in the hindrance factor was chosen to be 10%, and the pore radius corresponding to $H(\lambda)=0.9$ was chosen as the upper bound for a given permeant,[22] or ii) assuming that the pores within the hydrophilic dermis are infinite, and then using the pore radius calculated for the dermis in the context of the APPM as the upper limit on r_{pore}. Both methods were tested, and they yielded a similar upper limit of r_{pore} for calcein, approximately 300 Å.

In order to apply the APPM to the data, a linear regression was fit to each set of log *P* versus log *R* values. For the model to be applicable, it was required that the 95% confidence interval of the slope corresponding to every given data set include the theoretical value of -1 (see Eq. (2.3)). Once this test was carried out, and it was confirmed that the data was described by the APPM, a *C* value was determined using Eq. (2.3) for each data point tested. Subsequently, all of the individual *C* values within each data set were averaged to yield the *C* value for that data set. This *C* value was then used to calculate r_{pore} in the manner described above. Therefore: i) the reported r_{pore} value for a given data set was calculated from the mean value of *C* for that data set, and ii) the 95% confidence interval reported for r_{pore} was calculated from the 95% confidence interval for *C* for each data set. In general, all the statistical analyses reported in this study involve two-sampled t-tests, at 95% confidence, unless noted otherwise.

2.3.2 Calculating the Skin Porosity-to-Tortuosity Ratio

In order to gain deeper insight into the transdermal pathways present within each skin region, it is possible to again implement the APPM to calculate the ratio between the skin porosity, ε, and the skin tortuosity, τ, using the following expression:[22]

$$\left(\frac{\varepsilon}{\tau}\right)_i = \frac{1}{\left(\frac{R_i}{\Delta x}\right)\sigma_{sol} H\left(\lambda_{ion,i}\right)} \tag{2.6}$$

where the subscript i denotes a given skin sample, σ_{sol} is the electrical conductivity of PBS ($0.012\ \Omega^{-1}\text{cm}^{-1}$),[22] $H\left(\lambda_{ion,i}\right)$ is the hindrance factor for an ion calculated using Eq. (2.5), R_i is the skin electrical resistivity, and Δx is the thickness of the skin layer that provides the primary barrier to transport. For the non-LTRs and passive skin samples, Δx can adequately be defined as the thickness of the stratum corneum, or 13.1 μm.[40] Selecting an appropriate Δx value for LTRs will be further discussed in the Results section.

2.4 Results and Discussion

2.4.1 Dependence of LTR, non-LTR, and Total Calcein Permeabilities on Electrical Current Treatment Threshold and Ultrasound Frequency

Figure 2-2 shows the calcein permeability data for each of the three groups of samples tested (total, LTR, and non-LTR) at the three ultrasound frequencies considered (A - 20 kHz, B - 40 kHz, and C - 60 kHz). In addition, the passive group is included in these Figures for comparison to the calcein permeability of native skin. As illustrated in Figure 2-2, at all three frequencies, the permeability of calcein through the LTRs is much greater than those through all the other

skin regions. Additionally, it is noted that the permeability within LTRs is of similar magnitude to the permeability within dermis samples ($P = 1.8 \cdot 10^{-2}$ cm/hr, calculated as described in Section 2.2.4.5), suggesting that much of the barrier properties within the epidermis of these regions has been overcome. These findings are consistent with previous results at 20 kHz.[15] Moreover, at the three frequencies studied, the non-LTRs are also more permeable than the native skin samples, which is consistent with earlier findings at 20 kHz.[14, 17, 21] As expected, the calcein permeabilities of the total skin samples fall between those of the LTRs and the non-LTRs at each of the three frequencies studied, because these samples contain both types of skin regions.

Figure 2-2 also shows that for the total skin samples, at each of the three frequencies studied, the calcein permeability increases linearly as a function of the skin electrical current threshold (r^2=0.94-0.98). In spite of the observed upward linear trend in calcein permeability for the total skin samples, the permeabilities within the LTRs and the non-LTRs exhibit no dependence on the electrical current threshold based on statistical analysis of the data at the three frequencies studied. This indicates that, as the electrical current threshold increases, the permeability of the skin increases due to an increase in the area of the LTRs present on the skin. This is clearly seen in Table 2-1, where the LTR area increases with increasing skin electrical current threshold for the three frequencies studied. Additionally, by comparing the calcein permeability of the total skin samples, at each current threshold, as a function of ultrasound frequency, it is seen that the total calcein permeabilities generally decrease with increasing ultrasound frequency (Figures 2-2A-C). This suggests that the calcein permeation through the skin in the total skin samples is

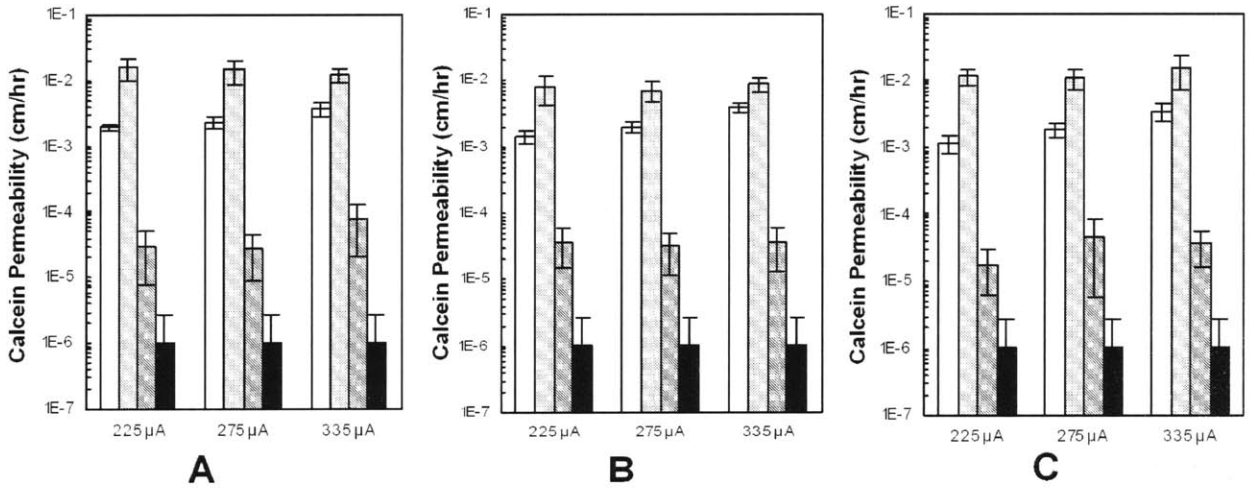

Figure 2-2. Calcein permeability for the total, LTR, non-LTR, and passive skin samples treated to electrical current thresholds of 225 µA, 275 µA, and 335 µA at the three ultrasound frequencies considered: 20 kHz (A), 40 kHz (B), and 60 kHz (C). Key: Total group (□); LTR group (▨); Non-LTR group (▧); Passive group (■). Error bars = ±1 SD. Each bar in each graph represents 8-12 samples, except for the passive group where the sample size is 20.

Table 2-1. LTR area as a function of skin electrical current threshold and ultrasound frequency. The total skin area of the samples is 1.77 cm^2.

Current (μA)	20 kHz		40 kHz		60 kHz	
	n	LTR Area (cm^2) [a]	n	LTR Area (cm^2) [a]	n	LTR Area (cm^2) [a]
225	18	0.197 ± 0.070	16	0.282 ± 0.079	15	0.154 ± 0.034
275	17	0.265 ± 0.055	19	0.399 ± 0.080	19	0.327 ± 0.102
335	17	0.531 ± 0.099	20	0.452 ± 0.066	21	0.417 ± 0.117

[a] Range corresponds to a 95% confidence interval.

more hindered with increasing frequency. This result will be discussed more thoroughly in the context of the APPM in the following sections.

Finally, by comparing the calcein permeability data in each skin region tested, one can quantify the relative perturbation in these regions by calculating a permeability enhancement ratio ($P/P_{passive}$). In general, LTR samples are over four orders-of-magnitude more permeable than native skin, and well over two orders-of-magnitude more permeable than non-LTR samples. In addition, non-LTRs are over thirty-fold more permeable than native skin. This again confirms the earlier finding that two levels of enhancement are observed when treating skin simultaneously with LFS at 20 kHz and a chemical enhancer, such as SLS.[14, 17, 21] In the following sections, possible causes leading to the observed two levels of enhancement will be discussed in more detail in the context of the effective aqueous skin pore radii in the different skin regions.

2.4.2 Determining Effective Aqueous Pore Radii in LTRs, non-LTRs, and Total Skin Samples as a Function of Ultrasound Frequency

Figure 2-3 shows the log P vs. log R plot used to analyze the 40 kHz LTR data in the context of the APPM. In order for the model to be applicable, it is first necessary to check whether each data set's linear regression has a slope that is not statistically different (95% confidence) from the theoretical value of -1 (see Section 2.3). The results of this analysis are reported in Table 2-2, which shows that all the data sets have slopes that are within valid limits for the APPM to be applicable. The r^2 values for all the data sets, except for the passive skin samples, are also within the expected range reported in previously published data.[22] Note that the low r^2 value

exhibited by the passive skin sample set can be rationalized as follows. The skin resistivity values for the passive skin samples are grouped very closely to each other, given the resistivity of native skin and the fact that it is required that the skin samples used possess sufficiently high initial resistivity to ensure that they are not damaged. Therefore, any scatter in the permeability data due to natural variations in the native skin has a very large effect on the r^2 value for this data set. Unlike in the LTR, non-LTR, and total skin samples, samples are not treated in a controlled manner to a pre-determined current threshold. Therefore, the data is very susceptible to natural variations in the skin barrier, which can be significant from sample-to-sample and especially between animals. Nevertheless, the passive skin samples provide a good baseline for comparison to the values obtained in the case of the LFS/SLS-treated skin samples and, therefore, have been included in Table 2-2.

The r_{pore} values corresponding to the different skin regions studied, calculated in the context of the APPM, are reported in Table 2-3. The total skin samples clearly exhibit a decrease in r_{pore} with increasing ultrasound frequency. Utilizing a two-sample t-test at 95% confidence, it was determined that, for the total skin samples, the difference between r_{pore} calculated at 20 kHz (105 Å) and 40 kHz (73.9 Å), and at 40 kHz and 60 kHz (50.7 Å) are statistically significantly different. It is also noted that a previous study by our group investigated the effect of different permeants on skin pore radii with 20 kHz LFS/SLS under nearly identical treatment conditions utilizing human skin.[23] In this study, the reported pore radii are very similar to the r_{pore} value reported here for calcein (molecular weight = 622.6 g/mol, r_{pore} = 105 Å) at 20 kHz, for two other hydrophilic permeants with molecular weights greater than 500 g/mol (for raffinose, r_{pore} = 98 Å

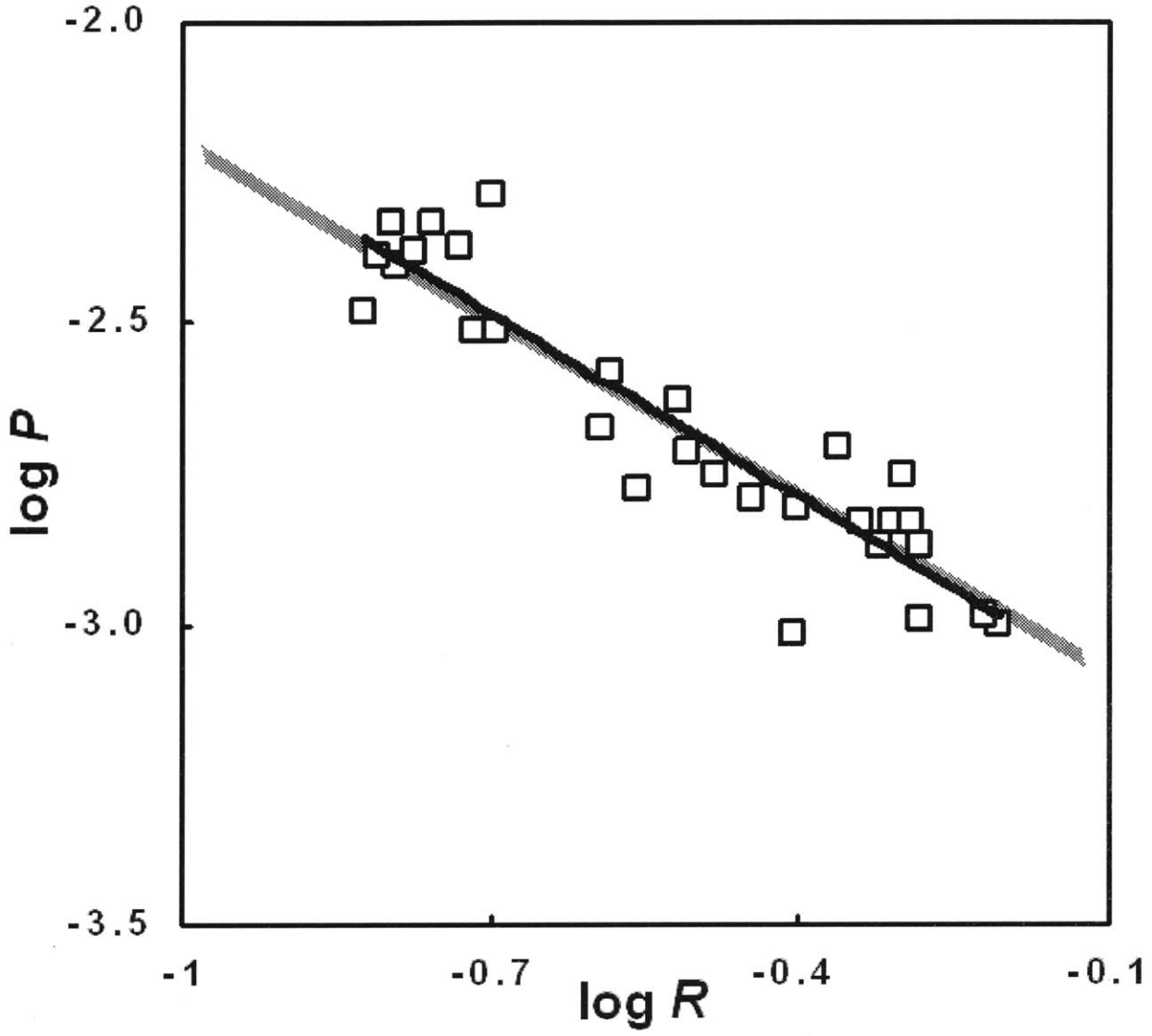

Figure 2-3. Sample log P vs. log R plot. Data shown (□) is for LTR samples treated at 40 kHz. Units of P are cm/hr and units of R are kOhm·cm^2. Key: solid black line – linear regression of the data, gray line – linear regression with theoretical slope of -1.

Table 2-2. Statistical analysis on the slopes of log P as a function of log R for all the data sets tested. The 95% confidence interval for the slope must contain the value -1 for the APPM to be applicable.

	Total			LTRs			Non-LTRs		
Frequency	n	Slope [a]	r^2	n	Slope [a]	r^2	n	Slope [a]	r^2
20 kHz	35	-0.92 ± 0.17	0.79	28	-1.01 ± 0.26	0.71	24	-1.24 ± 0.38	0.68
40 kHz	30	-1.02 ± 0.16	0.85	27	-1.02 ± 0.26	0.73	30	-1.13 ± 0.22	0.79
60 kHz	36	-1.08 ± 0.21	0.76	30	-0.95 ± 0.32	0.57	30	-1.07 ± 0.27	0.70
Passive	20	-1.14 ± 0.73	0.16						

[a] Range corresponds to a 95% confidence interval.

Table 2-3. Pore radii calculated for the total, LTR, non-LTR, and passive skin samples, as a function of the ultrasound frequency. The lower and upper bounds correspond to the endpoints of the 95% confidence interval of the pore radius.

	Total			LTRs			Non-LTRs		
Frequency	Lower	r_{pore} (Å)	Upper	Lower	r_{pore} (Å)	Upper	Lower	r_{pore} (Å)	Upper
20 kHz	81.5	105	148	-----	-----	-----	17.0	18.5	20.4
40 kHz	61.6	73.9	92.9	165	276	-----	17.2	18.2	19.4
60 kHz	43.6	50.7	61.1	97.2	161	-----	17.3	18.4	19.8
Passive	12.9	13.6	14.4						

and for inulin, r_{pore} = 95 Å). Another recent study also found that the average pore radius for porcine skin treated with 20 kHz LFS/SLS, under identical treatment conditions to those utilized in this manuscript, is 113 Å, utilizing sucrose as a model hydrophilic permeant.[38] This confirms that the data reported here at 20 kHz is consistent with the 20 kHz data reported previously.

In order to explain the observed change in the r_{pore} values with ultrasound frequency in the total skin samples, it is revealing to examine the frequency dependence of the r_{pore} values in the LTRs and non-LTRs. Table 2-3 clearly shows that within the non-LTRs, r_{pore} is independent of the applied ultrasound frequency. Specifically, the r_{pore} values in the non-LTRs remain nearly constant, ranging from 18.2 – 18.5 Å for the three ultrasound frequencies studied, with no statistically significant difference between the three samples. However, these r_{pore} values are statistically significantly larger than the r_{pore} value observed in the passive skin samples (r_{pore} = 13.6 Å). It is noted that the r_{pore} value for native skin that has been determined is consistent with r_{pore} values for native porcine skin reported in the literature (11 – 28 Å).[41-43] Although the calculated r_{pore} values for both the non-LTRs and native skin samples fall within the range of r_{pore} values reported in the literature for native skin, it is important to stress that, with very high statistical certainty (P<0.00001), the calculated r_{pore} values are in fact statistically significantly different in the non-LTR and native skin samples. Accordingly, although there is a statistically significant enhancement in r_{pore} within the non-LTRs relative to the native skin samples, the r_{pore} enhancement observed within the non-LTRs *is not frequency dependent*. On the other hand,

within the LTRs, Table 2-3 clearly shows that there is a frequency dependence of r_{pore}. Similar to what is observed for the total skin samples, as the ultrasound frequency decreases, the r_{pore} values increase from 161 Å at 60 kHz, to 276 Å at 40 kHz, and then to ∞ (>300 Å, the upper-bound for r_{pore} values that can be probed with calcein) at 20 kHz. Because of the observed frequency-independence of r_{pore} in the non-LTRs discussed above, the LTR findings suggests that the observed *increase in the r_{pore} values with decreasing ultrasound frequency* in the total skin samples is due primarily to the increase in the r_{pore} values within the LTRs. This result reflects the fact that the total skin samples consist of both LTRs and non-LTRs, with the majority of permeant transport occurring through the LTRs. As a result, the total skin samples exhibit a similar trend in r_{pore} with ultrasound frequency as do the LTRs. However, because the LTRs represent only a small fraction of the surface coverage of the total skin samples (see Table 2-1), the average r_{pore} values for the total skin samples are significantly lower than those for the LTRs (see Table 2-3).

2.4.3 Mechanisms of Enhancement in the Non-LTRs of Skin Treated with LFS/SLS

Many mechanisms have been proposed and tested to establish if they play a significant role in skin permeability enhancement with LFS. These include: i) acoustic cavitation in the coupling medium above the skin (stable and transient),[5, 6, 8, 9, 44] ii) thermal effects,[9, 44] and iii) convection (acoustic streaming and resulting boundary-layer reduction).[9, 44] Of these, only transient cavitation has been consistently identified as the primary mechanism of skin

permeability enhancement in LFS, especially transient cavitation events near the surface of the skin.[5, 8] These transient cavitation events near the skin surface can perturb the skin either by: i) collapsing as a liquid microjet at the skin surface (either by impacting the skin or impinging into the skin), or ii) spherical collapse near the skin surface (although it has been suggested that spherical collapse close to a membrane may not be a physically achievable process because the interaction between the membrane and the cavitation bubble will likely cause non-linear, or non-spherical, oscillations).[5, 45] Note that cavitation *within* the skin has been conclusively shown not to be a significant contributor to skin permeability enhancement when utilizing LFS, but can contribute at higher frequencies.[9] However, in nearly all the mechanistic LFS studies cited, SLS was not utilized in the skin treatment regimen. The absence of SLS is significant, because it has been shown at 20 kHz,[17] and confirmed in this paper at 20 kHz, 40 kHz, and 60 kHz, that two levels of enhancement are present only when a chemical enhancer, such as SLS, is present in the coupling medium during the LFS treatment. Furthermore, none of the mechanistic studies cited above have independently considered LTRs and non-LTRs. In fact, many of these studies were carried out before LTRs were discovered and were demonstrated to be regions of high permeability.[14] For these reasons, it is possible that a mechanism that may contribute to non-LTR permeabilization during the LFS/SLS treatment may have been overlooked in earlier studies. With the above in mind, the previously proposed mechanisms are next examined, in the context of the findings, to ascertain if they play a role in permeability and pore radius enhancement within non-LTRs.

It is well established that acoustic cavitation is a frequency-dependent process.[9, 10] Accordingly, it is unlikely that cavitation plays a major role in the observed enhancements within

the non-LTRs, because it was found that the r_{pore} values in the non-LTRs are frequency-independent (see Table 2-3). This only leaves heating of the coupling medium and acoustic streaming as potential mechanisms of enhancement in the non-LTRs. Because these experiments involve a pre-treatment of the skin with LFS and SLS, the only role that heating or acoustic streaming could play in permeability enhancement in the non-LTRs is to increase the flux of SLS into the skin (note that calcein is not present during the LFS/SLS skin treatment). This is because both heating of the coupling medium and acoustic streaming are not present in the donor solution post-treatment, and there is no SLS present in the donor solution during the steady-state calcein experiments. Furthermore, it has been shown that ultrasound-induced acoustic streaming can produce significant agitation of aqueous systems, leading to a decrease in the boundary layer above a membrane to an extent that the boundary layer is insignificant when compared to the boundary layer under passive conditions.[44] In addition, heating is also known to increase permeant diffusion coefficients, and it is therefore possible for this mechanism to increase the flux of SLS into the skin. This leads us to propose that SLS is present in elevated amounts within non-LTRs compared to native skin samples, but in far less amounts than in the highly-perturbed LTRs, due to a mechanism such as acoustic streaming or heating that is not as significant as cavitation. Note that acoustic streaming could operate as an enhancement mechanism by either causing a decrease in the boundary layer above the skin or by inducing convective flux of SLS into the skin. Each of these possibilities will be discussed in the following paragraph.

In order to test the hypothesis that there is increased uptake of SLS in the LTRs and non-LTRs compared to the native skin samples, experiments were conducted (see Section 2.2.5) to quantify the amount of SLS in LTRs, non-LTRs, and passive skin samples. Additionally, two groups of

samples were tested to isolate the effects of vigorous stirring and heating in the donor solution during treatment. Figure 2-4 shows a comparison of the penetration of SLS into the non-LTRs with those of the vigorously stirred, the heated, and the passive samples (note that the amount of SLS penetrating into the LTRs was not included in Figure 2-4, in order to more clearly compare the mechanisms associated with SLS penetration into the non-LTRs). It was found that the average amount of SLS in the non-LTRs, per unit area of skin, is $2.51 \cdot 10^{-6}$ mmol/mm^2, which is nearly 2 times greater than that in the native skin samples ($1.40 \cdot 10^{-6}$ mmol/mm^2). In addition, the average amount of SLS in the LTRs ($1.52 \cdot 10^{-5}$ mmol/mm^2), was found to be 11-fold greater than that in the native skin samples. This strongly confirms the hypothesis that SLS is present in increased levels in the non-LTRs compared to the native skin samples, but in far smaller amounts than in the highly-perturbed LTRs. Furthermore, it was found that the SLS concentration in the skin for the vigorously-stirred samples ($2.49 \cdot 10^{-6}$ mmol/mm^2) is statistically similar to that of the non-LTR samples (see 95% confidence intervals in Figure 2-4). However, the samples whose donor solutions were heated to 37°C showed no significant increase in SLS skin concentration ($1.62 \cdot 10^{-6}$ mmol/mm^2) over the passive samples (see 95% confidence intervals in Figure 2-4). Note that in the case of the vigorous stirring experiments, the direction of stirring is parallel to the skin surface (utilizing a stir bar). With this in mind, it is unlikely that convection into the skin is likely playing a role in increased SLS flux during these experiments and, therefore, the uptake of SLS is only increased due to a decrease in the concentration boundary layer above the skin. Therefore, these findings suggest that the dominant mechanism of SLS penetration into the non-LTRs is, in fact, acoustic streaming-induced reduction of the boundary layer above these skin regions.

Additionally, it is well-established that the effect of SLS perturbation on skin can increase r_{pore} values. Ghosh et al. demonstrated that native skin soaked in PBS has an average pore radius of 20±3 Å, while skin contacted with an SLS solution for five hours has an average pore radius of 33±5 Å.[41] This confirms that it is possible for r_{pore} to increase solely due to the exposure of the skin to SLS. Therefore, it was proposed that the observed increase in the r_{pore} values in the non-LTRs, and the resulting increase in calcein permeabilities, compared to native skin, is due mainly to the ultrasound-frequency independent process of SLS acting on these skin regions (note that the variability in native skin pore radius distribution may also play a role), where increased penetration of SLS in the non-LTRs is the result of a non-frequency-specific process such as acoustic streaming (and resulting boundary-layer reduction).

Furthermore, it is important to explain the origin of the observed >30-fold increase in calcein permeability within the non-LTRs, relative to the passive calcein permeability. For this purpose, the permeability of calcein through skin is modeled as follows:[40]

$$P_{calcein,\,i} = \frac{H\left(\lambda_{calcein}\right)_i D^{\infty}_{calcein}}{\Delta x} \cdot \left(\frac{\varepsilon}{\tau}\right)_i \tag{2.7}$$

where $P_{calcein,\,i}$ is the calcein permeability through skin sample i, ε_i is the skin porosity of sample i, τ_i is the skin tortuosity of sample i, and all the other variables were defined previously.

Using Eq. (2.7) to calculate the permeability of calcein through the non-LTR samples, relative to the passive permeability of calcein, and assuming that, in both the non-LTR and passive skin samples, the stratum corneum is the primary barrier to transport (Δx is constant), one obtains:

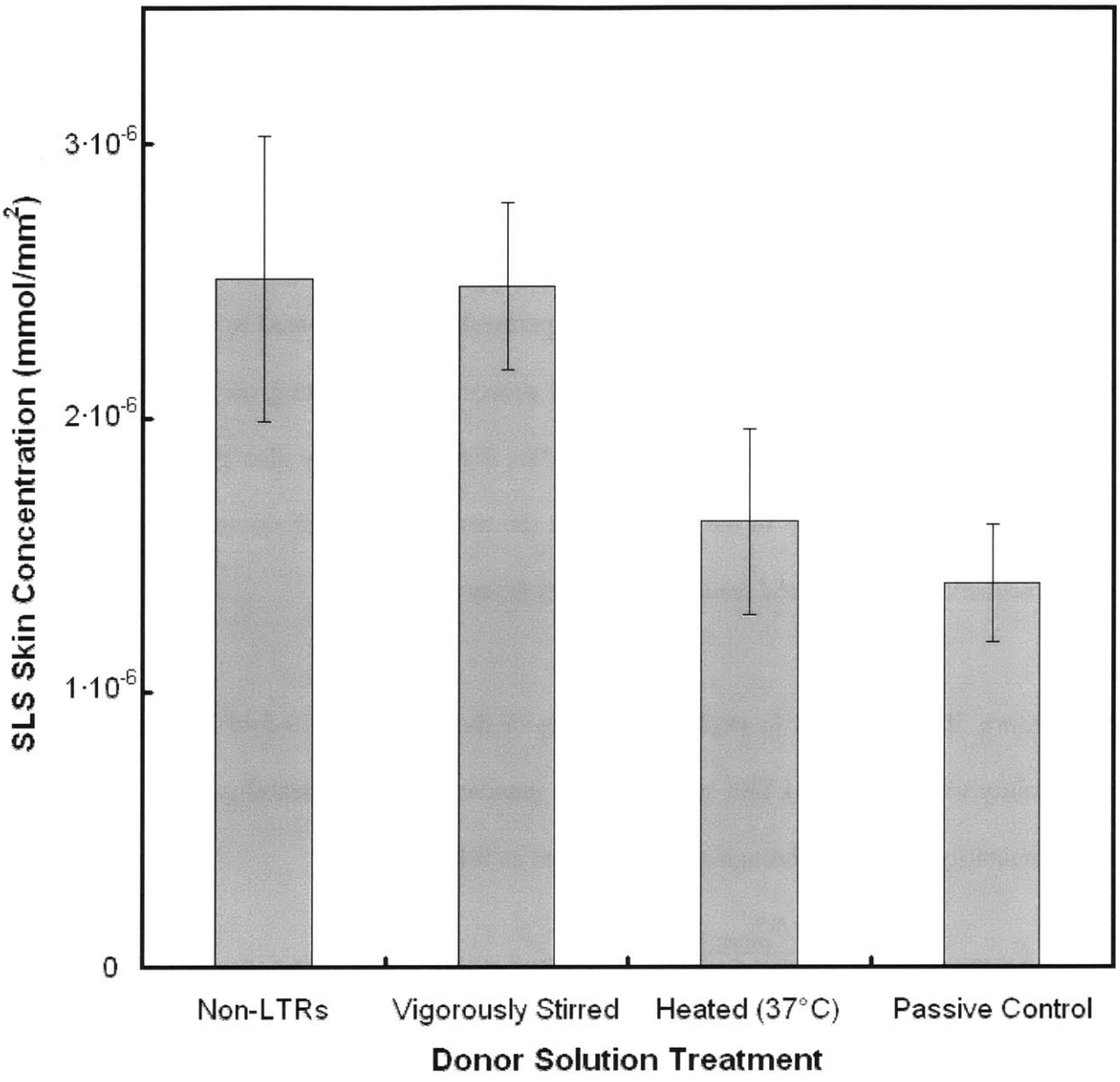

Figure 2-4. Concentration of SLS in skin treated under different experimental conditions in the donor solution, compared to that of non-LTRs. In each case, the total concentration of SLS in the donor solution was 1% (w/v), but stirring and heating (37° C) were varied in order to assess the importance of these two processes on SLS penetration within non-LTRs. Error bars shown are 95% confidence intervals.

$$\frac{P_{calcein,\,non-LTR}}{P_{calcein,\,passive}} = \frac{H\left(\lambda_{calcein}\right)_{non-LTR}}{H\left(\lambda_{calcein}\right)_{passive}} \cdot \left[\left(\frac{\varepsilon}{\tau}\right)_{non-LTR} \Big/ \left(\frac{\varepsilon}{\tau}\right)_{passive} \right] \tag{2.8}$$

Equation (2.8) clearly shows that the calcein permeability in the non-LTRs can increase relative to the passive calcein permeability due to: i) a decrease in calcein hindrance (due to an increase in the radii of the skin pores), and ii) an increase in ε/τ. Both of these quantities can be calculated utilizing Eqs. (2.5) and (2.8). Note that one can also use Eq. (2.6), in place of Eq. (2.8), to obtain very similar results when calculating the ratio of ε/τ in the non-LTRs and passive skin samples. However, Eq. (2.8) was used for simplicity. First, it was found that, over all the non-LTR samples (recall that there is no frequency dependence within non-LTRs), $\frac{H\left(\lambda_{calcein}\right)_{non-LTR}}{H\left(\lambda_{calcein}\right)_{passive}} = \frac{0.081}{0.020} = 4.1$. This suggests that the ~35% increase in pore radius observed within non-LTRs, compared to native skin, causes about a 4-fold decrease in calcein hindrance through the skin pores. Next, using Eq. (2.8), it was found that $\left(\frac{\varepsilon}{\tau}\right)_{non-LTR} \Big/ \left(\frac{\varepsilon}{\tau}\right)_{passive} = \frac{P_{calcein,\,non-LTR}}{P_{calcein,\,passive}} \cdot \left(\frac{H\left(\lambda_{calcein}\right)_{non-LTR}}{H\left(\lambda_{calcein}\right)_{passive}} \right)^{-1} = 36 \cdot (4.1)^{-1} = 8.8$. It is important to note that the increase in pore radius that was calculated for the non-LTRs is embedded within ε/τ, since ε is defined as the area of pores on the skin divided by the total skin area. Therefore, since an approximately 35% increase in pore radius between the non-LTR samples and native skin (18.4 Å and 13.6 Å, respectively) was observed, the increase in pore radius can only account for about a 2-fold ($a_{pore} \sim r_{pore}^2$) increase in ε/τ. However, it was just shown that ε/τ increases nearly 9-fold between the non-LTRs and the native skin samples. It therefore follows that the remaining ~4.5-fold increase in ε/τ must be due to either the creation of new pores or to a

decrease in τ. Furthermore, using the theoretical derivation found in Kushner *et al.*,[23] the following equation can be used to calculate the ratio between $\tau_{non-LTR}/\tau_{passive}$:

$$\tau = \frac{\left(6t_{lag}D_p^{\infty}H\left(\lambda_p\right)\right)^{1/2}}{\Delta x} \tag{2.9}$$

where t_{lag} is the lag time to reach steady-state diffusion and the remaining variables were defined previously.

Using Eq. (2.9) for the non-LTR and passive skin samples, with $\Delta x_{non-LTR} = \Delta x_{passive}$, the following results are obtained:

$$\frac{\tau_{non-LTR}}{\tau_{passive}} = \left(\frac{t_{lag,non-LTR}}{t_{lag,passive}} \cdot \frac{H\left(\lambda_p\right)_{non-LTR}}{H\left(\lambda_p\right)_{passive}}\right)^{1/2} \tag{2.10}$$

Then, substituting into Eq. (2.10), noting that t_{lag} is simply the x-intercept on a plot of P vs. time, one finds that $\frac{\tau_{non-LTR}}{\tau_{passive}} = \left(\frac{t_{lag,non-LTR}}{t_{lag,passive}} \cdot \frac{H\left(\lambda_p\right)_{non-LTR}}{H\left(\lambda_p\right)_{passive}}\right)^{1/2} = \left(\frac{3.1\text{ hr}}{14.2\text{ hr}} \cdot \frac{0.081}{0.020}\right)^{1/2} = 0.94$. This result implies that the tortuosity has decreased only slightly in the non-LTRs relative to the passive skin samples. Therefore, the majority of the remaining 4.5-fold decrease in ε/τ must be due to increases in porosity due to new pore creation. Nevertheless, it is important to recognize that it is quite possible that SLS acting on the skin can, by itself, cause a change in ε/τ. Indeed, it is well established that surfactants are potent transport enhancers, due to their ability to solubilize/extract lipids and denature corneocytes (keratin fibers).[46] In fact, in the same study in which Ghosh *et al.* investigated the increase in pore radius of skin treated passively with SLS,[41] compared to PBS controls, these authors found that the ε/τ ratio increased by nearly

an order-of-magnitude within samples treated with SLS compared to PBS controls, which is consistent with the findings in this study. One can certainly justify the potential of SLS to create new pores on the skin (an increase ε) via the denaturation of corneocytes, which is the most likely explanation for the observed increase in ε/τ based on the findings above. However, more importantly, the analysis presented above confirms that the combined increases in $H(\lambda_{calcein})$ and ε/τ can explain the observed >30-fold ($4.1\times 8.8 = 36$) increase in calcein permeability within the non-LTRs relative to native skin.

2.4.4 Mechanisms of Enhancement in the LTRs of Skin Treated with LFS/SLS

Next examining the observed trend in pore radii in the LTRs, as well as to the related observed trend in the total skin samples, it was found that there is a strong dependence of r_{pore} on the ultrasound frequency (see Table 2-3). This immediately suggests that cavitation is the primary mechanism of enhancement in the LTRs.[10, 12, 47] It is also worth stressing that several published papers have reported that transient cavitation events near the surface of the skin are the primary mechanism of overall skin permeability enhancement with LFS.[5, 6, 8, 9, 44] One study in particular concluded that cavitation, specifically in the vicinity of the skin, scales directly with overall calcein permeability through rat skin.[48] Accordingly, since it was concluded that cavitation is not a mechanism of enhancement in the non-LTRs, it follows that this mechanism must be the primary enhancement mechanism in the LTRs.

Further examination of the LTR data in Table 2-3 shows that the same inverse relationship between the cavitation bubble resonant radius and ultrasound frequency applies to the variation of r_{pore} with ultrasound frequency.[10-12] More specifically, it is well-established that the relationship between the ultrasound frequency (f) and the resonant bubble radius (r_{res}) satisfies the following relationship:[12]

$$r_{res} \cdot f = C_{sol} \tag{2.11}$$

where C_{sol} is a constant that depends on the properties of the solution in which cavitation is taking place.

Then, by proposing that cavitation microjet collapse onto the surface of the skin is the primary mechanism of skin perturbation and, therefore, that r_{pore} and r_{res} are related directly, it can be verified whether the r_{pore} values determined within the LTRs are consistent with the expected variation between the cavitation bubble radius and the ultrasound frequency. Using the same expression given in Eq. (2.11) to relate r_{pore} and f for the 40 kHz and 60 kHz LTR data, it is verified that $C_{sol,pore} = r_{res,40kHz} \cdot 40kHz = r_{res,60kHz} \cdot 60kHz$ (to less than 15% error), and an average $C_{sol,pore}$ value equal to $10.3 \cdot 10^3$ kHz$\cdot$Å is obtained. Using this $C_{sol,pore}$ value to calculate the expected r_{pore} value at 20 kHz, a value of 520 Å is obtained, which is greater than the infinite-pore limit that was calculated for calcein (r_{pore}>300 Å) and consistent with the data.

Similar to the non-LTR case, it is necessary to explain the origin of the observed increase in calcein permeability within the LTRs (greater than 4 orders-of-magnitude), relative to the

passive calcein permeability. However, in the LTR case, because of the decreased barrier properties of the stratum corneum, selecting a suitable value for Δx is more problematic. Fortunately, however, Eq. (2.6) shows that $\varepsilon/\tau \sim \Delta x$, while Eq. (2.7) shows that $P \sim (\Delta x)^{-1}$. As a result, the dependence of permeability on Δx cancels out in Eq. (2.7). For simplicity, in the following analysis it is assumed that, as is the case for non-LTRs and native skin, Δx is equal to the thickness of the stratum corneum (as has been assumed in previous studies of LTRs[14]). Using Eq. (2.7) for the LTRs and passive skin samples, it is found that:

$$\frac{P_{calcein,\,LTR}}{P_{calcein,\,passive}} = \frac{H(\lambda_{calcein})_{LTR}}{H(\lambda_{calcein})_{passive}} \cdot \left[\left(\frac{\varepsilon}{\tau}\right)_{LTR} \Big/ \left(\frac{\varepsilon}{\tau}\right)_{passive} \right] \tag{2.12}$$

Because the results of the analysis will change slightly based on the chosen frequency (recall the frequency dependence of the pore radius within LTRs, see Table 2-3), only the 40 kHz LTR data is considered, since this data lies between the data at 20 kHz and 60 kHz. Similar to the non-LTR analysis presented above, for the LTRs it is found that: $\frac{H(\lambda_{calcein})_{LTR}}{H(\lambda_{calcein})_{passive}} = \frac{0.84}{0.020} = 42$ and $\left(\frac{\varepsilon}{\tau}\right)_{LTR} \Big/ \left(\frac{\varepsilon}{\tau}\right)_{passive} = \frac{1.07 \cdot 10^{-3}}{4.17 \cdot 10^{-6}} = 256$. Using these results in Eq. (2.12), it is clearly seen that these two effects account for the observed 4 orders-of-magnitude ($42 \times 256 = 1.1 \cdot 10^4$) increase in calcein permeability. For completeness, it is important to stress that either: i) the Δx value used for the LTRs has been underestimated, because the predicted increase in ε/τ (256) is less than the increase expected solely from the 20-fold ($276/13.6 = 20$, see Table 2-3) increase in pore radius calculated for the 40-kHz LTRs with respect to native skin ($a_{pore} \sim r_{pore}^2 = 400$), or ii) the number of pores within the LTRs has decreased compared to native skin (this is not unreasonable, since the area of a single pore has increased by 400-fold, and therefore, multiple

native skin pores may have merged into a single LTR pore). Note that, with respect to point (i), if a larger Δx value was chosen for the LTR samples than for the passive skin samples, Eq. (2.12) would need to be modified as follows:

$$\frac{P_{calcein,\,LTR}}{P_{calcein,\,passive}} = \underbrace{\frac{H(\lambda_{calcein})_{LTR}}{H(\lambda_{calcein})_{passive}}}_{1} \cdot \underbrace{\frac{\Delta x_{passive}}{\Delta x_{LTR}}}_{2} \cdot \underbrace{\left[\left(\frac{\varepsilon}{\tau}\right)_{LTR} \Big/ \left(\frac{\varepsilon}{\tau}\right)_{passive}\right]}_{3} \tag{2.13}$$

However, as stated previously, this will have no effect on $\frac{P_{calcein,\,LTR}}{P_{calcein,\,passive}}$, but simply will cause term 2 in Eq. (2.13) to decrease linearly with increasing Δx_{LTR}, while term 3 in Eq. (2.13) will increase linearly with increasing Δx_{LTR} (recall that $\varepsilon/\tau \sim \Delta x$, see Eq. (2.6)). Therefore, in Eq. (2.13), the contributions of Δx_{LTR} in terms 2 and 3 will cancel each other. Furthermore, as there is no rigorous method to estimate Δx more accurately, Eq. (2.13) provides no additional useful information compared to Eq. (2.12). Also, it is noted that a similar analysis to that done for the non-LTRs using Eqs. (2.9) and (2.10), in order to determine the relative contributions of ε and τ, cannot be carried out for the LTRs because of the uncertainty in the precise value of Δx_{LTR}. In any case, regardless of the value of Δx_{LTR} assumed, the analysis presented here can explain the overall increase in calcein permeability observed within LTRs relative to native skin, since $\frac{P_{calcein,\,LTR}}{P_{calcein,\,passive}}$ does not depend on the value of Δx_{LTR} chosen.

Finally, it is important to recognize that the r_{res} values corresponding to the ultrasound frequencies considered here are on the order of tens of microns, while the r_{pore} values calculated in Table 2-3 are on the order of tens of nanometers. This, however, does not affect the

conclusion that transient cavitation collapses near the skin surface are the primary cause for the enlarged pores within LTRs. To reconcile the seemingly large difference between the determined r_{pore} values and the expected r_{res} values at each frequency, the following analysis will be conducted. First, it is well-known that the r_{res} values represent an upper bound on the average cavitation bubble size in aqueous solution.[49, 50] For example, Burdin et al. and Tsochatzidis et al. showed that at 20 kHz, although $r_{res} \sim 150$ μm, the average bubble radius was calculated to be between 3.15-5.25 μm, depending on the measurement method and the applied ultrasound amplitude, or approximately 25- to 50-fold smaller than the resonant radius.[49, 50] In fact, one of the main conclusions of these studies is that the mean measured bubble radius is much smaller than the resonant bubble radius. Second, it has been observed that when transient cavitation bubbles collapse as microjets at an interface, the radius of the impinging microjet is about one order-of-magnitude smaller than the radius of the collapsing cavitation bubble.[45, 51] Third, because the skin is an elastic membrane, it is likely to rebound to some extent after a microjet collapses on it. Although there has been no direct research into the actual physical size or shape of the pores left in the skin by collapsing acoustic cavitation microjets, an interesting analogy may be drawn to sharp punctures of the skin by needles and liquid jet injectors. Significant research has been conducted on the penetration of soft solids, such as skin and silicone rubbers, by sharp microscopic objects.[52, 53] For example, Shergold *et al.* found, utilizing pig skin and silicone rubbers, that the ratio between the persistent defect left in the skin and the diameter of a sharp tipped object was, in all cases, less than unity (tested for diameters of 300 μm – 2.0 mm), with this ratio ranging between ~0.25-0.6 at the surface of the samples.[53] In addition, Roxhed *et al.* found that a microneedle, with a diameter of 108 μm, left a persistent hole in human skin of only 50 μm, leading these authors to conclude that the persistent damage left in the skin was only

about half of the microneedle's shaft diameter.[54] This is relevant to the current analogy because it has recently been shown that liquid jet injectors also penetrate, and damage, the skin in the same manner as sharp-tipped objects puncturing soft materials, such as the skin.[55] Liquid jet injectors transport fluid into the skin by delivering a high-velocity liquid jet (100-200 m/s), having a radius as small as 15 μm, directed at the skin surface,[56] much like an acoustic microjet delivers a liquid jet at the surface of the skin (where the acoustic microjet is expected to have a diameter of ~1 μm or less and have a maximum jet velocity of 153 m/s directed towards the skin[45]). Therefore, the pore radius measured within LTRs are not necessarily equal to the actual radius of the collapsing acoustic microjet itself, but instead, may be equal to the persistent radius of the resulting pore left by the collapsing acoustic microjet. These three mechanisms combined can account for the approximately three orders-of-magnitude difference observed between the expected resonant bubble radii and the calculated r_{pore} values.

Additional research is needed to show definitively that cavitation microjets directed at the skin surface are the primary cause for the formation of pores within LTRs, which would require imaging of the cavitation field above the skin and the pores left within the skin. However, these findings, coupled with the mechanistic analysis described above, provide compelling evidence that this enhancement mechanism is the most likely cause for the observed trend in r_{pore} values seen in the LTRs.

2.5 Conclusions

In this study, it was shown that the pore radii in the non-LTRs are independent of ultrasound frequency, ranging from 18.2 – 18.5 Å. In addition, it was determined that the pore radii in the

non-LTRs are statistically significantly larger than the r_{pore} values for the native skin samples (13.6 Å), suggesting that a frequency-independent enhancement process is at play in these skin regions. Additional experiments were carried out to quantify the amount of SLS penetrating into LTRs and non-LTRs relative to native skin, and it was found that nearly twice as much SLS penetrates into the non-LTRs per unit area than into native skin. Furthermore, by studying different mechanisms of SLS penetration into skin, it was shown that boundary-layer reduction caused by acoustic streaming is the most likely cause for the increased SLS uptake within non-LTRs. Therefore, recognizing that SLS itself can increase pore radii in the skin,[41] it was concluded that a frequency-independent process, such as acoustic streaming, causes increased penetration of SLS into the skin, with SLS acting on the skin being the main contributor to the observed increase in pore radius. In the LTRs, it was observed that the pore radii increase dramatically with decreasing frequency (161 Å, 276 Å, and ∞ for 60 kHz, 40 kHz, and 20 kHz LFS, respectively). Accordingly, strong support was provided to the proposal that transient cavitation events near the skin surface, which are known to be frequency dependent,[10] are the primary mechanism of skin permeability enhancement in LTRs, which is consistent with previous literature findings.[5, 6, 8, 15, 21] The variation of the r_{pore} values with ultrasound frequency in the LTRs also suggests that transient cavitation microjets impinging on the skin surface can explain the observed values of the pore radii.

In Chapter 3, I build upon the knowledge of the role of surfactants in LFS treatment. Recall that, in this chapter, it was found that surfactants play a significant role in skin permeability enhancement within non-LTRs. Therefore, in Chapter 3, the focus is shifted to more deeply understand the effect of non-traditional surfactants in causing skin perturbation when combined

with LFS. Specifically, the fluorescent dye sulforhodamine B (SRB), which has been utilized in the past with LFS treatments as a colorimetric dye, is studied to understand if SRB, by itself, can have an effect on LFS treatment. Furthermore, in Chapter 3, the effect of combining the non-traditional surfactant SRB and a traditional surfactant, SLS, with LFS is investigated. Subsequently, in Chapter 4, the physical model presented in the present study is utilized to provide insight on the synergism between LFS and chemical penetration enhancers, such as surfactants.

2.A Correcting Sample Absorption Values to Account for Lipid Absorption

A series of twenty negative controls were carried out, identical to the experimental protocol described in Section 2.2.4.4, except that PBS was used in the donor chamber instead of 0.2% (w/v) calcein in PBS. This was done in order to test if background species, such as skin lipids, could absorb in the receiver solution at the maximum absorbance wavelength for calcein (λ = 494 nm). It was found that there is time-dependent absorbance at a wavelength of 494 nm for the negative controls. However, the level of absorbance was such that it only affected calcein permeability values significantly (>5%) when the total absorbance in the samples containing calcein was below 0.4. Therefore, only the non-LTR samples and the passive control samples were found to be affected significantly by background lipid absorption at 494 nm.

In order to properly account for background lipid absorption in the affected samples, the absorbance intensity as a function of wavelength was measured, in the range 420 nm – 550 nm, for the negative control samples and for samples containing known concentrations of pure

calcein. Figure 2-5 shows the variation of the absorbance with wavelength in: negative control samples containing skin lipids (Figure 2-5A), samples containing solely calcein (Figure 2-5B), and non-LTR samples containing a mixture of skin lipids and calcein (Figure 2-5C). One can clearly see that the curve in Figure 2-5C is a simple combination of the curves in Figures 2-5A and 2-5B.

Unfortunately, the variation in the absorption between samples for the negative controls was too large to simply average the lipid absorption at each sampling time point and then subtract it from the non-LTR and the passive sample data. Fortunately, however, the background absorption for all the negative control samples were found to have similar shapes, indicating that the absorption curve for any of these samples could be reproduced by multiplying a standard background curve (which was generated by averaging the lipid absorption at each wavelength over all the negative control samples) by a constant parameter associated with that given sample. Specifically,

$$A_i(\lambda) = c_i A_{sc}(\lambda) \tag{2.A1}$$

where $A_i(\lambda)$ is the absorption of sample *i* at a given wavelength (λ) between 420 – 550 nm, c_i is the constant background parameter associated with that sample, and $A_{sc}(\lambda)$ is the absorption at a given wavelength for the standard curve.

Therefore, the entire background curve for any sample can simply be defined by a single parameter. In addition, in the negative control samples, this parameter is essentially wavelength independent in the relevant range of 420 nm – 550 nm. This indicates that one can extract the background absorbance parameter at any wavelength, or range of wavelengths, and still reconstruct the entire background absorbance curve for the range of wavelengths between 420

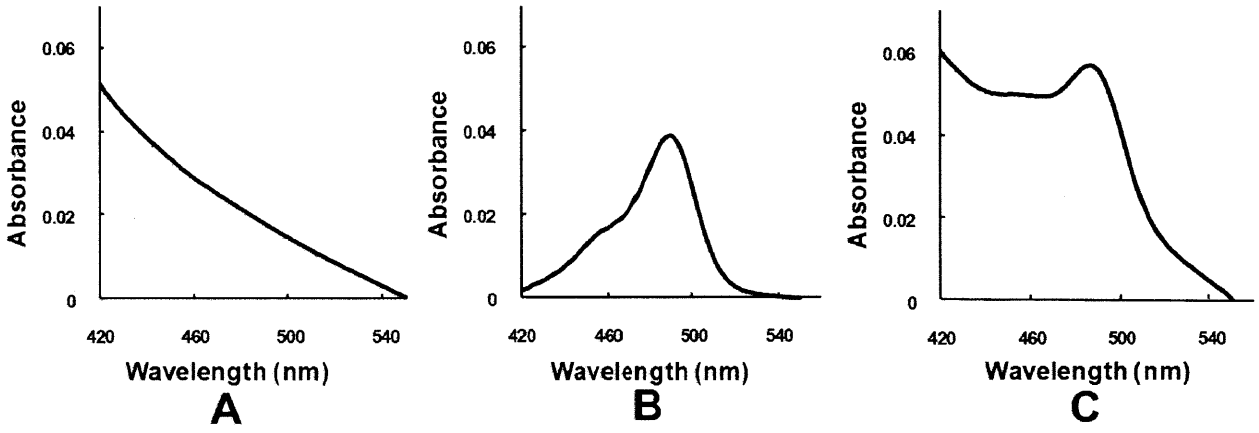

Figure 2-5. Absorption as a function of wavelength, in the range 420 – 550 nm, for: a background sample containing skin lipids (A), a pure calcein sample (B), and a non-LTR sample containing both calcein and skin lipids (C).

nm and 550 nm. An examination of the plots in Figure 2-5 shows that in the range 420-430 nm and 540-550 nm there is much larger absorption in the background curve (Figure 2-5A) than in the pure calcein curve (Figure 2-5B). As a result, the curve in Figure 2-5C closely resembles Figure 2-5A in these two regions. Therefore, in order to decompose a curve like that in Figure 2-5C into its corresponding background curve (Figure 2-5A) and pure calcein curve (Figure 2-5B), the background absorbance parameter was calculated in the range 420-430 nm and 540-550 nm by dividing the absorbance in these regions by the absorbance for that wavelength in the standard background curve. Subsequently, the simple arithmetic mean of these twenty-two values was calculated to obtain the background absorbance parameter for that sample, and the background curve was reconstructed by multiplying the calculated parameter by the standard background curve. The calculated background curve (such as Figure 2-5A) was then subtracted from the total curve (such as Figure 2-5C) in order to construct a pure calcein curve (such as Figure 2-5B) for that sample. The resulting curve was then used to calculate the concentration of calcein in the receiver chamber.

In order to validate that the decomposition method described above yields reproducible and reliable calcein concentrations, a series of 10 samples with predetermined absorption profiles of background lipids and predetermined absorption profiles of pure calcein were mixed. The actual concentration of calcein was compared to the value obtained using this decomposition method, and the difference between the calcein concentration calculated by the decomposition method and the actual calcein concentration in each case was found to be less than ~5%, thereby validating this method.

2.6 References

[1] J. Escobar-Chavez, D. Bonilla-Martínez, M. Villegas-González, I. Rodríguez-Cruz, C. Domínguez-Delgado, The Use of Sonophoresis in the Administration of Drugs Throughout the Skin. J Pharm Pharm Sci 12(1) (2009) 88.

[2] D. Levy, J. Kost, Y. Meshulam, R. Langer, Effect of ultrasound on transdermal drug delivery to rats and guinea pigs. J Clin Invest 83(6) (1989) 2074.

[3] S. Mitragotri, D. Blankschtein, R. Langer, Ultrasound-mediated transdermal protein delivery. Science 269(5225) (1995) 850-853.

[4] M. Johnson, S. Mitragotri, A. Patel, D. Blankschtein, R. Langer, Synergistic effects of chemical enhancers and therapeutic ultrasound on transdermal drug delivery. J Pharm Sci 85(7) (1996) 670-679.

[5] A. Tezel, S. Mitragotri, Interactions of inertial cavitation bubbles with stratum corneum lipid bilayers during low-frequency sonophoresis. Biophys J 85(6) (2003) 3502-3512.

[6] A. Tezel, A. Sens, S. Mitragotri, Investigations of the role of cavitation in low-frequency sonophoresis using acoustic spectroscopy. J Pharm Sci 91(2) (2002) 444-453.

[7] T. Terahara, S. Mitragotri, R. Langer, Porous resins as a cavitation enhancer for low-frequency sonophoresis. J Pharm Sci 91(3) (2002) 753-759.

[8] H. Tang, C. Wang, D. Blankschtein, R. Langer, An investigation of the role of cavitation in low-frequency ultrasound-mediated transdermal drug transport. Pharm Res 19(8) (2002) 1160-1169.

[9] S. Mitragotri, D. Blankschtein, R. Langer, Transdermal drug delivery using low-frequency sonophoresis. Pharm Res 13(3) (1996) 411-420.

[10] W. Gaertner, Frequency Dependence of Ultrasonic Cavitation. J Acoust Soc Am 26(6) (1954) 977-980.

[11] N. Khabeev, Resonance properties of soluble gas bubbles. Int J Heat Mass Tran 49(5-6) (2006) 1022-1026.

[12] T. Leighton, A. Walton, M. Pickworth, Primary Bjerknes forces. Eur J Phys(1) (1990) 47.

[13] S. Mitragotri, D. Ray, J. Farrell, H. Tang, B. Yu, J. Kost, D. Blankschtein, R. Langer, Synergistic effect of low-frequency ultrasound and sodium lauryl sulfate on transdermal transport. J Pharm Sci 89(7) (2000) 892-900.

[14] J. Kushner, D. Blankschtein, R. Langer, Experimental demonstration of the existence of highly permeable localized transport regions in low-frequency sonophoresis. J Pharm Sci 93(11) (2004) 2733-2745.

[15] A. Tezel, A. Sens, J. Tuchscherer, S. Mitragotri, Synergistic effect of low-frequency ultrasound and surfactants on skin permeability. J Pharm Sci 91(1) (2002) 91-100.

[16] J. Kushner, D. Blankschtein, R. Langer, Evaluation of hydrophilic permeant transport parameters in the localized and non-localized transport regions of skin treated simultaneously with low-frequency ultrasound and sodium lauryl sulfate. J Pharm Sci 97(2) (2008) 906-918.

[17] J. Kushner, D. Kim, P. So, D. Blankschtein, R. Langer, Dual-channel two-photon microscopy study of transdermal transport in skin treated with low-frequency ultrasound and a chemical enhancer. J Invest Dermatol 127(12) (2007) 2832-2846.

[18] A. Tezel, S. Dokka, S. Kelly, G. Hardee, S. Mitragotri, Topical delivery of anti-sense oligonucleotides using low-frequency sonophoresis. Pharm Res 21(12) (2004) 2219-2225.

[19] A. Tezel, A. Sens, S. Mitragotri, A theoretical analysis of low-frequency sonophoresis: dependence of transdermal transport pathways on frequency and energy density. Pharm Res 19(12) (2002) 1841-1846.

[20] A. Tezel, A. Sens, J. Tuchscherer, S. Mitragotri, Frequency dependence of sonophoresis. Pharm Res 18(12) (2001) 1694-1700.

[21] J. Kushner, D. Blankschtein, R. Langer, Heterogeneity in skin treated with low-frequency ultrasound. J Pharm Sci 97(10) (2008) 4119-4128.

[22] H. Tang, S. Mitragotri, D. Blankschtein, R. Langer, Theoretical description of transdermal transport of hydrophilic permeants: application to low-frequency sonophoresis. J Pharm Sci 90(5) (2001) 545-568.

[23] J. Kushner, D. Blankschtein, R. Langer, Evaluation of the porosity, the tortuosity, and the hindrance factor for the transdermal delivery of hydrophilic permeants in the context of the aqueous pore pathway hypothesis using dual-radiolabeled permeability experiments. J Pharm Sci 96(12) (2007) 3263-3282.

[24] SyracuseResearchCorporation, Interactive PhysProp Database Demo. http://www.syrres.com/what-we-do/databaseforms.aspx?id=386.

[25] P. Karande, A. Jain, S. Mitragotri, Relationships between skin's electrical impedance and permeability in the presence of chemical enhancers. J Control Release 110(2) (2006) 307-313.

[26] H. Tang, D. Blankschtein, R. Langer, Effects of low-frequency ultrasound on the transdermal permeation of mannitol: comparative studies with in vivo and in vitro skin. J Pharm Sci 91(8) (2002) 1776-1794.

[27] G. Kasting, L. Bowman, Dc Electrical-Properties of Frozen, Excised Human Skin. Pharm Res 7(2) (1990) 134-143.

[28] G. Kasting, L. Bowman, Electrical Analysis of Fresh, Excised Human Skin - a Comparison with Frozen Skin. Pharm Res 7(11) (1990) 1141-1146.

[29] J. Rosell, J. Colominas, P. Riu, R. Pallasareny, J. Webster, Skin Impedance from 1 Hz to 1 Mhz. IEEE T Bio-Med Eng 35(8) (1988) 649-651.

[30] R. Anderson, Optics of the skin. Clinical Photomedicine (1993) 19–35.

[31] R. Anderson, J. Parrish, The optics of human skin. J Invest Dermatol 77(1) (1981) 13-19.

[32] A. Bashkatov, E. Genina, V. Kochubey, V. Tuchin, Optical properties of human skin, subcutaneous and mucous tissues in the wavelength range from 400 to 2000 nm. J Phys D Appl Phys 38 (2005) 2543.

[33] S. Jacques, Origins of tissue optical properties in the UVA, visible, and NIR regions. Advances in Optical Imaging and Photon Migration 2 (1996) 364-370.

[34] I. Meglinski, S. Matcher, Quantitative assessment of skin layers absorption and skin reflectance spectra simulation. Physiol Meas 23 (2002) 741-753.

[35] P. Dechadilok, W. Deen, Hindrance factors for diffusion and convection in pores. Ind Eng Chem Res 45(21) (2006) 6953-6959.

[36] A. Tezel, A. Sens, S. Mitragotri, Description of transdermal transport of hydrophilic solutes during low-frequency sonophoresis based on a modified porous pathway model. J Pharm Sci 92(2) (2003) 381-393.

[37] A. Tezel, A. Sens, S. Mitragotri, Incorporation of lipophilic pathways into the porous pathway model for describing skin permeabilization during low-frequency sonophoresis. J Control Release 83(1) (2002) 183-188.

[38] J. Seto, B. Polat, R. Lopez, D. Blankschtein, R. Langer, Effects of ultrasound and sodium lauryl sulfate on the transdermal delivery of hydrophilic permeants: Comparative in vitro studies

with full-thickness and split-thickness pig and human skin. J Control Release 145(1) (2010) 26-32.

[39] D. Edwards, M. Prausnitz, R. Langer, J. Weaver, Analysis of enhanced transdermal transport by skin electroporation. J Control Release 34(3) (1995) 211-221.

[40] M. Johnson, D. Blankschtein, R. Langer, Evaluation of solute permeation through the stratum corneum: Lateral bilayer diffusion as the primary transport mechanism. J Pharm Sci 86(10) (1997) 1162-1172.

[41] S. Ghosh, D. Blankschtein, The role of sodium dodecyl sulfate (SDS) micelles in inducing skin barrier perturbation in the presence of glycerol. Int J Cosmetic Sci 30 (2007) 73.

[42] S. Ghosh, D. Blankschtein, Why is sodium cocoyl isethionate (SCI) mild to the skin barrier? An in vitro investigation based on the relative sizes of the SCI micelles and the skin aqueous pores. J Cosmet Sci 58(3) (2007) 229-244.

[43] P. Moore, S. Puvvada, D. Blankschtein, Challenging the surfactant monomer skin penetration model: Penetration of sodium dodecyl sulfate micelles into the epidermis. J Cosmet Sci 54 (2003) 29-46.

[44] J. Simonin, On the mechanisms of in vitro and in vivo phonophoresis. J Control Release 33(1) (1995) 125-141.

[45] S. Fong, E. Klaseboer, C. Turangan, B. Khoo, K. Hung, Numerical analysis of a gas bubble near bio-materials in an ultrasound field. Ultrasound Med Biol 32(6) (2006) 925-942.

[46] M. Prausnitz, S. Mitragotri, R. Langer, Current status and future potential of transdermal drug delivery. Nat Rev Drug Discov 3(2) (2004) 115-124.

[47] N. Khabeev, Resonance Properties of Vapor Bubbles. Pmm-J Appl Math Mec+ 45(4) (1981) 512-517.

[48] H. Ueda, M. Mutoh, T. Seki, D. Kobayashi, Y. Morimoto, Acoustic Cavitation as an Enhancing Mechanism of Low-Frequency Sonophoresis for Transdermal Drug Delivery. Biol Pharm Bull 32(5) (2009) 916-920.

[49] N. Tsochatzidis, P. Guiraud, A. Wilhelm, H. Delmas, Determination of velocity, size and concentration of ultrasonic cavitation bubbles by the phase-Doppler technique. Chem Eng Sci 56(5) (2001) 1831-1840.

[50] F. Burdin, N. Tsochatzidis, P. Guiraud, A. Wilhelm, H. Delmas, Characterisation of the acoustic cavitation cloud by two laser techniques. Ultrason Sonochem 6(1-2) (1999) 43-51.

[51] T. Kodama, Y. Tomita, Cavitation bubble behavior and bubble-shock wave interaction near a gelatin surface as a study of in vivo bubble dynamics. Appl Phys B-Lasers O 70(1) (2000) 139-149.

[52] O. Shergold, N. Fleck, Mechanisms of deep penetration of soft solids, with application to the injection and wounding of skin. P Roy Soc Lond A Mat 460(2050) (2004) 3037.

[53] O. Shergold, N. Fleck, Experimental investigation into the deep penetration of soft solids by sharp and blunt punches, with application to the piercing of skin. J Biomech Eng-T ASME 127 (2005) 838.

[54] N. Roxhed, T. Gasser, P. Griss, G. Holzapfel, G. Stemme, Penetration-enhanced ultrasharp microneedles and prediction on skin interaction for efficient transdermal drug delivery. J Microelectromech S 16(6) (2007) 1429.

[55] O. Shergold, N. Fleck, T. King, The penetration of a soft solid by a liquid jet, with application to the administration of a needle-free injection. J Biomech 39(14) (2006) 2593-2602.

[56] J. Schramm-Baxter, S. Mitragotri, Needle-free jet injections: dependence of jet penetration and dispersion in the skin on jet power. J Control Release 97(3) (2004) 527-535.

Chapter 3

The Effect of Non-Traditional Surfactants on Low-Frequency Ultrasound-Mediated Skin Permeability Enhancement: The Case of Sulforhodamine B

3.1 Introduction

As shown in Chapter 2.4.3, the addition of surfactants to the coupling solution during a low-frequency sonophoresis (LFS) treatment can have pronounced effects on the permeability and structural parameters of the skin. In this chapter, I will investigate how non-traditional surfactants, such as the dye sulforhodamine B (SRB), can also have a significant impact on skin permeability enhancement with LFS. Often, the amphiphilicity of non-traditional surfactants is not recognized, and therefore, these effects can be overlooked, leading to unintended effects, especially when combined with other surfactants. This chapter will investigate the effects of a non-traditional surfactant, SRB, and the combination of a non-traditional surfactant and a traditional surfactant, sodium lauryl sulfate (SLS), on skin permeability enhancement by LFS.

Rhodamine dyes are a class of xanthene-derived molecules that are commonly used as laser dyes and fluorescent probes. Although most rhodamine dyes are cationic or have a net neutral charge (zwitterionic), there are forms of these dyes that have been imparted with added water solubility, and a net negative charge, by aromatic sulfonation of the phenyl pendant group. One such molecule, sulforhodamine B (SRB, see Figure 3-1), has been used extensively during the last few decades as: (i) a fluid-phase tracer,[1-3] (ii) a principal component in an assay for cytotoxocity,[4-5] and (iii) a model hydrophilic probe,[6-19] among others.

In spite of the widespread use of SRB, investigations into its chemical nature, especially with respect to its surface activity and interactions with surfactants, have been limited in scope in comparison to research done on other dyes, including several other rhodamines. For example, dyes such as rhodamine B[20-24] and rhodamine 6G[22, 25-27] have been studied extensively with regards to: (i) their adsorption at oil/water or air/water interfaces, (ii) their aggregation in aqueous solution as either dimers or higher-order aggregates, and (iii) their interactions with surfactant monomers and micelles. Many other fluorescent dyes, such as rose Bengal[28, 29] and various porphyrins,[30, 31] have also been studied with regards to their interactions with surfactants and their solubilization within, or association with, micelles. This is because dye-surfactant interactions can lead to the break-up of dye dimers or to the solubilization of dyes in the palisade layer or non-polar core of micelles, both of which can have dramatic consequences on the dye absorption and fluorescence wavelength and intensity.[32, 33] For example, an amplification of fluorescence has even been observed for certain fluorophores when they associate with surfactants.[34-36]

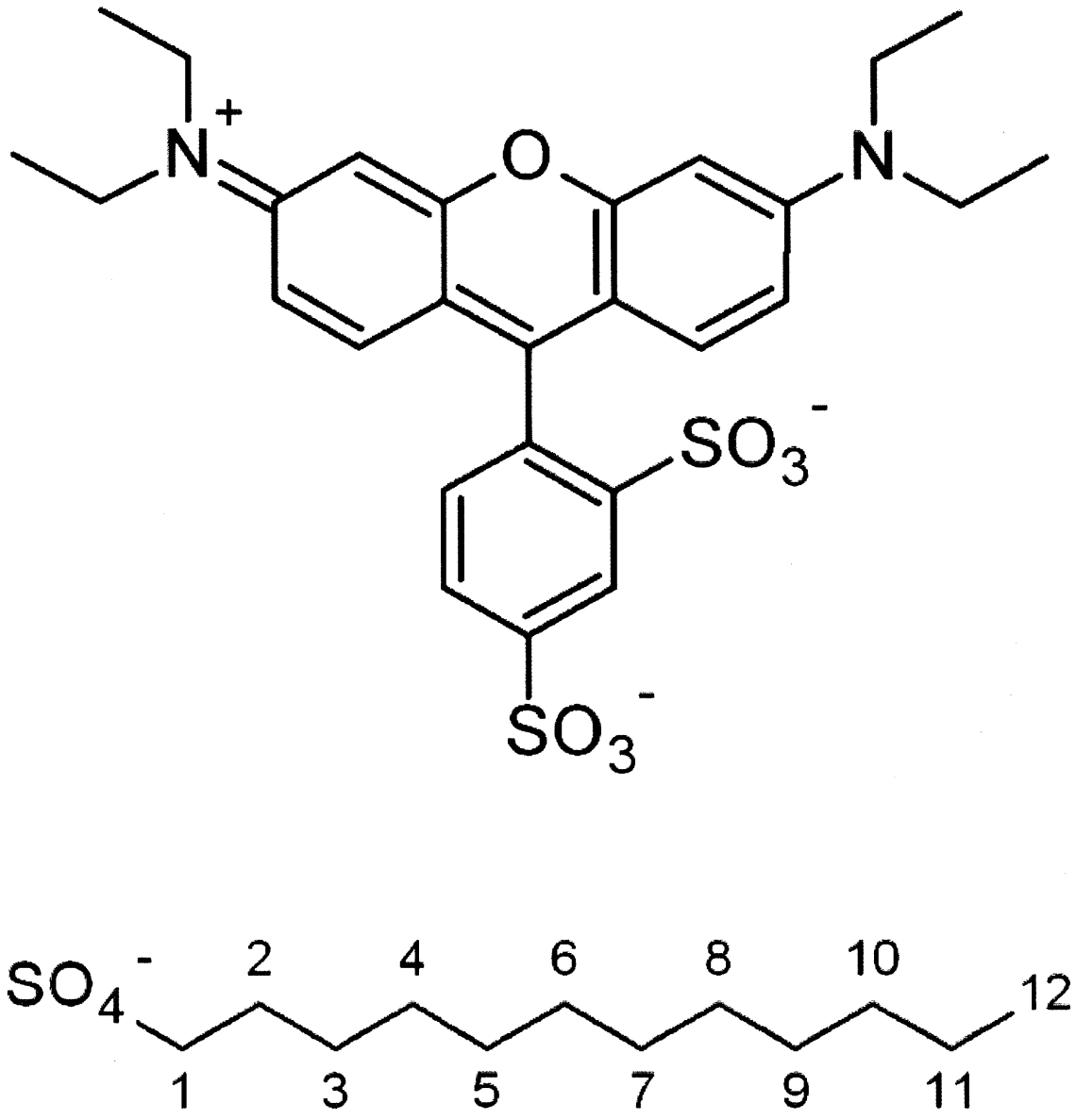

Figure 3-1. Chemical structures of sulforhodamine B (top) and sodium lauryl sulfate (bottom), where the sodium counterion corresponding to both molecules is not shown for clarity.

Like many dyes, SRB is known to dimerize in solution,[20] and belongs to a family of dyes that have been shown to include amphiphiles (such as the aforementioned rhodamine B[24] and rhodamine 6G[25]). However, in contrast to other rhodamine dyes, SRB adsorption has only been studied with respect to charged surfaces (such as cationic octadecylamine Langmuir-Blodgett films and anionic silica glass[37-39]), with minimal investigation into its activity at polar/non-polar interfaces or its potential interaction with surfactants in aqueous solutions. The likely reason for this lack of investigation is due to the relatively high water solubility of SRB compared to other rhodamine dyes, which has led some to designate SRB as a "model hydrophilic" fluorescent probe.[6-19] However, as will be demonstrated experimentally in this paper, SRB does not behave as a simple salt, and has the ability to: (i) adsorb at an air-water interface, causing a decrease in surface tension, and (ii) interact strongly with surfactants in aqueous media, inducing significant changes in the driving force for micellization, as evidenced by a significant decrease in the critical micelle concentration (cmc) of SLS upon mixing with SRB.

In the present study, the amphiphilic nature of SRB is investigated both experimentally and using molecular dynamics simulations. Experimentally, surface tension measurements are used to study SRB adsorption at air/water interfaces, including its ability to affect the cmc of the commonly-used anionic surfactant, SLS. The extent of SRB incorporation into SLS micelles is also investigated experimentally. To elucidate the experimental findings, bulk and interfacial molecular dynamics (MD) simulations of SRB in aqueous solution were conducted, both in the absence and in the presence of SLS. Such simulations provide a useful means for elucidating

dye-surfactant interactions, and may be applied more broadly to other dyes, thus minimizing the need for rigorous spectroscopic experimental measurements.

Finally, to illustrate the implications of the amphiphilic nature of SRB, an interesting case study on the effect of SRB on transdermal drug delivery using low-frequency ultrasound is presented. Amphiphilic molecules are known to act synergistically with low-frequency ultrasound in inducing skin permeability enhancement, which motivated the case study to further test the amphiphilicity of SRB.[40, 41] The results obtained with SRB are compared to those obtained with the non-amphiphilic dye allura red (red food coloring).

3.2 Experimental

3.2.1 Materials

SRB, SLS, and phosphate buffered saline (PBS) were obtained from Sigma-Aldrich Company (St. Louis, MO). Allura red was obtained from TCI America (Portland, OR). All chemicals were used as received. Milli-Q (Millipore Corporation, Billerica, MA) water was used for the preparation of all aqueous solutions.

3.2.2 Surface Tension Measurements

The surface tensions of aqueous solutions of SLS, SRB, and SLS in 9 mM SRB were measured as a function of concentration using a Krüss K11 tensiometer (Hamburg, Germany). The plate method was utilized with a titanium Wilhelmy plate (Krüss, wetting length of 42 mm). For each measurement, twenty surface tension readings were obtained, three seconds apart, and the final

ten readings were averaged to yield the surface tension for that measurement (with the first ten measurements serving as an equilibration period). Surface tension measurements of each solution considered were repeated until consistent values were obtained for three consecutive measurements (<0.1 mN/m variation at 25±1°C). These three measurements were then averaged to yield the surface tension of the solution reported here.

3.2.3 Determination of the Amount of SRB Unbound to SLS Micelles

In order to determine the amount of SRB incorporated into SLS micelles, aqueous solutions of 9 mM SRB were prepared, with varying concentrations of SLS (0 – 64 mM). 5 mL of each solution was then added to 10,000 molecular weight (MW) filter centrifugation tubes (Sartorius Stedim Biotech, Goettingen, Germany) and subsequently centrifuged at 900 *g* for 2 minutes. Since the aggregation number of an SLS micelle is ~50 and SLS has a MW of 288.4 g/mol,[42-44] the MW of an SLS micelle is greater than the MW threshold for the selected filter membrane. Assuming that any formed SRB/SLS micelles have an aggregation number comparable to, or larger than, that of an SLS micelle, SRB is expected to be present in the filtrate in only its unbound form (i.e., in monomeric or dimeric form). Note that the rotational speed and duration of centrifugation were chosen such that less than 10% of the solution would pass through the filter (0.2 – 0.4 mL). This limits the extent of micelle disassociation in the retentate, which is similar to previously reported protocols used to separate monomers from self-assembled aggregates.[45] 20 μL of the permeate was then diluted to 20 mL (1000-fold dilution), to ensure that the SRB molecules being assayed were in monomeric form. The concentration of SRB was then quantified using a UV/VIS spectrophotometer (DU800, Beckman Coulter Inc., Brea, CA) at a wavelength of 560 nm (the observed peak absorbance of SRB). For each SLS concentration

considered, the amount of unbound SRB was then reported as the ratio of the concentration of SRB in the filtrate divided by the initial amount of SRB in solution (9 mM).

3.2.4 Testing the Ability of SRB to Enhance Skin Permeability

Previously published protocols[46, 47] were utilized for the storage and preparation of skin samples. Skin samples utilized in the study were harvested from the back and flank of Yorkshire pigs in accordance with the MIT Committee on Animal Care. Skin electrical resistivity, R, is known to scale directly with skin permeability, and provides an accurate, instantaneous measure of the structural state of the skin.[48] Previously published method[46-49] were followed to measure R of each skin sample. Pre-treatment of skin samples by low-frequency ultrasound was also carried out according to previously published methods,[46, 47] at an intensity of 7.5 W/cm^2, duty cycle of 50% (5 s on, 5 s off), and tip displacement of 3 mm for 10 minutes of ON time (replacing the coupling medium every two minutes to minimize thermal effects). The coupling media utilized in the experiments are reported in Section 3.3.3. Interested readers should refer to Refs. [46-49] for complete experimental details.

3.2.5 Molecular Dynamics Simulations

To simulate the adsorption of a single SRB molecule at the air/water interface, an SRB molecule was initially positioned at the center of a water box. The size of the water box was chosen to be sufficiently large ($4 \times 4 \times 10$ nm^3) such that the concentration of SRB in water (10.4 mM) corresponds to less than one-half of its experimental solubility. The water box was sandwiched between two large layers of vacuum ($4 \times 4 \times 5$ nm^3 each) in order to mimic the air/water interfaces. Note that in all the simulations reported here, sodium counterions were added by

replacing the corresponding number of water molecules to maintain electroneutrality of the simulated systems. As the simulation proceeded, the SRB molecule gradually diffused and eventually adsorbed at the air/water interface after 25 ns. The simulation was run for an additional 15 ns for data collection. For simulations testing the adsorption of SRB dimers at the air/water interface, SRB molecules were initially placed randomly at the interface. Simulations were then run in an identical fashion to the single SRB monomer case described above. After equilibration, both SRB monomers and dimers were observed in the bulk solution and adsorbed at the interface. To determine the dimer hydration data, the longest adsorbed stable SRB dimer was selected and tracked for 4 ns for the data analysis.

Following the procedure introduced by Stephenson *et al.*, the relative hydration of each atomic group in SRB was defined as the ratio between the number of water contacts around each atomic group computed in the SRB adsorption simulation, relative to the number of water contacts computed in the SRB monomer simulation.[50] Note that the SRB monomer simulation was carried out by solvating and equilibrating a single SRB molecule in a water box for 5 ns.

To simulate the aggregation of SRB molecules in the bulk water phase, the SRB molecules were positioned randomly in the simulation box, followed by solvating them with randomized water molecules. Five different SRB concentrations were considered, corresponding to 6 to 49 SRB molecules in the simulation box. Each simulation was equilibrated for 30 ns with the last 10 ns used for data analysis. During the bulk simulations, the formation of SRB dimers was observed and dominated the population of SRB aggregates (with few monomers and trimers observed). In order to better understand the orientation between SRB molecules that form dimers, the angular

distribution function of the angle between the pendant groups of SRB molecules in the dimeric state were computed for the lowest SRB concentration case.

To simulate the interactions between the SRB and SLS molecules, 10 SRB and 40 SLS molecules were positioned randomly in the simulation box, followed by solvating them with randomized water molecules. Note that the total number of SRB and SLS molecules was selected to be similar to the aggregation number of an SLS micelle (~50). A second simulation was also conducted, keeping the concentration of SLS and SRB constant, but with 30 SRB and 120 SLS molecules in the simulation box. The larger simulation was conducted to check the hydration calculations, because it is known that the amount of free monomer present can effect the micelle aggregation number due to the long times scales associated with micellar fission.[51] The simulations were equilibrated for 60 ns, with the last 30 ns used for data analysis. Two SRB-SLS micelles were formed during the 50 molecule simulation and eventually stabilized, with ~6 micelles forming in the larger simulation. Relative hydration calculations for both simulations were carried out and the values obtained were found to be nearly identical. The relative hydration diagram reported in the text corresponds to that of the larger micelle in the 50 molecule simulation. Note that the relative hydrations of the SRB and SLS molecules in this case were defined as the number of water contacts around each atomic group in the micellar state relative to the hydration of that atomic group in a bulk aqueous monomer simulation.[50] The SLS monomer simulation was conducted as discussed earlier for the SRB case.

Water molecules were modeled using the standard SPC/E model,[52] with bond lengths constrained using the SETTLE algorithm.[53] SRB and SLS molecules were modeled using the

OPLS-AA force field.[54] Previously published force-field parameters were utilized for SLS and rhodamine dyes.[55, 56] The +1 charge on the xanthene structure was delocalized symmetrically over the xanthene rings, as in previously published studies[55] (note that the depiction of a localized +1 charge in Figure 3-1 is for illustrative purposes only). Bond lengths in the SRB and SLS molecules were constrained using the parallel version of the LINCS algorithm.[57, 58] van der Waals (vdW) attractions and hard-core steric repulsions were treated with a cutoff distance of 0.9 nm, which falls within the typical range of cutoff values used in other studies.[59, 60] The vdW attractions and the hard-core steric repulsions between different atoms were calculated from the Lennard-Jones potential using the standard geometric averaging rule which is implemented in the OPLS-AA force field.[54] Long-range electrostatic interactions were treated using the particle mesh Ewald (PME) summation method.[61, 62] The equations of motion were integrated with a time step of 2 fs using the Verlet (Leap-Frog) algorithm.[63, 64] SRB adsorption at the air/water interface was simulated under the NVT ensemble (constant number of atoms, constant volume, and constant temperature of 298.15 K), while all the other simulations were conducted under the NPT ensemble (constant pressure of 1 bar instead of constant volume) in order to best mimic the experimental conditions. The velocity-rescaled Berendsen thermostat was implemented to maintain a constant temperature in the simulated system.[65] The pressure was coupled to an isotropic Berendsen barostat.[66] Periodic boundary conditions were applied in all three directions. The trajectories corresponding to all the atoms in the system were saved every 10,000 steps (20 ps) to satisfy the ergodicity criterion for data analysis.[67] All the simulations presented here were carried out using the GROMACS 4.0 software package.[68]

3.3 Results and Discussion

3.3.1 Adsorption of SRB at the Air/Water Interface

The surface tension measurements revealed that SRB adsorbs at the air/water interface, as reflected in the observed concentration-dependent reduction in the surface tension of aqueous SRB solutions (see Figure 3-2, open circles). This behavior is in stark contrast with the effect of allura red (red food coloring), where no decrease in surface tension is observed as a function of concentration with this non-amphiphilic dye (see Figure 3-2, black diamonds). At the highest SRB concentration considered (22 mM), the surface tension reduction was found to be ~23 mN/m, which is quite significant considering that SLS was found to decrease the surface tension of water by ~33 mN/m above its cmc. The surface excess of SRB was calculated from the Gibbs Adsorption Equation,[69] assuming complete dissociation of sodium ions from the sulfonate groups, in the linear region of the data (2-22 mM) and found to be $1.18 \cdot 10^{-6}$ mol/m^2, which corresponds to 140 Å^2/molecule. As a point of comparison, the surface excess of SLS was found to be $3.56 \cdot 10^{-6}$ mol/m^2, in the linear region below the cmc (3-7 mM, Figure 3-2, open squares), which corresponds to 46.6 Å^2/molecule, a value that is consistent with previously reported values (for example, 46 Å^2/molecule at 4 mM[70]). The higher surface excess of SLS, relative to that of SRB, reflects the fact that more SLS molecules can adsorb at the interface, per unit area, than SRB molecules. In view of the chemical structures of SRB and SLS shown in Figure 3-1, this result is expected because SRB is generally bulkier than SLS.

MD simulations of SRB molecules near the air/water interface were carried out to elucidate the adsorption behavior of SRB. The final state of the simulation, with a single SRB molecule adsorbed at a clean air/water interface, is shown in Figure 3-3B. Figure 3-3A shows the relative

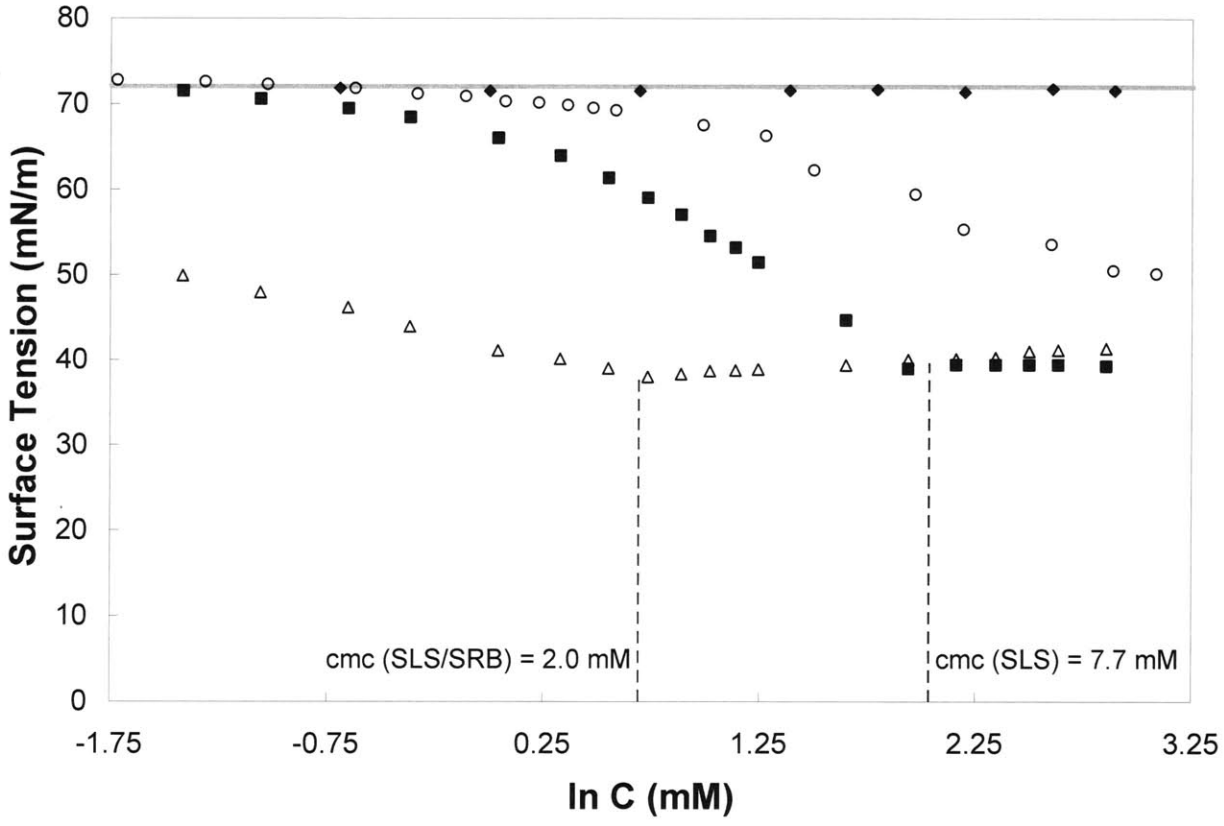

Figure 3-2. Surface tension versus concentration data for aqueous solutions of allura red (◆), SRB (○), SLS(■), and SLS with 9 mM SRB (△). The vertical dashed lines denote the cmc's of the specified solutions. The horizontal gray line represents the measured surface tension of pure water.

hydration of different atomic groups in the SRB molecule when adsorbed at the air/water interface, relative to the fully-hydrated state in bulk aqueous solution (note that the atomic groups in Figure 3-3A correspond to the SRB structure shown in Figure 3-1). In addition, note that in the simulations, the pendant group and the three-ringed xanthene structure actually lie out of plane from each other, contrary to the two-dimensional representation used in the figures for clarity. As expected, the simulation revealed that the pendant group of SRB, which contains the two charged sulfonate atomic groups, resides within the bulk aqueous phase. Conversely, a clear division is observed in the xanthene structure, with the carbon groups located closest to the pendant group remaining significantly hydrated (as reflected in the relative hydration of these groups being greater than 0.6), with the rest of the SRB molecule in various states of dehydration (relative hydrations less than 0.6), indicating that these groups are located, on average, in the air phase. It has been previously shown, in similar investigations regarding the relative hydration of amphiphilic molecules in micelles, that relative hydration values greater than 0.6 correspond to the hydrophilic domain of the surfactant molecule (the "head"), while hydration values below 0.6 correspond to the hydrophobic region of the surfactant molecule (the "tail").[71] Therefore, extending this criterion to a molecule adsorbed at an interface, a clear division between head and tail regions of SRB can be made by laterally bisecting the xanthene structure, with the section of SRB containing the pendant group comprising the head of the surfactant. The combined experimental and simulation data conclusively demonstrates that SRB is indeed an amphiphile and preferentially adsorbs at the air/water interface.

Note that no cmc is observed for SRB in aqueous solution (the open circles in Figure 3-2), because a solubility limit is reached before reaching a plateau in the surface tension versus

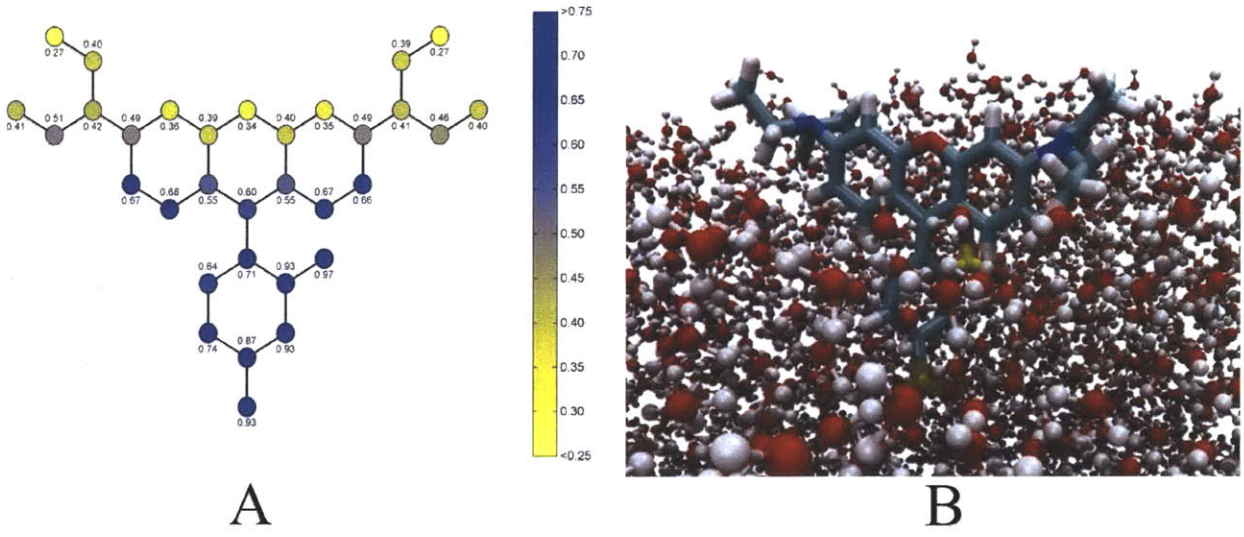

Figure 3-3. A: Relative hydration of an SRB molecule adsorbed at the air/water interface. The blue color corresponds to a group with hydration similar to that in bulk aqueous solution, while the transition to yellow corresponds to groups in less hydrated states. The number adjacent to each atomic group denotes the relative hydration. B: Equilibrium MD simulation snapshot showing an SRB molecule adsorbed at the air/water interface. Color legend: yellow – sulfur, red – oxygen, white – hydrogen, blue/green – carbon, and dark blue – nitrogen.

concentration curve. This should be contrasted with the behavior of SLS in aqueous solution, which exhibits a clear plateau in surface tension at its cmc (7.67 mM, see the open squares in Figure 3-2). MD simulations were carried out at various SRB concentrations in bulk aqueous solution to elucidate this finding. The simulations revealed primarily dimer formation at all SRB concentrations tested, with very few trimers, and no higher-order SRB aggregates observed, thus confirming the inability of SRB to form conventional micelles by itself. The ability of SRB to form dimers in aqueous solution has previously been shown experimentally.[20] At the higher SRB concentrations simulated, most of the SRB molecules formed dimers, with few SRB monomers observed. The dimers (see Figure 3-4A) were found to lie approximately parallel to each other in the plane of the xanthene rings, where the most likely angle between the plane of the pendant groups of each SRB molecule was found to be 75° (for a definition of α, see Figure 3-4A). The angular distribution function of the angle between the pendant groups, α, of the two SRB molecules forming the dimer is shown in Figure 3-4B.

In MD simulations carried out at higher SRB surface concentrations, dimers were observed to form at the air/water interface, as shown in Figure 3-5B, along with adsorbed SRB monomers. SRB molecules were found to interchange between monomeric and dimeric states in the time scales of the simulation, although some stable adsorbed dimers were observed to exist for large durations of the simulation (> 4 ns). The relative hydration of SRB in a stable adsorbed dimer (see Figure 3-5A) was distinctly different than that in the adsorbed monomer state (see Figure 3-3A). Specifically, it was observed that one of the SRB molecules in the adsorbed dimer was oriented approximately parallel to the air/water interface (see Figure 3-5B), as in the case of an adsorbed monomer, while the other molecule was offset by approximately 75°, as expected from

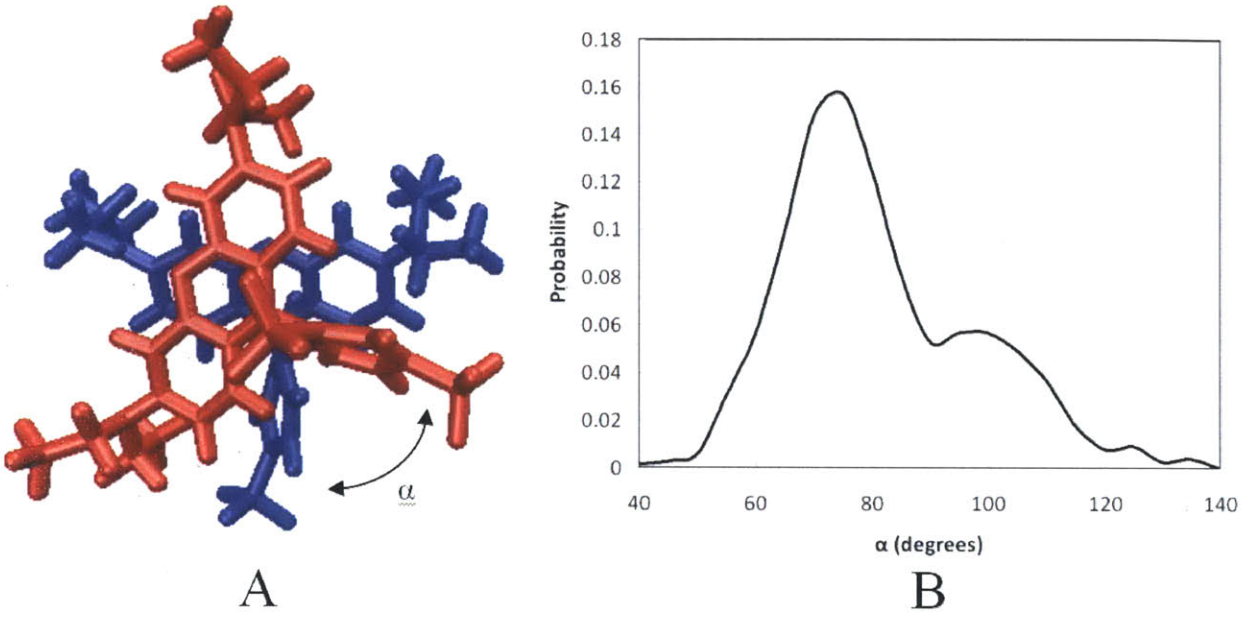

Figure 3-4. A: MD simulation snapshot of the orientation of an SRB dimer in bulk aqueous solution, where α is the angle between the planes of the pendant groups of each SRB molecule in the dimer (each SRB molecule is shown in a different color for clarity). B: Angular distribution function of α.

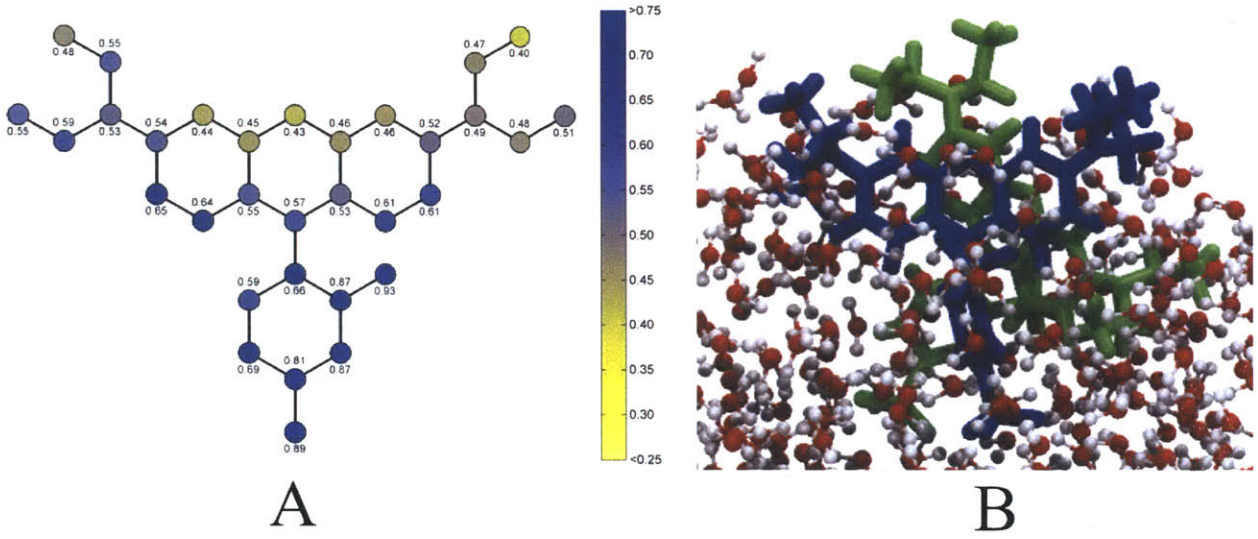

Figure 3-5. A: Relative hydration of an SRB molecule adsorbed at the air/water interface in the dimer state. The blue color corresponds to groups with hydration similar to that in bulk aqueous solution, while the transition to yellow color corresponds to groups in less hydrated states. The number adjacent to each atomic group denotes the relative hydration. B: Equilibrium MD simulation snapshot of SRB adsorbed at the air/water interface in the dimer state. The two SRB molecules of the adsorbed dimer are shown in different colors for clarity.

the angular distribution function in Figure 3-4B. However, due to the fact that the offset SRB molecule in the dimer extends upward into the air phase, the SRB molecule parallel to the surface of the air/water interface was forced slightly deeper into the water phase than in the case of an adsorbed SRB monomer. When averaged over both SRB molecules in the dimer (each SRB molecule may alternatively be found parallel to the air/water interface during the simulation, as the dimer rotates), greater hydration of the SRB molecule was observed in the adsorbed dimer state than in the adsorbed monomer state, which is clearly seen by comparing Figure 3-5A and Figure 3-3A. In spite of the difference in hydration states, the same qualitative relative hydration profile trends are seen between adsorbed SRB monomers and dimers, with much greater hydration of the sulfonate-containing pendant group and decreased hydration in groups further away from the pendant group. However, because the adsorbed SRB monomer can extend further into the air phase, compared to the average configuration of an SRB molecule adsorbed at the interface as a dimer, there is greater dehydration of the groups furthest from the pendant group for the monomer case relative to the dimer case.

3.3.2 Interaction of SRB with SLS in Aqueous Solution

The absorption and emission of fluorescent dyes can be strongly affected by their interactions with surfactants. Figure 3-6A clearly shows how the visible color and opacity of a 9 mM SRB aqueous solution changes when the concentration of SLS is varied between 0 – 64 mM. Furthermore, the addition of SRB to aqueous solutions containing SLS was found to decrease the cmc of SLS from a value of 7.67 mM (without SRB), to a value of 2.00 mM (with 9 mM SRB, see Figure 3-2). As a point of comparison, the cmc of SLS in allura red (which has been shown to be non-amphiphilic, see black diamonds in Figure 3-2), was tested and found to remain

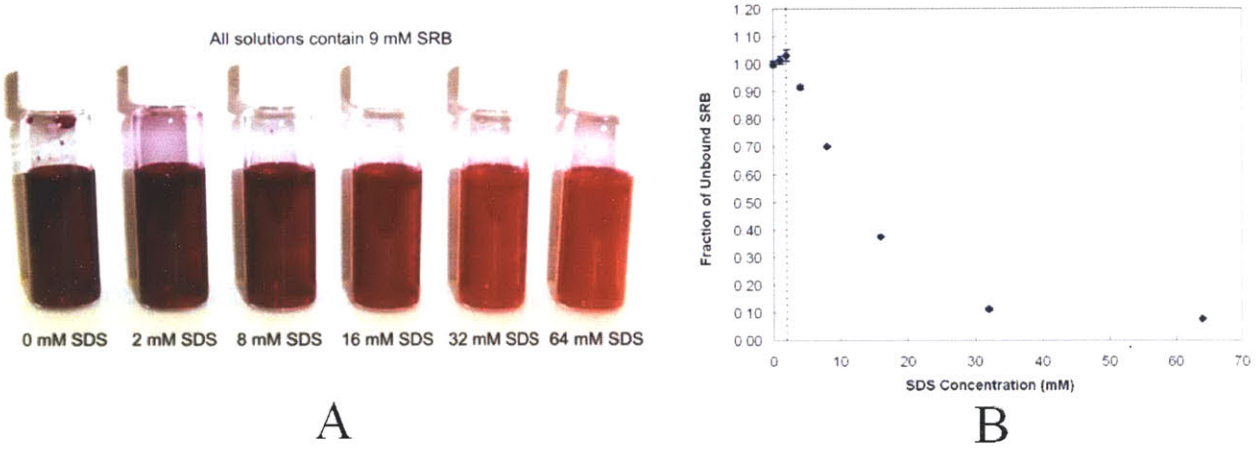

Figure 3-6. A: Color change in 9 mM aqueous solutions of SRB with increasing SLS concentration. B: Fraction of SRB molecules that are not incorporated into SLS micelles, relative to the total concentration of SRB in solution, as a function of SLS concentration. The vertical dashed line corresponds to the cmc of SLS in a 9 mM SRB solution (2.0 mM), and the error bars correspond to a 95% confidence interval on the data.

equal to the cmc of SLS (cmc = 7.62 mM) at low allura red concentrations (0.5 mM). Note that at higher concentrations of allura red, or any salt, there will be a decrease in the cmc due to electrostatic screening and counter-ion binding effects. At 9 mM allura red, the cmc of SLS was found to be 4.50 mM, which is still higher than that found for SLS in 9 mM SRB, despite allura red being a 1:2 electrolyte (2 additional sodium ions per mole of allura red) and SRB being a 1:1 electrolyte (1 additional sodium ion per mole of SRB). Clearly, this shows that the inclusion of the amphiphilic SRB increases the thermodynamic driving force for micellization compared to the non-amphiphilic allura red, as ionic effects alone cannot explain the observed decrease in the cmc. In addition, Figure 3-6B shows that SRB is incorporated within SLS micelles, as reflected by a decrease in the fraction of unbound SRB monomers with increasing SLS concentration (the total SRB concentration in each solution is constant at 9 mM). At an SLS concentration which is twice the cmc of SLS in the presence of 9 mM SRB (4 mM SLS), approximately 10% of the SRB molecules are incorporated into SLS micelles. Furthermore, at 16 times the cmc of SLS in the presence of 9 mM SRB (32 mM), nearly 90% of the SRB molecules are incorporated into SLS micelles (see the fraction of unbound SRB in Figure 3-6B at the specified SLS concentrations). At intermediate SLS concentrations (between 4-16 mM SLS), the molar ratio between SLS and SRB in the micelles is about 3:1, with the molar ratio increasing as the concentration of SLS increases thereafter (5:1 at 32 mM and 10:1 at 64 mM). Note that the term "incorporated into SLS micelles" is used rather than "co-micellized", because the solubility limit of SRB precludes single-component SRB micelle formation in aqueous solution, in spite of the clear amphiphilicity exhibited by SRB.

In order to gain a molecular-level understanding of the experimental observations made, including the incorporation of SRB molecules into SLS micelles, MD simulations were carried out on systems comprising SLS and SRB. In the initial configuration of these simulations, the SRB and SLS molecules were randomly placed and oriented in the simulation box. Self-assembly was observed to occur as the simulation proceeded. An equilibrium snapshot of the final configuration of one of the micelles that formed is shown in Figure 3-7B. The molar ratio of SLS to SRB in the simulated micelles is approximately 6:1, which is in general agreement with the experimental data at high concentrations of SLS, reported in the previous paragraph. The SRB molecules were found to be incorporated in the palisade layer (head region) of the SRB/SLS micelles. An examination of the average relative hydration of SRB molecules incorporated in SLS micelles (see Figure 3-7A), reveals that the majority of the atomic groups of the SRB molecule are incorporated in the micelle, with only the sulfonate groups, and adjacent atomic groups, remaining hydrated to a significant extent (relative hydrations of 0.74 – 0.95). This is in contrast with the adsorption of SRB at the air/water interface (see Figure 3-3A), where the entire pendant group and a portion of the xanthene structure exhibit high levels of hydration (0.60 – 0.97). Comparing the hydration levels of SLS and SRB in the micelle state (Figure 3-7A, where the atomic groups correspond to the structure shown in Figure 3-1), it is clear that the sulfonate groups of SRB (relative hydration equal to 0.80 – 0.95) and the sulfate group of SLS (relative hydration equal to 0.80) are located within approximately the same radial shell of the micelle (forming the outer shell of the micelle). Meanwhile, the remainder of the SRB molecule extends into the micelle core (relative hydrations equal to 0.36 – 0.57), in the same radial shell where carbons 1 – 3 of the SLS molecules reside (relative hydrations equal to 0.33 – 0.55, see

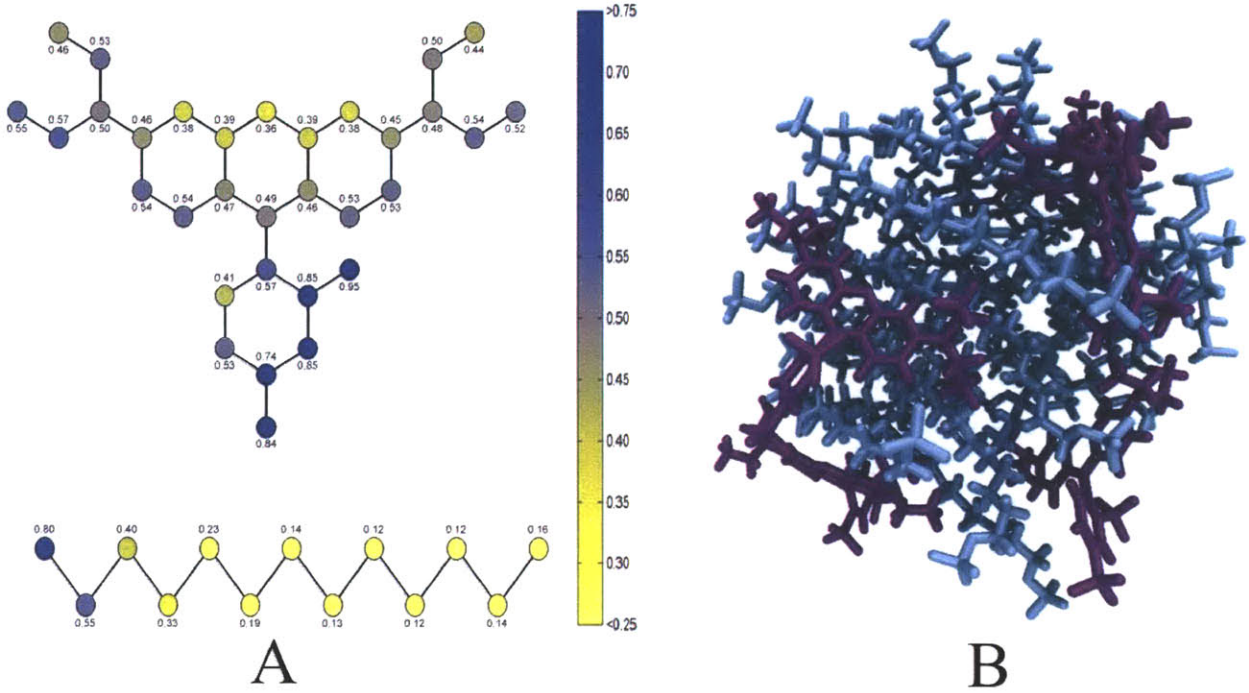

Figure 3-7. A: Relative hydration of an SRB molecule solubilized in an SLS micelle. The blue color corresponds to groups with hydration similar to that in bulk aqueous solution, while the transition to yellow color corresponds to groups in less hydrated states. The number adjacent to each atomic group denotes the relative hydration. B: Equilibrium MD simulation snapshot of SRB incorporated into an SLS micelle. Blue corresponds to SLS molecules, while purple corresponds to SRB molecules.

Figure 3-1 for the carbon labeling of SLS). In the simulations, the xanthene structure of the SRB molecule was not found to extend deeply into the micelle core. This is due to: (i) packing considerations, which include the large, rigid planar configuration of the xanthene structure relative to the more flexible configuration of the SLS tail, and (ii) electrostatic considerations, which involves the net +1 charge partially distributed across the xanthene structure. Moreover, no SRB dimers were observed in the simulations when SLS micelles were present. SRB absorbance is known to red-shift in the monomeric state, compared to the dimer state (spectral data for SRB in the monomer and dimer states can be found in Chambers *et al.*).[20] Therefore, this finding can explain the observed color shift in the aqueous SRB solutions with increasing SLS concentration (see Figure 3-6A).

3.3.3 Case Study: Implications of the Amphiphilic Nature of SRB on Ultrasound-Mediated Transdermal Drug Delivery

Many chemical skin penetration enhancers, particularly amphiphiles, are known to induce synergistic enhancement in skin permeability when combined with low-frequency ultrasound.[40, 41] Since SRB exhibits amphiphilic character, as demonstrated above, and has been used extensively in transdermal research under the assumption that it behaves as an inert fluorescent probe,[6, 8, 12,14, 16-19, 41, 49, 72-76] the possibility that SRB could act alone as a skin penetration enhancer was investigated. An SRB concentration of 9 mM was utilized, which is a commonly used concentration of SRB in transdermal research.[8, 41, 49, 73-75] To quantify skin permeability enhancement, an enhancement ratio (ER) was calculated, where ER is defined as the ratio of the post-treatment skin resistivity at steady state (18 hours post-ultrasound treatment), and the initial skin resistivity of that sample (prior to ultrasound treatment). Skin

Table 3-1. Steady-state enhancement ratio of skin samples treated with the specified coupling medium and low-frequency ultrasound (20 kHz, 7.5 W/cm^2, 10 minutes).

Coupling Medium[b]	n	Enhancement Ratio[a]
Water	10	1.71 ± 0.67
9 mM Allura Red	10	1.87 ± 0.62
9 mM SRB	11	54.0 ± 19.6
9 mM SLS	11	79.6 ± 27.1

[a] Error bars correspond to a 95% confidence interval on the data.

[b] All solutions are aqueous, containing only the specified components.

resistivity is known to scale directly with skin permeability.[48, 77] The results of these experiments are summarized in Table 3-1.

Table 3-1 shows that skin samples treated with water/ultrasound (control) had a statistically similar enhancement ratio (ER=1.71±0.67) as those treated with an aqueous solution of 9 mM allura red/ultrasound (ER=1.87±0.62, two-sample t-test at 95% confidence). However, the ER corresponding to skin samples treated with an aqueous solution of 9 mM SRB/ultrasound was found to be 30-fold greater than the controls (54.0±19.6), which is a statistically significant difference (p-value = 0.004, p-value must be below 0.05 for there to be a statistically significant difference at 95% confidence). This clearly shows the ability of SRB to act as a skin permeability enhancer when combined with low-frequency ultrasound, thus further demonstrating its amphiphilic nature. For comparison, the ER for 9 mM SLS (a known surfactant and skin penetration enhancer) is also shown in Table 3-1 (79.6±27.1). Interestingly, the ERs of SRB and SLS are not statistically significantly different, owing to the generally large variance associated with each sample (p-value = 0.15), but also confirming that SRB is a statistically significant skin penetration enhancer.

Note, however, that SRB alone (in the absence of LFS) does not act as a skin permeability enhancer. Specifically, in Figure 3-8 (gray bars) shows that both allura red and SRB at high (9 mM) and low (0.45 mM) concentrations have no significant impact on the enhancement ratio of skin after 18 hours of passive contact. The inability of SRB to act as a passive skin permeability enhancer is likely due to its high molecular weight (559 g/mol), and therefore, is limited in perturbing the skin appreciably due to its failure to penetrate the skin in significant amounts.

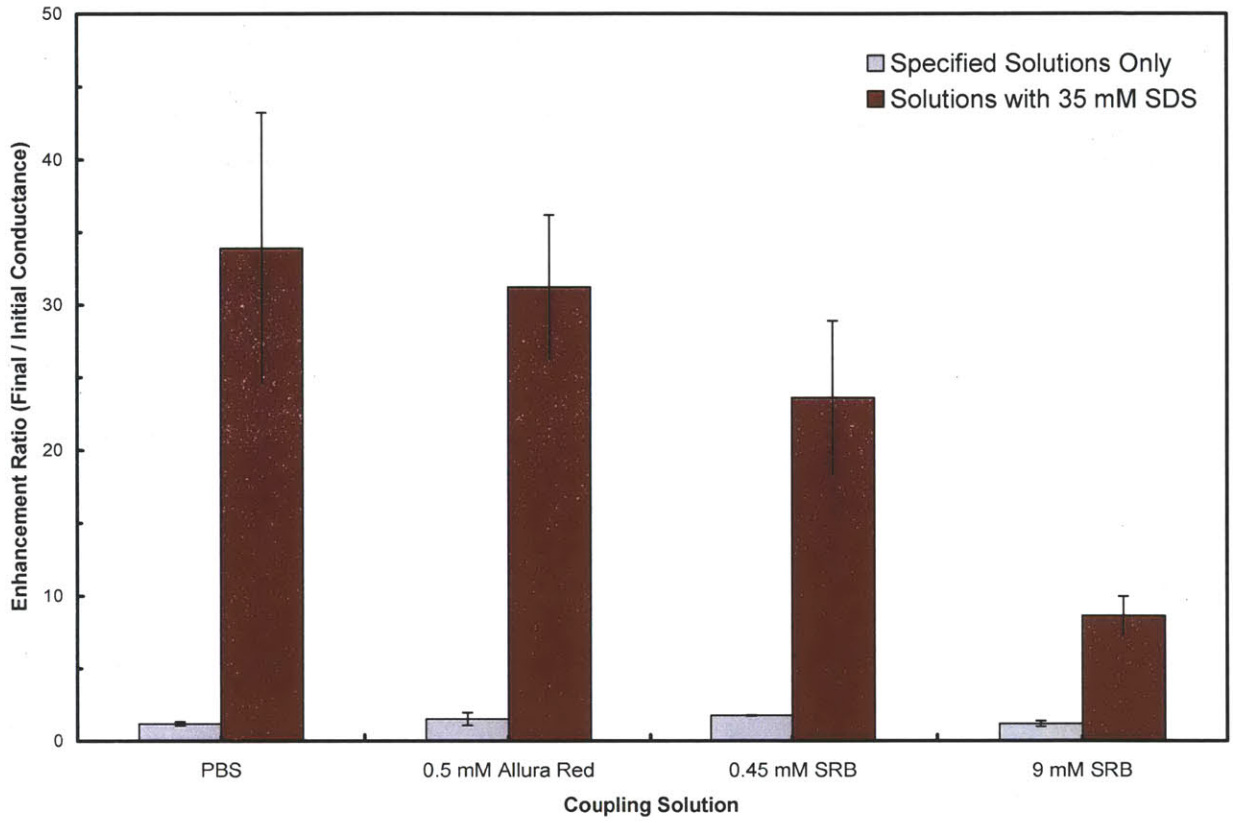

Figure 3-8. Enhancement ratios of skin samples treated passively for 18 hours with various coupling solutions. Gray bars correspond to solutions containing only those specified, while red bars contain specified solutions and 35 mM sodium lauryl sulfate.

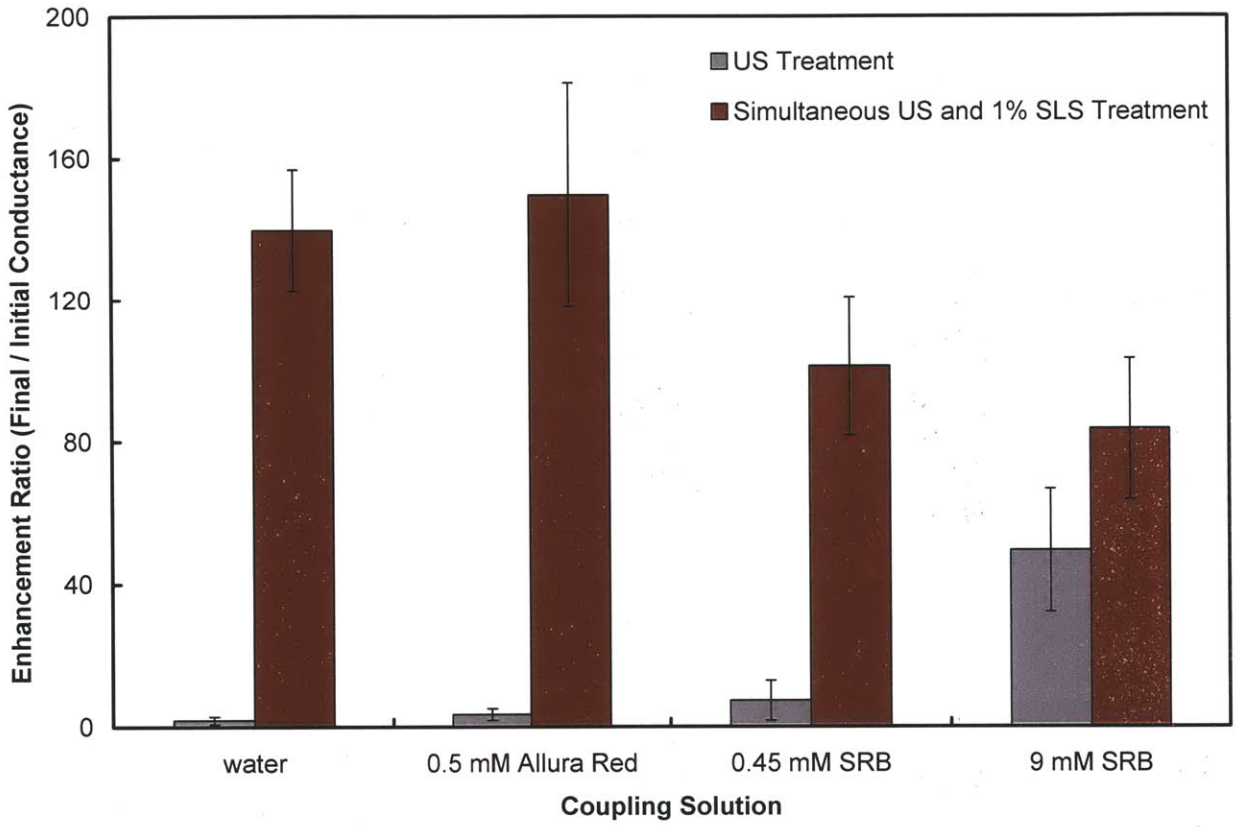

Figure 3-9. Steady-state (18 hour) enhancement ratios of skin samples treated with LFS for 10 minutes with various coupling solutions. Gray bars correspond to solutions containing only those specified, while red bars contain specified solutions and 35 mM sodium lauryl sulfate.

However, when 35 mM SLS is added to the solutions, it is observed that, while the non-amphiphilic allura red has no affect on the enhancement ratio of SLS, the addition of SRB to the solution has an antagonistic effect (Figure 3-8, red bars). This finding is not surprising considering that it was shown that SRB is also amphiphilic and has the ability to incorporate into SLS micelles. Therefore, as Figure 3-8 shows, the antagonistic effect increases with increasing SRB concentration, where the observed decrease in enhancement ratio is likely due to an increase in the size of the micelles as more SRB is incorporated into them. Therefore, the larger SLS/SRB micelles encounter greater steric hindrance when trying to enter the aqueous skin pores. As a result, their diffusion into the skin is decreased, causing less perturbation to the skin. A similar antagonistic effect is seen when SRB is added to SLS coupling solutions for simultaneous treatment with LFS (see Figure 3-9). In this case, again, the presence of the non-amphiphilic allura red has no impact on the steady-state enhancement ratio of SLS. On the other hand, the addition of SRB to the SLS coupling solution has a clearly negative impact on the enhancement ratio observed. Therefore, it is evident that the use of SRB with other surfactants for LFS treatments can have pronounced, unintended effects on bulk and interfacial properties of the solution that manifest as changes in the level of skin perturbation induced.

3.4 Conclusions

We have demonstrated that SRB is an amphiphilic molecule that preferentially adsorbs at an air/water interface, bringing about a considerable decrease in the surface tension of pure water (23 mN/m reduction). MD simulations revealed that SRB is thermodynamically stable in its adsorbed state, both as monomers and dimers, with clearly defined head and tail regions as quantified by the hydration of its atomic groups, similar to conventional surfactants.

Furthermore, SRB was shown to be able to incorporate into SLS micelles, which results in a dramatic decrease in the cmc of SLS. Because of its incorporation into SLS micelles, SRB was observed to have a significant shift in color and opacity in aqueous solution with increasing SLS concentration. MD simulations revealed that the SRB molecules reside mainly in the palisade layer of the SLS micelles. A case study on skin permeability enhancement by ultrasound and SRB showed that SRB acts as a synergistic skin penetration enhancer, much like many traditional surfactants.

The study presented here shows that even highly water soluble fluorescent dyes can behave as amphiphiles. In many previous studies, SRB has been assumed to be an inert dye and, therefore, was utilized as a simple colorimetric dye or model hydrophilic permeant. However, the present study shows that one must pay careful attention when selecting an appropriate dye, or fluorescent probe, in a given system. SRB can interact strongly with other surfactants, inducing significant changes in bulk and interfacial properties of aqueous solutions. It is therefore recommended that if a fluorescent probe is not needed, it is best to choose the simplest possible dye, such as allura red (red food coloring). If, however, a fluorescent dye is required, special care should be taken to ensure that the dye does not interact with other components of the system. The present study also demonstrates that molecular dynamics simulations can be utilized effectively to study the organization and hydration of dyes in bulk solution, at interfaces, and in micellar environments. These types of studies have previously been carried out using more tedious, experimentally-intensive spectroscopic methods. However, using the approach presented here, it may be possible to more easily investigate multiple fluorescent dyes in order to aid in the selection of an appropriate dye for a given system.

The synergism observed between LFS and amphiphiles, such as SRB and SLS, which was demonstrated in the study presented in this chapter, will be investigated further in Chapter 4. Prior to the work conducted in Chapter 4, the mechanism that leads to the synergism between LFS and chemical enhancers, such as SRB and SLS, was previously not well understood from a quantitative perspective. In the next chapter, insight gained from the preceding chapters, especially regarding the physical mechanistic picture proposed in Chapter 2, will be utilized to solve for flux equations that will provide insight into the direct mechanism of increased skin penetration of chemical enhancers when treated simultaneously with LFS.

3.5 References

[1] H. Behrens, U. Beims, H. Dieter, G. Dietze, T. Eikmann, T. Grummt, H. Hanisch, H. Henseling, W. Käß, H. Kerndorff, Toxicological and ecotoxicological assessment of water tracers. Hydrogeol J 9(3) (2001) 321-325.

[2] T. Kasnavia, D. De Vu, Fluorescent dye and media properties affecting sorption and tracer selection. Ground Water 37(3) (1999) 376-381.

[3] N. Takahashi, T. Kishimoto, T. Nemoto, T. Kadowaki, H. Kasai, Fusion pore dynamics and insulin granule exocytosis in the pancreatic islet. Science 297(5585) (2002) 1349.

[4] V. Vichai, K. Kirtikara, Sulforhodamine B colorimetric assay for cytotoxicity screening. Nat Protoc 1(3) (2006) 1112-1116.

[5] P. Skehan, R. Storeng, D. Scudiero, A. Monks, J. McMahon, D. Vistica, J. Warren, H. Bokesch, S. Kenney, M. Boyd, New colorimetric cytotoxicity assay for anticancer-drug screening. J Natl Cancer I 82(13) (1990) 1107.

[6] S. Ghosh, D. Kim, P. So, D. Blankschtein, Visualization and quantification of skin barrier perturbation induced by surfactant–humectant systems using two-photon fluorescence microscopy. Int J Cosmetic Sci 31(4) (2009) 323-324.

[7] J. Jiang, D. Geroski, H. Edelhauser, M. Prausnitz, Measurement and prediction of lateral diffusion within human sclera. Invest Ophth Vis Sci 47(7) (2006) 3011.

[8] J. Kushner, D. Kim, P. So, D. Blankschtein, R. Langer, Dual-channel two-photon microscopy study of transdermal transport in skin treated with low-frequency ultrasound and a chemical enhancer. J Invest Dermatol 127(12) (2007) 2832-2846.

[9] J. Lee, S. Jee, C. Chan, W. Lo, C. Dong, S. Lin, The effects of depilatory agents as penetration enhancers on human stratum corneum structures. J Invest Dermatol 128(9) (2008) 2240-2247.

[10] Y. Lin, H. Skaff, T. Emrick, A. Dinsmore, T. Russell, Nanoparticle assembly and transport at liquid-liquid interfaces. Science 299(5604) (2003) 226.

[11] R. Saito, M. Krauze, C. Noble, M. Tamas, D. Drummond, D. Kirpotin, M. Berger, J. Park, K. Bankiewicz, Tissue affinity of the infusate affects the distribution volume during convection-enhanced delivery into rodent brains: Implications for local drug delivery. J Neurosci Meth 154(1-2) (2006) 225-232.

[12] C. Simonsson, M. Smedh, C. Jonson, A.-T. Karlberg, M.B. Ericson, Two photon microscopy for studies of xenobiotics in human skin. Biophotonics 2007: Optics in Life Science, Vol. 6633, SPIE, Munich, Germany, 2007, pp. 663320-663329.

[13] N. Takahashi, T. Nemoto, R. Kimura, A. Tachikawa, A. Miwa, H. Okado, Y. Miyashita, M. Iino, T. Kadowaki, H. Kasai, Two-photon excitation imaging of pancreatic islets with various fluorescent probes. Diabetes 51(suppl 1) (2002) S25.

[14] B. Yu, C. Dong, P. So, D. Blankschtein, R. Langer, In vitro visualization and quantification of oleic acid induced changes in transdermal transport using two-photon fluorescence microscopy. J Invest Dermatol 117(1) (2001) 16-25.

[15] B. Yu, C. Dong, P. So, D. Blankschtein, R. Langer, Application of two-photon microscopy to elucidate oleic-acid-induced changes in microscale transdermal transport processes. Proc. SPIE, Vol. 4262, 2001, p. 217.

[16] B. Yu, K. Kim, P. So, D. Blankschtein, R. Langer, Topographic heterogeneity in transdermal transport revealed by high-speed two-photon microscopy: Determination of representative skin sample sizes. J Invest Dermatol 118(6) (2002) 1085-1088.

[17] B. Yu, K. Kim, P. So, D. Blankschtein, R. Langer, Visualization of oleic acid-induced transdermal diffusion pathways using two-photon fluorescence microscopy. J Invest Dermatol 120(3) (2003) 448-455.

[18] C.Y. Dong, B. Yu, P.D. Kaplan, P.T. So, Performances of high numerical aperture water and oil immersion objective in deep-tissue, multi-photon microscopic imaging of excised human skin. MICROSC RES TECHNIQ

Microsc Res Techniq 63(1) (2004) 81-86.

[19] S. Lin, J. Lee, C. Lin, C. Chan, M. Lin, C. Wang, T. Tsai, S. Jee, C. Dong, Investigation of the mechanism of transdermal penetration enhancer-a comparison of multiphoton microscopy and electron microscopy. Proc. of SPIE, Vol. 6842, 2008, pp. 684203-684201.

[20] R. Chambers, T. Kajiwara, D. Kearns, Effect of dimer formation on the electronic absorption and emission spectra of ionic dyes. Rhodamines and other common dyes. J Phys Chem-US 78(4) (1974) 380-387.

[21] N. Maiti, M. Krishna, P. Britto, N. Periasamy, Fluorescence dynamics of dye probes in micelles. J Phys Chem B 101(51) (1997) 11051-11060.

[22] H. Tajalli, A. Ghanadzadeh Gilani, M. Zakerhamidi, M. Moghadam, Effects of surfactants on the molecular aggregation of rhodamine dyes in aqueous solutions. Spectrochim ACTA A 72(4) (2009) 697-702.

[23] T. Uchida, A. Yamaguchi, T. Ina, N. Teramae, Observation of molecular association at liquid/liquid and solid/liquid interfaces by second harmonic generation spectroscopy. J Phys Chem B 104(51) (2000) 12091-12094.

[24] T. Osakai, H. Yamada, H. Nagatani, T. Sagara, Potential-Dependent Adsorption of Amphoteric Rhodamine Dyes at the Oil/Water Interface as Studied by Potential-Modulated Fluorescence Spectroscopy. J Phys Chem C 111(26) (2007) 9480-9487.

[25] R. Greef, J. Frey, J. Robinson, L. Danos, Adsorption of rhodamine 6G at the water-air interface. Phys Status Solidi 5(5) (2008) 1187-1189.

[26] V. Kelkar, B. Valaulikar, J. Kunjappu, C. Manohar, Aggregation characteristics of laser dye Rhodamine 6G in aqueous surfactant solutions. Photochem Photobiol 52(4) (1990) 717-721.

[27] W. Malik, P. Chand, Absorption studies on the binding of dyes with ionic surfactants. J Electroanal Chem 40(2) (1972) 385-392.

[28] P. Bilksi, C. Chignell, Properties of differently charged micelles containing rose bengal: application in photosensitization studies. J Photoch Photobio A 77(1) (1994) 49-58.

[29] P. Bilski, R. Holt, C. Chignell, Premicellar aggregates of Rose Bengal with cationic and zwitterionic surfactants. J Photoch Photobio A 110(1) (1997) 67-74.

[30] Z. El-Hachemi, G. Mancini, J. Ribo , A. Sorrenti, Role of the Hydrophobic Effect in the Transfer of Chirality from Molecules to Complex Systems: From Chiral Surfactants to Porphyrin/Surfactant Aggregates. J Am Chem Soc 130(45) (2008) 15176-15184.

[31] N. Maiti, S. Mazumdar, N. Periasamy, J-and H-Aggregates of Porphyrin- Surfactant Complexes: Time-Resolved Fluorescence and Other Spectroscopic Studies†. J Phys Chem B 102(9) (1998) 1528-1538.

[32] M. Garcia, A. Sanz-Medel, Dye-surfactant interactions: a review. Talanta 33(3) (1986) 255-264.

[33] F. Gadelle, W.J. Koros, R.S. Schechter, Solubilization Isotherms of Aromatic Solutes in Surfactant Aggregates. J Colloid Interf Sci 170(1) (1995) 57-64.

[34] H. Hachisako, R. Murakami, Intense fluorescence-inducing amphiphile in cationic dyes and its applicability. Chem Commun 2006(10) (2006) 1073-1075.

[35] H. Hachisako, N. Ryu, R. Murakami, Molecular structural requirements, dye specificity, and application of anionic peptide amphiphiles that induce intense fluorescence in cationic dyes. Org Biomol Chem 7(11) (2009) 2327-2337.

[36] D. Yu, Q. Zhang, C. Wu, Y. Wang, L. Peng, D. Zhang, Z. Li, Y. Wang, Highly Fluorescent Aggregates Modulated by Surfactant Structure and Concentration. J Phys Chem B 114 (2010) 8934-8940.

[37] M. Ferrer, F. del Monte, Study of the Adsorption Process of Sulforhodamine B on the Internal Surface of Porous Sol- Gel Silica Glasses through Fluorescence Means. Langmuir 19(3) (2003) 650-653.

[38] K. Ray, R. Badugu, J. Lakowicz, Sulforhodamine Adsorbed Langmuir- Blodgett Layers on Silver Island Films: Effect of Probe Distance on the Metal-Enhanced Fluorescence. J Phys Chem C 111(19) (2007) 7091-7097.

[39] K. Ray, H. Nakahara, Adsorption of Sulforhodamine Dyes in Cationic Langmuir-Blodgett Films: Spectroscopic and Structural Studies. J Phys Chem B 106(1) (2002) 92-100.

[40] S. Mitragotri, D. Ray, J. Farrell, H. Tang, B. Yu, J. Kost, D. Blankschtein, R. Langer, Synergistic effect of low-frequency ultrasound and sodium lauryl sulfate on transdermal transport. J Pharm Sci 89(7) (2000) 892-900.

[41] A. Tezel, A. Sens, J. Tuchscherer, S. Mitragotri, Synergistic effect of low-frequency ultrasound and surfactants on skin permeability. J Pharm Sci 91(1) (2002) 91-100.

[42] C.D. Bruce, M.L. Berkowitz, L. Perera, M.D.E. Forbes, Molecular Dynamics Simulation of Sodium Lauryl Sulfate Micelle in Water:â€‰ Micellar Structural Characteristics and Counterion Distribution. J Phys Chem B 106(15) (2002) 3788-3793.

[43] J.M. Chen, T.M. Su, C.Y. Mou, Size of sodium lauryl sulfate micelle in concentrated salt solutions. J Phys Chem-US 90(11) (1986) 2418-2421.

[44] B. Jönsson, B. Lindman, K. Holmberg, B. Kronberg, Surfactants and polymers in aqueous solution, John Wiley & Sons Chichester, 1998.

[45] M. James-Smith, K. Alford, D. Shah, Effect of long-chain alcohols on SLS partitioning to the oil/water interface of emulsions and on droplet size. J Colloid Interf Sci 315(1) (2007) 307-312.

[46] J. Seto, B. Polat, R. Lopez, D. Blankschtein, R. Langer, Effects of ultrasound and sodium lauryl sulfate on the transdermal delivery of hydrophilic permeants: Comparative in vitro studies

with full-thickness and split-thickness pig and human skin. J Control Release 145(1) (2010) 26-32.

[47] B.E. Polat, J.E. Seto, D. Blankschtein, R. Langer, Application of the aqueous porous pathway model to quantify the effect of sodium lauryl sulfate on ultrasound-induced skin structural perturbation. J Pharm Sci 100(4) (2011) 1387-1397.

[48] B.E. Polat, P.L. Figueroa, D. Blankschtein, R. Langer, Transport pathways and enhancement mechanisms within localized and non-localized transport regions in skin treated with low-frequency sonophoresis and sodium lauryl sulfate. J Pharm Sci 100(2) (2011) 512-529.

[49] J.E. Seto, B.E. Polat, R.F.V. Lopez, D. Blankschtein, R. Langer, Effects of ultrasound and sodium lauryl sulfate on the transdermal delivery of hydrophilic permeants: Comparative in vitro studies with full-thickness and split-thickness pig and human skin. J Control Release 145(1) (2010) 26-32.

[50] P. Karande, A. Jain, S. Mitragotri, Relationships between skin's electrical impedance and permeability in the presence of chemical enhancers. J Control Release 110(2) (2006) 307-313.

[51] J. Kushner IV, D. Blankschtein, R. Langer, Experimental demonstration of the existence of highly permeable localized transport regions in low-frequency sonophoresis. J Pharm Sci 93(11) (2004) 2733-2745.

[52] B.C. Stephenson, K. Beers, D. Blankschtein, Complementary Use of Simulations and Molecular-Thermodynamic Theory to Model Micellization. Langmuir 22(4) (2006) 1500-1513.

[53] M. Sammalkorpi, M. Karttunen, M. Haataja, Structural properties of ionic detergent aggregates: a large-scale molecular dynamics study of sodium lauryl sulfate. J Phys Chem B 111(40) (2007) 11722-11733.

[54] H.J.C. Berendsen, J.R. Grigera, T.P. Straatsma, The missing term in effective pair potentials. J Phys Chem-US 91(24) (1987) 6269-6271.

[55] S. Miyamoto, P.A. Kollman, Settle: An analytical version of the SHAKE and RATTLE algorithm for rigid water models. J Comput Chem 13(8) (1992) 952-962.

[56] W.L. Jorgensen, D.S. Maxwell, J. Tirado-Rives, Development and Testing of the OPLS All-Atom Force Field on Conformational Energetics and Properties of Organic Liquids. J Am Chem Soc 118(45) (1996) 11225-11236.

[57] B. Stephenson, K. Beers, D. Blankschtein, Quantifying the Hydrophobic Effect. 3. A Computer Simulation- Molecular-Thermodynamic Model for the Micellization of Ionic and Zwitterionic Surfactants in Aqueous Solution. J Phys Chem B 111(5) (2007) 1063-1075.

[58] S. Dare-Doyen, D. Doizi, P. Guilbaud, F. Djedaini-Pilard, B. Perly, P. Millie, Dimerization of Xanthene Dyes in Water: Experimental Studies and Molecular Dynamic Simulations. J Phys Chem B 107(50) (2003) 13803-13812.

[59] B. Hess, P-lincs: A parallel linear constraint solver for molecular simulation. J Chem Theory Comput 4(1) (2008) 116-122.

[60] B. Hess, H. Bekker, H.J.C. Berendsen, J.G.E.M. Fraaije, LINCS: A linear constraint solver for molecular simulations. J Comput Chem 18(12) (1997) 1463-1472.

[61] N. Tummala, A. Striolo, SLS Surfactants on Carbon Nanotubes: Aggregate Morphology. ACS Nano 3(3) (2009) 595-602.

[62] Z. Xu, X. Yang, Z. Yang, A Molecular Simulation Probing of Structure and Interaction for Supramolecular Sodium Lauryl Sulfate/Single-Wall Carbon Nanotube Assemblies. Nano Lett 10(3) (2010) 985-991.

[63] T. Darden, D. York, L. Pedersen, Particle mesh Ewald: An N log (N) method for Ewald sums in large systems. J Chem Phys 98 (1993) 10089.

[64] U. Essmann, L. Perera, M. Berkowitz, T. Darden, H. Lee, L. Pedersen, A smooth particle mesh Ewald method. J Chem Phys 103(19) (1995) 8577-8593.

[65] R.W. Hockney, S.P. Goel, J.W. Eastwood, Quiet high-resolution computer models of a plasma. J Comput Phys 14(2) (1974) 148-158.

[66] L. Verlet, Computer. Phys Rev 159 (1967) 98-103.

[67] G. Bussi, D. Donadio, M. Parrinello, Canonical sampling through velocity rescaling. J Chem Phys 126 (2007) 014101.

[68] H. Berendsen, J. Postma, W. Van Gunsteren, A. DiNola, J. Haak, Molecular dynamics with coupling to an external bath. J Chem Phys 81 (1984) 3684.

[69] A. Leach, Molecular modelling: principles and applications, Addison-Wesley Longman Ltd, 2001.

[70] B. Hess, C. Kutzner, D. van der Spoel, E. Lindahl, GROMACS 4: Algorithms for Highly Efficient, Load-Balanced, and Scalable Molecular Simulation. J Chem Theory Comput 4(3) (2008) 435-447.

[71] P. Hiemenz, R. Rajagopalan, Principles of Colloid and Surface Chemistry, 3rd Edition, Marcel Dekker, Inc., New York, 1997, pp. 327-330.

[72] I. Purcell, J. Lu, R. Thomas, A. Howe, J. Penfold, Adsorption of sodium lauryl sulfate at the surface of aqueous solutions of poly (vinylpyrrolidone) studied by neutron reflection. Langmuir 14(7) (1998) 1637-1645.

[73] B.C. Stephenson, A. Goldsipe, K.J. Beers, D. Blankschtein, Quantifying the Hydrophobic Effect. 2. A Computer Simulationâ''Molecular-Thermodynamic Model for the Micellization of

Nonionic Surfactants in Aqueous Solution. The Journal of Physical Chemistry B 111(5) (2007) 1045-1062.

[74] M. Kirjavainen, A. Urtti, I. Jääskeläinen, T. Marjukka Suhonen, P. Paronen, R. Valjakka-Koskela, J. Kiesvaara, J. Mönkkönen, Interaction of liposomes with human skin in vitro -- The influence of lipid composition and structure. BBA-Lipid Lipid Met 1304(3) (1996) 179-189.

[75] S. Paliwal, G.K. Menon, S. Mitragotri, Low-Frequency Sonophoresis: Ultrastructural Basis for Stratum Corneum Permeability Assessed Using Quantum Dots. J Invest Dermatol 126(5) (2006) 1095-1101.

[76] A. Tezel, A. Sens, S. Mitragotri, A Theoretical Analysis of Low-Frequency Sonophoresis: Dependence of Transdermal Transport Pathways on Frequency and Energy Density. Pharm Res 19(12) (2002) 1841-1846.

[77] A. Tezel, A. Sens, J. Tuchscherer, S. Mitragotri, Frerquency Dependence of Sonophoresis. Pharm Res 18(12) (2001) 1694-1700.

Chapter 4

A Physical Mechanism to Explain the Synergism in Transdermal Enhancement between Low-Frequency Ultrasound and Chemical Penetration Enhancers

4.1 Introduction

In Chapter 3, I demonstrated the extremely large synergistic effect that combining low-frequency sonophoresis treatment with a chemical penetration enhancer (CPE), such as sodium lauryl sulfate (SLS) or sulforhodamine B, can have on the extent of skin perturbation induced. In this chapter, I will study directly the physical mechanisms that lead to this synergistic effect, including how it varies with the nature of the CPE considered. This will allow us to gain a deeper understanding of how ultrasound-induced cavitation bubbles interact with various CPEs.

The use of low-frequency sonophoresis (LFS) for the transdermal delivery of drugs has been shown to be a feasible and emerging method of local, regional, and systemic drug delivery, which allows for the minimization of side effects associated with oral and intravenous delivery.[1, 2] When combined with CPEs, such as SLS, LFS treatment has been shown to result in a synergistic effect in skin permeability enhancement.[3, 4] This synergism has been studied to a large extent experimentally, demonstrating that combined treatment with LFS and CPEs (primarily surfactants) allows for decreased treatment times, decreased energy-input requirements, increased skin permeability, higher-connectivity of lacunar regions in the stratum corneum, and less physical skin perturbation compared to the LFS treatment alone.[3-6] The origin of this synergism is the ability of LFS to not only increase the penetration of CPEs into the skin, but also to deliver CPEs deeply into the skin, including increasing their dispersion in the skin.[3] In the absence of LFS, CPEs are generally limited in their passive diffusion into the skin, owing to the innate barrier properties of the outermost layer of the skin, the stratum corneum. On the other hand, when LFS assists the delivery of CPEs directly into the stratum corneum, these molecules are no longer limited by passive diffusion, thereby allowing them to induce increased chemical perturbation to the skin, in addition to the physical perturbation induced by the LFS treatment.

In spite of establishing that increased penetration and dispersion of CPEs in the skin by LFS is the origin of their synergism, to date, no direct mechanism has been proposed to explain how LFS increases the penetration of CPEs into the skin. Other studies have investigated the synergism between LFS and specific CPEs, such as SLS, more closely, and found that their simultaneous use causes subtle changes in the skin, such as altered pH profiles.[7] However, to

my knowledge, no previous investigations have explained or proposed a model as to why there is a general increase in the penetration of CPEs into the skin when treated simultaneously with LFS, which would explain this commonly observed synergism.

In this study, I propose a physical mechanism that explains why *all* CPEs exhibit synergism with LFS, as well as why surfactants, specifically, exhibit greater synergism with LFS than non-amphiphilic CPEs. In addition to proposing a physical mechanism, a kinetic-transport model is presented to explain the synergism quantitatively, by solving explicitly for the expected CPE flux into LFS-treated skin, with supporting data from experiments conducted with both amphiphilic and non-amphiphilic CPEs.

4.2. Experimental

4.2.1 Materials

SLS, octyl glucoside (OG), and propylene glycol (PG), were obtained from Sigma-Aldrich Company (St. Louis, MO). C_{14}-labeled SLS, OG, and PG were obtained from American Radiolabeled Chemicals (St. Louis, MO). Hionic-Fluor, a scintillation cocktail, and Soluene, a tissue solubilizer, were obtained from Perkin-Elmer (Waltham, MA). Allura red (red food coloring) was obtained from TCI America (Portland, OR). All chemicals were used as received. Milli-Q water (Millipore Corporation, Billerica, MA) was used for the preparation of all aqueous solutions.

4.2.2 Surface Tension Measurements

The surface tensions of aqueous solutions of the two amphiphiles, SLS and OG, were measured as a function of concentration using a Krüss K11 tensiometer (Hamburg, Germany). The Wilhelmy-plate method was utilized with a titanium plate (Krüss, wetting length of 42 mm). For each measurement, twenty surface tension readings were obtained, three seconds apart, and the final ten readings were averaged to yield the surface tension for that measurement (with the first ten measurements serving as an equilibration period). Surface tension measurements of each solution considered were repeated until consistent values were obtained for three consecutive measurements (<0.1 mN/m variation). These three measurements were then averaged to yield the surface tension of the solution. The surface tension measurements were utilized to deduce the critical micelle concentration (cmc) of the surfactants, SLS and OG. This was accomplished by determining the intersection of the linear region below and above the cmc in a plot of surface tension vs. log surfactant concentration.[8]

4.2.3 Preparation and Treatment of Skin Samples by LFS and CPEs

Previously published protocols were utilized for the storage and preparation of skin samples.[9-15] These protocols have been approved by the MIT Committee on Animal Care. Briefly, skin was harvested from the back and flank of Female Yorkshire pigs, sectioned into 25-mm strips, and stored at -85 °C for up to 6 months. Before use in experiments, the skin was thawed for 1 hour in PBS and all excess hair and subcutaneous fat were removed. Full-thickness skin samples were utilized without further preparation. The skin was then cut into 25 mm by 25 mm samples, for use in the 15-mm inner diameter diffusion cells (PermeGear, Hellertown, PA).

Treatment of skin samples was carried out according to previously published methods. [9-15] Skin treatment was carried out with a 20 kHz ultrasound horn (VCX 500, Sonics and Materials, Inc., Newtown, CT), under the following experimental conditions: intensity - 7.5 W/cm^2, duty cycle – 100%, and tip displacement - 3 mm. The coupling solution between the skin and the ultrasound horn contained aqueous solutions of SLS (1- 100 mM), OG (4 – 100 mM), and PG (100 – 700 mM) with 0.5 mM allura red (used for visualization of LTRs only, see Figure 4-1). The concentration of CPEs was selected so that they produced consistently large enough LTRs to allow sampling utilizing the techniques discussed in Section 4.2.4. Note that dilute allura red solutions have previously been shown not to interact strongly with other surfactants, or affect bulk or interfacial properties of aqueous surfactant solutions.[14] The concentration of radio-labeled permeant in the solutions was chosen to be between 0.3 – 0.5 μCi/mL, in order to ensure that the fluxes of the radio-labeled materials into the skin were at a level which is significantly higher than the background values. After every 40 s of LFS treatment, the coupling medium (volume = 1.5 mL) was changed in order to minimize thermal effects (i.e., to maintain the temperature within 10 °C of room temperature), and samples were treated for a total of 10 minutes. Note that for these studies, LFS treatment was applied continuously, rather than in a pulsed manner as was conducted in the other chapters of this thesis, so that there was no additional passive flux associated with application of permeants during the LFS treatment. Untreated skin samples were prepared in the same manner as other samples, but were contacted with the coupling solutions for 10 minutes without ultrasound treatment. Following treatment, samples were rinsed thoroughly in order to remove all excess material from the skin surface prior to sampling of the tissue.

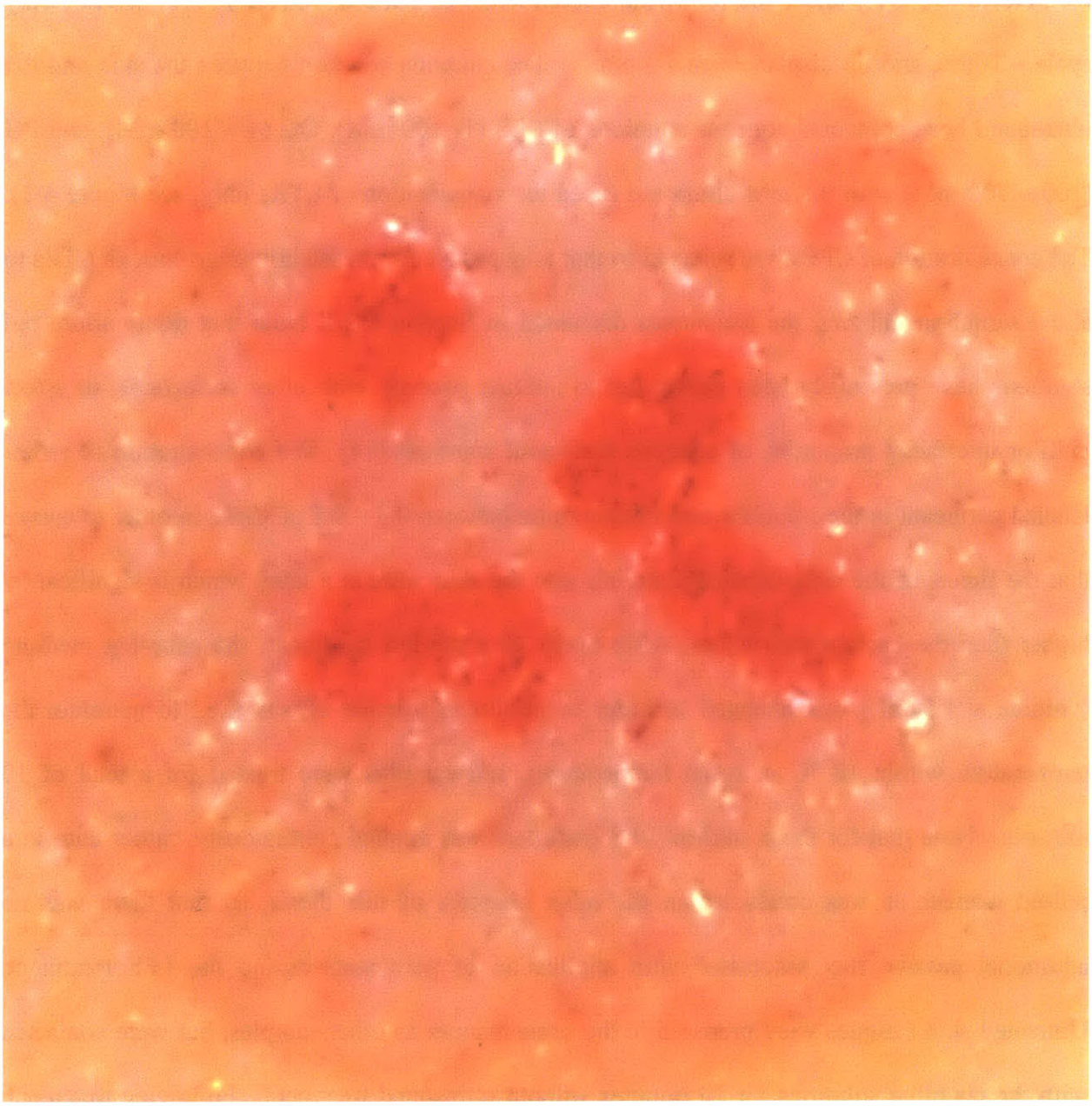

Figure 4-1. Skin sample treated with 4 mM octyl glucoside and 20 kHz LFS for 10 minutes. Regions stained by allura red are LTRs and unstained regions are non-LTRs.

4.2.4 Quantifying the Flux of CPEs into LTRs, non-LTRs, and Untreated Skin Samples

In order to quantify the amount of radio-labeled SLS, OG, and PG penetrating into the localized transport regions (LTRs, see Figure 4-1), the non-LTRs, and the untreated skin samples, samples were first blotted dry with lab tissue to remove all excess fluid on the surface of the skin. In samples treated with LFS, LTRs were identified visually because they were stained a deep red by the allura red dye, while non-LTRs were not stained to a noticeable extent (see Figure 4-1). In the timeframe of the experiments (10 minutes), permeants were not found to pass through the skin samples into the receiver compartment of the Franz diffusion cell. Therefore, the flux of permeant in each of the LTR and non-LTR regions was sampled by simply removing that portion of the skin using a spherical cutting tool (similar to a hole-puncher).[16] Two diameters were utilized, 1 mm and 2.5 mm, depending on the area of the LTR being sampled. Non-LTRs were only sampled utilizing the 2.5 mm – diameter cutting tool, because these regions comprised larger areas of the skin surface. Note that this sampling method has been successfully utilized in previous studies for the quantification of radio-labeled permeants within LTRs and non-LTRs.[16] On each skin sample, it was typically possible to sample 2-5 LTR samples and 5-8 non-LTR samples (since the non-LTRs occupy larger areas on the skin), with a total of 8-10 samples typically taken from each piece of treated skin. The skin samples were then solubilized using Soluene-350 (1.5 mL), and the amount of radio-labeled permeant was quantified using a Tri-Carb Liquid Scintillation Counter (Perkin-Elmer), utilizing the scintillation cocktail Hionic-Fluor (5 mL). This process was repeated for 4-5 skin samples for each chemical penetration enhancer at each concentration tested. Untreated skin samples were contacted for 10 minutes with a coupling solution which was identical to that used in the previous treatments, but in the

absence of LFS. For untreated samples, the entire skin sample that contacted the solution (with area of 1.77 cm^2) was used to quantify the amount of radio-labeled permeant in the skin. For the larger samples, 5 mL of Soluene-350 and 15 mL of Hionic-Fluor were utilized in the analysis of each sample. This process was repeated for 4-5 skin samples for each CPE considered at each concentration tested. For all samples, the concentration of the CPE was normalized by the surface area of that sample and by the application time (10 minutes = 600 s) in order to calculate the average flux into the skin in that area for the duration of the experiment. Note that in all the plots shown here, error bars correspond to 95% confidence intervals.

4.3. Theory

4.3.1 The Physical Picture

The basis of the physical mechanism underlying the synergism between LFS and CPEs is the physical picture proposed in Chapter 2.[16] In this study, it was found that acoustic cavitation microjets impinge on the skin primarily within LTRs, while acoustic streaming is the main mechanism of increased permeant uptake within non-LTRs (see Figure 4-2). The presence of acoustic cavitation microjets has a pronounced impact on the flux of permeants into the skin within LTRs, as discussed next in Section 4.3.2.

4.3.2 Modeling the Flux of CPEs into the Skin

The synergism between LFS and CPEs, specifically surfactants, was previously shown to occur due to increased penetration and dispersion of these molecules in the skin.[3] However, no physical mechanism was proposed to explain *how* LFS induces greater penetration of surfactants

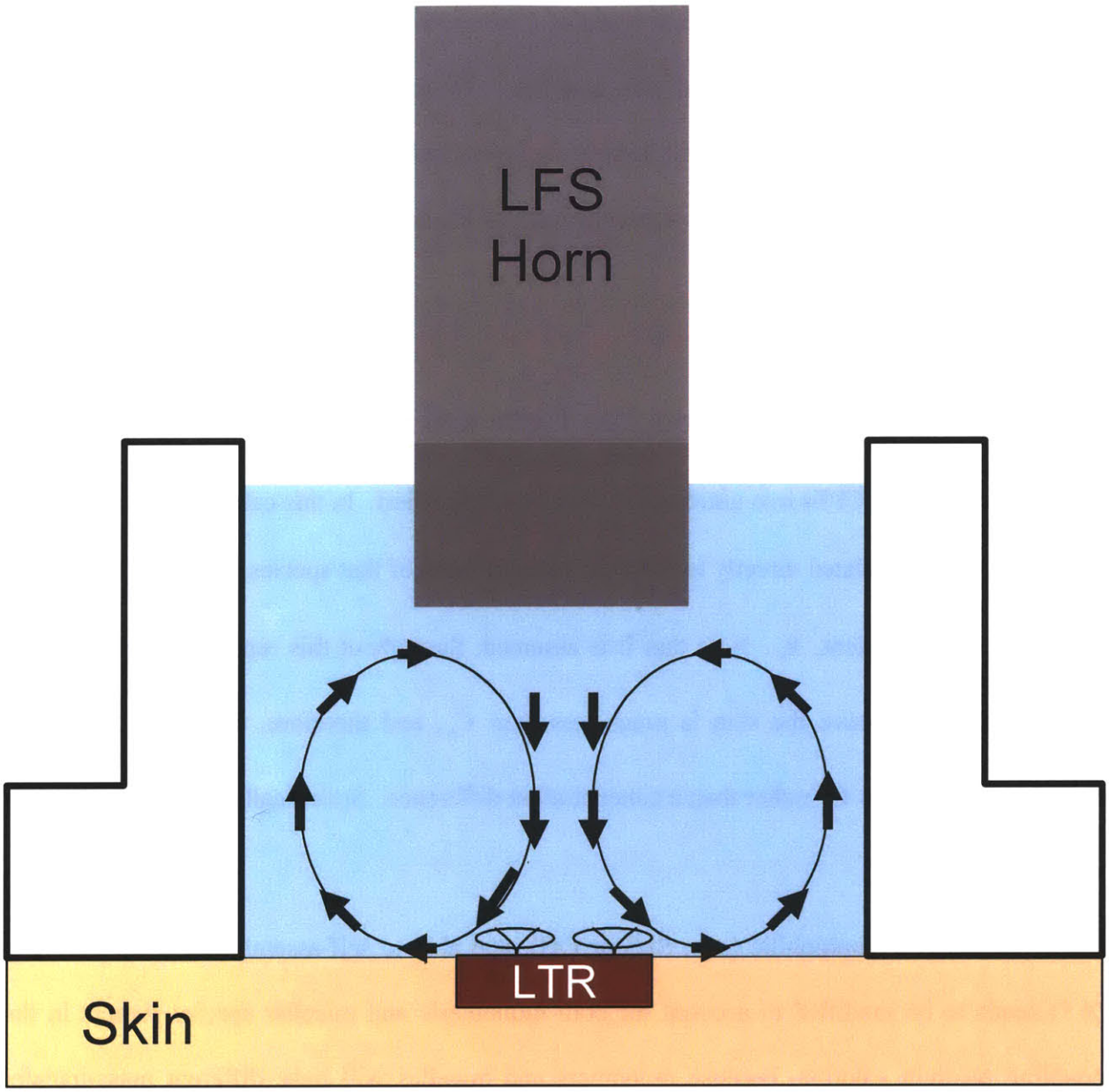

Figure 4-2. Illustration of the physical mechanisms occurring during LFS treatment of skin. The top chamber of a Franz diffusion cell is shown in the illustration. Arrows represent an enhancement in stirring induced by acoustic streaming, with microjet collapse occurring above the LTR.

and other CPEs into the skin. In this section, the physical picture presented in Figure 4-2 will be utilized to model the fluxes of different types of CPEs into untreated skin samples and into the non-LTRs and LTRs of LFS-treated skin samples. Through this analysis, the origin of the synergism between LFS and CPEs will become apparent, including why amphiphilic CPEs (such as OG or SLS) exhibit even greater synergism with LFS than non-amphiphilic CPEs (such as PG).

4.3.2.1 The Flux of Permeants into Untreated Skin

Modeling the flux of CPEs into untreated skin is straightforward. In this case, permeant flux into the skin, $J_{passive}$, is related directly to the bulk concentration of that species, C_b, by a diffusional mass-transfer coefficient, k_m. Note that it is assumed, throughout this report, that the aqueous concentration just above the skin is much less than C_b, and therefore, the driving force for diffusion is written as C_b rather than a concentration difference. Specifically,

$$J_{passive} = k_m C_b \tag{4.1}$$

If the permeant is amphiphilic (e.g., SLS or OG), and able to self-assemble into micelles, Eq. (4.1) needs to be modified to account for both monomeric and micellar species present in the coupling medium solution, because monomers and micelles will have different mass-transfer coefficients relating their fluxes into the skin to the corresponding bulk concentrations. Taking both monomers (*mon*) and micelles (*mic*) into account results in the following expression for $J_{passive}$, for the case of amphiphilic permeants above their cmc (the surfactant concentration beyond which micelles form):

$$J_{passive} = k_{m,mon} C_{cmc} + k_{m,mic} n_{agg} C_{b,mic} \tag{4.2}$$

where $k_{m,mon}$ is the mass-transfer coefficient of the amphiphilic monomers, C_{cmc} is the critical micelle concentration (cmc) of the surfactant, $k_{m,mic}$ is the mass-transfer coefficient of a monomer incorporated into a micelle, n_{agg} is the aggregation number of the micelles, and $C_{b,mic}$ is the bulk concentration of micelles in solution.

We can then relate $C_{b,mic}$ to the experimentally controllable variable C_b through the following relation:

$$C_{b,mic} = \left(\frac{C_b - C_{cmc}}{n_{agg}} \right) \tag{4.3}$$

Substituting Eq. (4.3) into Eq. (4.2) yields the following relation for the simultaneous flux of monomeric and micellar species into the skin:

$$J_{passive} = k_{m,mic} C_b + \left(k_{m,mon} - k_{m,mic} \right) C_{cmc} \tag{4.4}$$

4.3.2.2 The Flux of Permeants into the Non-LTRs of LFS-Treated Skin

As stated in Section 4.3.1, the flux of permeants into non-LTRs is enhanced solely by a decrease in the bulk solution resistance due to an increase in stirring induced by acoustic streaming. Therefore, the expressions for the fluxes of monomers and micelles into non-LTRs of LFS-treated skin are similar to those in the untreated case, albeit with enhanced mass-transfer coefficients. In particular, for both non-amphiphilic and amphiphilic permeants below their cmc (where only monomers are present), the flux into the skin can be modeled as follows:

$$J_{non-LTR} = k'_m C_b \tag{4.5}$$

where the prime indicates an enhanced mass-transfer coefficient.

Similarly to the untreated case, above the cmc, when both monomers and micelles are present in solution, the resulting equation relating the overall non-LTR flux to the bulk concentration is given by:

$$J_{non-LTR} = k'_{m,mic} C_b + \left(k'_{m,mon} - k'_{m,mic}\right) C_{cmc} \tag{4.6}$$

where the primes indicate enhanced mass-transfer coefficients.

4.3.2.3 The Flux of Permeants into the LTRs of LFS-Treated Skin

Modeling the flux of permeants into the LTRs of LFS-treated skin is not as straightforward as in the untreated or non-LTR cases, because the impingement of acoustic cavitation microjets within these regions must be accounted for, in addition to the convection-enhanced diffusional contribution to the flux. First, let us consider the case of a non-amphiphilic (NA) permeant, where adsorption of molecules onto the cavitation bubbles is not possible since they are not surface active. In this case, the flux of permeant into the skin is dependent on two contributions: (i) a convection-enhanced diffusional contribution, similar to that in the non-LTR case, and (ii) a contribution related to the amount of bulk fluid "injected" into the skin as a result of each acoustic cavitation microjet collapse at the skin surface. Specifically, the amount of permeant delivered per microjet collapse is equivalent to the volume of bulk fluid transported into the skin per cavitation microjet collapse on the skin surface (v_{cav}) multiplied by the bulk concentration of that species (C_b). Incorporating this contribution results in the following expression:

$$J_{LTR,NA} = \underbrace{k''_m C_b}_{\text{Diffusive Flux}} + \underbrace{\dot{n}_{cav} v_{cav} C_b}_{\text{Convective Flux}} \tag{7}$$

where the double-prime indicates that the diffusive mass-transfer coefficient ($k_m^{"}$) may be different from the diffusive mass-transfer coefficient (k_m') in the non-LTR case (see Eq. (4.5)) and $\dot{n}_{\text{cav}}$ is the number of acoustic cavitation microjet collapses per LTR area per unit time.

Collecting terms, Eq. (4.7) can be simplified as follows:

$$J_{LTR,NA} = \left(k_m^{"} + \dot{n}_{\text{cav}} v_{\text{cav}}\right) C_b \tag{8}$$

Equation (4.8) shows that the flux of non-amphiphilic species into the skin should be directly proportional to the bulk concentration, C_b, but to a much greater extent than in the untreated or non-LTR cases (see Eqs. (4.1) and (4.5)).

4.3.2.4 The Flux of Amphiphilic Permeants into the LTRs of LFS-Treated Skin below their CMC

In the case of the surface-active amphiphilic permeants, an additional contribution to the flux must be accounted for—the amount of permeant that is adsorbed at the gas/water interface of the cavitation bubbles (see Figure 4-3). Note that previous sonochemical studies have established that there is an accumulation of surfactants at the gas/water interface of acoustic cavitation bubbles.[17]

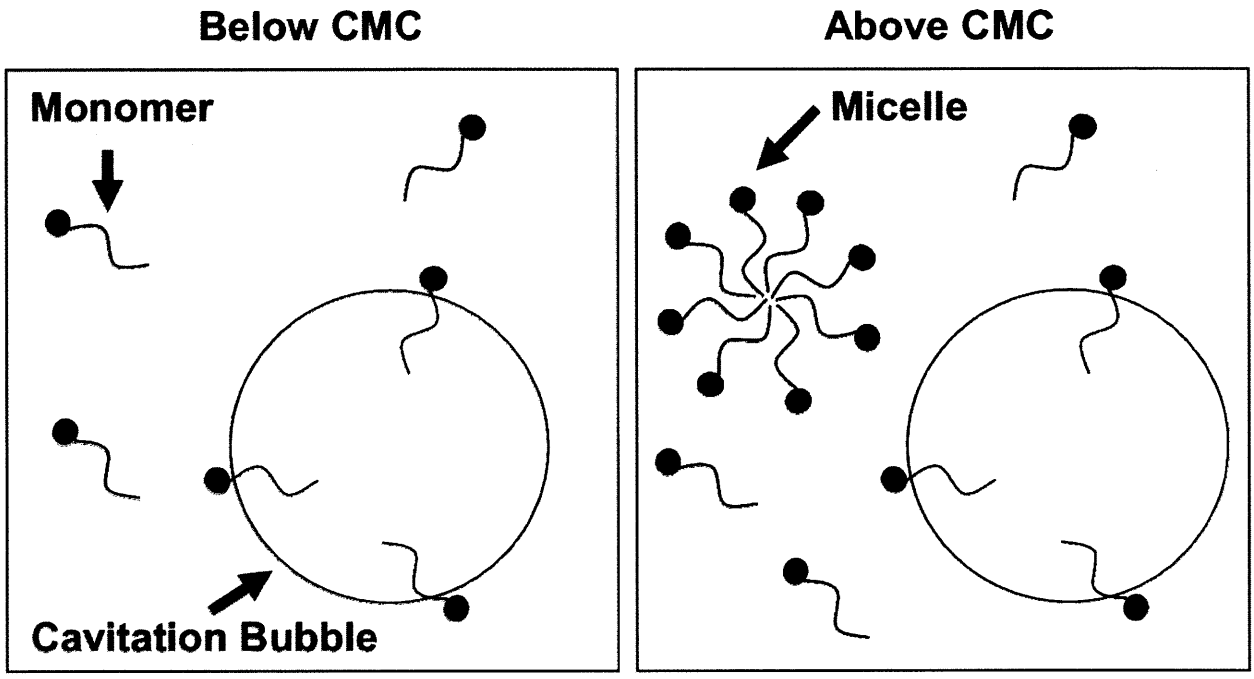

Figure 4-3. Schematic illustration of amphiphilic monomers adsorbing to an acoustic cavitation bubble. Note that only the monomers can adsorb to cavitation bubbles and, therefore, the adsorbed monomer concentration is constant above the cmc.

For the case of amphiphilic (A) permeants below their cmc, their flux within LTRs is modeled by modifying Eq. (4.8) as follows:

$$J_{LTR,A} = \underbrace{k_m'' C_b}_{\text{Diffusive Flux}} + \underbrace{\dot{n}_{cav} v_{cav} C_b}_{\text{Convective Flux}} + \underbrace{\dot{n}_{cav} A_{cav} \Gamma}_{\text{Adsorptive Flux}} \quad (4.9)$$

where A_{cav} is the average surface area of an acoustic cavitation bubble, and Γ is the equilibrium concentration of surfactant species adsorbed at the cavitation bubble interface. The justification for the assumption that Γ is reaching equilibrium will be discussed in Section 4.4.3.1.

To find an expression for Γ, it is assumed that only monomers can adsorb to, and desorb from, the gas/water interface (see Figure 4-4). In addition, because the quantity of permeant transported onto the cavitation bubbles and into the skin is small relative to the total permeant concentration in solution, the concentration of monomers and micelles in solution may be assumed to be constant. As a result, the equilibrium between monomers and micelles will be assumed to remain unperturbed at concentrations above the cmc (see Section 4.4.3.1). For simplicity, the dependence of Γ on C_b will be modeled by utilizing Henry's adsorption isotherm, which is valid for dilute surface concentrations and has been previously used to model SLS adsorption at an air/water interface.[18, 19] This gives us the expression:

$$\Gamma = K_H C_b \quad (4.10)$$

where K_H is the Henry equilibrium adsorption constant for a given amphiphilic permeant, and is defined as $K_H = K_L \Gamma_\infty$, where K_L is the equilibrium adsorption coefficient of the amphiphile (defined as the ratio of the rate of amphiphile adsorption to the rate of amphiphile desorption, k_a/k_d, see Figure 4-4), and Γ_∞ is the maximum surface concentration of the amphiphile. The

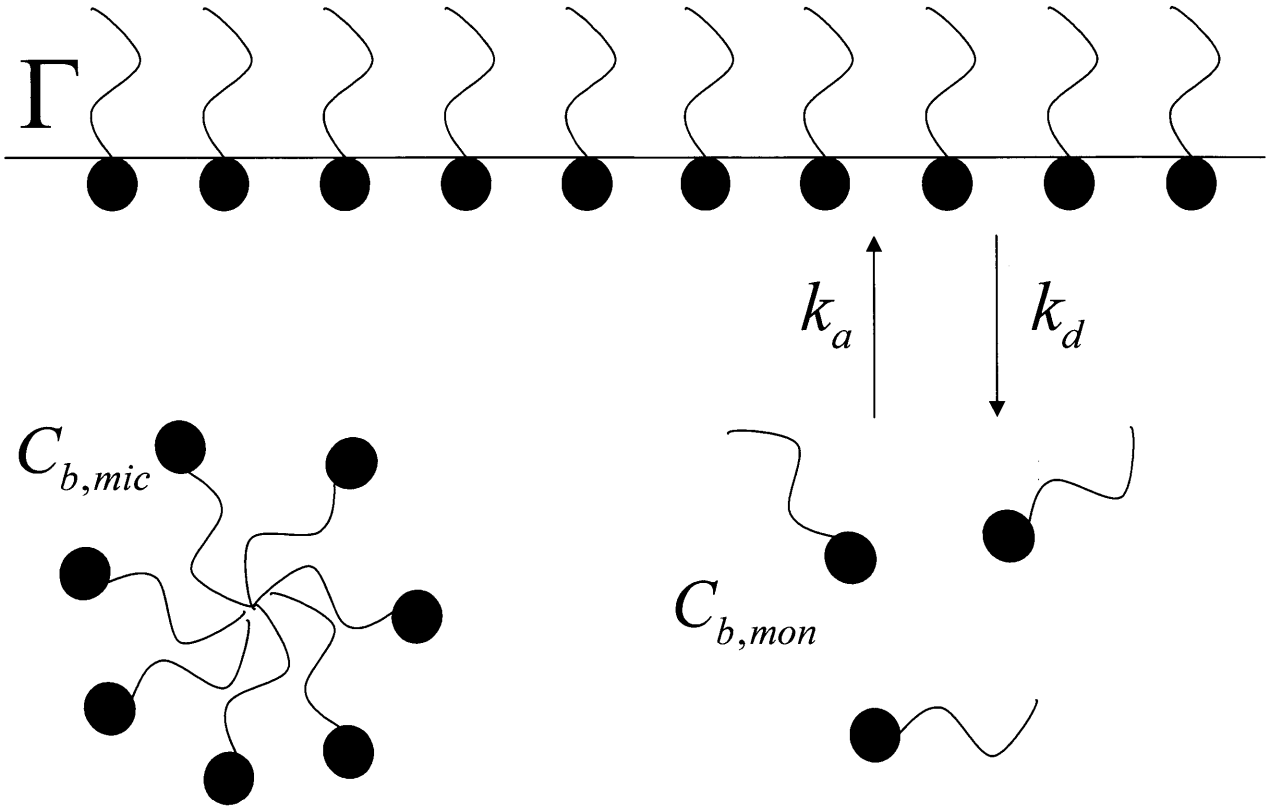

Figure 4-4. Surfactant adsorption model utilized. Only monomers can adsorb to, and desorb from, the gas/water cavitation bubble interface. Monomers and micelles are assumed to be at equilibrium.

specific values of K_L and Γ_∞ are not important in the context of this discussion and, therefore, the lumped K_H parameter will be utilized throughout the paper.

Substituting Eq. (4.10) into Eq. (4.9), the flux of the amphiphilic permeant into LTRs, below the cmc, is modeled as follows:

$$J_{LTR,A} = \underbrace{k_m^{"} C_b}_{\text{Diffusive Flux}} + \underbrace{\dot{n}_{\text{cav}} v_{\text{cav}} C_b}_{\text{Convective Flux}} + \underbrace{\dot{n}_{\text{cav}} A_{cav} K_H C_b}_{\text{Adsorptive Flux}} \tag{4.11}$$

Collecting terms, Eq. (4.11)) can be simplified as follows:

$$J_{LTR,A} = \left[k_m^{"} + \dot{n}_{\text{cav}} \left(v_{\text{cav}} + A_{cav} K_H \right) \right] C_b \tag{4.12}$$

Equation (4.12) indicates that the flux of amphiphilic permeants into LTRs, below their cmc, should be even greater than that of non-amphiphilic permeants (see Eq. (4.8)).

4.3.2.5 The Flux of Amphiphilic Permeants into the LTRs of LFS-Treated Skin Above their CMC

Because micelles cannot directly adsorb to the gas/water interface of cavitation bubbles, the model must be modified above the cmc to account for the presence of both monomers and micelles. Using Eq. (4.6) to model the diffusive flux above the cmc and now holding the concentration of monomers constant at the cmc, one obtains:

$$J_{LTR,A} = \underbrace{k''_{m,mic} C_b + \left(k''_{m,mon} - k''_{m,mic} \right) C_{cmc}}_{\text{Diffusive Flux}} + \underbrace{\dot{n}_{\text{cav}} v_{\text{cav}} C_b}_{\text{Convective Flux}} + \underbrace{\dot{n}_{\text{cav}} A_{cav} K_H C_{cmc}}_{\text{Adsorptive Flux}} \tag{4.13}$$

where the double-prime indicates that $k_{m,mic}^{"}$ and $k_{m,mon}^{"}$ may be different from $k'_{m,mic}$ and $k'_{m,mon}$ for the flux into the non-LTRs.

Collecting terms, Eq. (4.13) can be simplified as follows:

$$J_{LTR,A} = \left[\left(k''_{m,mon} - k''_{m,mic}\right) + \dot{n}_{\text{cav}} A_{cav} K_H\right] C_{cmc} + \left(k''_{m,mic} + \dot{n}_{\text{cav}} v_{\text{cav}}\right) C_b \tag{4.14}$$

Note that the slope of the $J_{LTR,A}$ vs. C_b curve is equal to that corresponding to a non-amphiphilic species in Eq. (4.8). This result will be analyzed further in Section 4.4.3.2.

4.3.2.6 Summary of Expected Trends in the Flux Data

As shown in Sections 4.3.2.1 - 4.3.2.2, the flux of both amphiphilic and non-amphiphilic species into untreated skin and the non-LTRs of LFS-treated skin should follow similar trends (see Section 4.4.1). However, due to the enhanced stirring induced by acoustic streaming, the flux into the non-LTRs should be increased relative to that into untreated skin (compare Eqs. (4.1) and (4.4) to Eqs. (4.5) and (4.6)). This suggests that the slope observed for the flux vs. bulk concentration curve should be greater in the non-LTR case than in the case of untreated skin. Within LTRs, the expected flux of non-amphiphilic permeants should be dominated by a convective term associated with the collapse of acoustic cavitation microjets (see Section 4.4.2). Furthermore, for amphiphilic permeants below their cmc (amphiphilic monomers), the flux into the LTRs is expected to be further enhanced due to the adsorption of the amphiphiles onto the surface of cavitation bubbles (see Section 4.4.3). However, above the cmc of amphiphilic permeants, the slope of the flux vs. bulk concentration curve should revert to a value which is similar to that of a non-amphiphilic molecule because micelles are not able to adsorb at the surface of cavitation bubbles (see Eqs. (4.8) and (4.14)).

It is therefore hypothesized that the origin of the increase in the penetration of CPEs into the skin induced by LFS, and consequently their synergism, results from the cavitation-related convective

and adsorptive contributions to the flux. Specifically, the flux into the LTRs of any permeant that acts as a CPE will be enhanced by the convective flux contribution. In addition, the flux of amphiphilic permeants (e.g., surfactants) will be enhanced even further due to their ability to adsorb at the surface of acoustic cavitation bubbles, thereby generating an even greater flux into the skin. The concepts of convective and adsorptive fluxes will be tested in Section 4.4 by utilizing a non-amphiphilic CPE, propylene glycol (PG), and two amphiphilic CPEs, sodium lauryl sulfate (SLS, an anionic surfactant) and octyl glucoside (OG, a nonionic surfactant). The simplifications and assumptions made in the derivation of the flux model presented in Section 4.3 will be analyzed and justified in Section 4.4.3.1.

4.4 Results and Discussion

To test the flux model presented in Section 4.3, the fluxes of three CPEs into the skin were investigated, in both LFS-treated and untreated skin. LFS-treated skin samples consisted of both LTRs and non-LTRs (see Figure 4-1), and each of the regions were sampled as discussed in Section 4.2.4. The first CPE tested was PG, a non-amphiphilic, low-molecular weight (MW = 76 Da) molecule that is completely miscible in water. The other two CPEs, SLS and OG, are both amphiphilic molecules. Specifically, SLS is an anionic surfactant (MW = 288 Da), whose micelles have an aggregation number of ~60,[20] indicating that SLS micelles have a molecular weight of about 17 kDa. OG is a nonionic surfactant (MW = 292 Da), whose micelles have an aggregation number of ~90,[21] indicating that OG micelles have a molecular weight of about 26 kDa.

4.4.1 Flux of Permeants into Untreated Skin and the Non-LTRs of LFS-Treated Skin

As discussed in Section 4.3.2.1, the flux of any given monomeric permeant into untreated skin is expected to be directly proportional to the bulk permeant concentration in solution, as related by a mass-transfer coefficient, k_m, which is specific to that permeant (see Eq. (4.1)). If micelles are present in solution, both amphiphiles in monomeric and micellar states are expected to have different mass-transfer coefficients ($k_{m,mon}$ and $k_{m,mic}$, respectively), with the amphiphilic molecules present within micelles expected to have decreased mobility relative to the monomers (that is, $k_{m,mon} > k_{m,mic}$). The fluxes of monomeric and micellar permeants into the non-LTRs of LFS-treated skin samples are expected to follow the same trend as in untreated skin, but with enhanced mass-transfer coefficients ($k'_{m,mon}$ and $k'_{m,mic}$, respectively), as a result of the decreased bulk resistance due to enhanced stirring caused by acoustic streaming (see Section 4.3.1). The flux of PG, OG, and SLS into untreated skin and the non-LTRs of LFS-treated skin are shown in Figures 4-5, 4-6, and 4-7, with the corresponding mass-transfer coefficients calculated from these plots summarized in Table 4-1. Recall that for the amphiphilic permeants (OG and SLS), the slope below the cmc is equivalent to $k_{m,mon}$ for the untreated skin samples and to $k'_{m,mon}$ for the non-LTR samples. Similarly, the slope above the cmc is equivalent to $k_{m,mic}$ for the untreated skin samples and to $k'_{m,mic}$ for the non-LTR samples. In the analysis of the data, the y-intercept of the linear regressions for the non-amphiphilic permeant (PG), as well as for the amphiphilic permeants (OG and SLS) below their cmc, were forced to zero, because a non-zero y-intercept has no physical meaning in the context of the flux model. The cmc's of OG and SLS were found experimentally to be 18 mM and 7.7 mM, respectively, utilizing surface tension

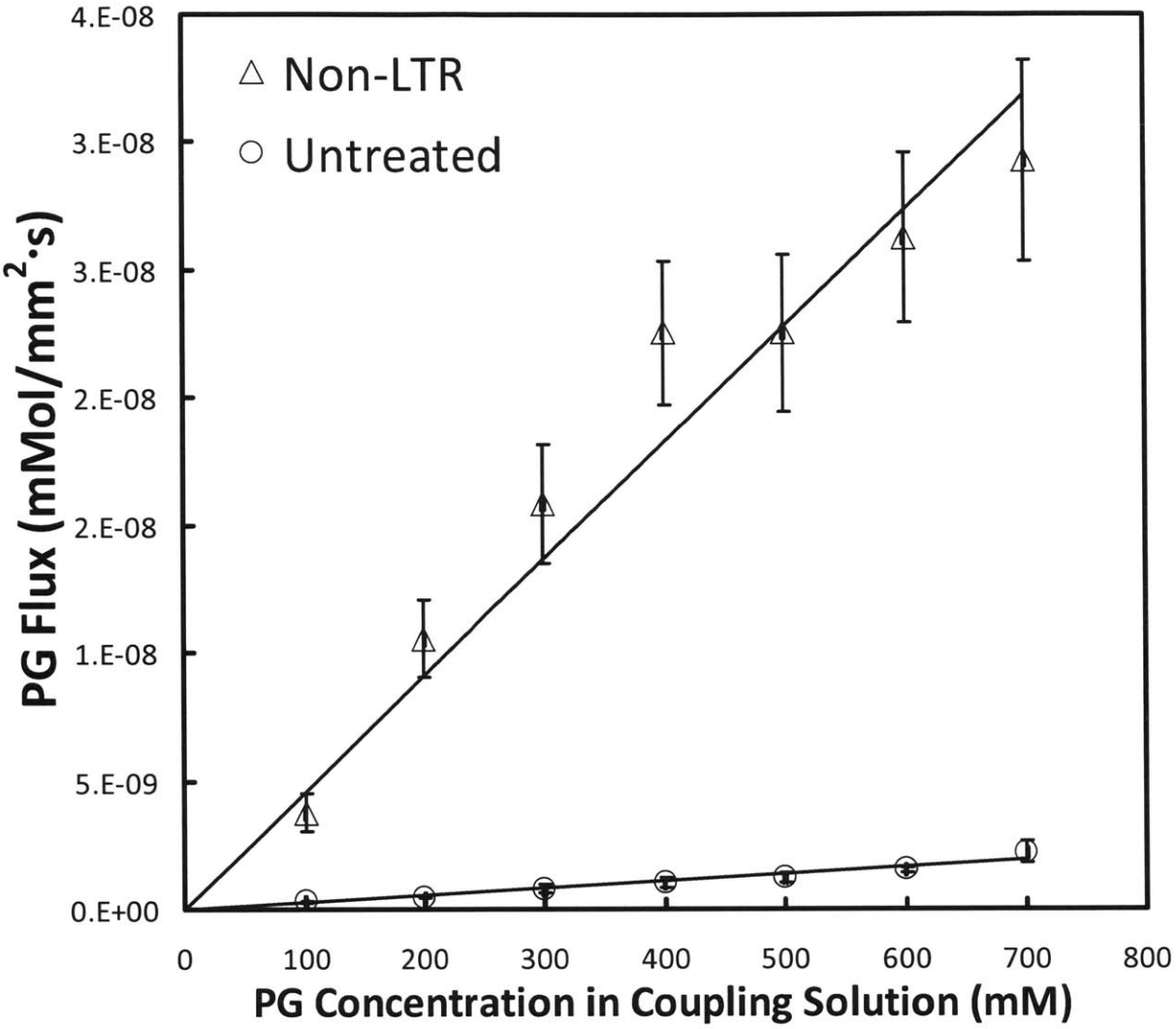

Figure 4-5. Flux of PG into untreated skin and the non-LTRs of LFS-treated skin as a function of PG concentration in bulk solution. The corresponding mass-transfer coefficients derived from the slopes of this data are reported in Table 4-1.

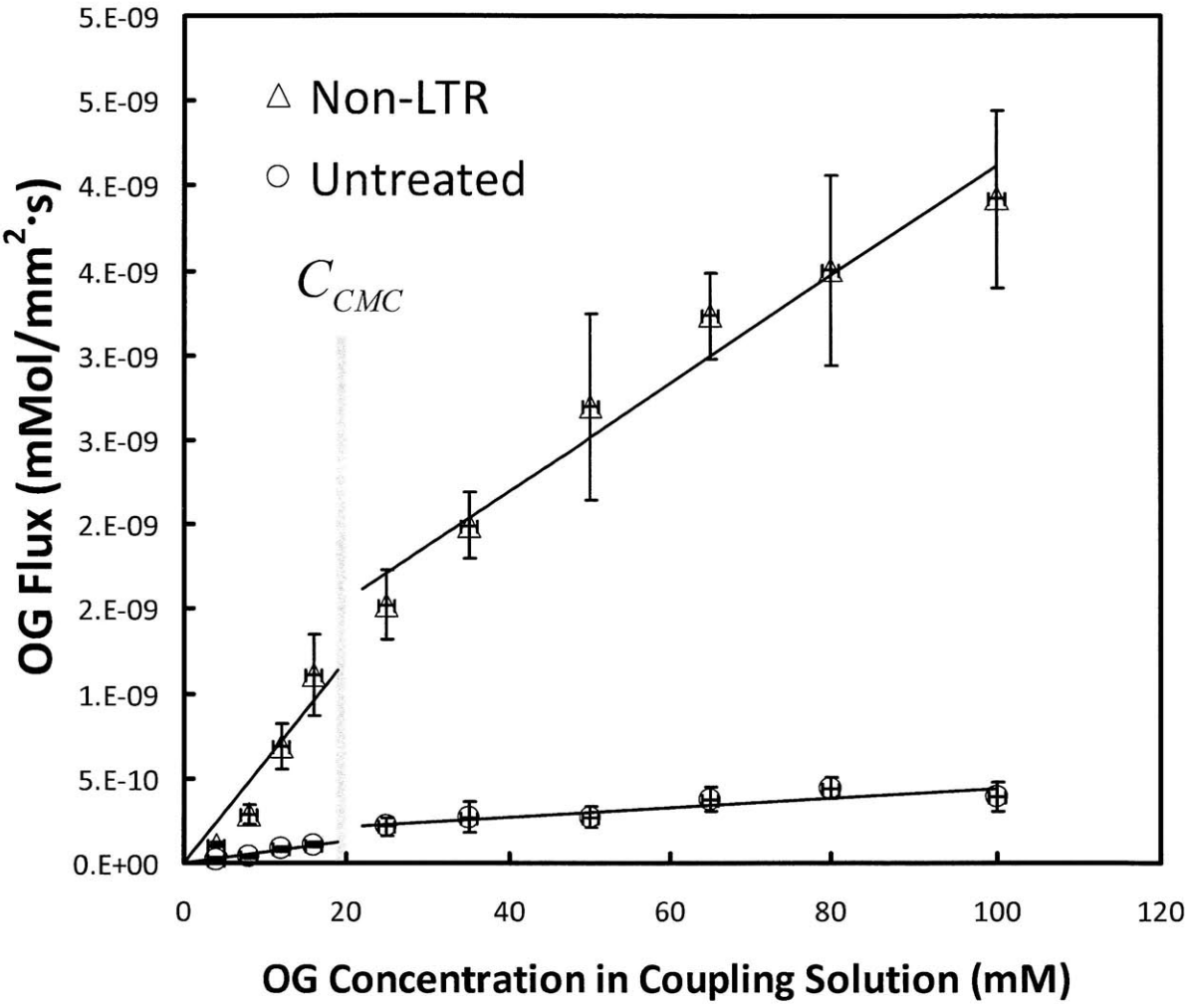

Figure 4-6. Flux of OG into untreated skin and the non-LTRs of LFS-treated skin as a function of OG concentration in bulk solution. The corresponding mass-transfer coefficients derived from the slopes of this data are reported in Table 4-1.

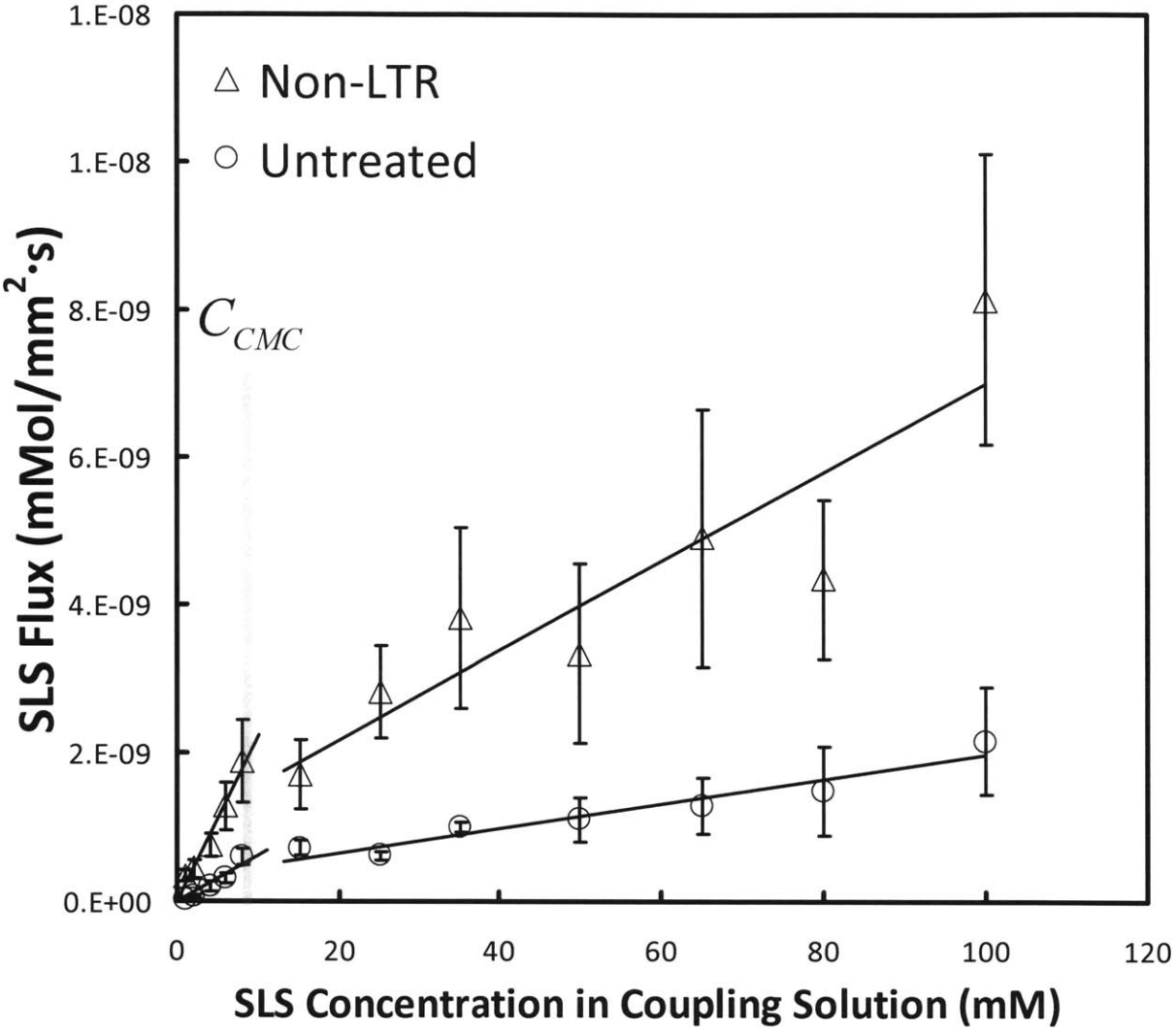

Figure 4-7. Flux of SLS into untreated skin and the non-LTRs of LFS-treated skin as a function of SLS concentration in bulk solution. The corresponding mass-transfer coefficients derived from the slopes of this data are reported in Table 4-1.

Table 4-1. Mass-transfer coefficients of PG, OG, and SLS into untreated skin and the non-LTRs of LFS-treated skin. Values were calculated from the slopes of the linear regressions shown in Figure 4-7, with the corresponding r^2 values calculated based on the mean flux value at each concentration reported.

CPE	Untreated Skin				Non-LTRs			
	$k_{m,mon}$	r^2	$k_{m,mic}$	r^2	$k'_{m,mon}$	r^2	$k'_{m,mic}$	r^2
PG	$2.7 \cdot 10^{-9}\ m/s$	0.95	no cmc		$4.6 \cdot 10^{-8}\ m/s$	0.93	no cmc	
OG	$6.5 \cdot 10^{-9}\ m/s$	0.93	$2.8 \cdot 10^{-9}\ m/s$	0.80	$6.0 \cdot 10^{-8}\ m/s$	0.87	$3.2 \cdot 10^{-8}\ m/s$	0.96
SLS	$6.3 \cdot 10^{-8}\ m/s$	0.90	$1.7 \cdot 10^{-8}\ m/s$	0.93	$2.2 \cdot 10^{-7}\ m/s$	0.97	$6.0 \cdot 10^{-8}\ m/s$	0.82

measurements (see Section 4.2.2). Note that there is good agreement between the break in the flux curves shown in Figures 4-6 and 4-7 and the experimentally deduced cmc values, as is expected within the formulated flux model.

Figures 4-5 to 4-7, as well as Table 4-1, show that the untreated skin and non-LTR data follow the trends predicted in Sections 4.3.2.1 and 4.3.2.2, respectively. In other words, for each permeant considered, the flux vs. bulk concentration curves follow similar trends in both the untreated and non-LTR skin samples, with an enhancement observed in the non-LTR samples relative to the untreated samples. In the case of the nonionic permeants, the mass transfer coefficients increase by approximately one order-of-magnitude for both PG and OG monomers, as well as for the OG micelles, in the non-LTR samples relative to the untreated skin samples (see Table 4-1). For SLS monomers and micelles, the increase in the mass-transfer coefficients between the non-LTR samples and the untreated skin samples is about 4-fold in each case (see Table 4-1). The increase in the flux of SLS in the non-LTRs relative to the untreated skin samples is less than in the case of the nonionic species because: (i) both the skin and SLS are negatively charged, and therefore, partitioning of the ionic molecules into the skin may be a limiting factor, and (ii) $k_{m,mon}$ and $k_{m,mic}$ are larger for SLS than for PG and OG (see Table 4-1), and, as a result, there may be less inherent bulk resistance to SLS flux into the skin, which would result in acoustic streaming having a less significant role in increasing the mass-transfer coefficients of SLS into the non-LTRs of LFS-treated skin.

4.4.2 Flux of Non-Amphiphilic Permeants into the LTRs of LFS-Treated Skin

As shown in Section 4.3.2.3, the flux into the LTRs of LFS-treated skin depends on the amount of material delivered into the skin due to the impingement of microjets in these regions (as reflected in $\dot{n}_{cav} \cdot v_{cav}$), in addition to a less significant diffusive flux term (k_m''). This cavitation-related contribution is effectively a convective flux, and therefore may be expressed as follows:

$$J_V = V \cdot C_b \tag{4.15}$$

where V is an effective convective velocity associated with the impingement of microjets and is equivalent to $\dot{n}_{cav} \cdot v_{cav}$, in terms of the variables defined previously. Therefore, regardless of the size of the permeant being delivered, this convective flux contribution should be constant as long as the cavitation field remains constant (i.e., $\dot{n}_{cav}$ and v_{cav} do not change) and there is no additional flux associated with the adsorption of molecules to the cavitation bubbles (as is the case for amphiphilic permeants).

The flux of PG into the LTRs of LFS-treated skin as a function of PG bulk concentration is presented in Figure 4-8. Figure 4-8 shows that as predicted by the flux model for this non-amphiphilic molecule, the data is linear (see Eq. (4.12)), but with a much larger flux than in the case of the non-LTRs (see Eq. (4.5)). Because the LTRs and the non-LTRs were sampled from the same pieces of skin (both LTRs and non-LTRs are present on LFS-treated skin samples, see Figure 4-1), the importance of the convective contribution relative to that of the diffusive contribution can be gauged by assuming $k'_{m,PG} \sim k''_{m,PG}$. Making this assumption, it follows that the slope in Figure 4-8, $5.1 \cdot 10^{-7}\ m/s$ (see Table 4-2), is over an order-of-magnitude greater than

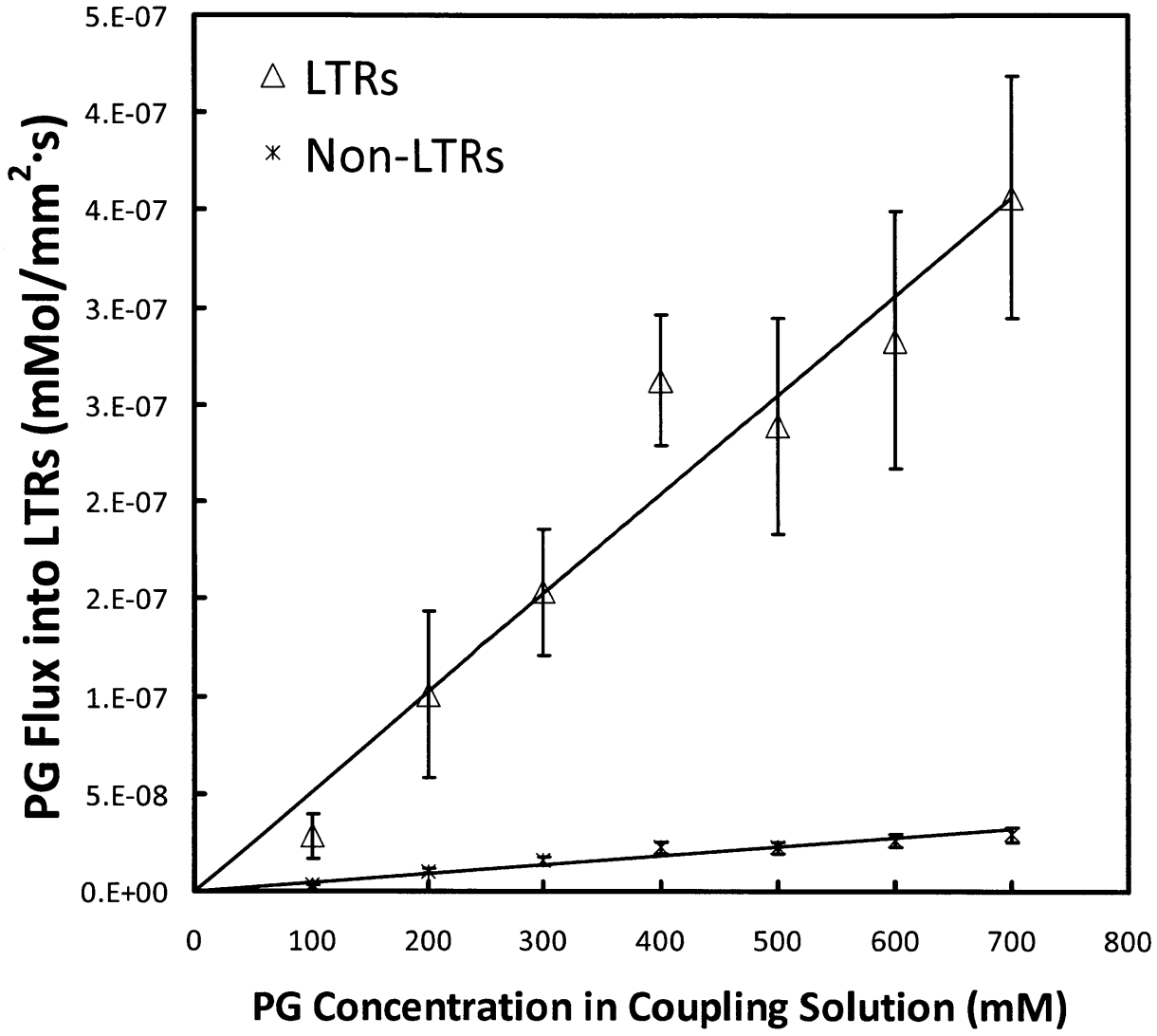

Figure 4-8. Flux of PG into the LTRs of LFS-treated skin as a function of PG concentration in the LFS coupling solution.

$k'_{m,PG}$ ($4.6 \cdot 10^{-8}\, m/s$, see Table 4-1). Accordingly, to leading order, the flux of PG into the LTRs of LFS-treated skin is proportional to the convective contribution. Therefore, to a good approximation, it can be assumed that the diffusive contribution to the flux is negligible in the LTRs (see Eq. (4.7)), and that the flux of non-amphiphilic permeants into the LTRs is given by:

$$J_{LTR,NA} = \dot{n}_{cav} v_{cav} \cdot C_b = V \cdot C_b \tag{4.16}$$

Furthermore, in the context of the flux model, it is important to recognize that the flux of amphiphilic permeants into the LTRs of LFS-treated skin, above their cmc, exhibits the same dependence on the permeant bulk concentration as do non-amphiphilic permeants Accordingly, Eq. (4.16) will become useful in analyzing the OG and SLS data at concentrations above the cmc for each permeant, and in supporting the flux model (see Section 4.4.3.2).

4.4.3 Flux of Amphiphilic Permeants into the LTRs of LFS-Treated Skin

As discussed in Section 4.3, in addition to the convective contribution to the flux, which is significant within the LTRs of LFS-treated skin, an adsorptive contribution to the flux must also be included to model the flux of amphiphilic species within LTRs. This is due to the fact that amphiphiles can adsorb to the surface of cavitation bubbles and be transported into the skin, in addition to being delivered into the skin due to convection induced by the impingement of acoustic cavitation microjets.

4.4.3.1 Assumptions of the Model

In order to estimate the concentration of adsorbed amphiphiles in the context of the flux model, the following simplifying assumptions are implemented.

1. The concentrations of bulk monomers, $C_{b,mon}$, and bulk micelles, $C_{b,mic}$, are constant in the LFS coupling solution, and therefore, equilibrium between these two species is maintained throughout the LFS treatment.

   - In order to test this assumption, the amount of permeant transported into the skin was compared to the total amount of permeant in the LFS coupling solution. Typically, the total surface coverage of LTRs is 5-20% and that of non-LTRs is 80-95%. Because more permeant enters LTRs than non-LTRs, assuming that 20% of the skin samples contain LTRs should provide an high-end estimate. Multiplying the LTR fluxes found in Figures 4-8 to 4-10 and the non-LTR fluxes found in Figures 4-5 to 4-7 by the treatment time (600 s) and the skin surface area of each region (with a total area of 177 mm^2), it is found that for both OG and SLS, the upper threshold for the amount of permeant transported into the skin is <1% of that in bulk solution, thereby validating assumption 1.

2. The cavitation bubbles are at adsorption equilibrium when collapsing at the skin surface.

   - In order to test this assumption, one must compare the lifetime of an average cavitation bubble with the time scale associated with monomer adsorption onto a cavitation bubble. The average velocity of cavitation bubbles at 20 kHz, generated using equipment which is similar to the one utilized in the present study, was reported to be 1.007 m/s.[22] In these experiments, the ultrasound horn is positioned 3 mm from the skin surface. Therefore, taking the characteristic length scale to be of order 1 mm, it is found that the average bubble lifetime is on the order of 1 ms. In the context of Henry's adsorption isotherm used in this analysis, the relevant adsorption parameters could only be found for SLS. Specifically, taking into account the characteristic length scale of SLS adsorption (the distance an SLS molecule must travel in the bulk solution to adsorb to the

gas/water interface) , which is reported to be of the order $1 \cdot 10^{-7} m$,[18] and the rate of SLS adsorption (k_a), which was reported to range between $5.5 \cdot 10^{-4} - 3\ m/s$ below the cmc,[19] the timescale for adsorption of SLS onto the cavitation bubbles is estimated to be ~0.03-180 μs, which is significantly faster than 1 ms. It then follows that the equilibrium assumption (assumption 2) is valid, since the timescale for adsorption is much faster than the average lifetime of a bubble.

3. As stated in Section 4.3, the derivation of the flux model assumes that the cavitation field parameters, $\dot{n}_{cav}$, v_{cav}, and A_{cav}, do not vary significantly during these experiments. In this respect, sonochemical research has shown that there is not much dependence of sonoluminescense and other indicators of the cavitation field on CPE concentration at low frequencies (e.g., 20 kHz).[23] For example, the presence of methacrylic acid (a small organic compound that is soluble in both water and organic solvents), at concentrations up to 65 mM, was shown to only decrease sonoluminescense on the order of 10% at 20 kHz. Moreover, surface tension effects have also been shown to not greatly affect indicators of the cavitation field, such as sonoluminescence.[24] It is also noted that above the cmc of each amphiphile, the surface tension should not change greatly and, therefore, only electrostatic effects may cause changes in the cavitation field parameters for the majority of concentrations tested in this study (see Section 1.4.2.1). Therefore, at the operating frequency used in the present study (20 kHz), assumption 3 is assumed to be reasonable, and is required for the direct analysis of the data presented in the following sections. Potential violations of this assumption that lead to deviations from the described flux model will be analyzed in Section 4.4.3.4.

4.4.3.2 Fluxes of OG and SLS into the LTRs of LFS-Treated Skin

As discussed in Section 4.3.2.3, the flux of amphiphilic permeants into LTRs, below their cmc, should be larger than that of non-amphiphilic permeants, because of the additional contribution of the surface adsorptive flux (see Eq. (4.11)). As the amphiphilic permeant concentration increases beyond its cmc, the slope of the flux vs. bulk concentration curve should revert to that expected for a non-amphiphilic permeant, as shown in Eq. (4.16), because micelles cannot adsorb onto the surface of cavitation bubbles.

Figures 4-9 and 4-10 show that the fluxes of both OG and SLS, below their cmc's, are greater than the flux of PG (compare the data points to the dashed lines in Figures 4-9 and 4-10). This follows from the flux model (compare Eqs. (4.9) and (4.7)) because the flux of amphiphilic permeants into the skin over this concentration range depends on both the adsorptive flux and the convective flux. By comparing the slopes of the OG and SLS data to the slope of the PG data (see Table 4-2), it follows that the adsorptive flux accounts for 30% of the OG flux into the skin and 73% of the SLS flux into the skin below the cmc for each amphiphile. In the context of the flux model, the difference in the slopes of the OG and SLS data below the cmc of each amphiphile reflects the different K_H values associated with each amphiphile (see Eq. (4.12)). Further discussion about the kinetic adsorption parameters of OG and SLS is presented in Section 4.4.3.3.

However, as predicted by the flux model (see Eq. (4.16)), the slopes above the cmc's of both OG and SLS are nearly identical to that of the PG data (within 10% error, see Table 4-2). This indicates that both small molecules, such as OG (MW = 76 Da), and large micellar aggregates

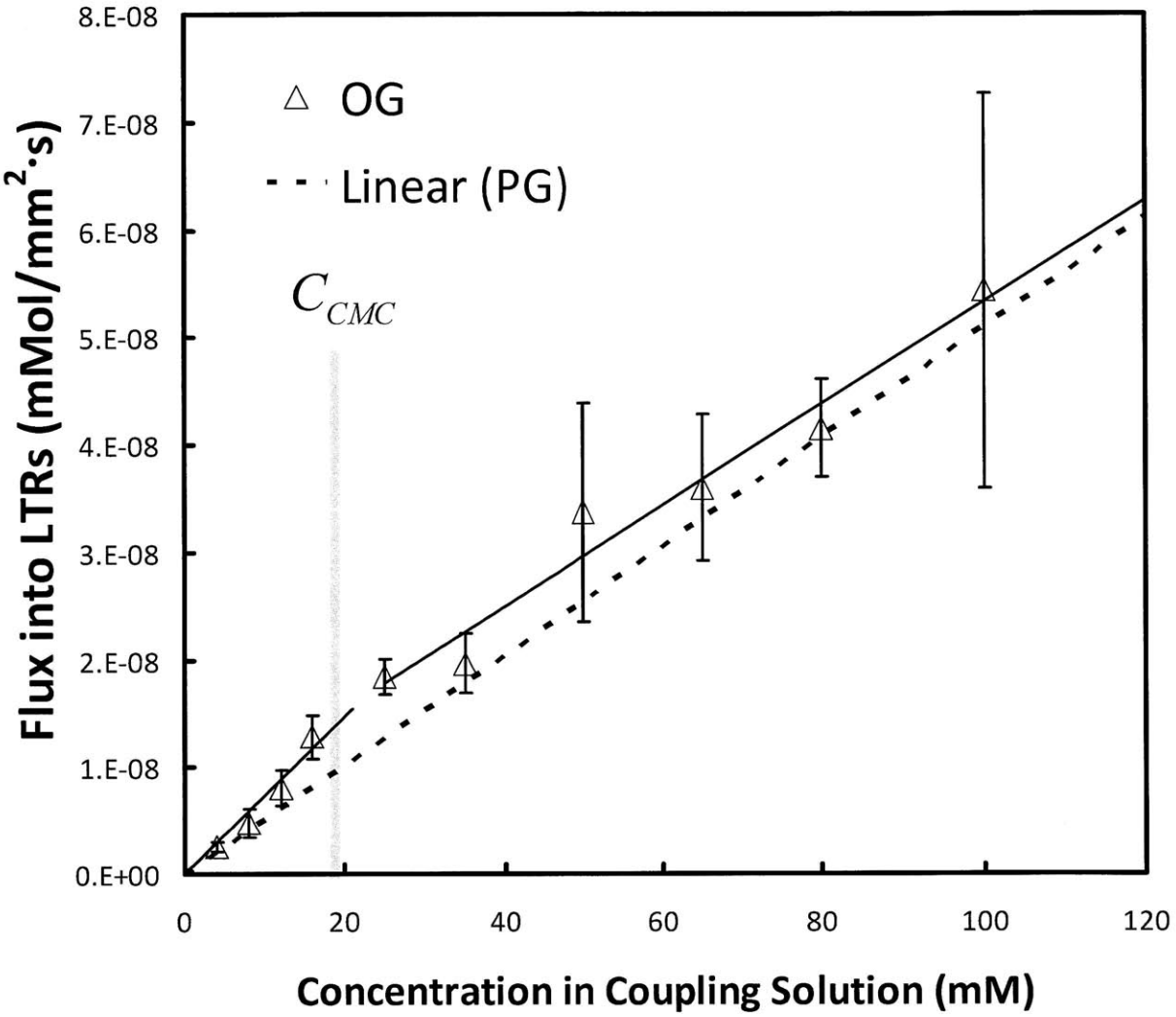

Figure 4-9. Flux of OG into the LTRs of LFS-treated skin as a function of OG concentration in the LFS coupling solution. The dashed line corresponds to the flux of PG, and is included for comparison purposes.

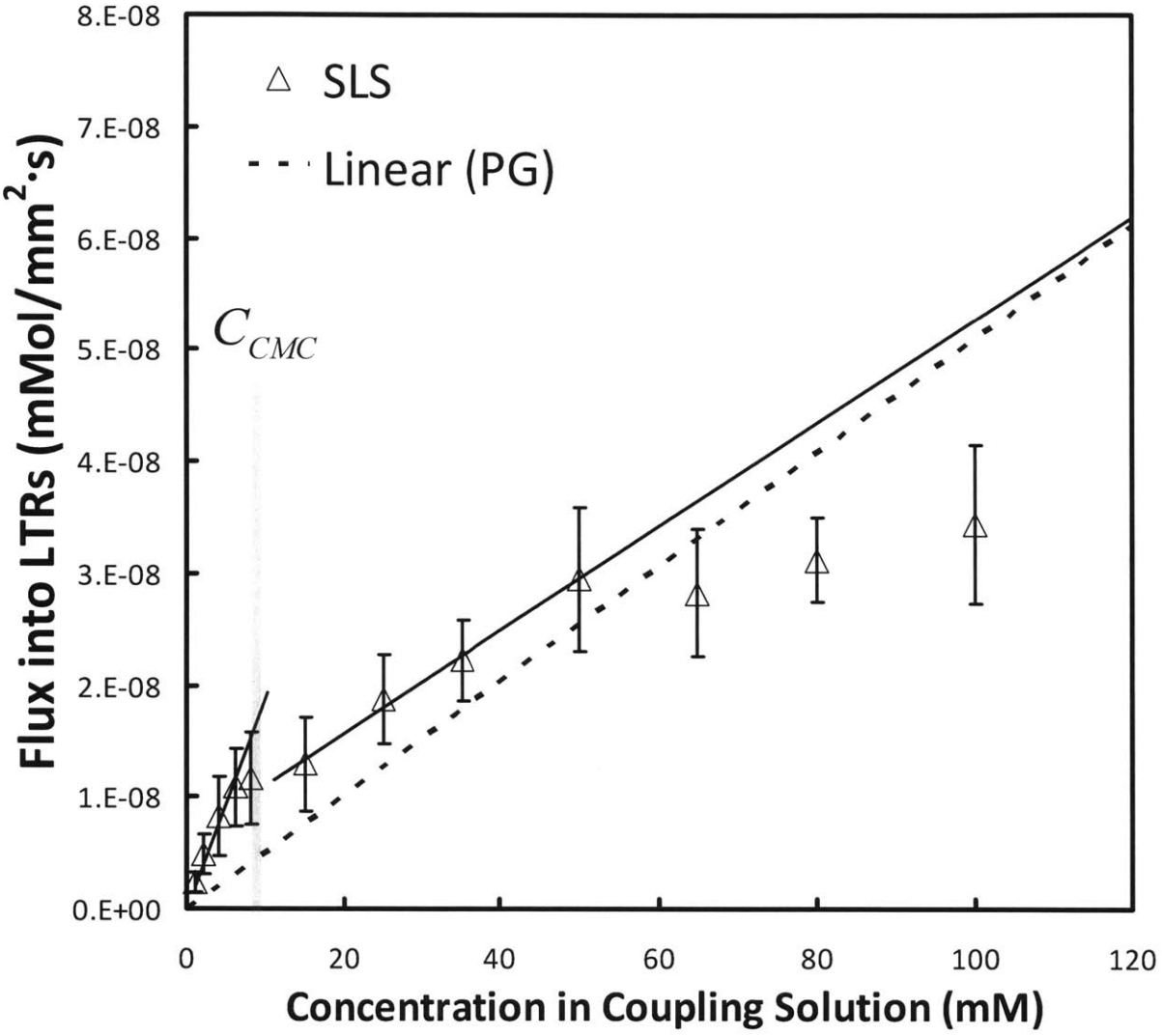

Figure 4-10. Flux of SLS into the LTRs of LFS-treated skin as a function of SLS concentration in the LFS coupling solution. The dashed line corresponds to the flux of PG, and is included for comparison purposes.

Table 4-2. Slopes of the permeant flux vs. bulk coupling medium concentration curves, both below and above the cmc of the tested CPEs. The corresponding r^2 values were calculated based on the mean flux value at each concentration.

Species	$\dot{n}_{cav}\left(v_{cav}+A_{cav}K_H\right)$ (slope below cmc)		$\dot{n}_{cav}\cdot v_{cav}$ (slope above cmc)	
	value	r^2	value	r^2
PG	no cmc		$5.1\cdot10^{-7}\ m/s$	0.94
OG	$7.3\cdot10^{-7}\ m/s$	0.95	$4.7\cdot10^{-7}\ m/s$	0.97
SLS	$1.9\cdot10^{-6}\ m/s$	0.95	$4.6\cdot10^{-7}\ m/s$ (from 8-50 mM)	0.99

(MW = 17-26 kDa) are transported into the skin at nearly the same rate! This result is indicative of convective transport (see Eq. (4.15)), which in this case results from the collapse of acoustic cavitation microjets, and fits the expected trends of the flux model. It is important to stress that, for the SLS data presented in Figure 4-10, the flux model no longer fits the data at and above a threshold SLS concentration of 65 mM, since the data falls below the predicted trend line. Because the flux model still holds at similar concentrations of the nonionic amphiphile OG (see Figure 4-9), it is likely that electrostatic effects may be the cause of the observed deviation from the flux model above a threshold concentration for the charged, anionic SLS amphiphile. Further analysis and discussion of this deviation is presented in Section 4.4.3.4.

4.4.3.3 Analysis of Kinetic and Cavitation-Related Variables Deduced from the Flux Model

Equation (4.13) derived in Section 4.3.2.3 to model the flux of permeants into the LTRs of LFS-treated skin contains four variables, $\dot{n}_{\text{cav}}$, v_{cav}, A_{cav}, and K_H, of which the species-specific K_H variable is only relevant for amphiphilic permeants. Therefore, given that there are a total of *five* unknown variables (including K_H for OG and SLS) and there are a total of three equations relating them (those corresponding to PG, OG, and SLS), two variables must be accurately estimated in order to be able to fully define the system. This analysis is critical in determining whether the quantitative values derived from the flux model are realistic, and therefore in further substantiating the flux model.

A logical starting point in this analysis involves estimating the two variables that depend on the size of the cavitation bubbles, v_{cav} and A_{cav}. Specifically, v_{cav} is the volume of bulk fluid delivered into the skin by each collapsing cavitation bubble, and A_{cav} is the average surface area of a cavitation bubble. Therefore, v_{cav} and A_{cav} will first be related to the average cavitation bubble radius to eliminate one unknown. First, the dependence of v_{cav} on the average size of a cavitation bubble before it collapses onto the skin will be analyzed. To leading order, the simplest scenario assumes that the amount of volume that a cavitation bubble delivers into the skin is directly proportional to the volume of fluid that it displaces in solution. In other words, for a spherical cavitation bubble v_{cav} and R_{cav} are simply related as follows:

$$v_{cav} = \frac{4}{3}\pi R_{cav}^3 \tag{4.17}$$

where R_{cav} is the average radius of a cavitation bubble prior to its collapse on the skin surface.

Similarly, the average surface area of a cavitation bubble is related to R_{cav} as follows:

$$A_{cav} = 4\pi R_{cav}^2 \tag{4.18}$$

Equations (4.17) and (4.18) allow us to express v_{cav} and A_{cav} in terms of the single variable, R_{cav}. Therefore, if R_{cav} can be estimated, the three equations corresponding to the fluxes of PG, OG, and SLS into LTRs can be solved explicitly. Interestingly, a previous study conducted using similar equipment to the one used here, at 20 kHz, found that the number average diameter of cavitation bubbles is 6.3 μm, corresponding to a number average radius of 3.15 μm.[22] Using this R_{cav} value in Eq. (4.17), it is found that:

$$v_{cav} = \frac{4}{3}\pi R_{cav}^3 = \frac{4}{3}\pi\left(3.15\cdot 10^{-6} m\right)^3 = 1.31\cdot 10^{-16} m^3 \tag{4.19}$$

Utilizing the PG data, v_{cav} from Eq. (4.19) can be substituted in Eq. (4.16), utilizing the slope of the PG curve reported in Table 4-2, to solve for $\dot{n}_{cav}$ as follows:

$$\dot{n}_{cav} = \frac{\frac{J_{LTR,NA}}{C_b}}{v_{cav}} = \frac{PG\ slope}{v_{cav}} = \frac{\dot{n}_{cav} \cdot v_{cav}}{v_{cav}} = \frac{5.1 \cdot 10^{-7}\ m/s}{1.31 \cdot 10^{-16}\ m^3} microjets = 3.9 \cdot 10^{9} \frac{microjets}{m^2 \cdot s} \quad (20)$$

Our group has previously reported that typical LTR areas formed at 20 kHz during a 10 minute treatment at an US intensity of 7.5 W/cm^2 are $10-40\ mm^2$ (for a sample having a total area of 177 mm^2, such as the one considered here).[9] Accordingly, the data suggests there are on the order of 10^7 cavitation bubble collapses into LTRs during a typical 10-minute ultrasound treatment at the conditions examined here.

Next, the remaining two unknown variables are considered, $K_{H,OG}$ and $K_{H,SLS}$, the equilibrium adsorption coefficients for OG and SLS, respectively. Substituting the slopes of the OG and SLS curves below their cmc (see Table 4-2), in addition to A_{cav} from Eq. (4.18) and the values of v_{cav} and $\dot{n}_{cav}$ calculated in Eqs. (4.19) and (4.20), respectively, in the expression for the expected slope for amphiphilic permeants below the cmc, $\dot{n}_{cav}\left(v_{cav} + A_{cav}K_H\right)$, yields:

For OG: $$7.3 \cdot 10^{-7}\ m/s = 3.9 \cdot 10^{9} \frac{microjets}{m^2 \cdot s}\left[1.3 \cdot 10^{-16} m^3 + 4\pi\left(3.15 \cdot 10^{-6} m\right)^2 \cdot K_{H,OG}\right] \quad (4.21)$$

For SLS: $$1.9 \cdot 10^{-6}\ m/s = 3.9 \cdot 10^{9} \frac{microjets}{m^2 \cdot s}\left[1.3 \cdot 10^{-16} m^3 + 4\pi\left(3.15 \cdot 10^{-6} m\right)^2 \cdot K_{H,OG}\right] \quad (4.22)$$

Solving Eqs. (4.21) and (4.22) results in values of $K_{H,OG} = 4.6 \cdot 10^{-7} m$ and $K_{H,SLS} = 2.9 \cdot 10^{-6} m$. Because OG has not been studied as widely as SLS, typical $K_{H,OG}$ values for the adsorption of OG onto a static, planar air/water interface could not be found in the literature. Therefore, to verify that this data is reasonable, the $K_{H,SLS}$ values deduced from the experiments will be compared to reported literature values of the equilibrium SLS adsorption rate to a static, planar air/water interface, $K_{H,SLS}^{\exp}$. Typical values for $K_{H,SLS}^{\exp}$ are reported to be between $1.1 - 1.5 \cdot 10^{-6} m$.[18] Therefore, it is found that the $K_{H,SLS}$ value deduced from the experimental data is slightly larger than the previously reported values corresponding to adsorption to a stagnant, planar interface. Recognizing that the calculation of $K_{H,SLS}$ made use of several assumptions, the estimated value of $K_{H,SLS} = 2.9 \cdot 10^{-6} m$ is generally consistent with the reported literature values. For example, if the average cavitation bubble radius was one half of the values assumed here (3.15 μm), that is if R_{cav}=1.6 μm, then the estimated $K_{H,SLS}$ value would be $1.5 \cdot 10^{-6} m$ and fully consistent with the range of $K_{H,SLS}^{\exp}$ values reported in the literature. In fact, it is reasonable that the cavitation bubbles present in the system may be smaller than those previously reported in [22] because the distance from the ultrasound transducer at which the reported bubble diameters were measured was 30 mm. On the other hand, in these experiments, the distance between the ultrasound transducer and the skin surface is only 3 mm. Accordingly, cavitation bubbles in the system have less time to grow by rectified diffusion and should possess smaller radii. Moreover, the fact that the $K_{H,SLS}$ value found here is in general agreement with the $K_{H,SLS}^{\exp}$ literature values is also consistent with the reported observation that the kinetics of SLS adsorption onto an air/water interface is adsorption-rate limited and not diffusion-rate

limited.[19] Therefore, the convective processes associated with the applied ultrasound field should not have a significant effect on the adsorption of SLS monomers onto the cavitation bubble surface.

4.4.3.4 Deviation of the Experimental Data from the Flux Model beyond a Threshold Concentration in the Case of Charged Amphiphiles (SLS)

As discussed in Section 4.4.3.2, for the charged, anionic amphiphile SLS, the expected LTR flux data deviates from that predicted by the flux model (at concentrations at and above 65 mM, see Figure 4-10). Because the observed deviation from the expected flux model prediction is only observed for the case of the ionic SLS, electrostatic effects are the probable cause for this deviation. In order to further rationalize the observed deviation, the assumptions in the flux model that may change due to electrostatic effects must be identified. Examination of Eq. (4.14) reveals that $\dot{n}_{cav}$ and v_{cav} are the only variables related to the cavitation field that appears in the slope of the flux equation for amphiphilic permeants above their cmc. It is important to stress, before proceeding any further, that in nearly all ultrasound experimental treatment protocols, including clinical uses of this technology,[25] the concentration of SLS used is 1 wt% (35 mM) or lower. Therefore, operating in the SLS concentration region where deviation from the expected flux model prediction is observed (>65 mM) is not typical.

Previous sonochemical studies have investigated the effect of amphiphiles, including SLS, on the activity and properties of acoustic cavitation bubbles.[23, 24, 26, 27] Some of these studies have even compared the effect of ionic and nonionic amphiphiles, revealing the importance of electrostatic effects.[26] Specifically, at low ionic concentrations (1-2 mM), without added salt,

charging the surface of a cavitation bubble with ionic amphiphiles can produce stabilization and repulsive effects between bubbles. This phenomenon was likely not observed in the experiments because experiments were only conducted at one data point in this range (1 mM). However, the presence of an electrolyte (either in the form of an added ionic amphiphile or through the addition of other salts) can result in electrostatic screening which can have the inverse effect. This phenomenon has been studied with SLS at 1 mM.[24] Specifically, it was found that with 1 mM SLS in water (Debye screening length ~ 10 nm, see Figure 4-11), electrostatic repulsions between negatively-charged cavitation bubbles were able to inhibit bubble coalescence. However, when 100 mM sodium chloride was added to the SLS solution, decreasing the Debye screening length to ~ 1 nm, the secondary Bjerknes (attractive) force was found to dominate. Therefore, the authors concluded that at high ionic concentrations, Bjerknes (attractive) forces dominate, which may allow for bubble coalescence to take place.[24] In this system, no salt is added. Therefore, the only mechanism leading to a decrease in the Debye screening length, and an associated shift in bubble coalescence, is the addition of more negatively-charged SLS to the coupling solution. The Debye screening length, κ^{-1}, is defined as follows: [8]

$$\kappa^{-1} = \left[\left(\frac{e_0^2}{\varepsilon k_B T} \right) \sum_i z_i^2 n_{i\infty} \right]^{-\frac{1}{2}} \tag{4.24}$$

where e_0 is the electronic charge ($1.6 \cdot 10^{-19} C$), $\varepsilon = \varepsilon_0 \varepsilon_r$ is the dielectric permittivity of the medium ($\varepsilon_0 = 8.85 \cdot 10^{-12} \frac{C^2}{J \cdot m}$; for water, $\varepsilon_r = 78.54$), k_B is the Boltzmann constant ($1.38 \cdot 10^{-23} J/K$), T is the absolute temperature, z_i is the valence of species *i*, $n_{i\infty}$ is the bulk concentration of species *i*, and *i* indicates that the summation is over all ionic species. Note that

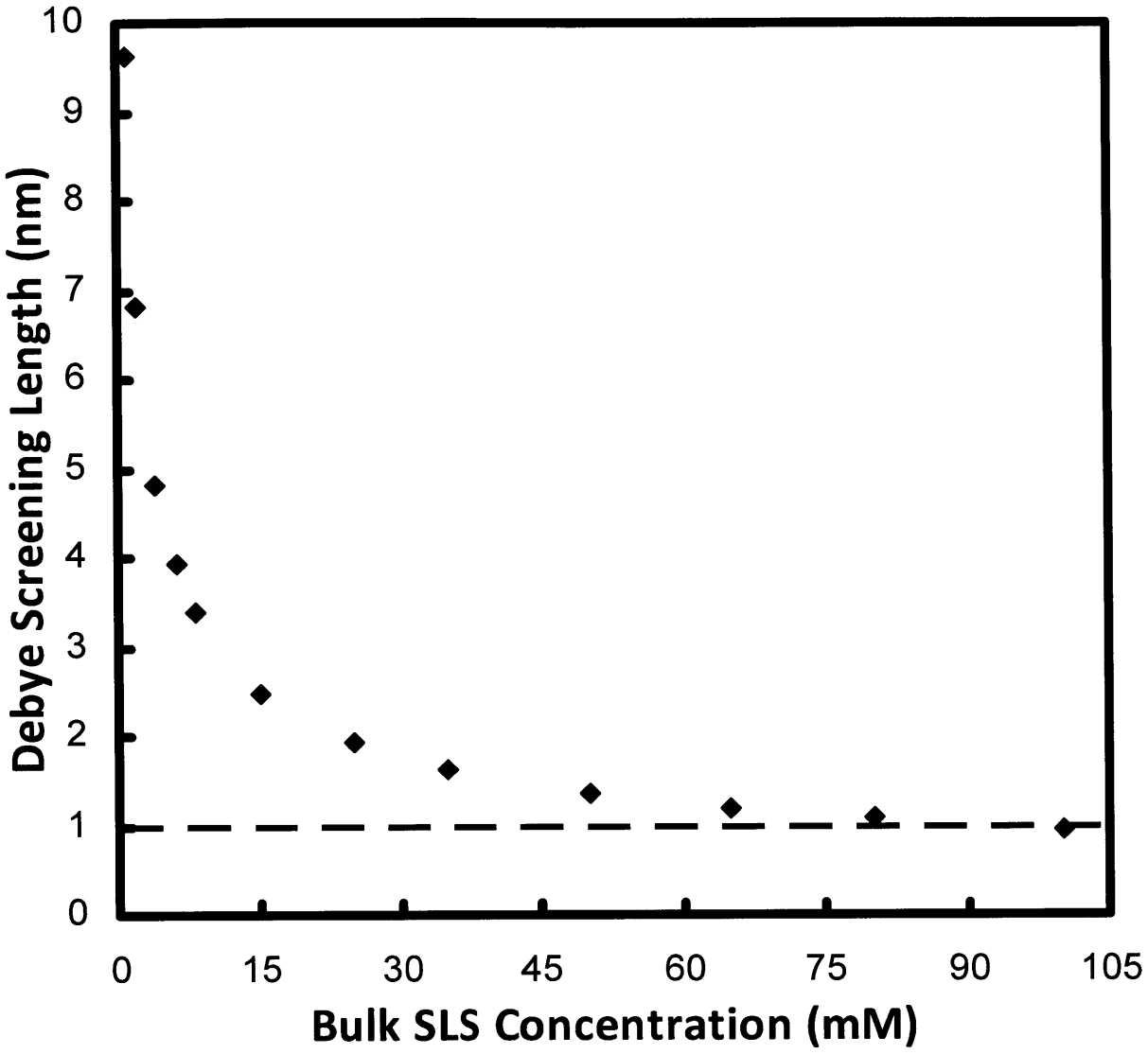

Figure 4-11. Debye screening length as a function of SLS concentration, assuming complete dissociation. The dashed, horizontal line corresponds to a value of 1 nm.

κ^{-1} is a property of the solution and is independent of the properties of the cavitation bubbles present in the solution.

Assuming complete dissociation of SLS, Figure 4-11 shows the dependence of κ^{-1} on bulk SLS concentration. Figure 4-11 shows that a value of κ^{-1}=1 nm is only approached at bulk SLS concentrations which are equal to or exceed 65 mM, corresponding to the threshold SLS concentration beyond which the flux model prediction begins to deviate from the experimental flux data (see Figure 4-10). Therefore, it is plausible that the cavitation-related parameters, $\dot{n}_{cav}$ and v_{cav}, which were assumed to be constant in the flux model may begin to change at SLS concentrations above this threshold due to increased bubble coalescence. One possible explanation could be that increased coalescence of cavitation bubbles in the bulk solution may lead to instability and collapse of the cavitation bubbles prior to reaching the skin surface. In that case, the efficiency of bubble transfer to the skin surface may be decreased, thereby decreasing the number of cavitation bubbles collapsing at the skin surface. Such a process would result in a decrease in the flux of SLS into the skin (lower $\dot{n}_{cav}$), as reflected in the flux data beyond concentrations of 65 mM (see Figure 4-10).

4.5 Conclusions

In this study, a physical mechanism that explains how LFS increases the transdermal uptake of CPEs is presented. Specifically, the findings suggest that the origin of the observed synergism between LFS and CPEs is the ability of LFS to increase the penetration and dispersion of CPEs by direct deposition of permeants into the LTRs of LFS-treated skin through the collapse of

acoustic cavitation microjets. Moreover, amphiphilic permeants exhibit even greater synergism with LFS than non-amphiphilic permeants because their flux into the skin is further enhanced by the adsorption of amphiphilic monomers to the surface of the cavitation bubbles. Therefore, in addition to a convective flux induced by the collapse of acoustic cavitation microjets that drives all CPEs, amphiphilic CPEs adsorbed to cavitation bubbles are also directly deposited into the skin. More modest increases in the uptake of CPEs into the non-LTRs of LFS-treated skin, relative to untreated skin, were also observed (as predicted recently[16]) and are consistent with the prediction of the flux model.

The elucidation of the mechanism of deposition of amphiphilic CPEs into LFS-treated skin may help to explain other interesting phenomena reported in the literature. For example, in some cases, extreme synergism or antagonism in skin permeability enhancement has been reported between LFS and binary mixtures of surfactants.[4] In the context of the findings here, synergism in these cases may be due to more efficient adsorption or packing of multiple surfactants on the surface of cavitation bubbles, while antagonism may be a result of decreased adsorption onto cavitation bubbles. Moreover, these trends may depend on the monomer concentration of each amphiphile in solution, since it was shown that only monomers can adsorb to the surface of cavitation bubbles. Therefore, a dramatic decrease in the cmc of binary surfactant mixtures may lead to antagonism between the surfactants comprising the mixtures, while an increase in the cmc may explain an even stronger synergism with LFS. Accordingly, an exciting area of future research may involve testing the flux of binary surfactant mixtures into the LTRs of LFS-treated skin. Additional areas of experimentation that may also be of interest

include further testing of charged surfactants, including cationic or zwitterionic surfactants, to further confirm the trends observed here with SLS (anionic) and OG (nonionic).

In Chapter 5, the mechanistic investigation into the synergism between LFS and CPEs presented in this chapter will be utilized to study this synergism from a different perspective. Specifically, the next chapter will discuss the effect of LFS/CPE synergism in terms of its effect on skin structural perturbation, including how the addition of a CPE to the LFS coupling medium induces changes in structural parameters associated with the skin.

4.6 References

[1] B.E. Polat, D. Blankschtein, R. Langer, Low-frequency sonophoresis: application to the transdermal delivery of macromolecules and hydrophilic drugs. Expert Opin Drug Del 7(12) (2010) 1415-1432.

[2] B.E. Polat, D. Hart, R. Langer, D. Blankschtein, Ultrasound-mediated transdermal drug delivery: Mechanisms, scope, and emerging trends. J Control Release doi:10.1016/j.jconrel.2011.01.006 (in press) (2011).

[3] S. Mitragotri, D. Ray, J. Farrell, H. Tang, B. Yu, J. Kost, D. Blankschtein, R. Langer, Synergistic effect of low-frequency ultrasound and sodium lauryl sulfate on transdermal transport. J Pharm Sci 89(7) (2000) 892-900.

[4] A. Tezel, A. Sens, J. Tuchscherer, S. Mitragotri, Synergistic effect of low-frequency ultrasound and surfactants on skin permeability. J Pharm Sci 91(1) (2002) 91-100.

[5] S. Paliwal, G. Menon, S. Mitragotri, Low-frequency sonophoresis: ultrastructural basis for stratum corneum permeability assessed using quantum dots. J Invest Dermatol 126(5) (2006) 1095-1101.

[6] B.E. Polat, J.E. Seto, D. Blankschtein, R. Langer, Application of the aqueous porous pathway model to quantify the effect of sodium lauryl sulfate on ultrasound-induced skin structural perturbation. J Pharm Sci 100(4) (2011) 1387-1397.

[7] I. Lavon, N. Grossman, J. Kost, The nature of ultrasound-SLS synergism during enhanced transdermal transport. J Control Release 107(3) (2005) 484-494.

[8] P. Hiemenz, R. Rajagopalan, Principles of Colloid and Surface Chemistry, 3rd Edition, Marcel Dekker, Inc., New York, 1997, pp. 327-330.

[9] J. Kushner, D. Blankschtein, R. Langer, Experimental demonstration of the existence of highly permeable localized transport regions in low-frequency sonophoresis. J Pharm Sci 93(11) (2004) 2733-2745.

[10] J. Kushner, D. Blankschtein, R. Langer, Evaluation of the porosity, the tortuosity, and the hindrance factor for the transdermal delivery of hydrophilic permeants in the context of the aqueous pore pathway hypothesis using dual-radiolabeled permeability experiments. J Pharm Sci 96(12) (2007) 3263-3282.

[11] J. Kushner, D. Blankschtein, R. Langer, Evaluation of hydrophilic permeant transport parameters in the localized and non-localized transport regions of skin treated simultaneously with low-frequency ultrasound and sodium lauryl sulfate. J Pharm Sci 97(2) (2008) 906-918.

[12] J. Kushner, D. Kim, P. So, D. Blankschtein, R. Langer, Dual-channel two-photon microscopy study of transdermal transport in skin treated with low-frequency ultrasound and a chemical enhancer. J Invest Dermatol 127(12) (2007) 2832-2846.

[13] R.F.V. Lopez, J.E. Seto, D. Blankschtein, R. Langer, Enhancing the transdermal delivery of rigid nanoparticles using the simultaneous application of ultrasound and sodium lauryl sulfate. Biomaterials 32(3) (2011) 933-941.

[14] B.E. Polat, S. Lin, J.D. Mendenhall, B. VanVeller, R. Langer, D. Blankschtein, Experimental and Molecular Dynamics Investigation into the Amphiphilic Nature of Sulforhodamine B. J Phys Chem B 115(6) (2011) 1394-1402.

[15] J. Seto, B. Polat, R. Lopez, D. Blankschtein, R. Langer, Effects of ultrasound and sodium lauryl sulfate on the transdermal delivery of hydrophilic permeants: Comparative in vitro studies with full-thickness and split-thickness pig and human skin. J Control Release 145(1) (2010) 26-32.

[16] B.E. Polat, P.L. Figueroa, D. Blankschtein, R. Langer, Transport pathways and enhancement mechanisms within localized and non-localized transport regions in skin treated with low-frequency sonophoresis and sodium lauryl sulfate. J Pharm Sci 100(2) (2011) 512-529.

[17] B. Yim, H. Okuno, Y. Nagata, R. Nishimura, Y. Maeda, Sonolysis of surfactants in aqueous solutions: an accumulation of solute in the interfacial region of the cavitation bubbles. Ultrason Sonochem 9(4) (2002) 209-213.

[18] C.H. Chang, N.H.L. Wang, E.I. Franses, Adsorption dynamics of single and binary surfactants at the air/water interface. Colloid Surface 62(4) (1992) 321-332.

[19] C.-H. Chang, E.I. Franses, Adsorption dynamics of surfactants at the air/water interface: a critical review of mathematical models, data, and mechanisms. Colloid Surface A 100 (1995) 1-45.

[20] R.L. Kay, K.S. Lee, Micelle molecular parameters from surfactant ionic mobilities. J Phys Chem 90(21) (1986) 5266-5271.

[21] K. Kameyama, T. Takagi, Micellar properties of octylglucoside in aqueous solutions. J Colloid Interf Sci 137(1) (1990) 1-10.

[22] N. Tsochatzidis, P. Guiraud, A. Wilhelm, H. Delmas, Determination of velocity, size and concentration of ultrasonic cavitation bubbles by the phase-Doppler technique. Chem Eng Sci 56(5) (2001) 1831-1840.

[23] G.J. Price, M. Ashokkumar, F. Grieser, Sonoluminescence Emission from Aqueous Solutions of Organic Monomers. J Phys Chem B 107(50) (2003) 14124-14129.

[24] N. Segebarth, O. Eulaerts, J. Reisse, L.A. Crum, T.J. Matula, Correlation between Acoustic Cavitation Noise, Bubble Population, and Sonochemistry. J Phys Chem B 106(35) (2002) 9181-9190.

[25] S. Skarbek-Borowska, B.M. Becker, K. Lovgren, A. Bates, P.A. Minugh, Brief Focal Ultrasound With Topical Anesthetic Decreases the Pain of Intravenous Placement in Children. Pediatr Emerg Care 22(5) (2006) 339-345.

[26] M. Ashokkumar, M. Hodnett, B. Zeqiri, F. Grieser, G.J. Price, Acoustic Emission Spectra from 515 kHz Cavitation in Aqueous Solutions Containing Surface-Active Solutes. J Am Chem Soc 129(8) (2007) 2250-2258.

[27] G.J. Price, M. Ashokkumar, M. Hodnett, B. Zequiri, F. Grieser, Acoustic Emission from Cavitating Solutions Implications for the Mechanisms of Sonochemical Reactions. J Phys Chem B 109(38) (2005) 17799-17801.

Chapter 5

Application of the Aqueous Porous Pathway Model to Quantify the Effect of Sodium Lauryl Sulfate on Ultrasound-Induced Skin Structural Perturbation

5.1 Introduction

The study presented in Chapter 4 provides a better understanding of the mechanisms by which low-frequency ultrasound exhibits synergism with both amphiphilic and non-amphiphilic chemical penetration enhancers. Specifically, it was demonstrated that transient cavitation microjets collapsing on the skin surface are responsible for the observed large synergistic effect. However, the effect of these collapsing microjets on the skin structure is not fully understood. In this chapter, I expand upon the mechanistic insight gained in the previous chapter by studying the synergistic effect between low-frequency ultrasound and sodium lauryl sulfate (SLS) from the perspective of its effect on the skin structure.

Enhancement of skin permeability by the application of ultrasound is referred to as sonophoresis. Although the use of ultrasound for transdermal delivery of therapeutics dates back to the 1950s, extensive research in this area has only taken place in the past two decades.[1, 2] In the early years of sonophoresis research, therapeutic frequencies, ranging from 1-3 MHz, were most common.[3-5] However, a significant shift in the methodology and understanding of sonophoresis took place once the switch was made to low-frequency sonophoresis (LFS, utilizing frequencies in the range of 20 – 100 kHz), because it was possible to achieve even greater skin permeability enhancements compared to therapeutic frequencies.[6] Following this shift, research on the mechanisms of LFS showed conclusively that cavitation above the skin, in the aqueous coupling medium, is the primary mechanism of enhancement.[7, 8] Much of this initial mechanistic research involving LFS was done utilizing pure aqueous media, containing no chemical enhancers in the coupling solution.[6-9] However, another breakthrough in the field occurred when it was shown that combining LFS with a chemical enhancer, specifically a surfactant such as SLS, caused a synergistic effect, resulting in orders-of-magnitude improvements in skin permeability enhancement over the application of LFS alone.[10-14] Since that time, the synergistic effect between chemical enhancers (mainly SLS) and LFS has been well documented,[2, 10-12, 15] although the precise physical mechanisms responsible for the observed synergism are still not well understood. Nearly all previous studies on LFS/SLS synergism have focused primarily on the effect of a simultaneous SLS and LFS treatment in order to increase skin permeability to different solutes. Although the extent to which LFS/SLS enhances skin permeability, relative to LFS alone, is generally well understood, very little is known about how these synergistic enhancers affect the skin structure itself. To date, only a small number of publications have commented on the structural changes in skin treated with

LFS/SLS and LFS.[16-18] These studies provided useful microscopy-based insight into the structural changes that occur when LFS/SLS and LFS are applied to skin. In the present study, the aqueous porous pathway model (APPM) is implemented to probe changes in skin structural parameters and to draw quantitative conclusions about the role of SLS in inducing skin perturbation.

With the above in mind, it is clear that a quantitative study investigating the effect of LFS/SLS on skin structural parameters, compared to that of LFS alone, would provide significant insight on how adding SLS to the LFS coupling medium affects skin perturbation. Furthermore, because LFS/SLS combines both physical and chemical enhancement mechanisms, while LFS acts solely in a physical manner, it is likely that the mechanical properties of the skin model used may also play an important role in determining the extent of skin perturbation.[9, 19, 20] Specifically, pig full-thickness skin (FTS), which possesses a full dermal backing, may impart increased mechanical support to the skin in response to the physical perturbation induced by LFS, relative to pig split-thickness skin (STS, dermatomed to 700 μm thickness). In fact, Seto *et al.* have recently shown that when treating skin with LFS/SLS at 20 kHz, the thickness of the skin plays a significant role in determining the extent of skin perturbation in human skin models (250 μm STS, 700 μm STS, and FTS), while in pig skin models, skin thickness does not play a significant role (700 μm STS and FTS).[19] Moreover, the difference in LFS/SLS treatment times for pig and human 700 μm STS reported by Seto *et al.* led the authors to propose that intrinsic skin differences (e.g., dermal elastic fiber content) may explain the observed differences. In this study, I utilize an approach similar to the one used by Seto *et al.* to gauge overall skin perturbation. Specifically, APPM is utilized to calculate two skin structural

parameters: (i) log C, which is related to the average radius of the aqueous skin pores, and (ii) the porosity-to-tortuosity ratio (ε/τ). The structural parameters of skin treated with LFS/SLS and LFS are compared to that of untreated skin (for both FTS and STS), to better understand the effect of SLS on skin structural perturbation and transdermal pathways when utilized in combination with LFS. Furthermore, the reproducibility and predictability of the LFS/SLS and LFS treatments is explored by comparing: (i) the width of the 95% confidence intervals for the structural parameters calculated, (ii) the correlation coefficient observed between the permeability and the resistivity of skin samples (see Theory section), and (iii) the trends observed in treatment times for skin samples treated to different extents of skin electrical resistivity. Clearly, the reproducibility and predictability of skin permeability enhancement are essential for the successful clinical implementation of this technology.[21, 22]

With the above motivation and background in mind, it is important to stress that the study presented here is the first one to investigate the synergism between LFS and SLS in the context of quantifying skin structural perturbation, while utilizing a *fixed skin electrical resistivity protocol*. It is noteworthy that previous studies have focused primarily on fixed treatment time protocols (typically treating skin samples with LFS for 10 minutes in the presence and in the absence of SLS).[11, 12, 15] The present study differs from previous ones in that skin samples were treated with both LFS/SLS and LFS to attain a wide range of skin electrical resistivity levels, allowing treatment times to vary in order to reach those levels. This modification in the treatment protocol is significant, because treating skin samples with LFS for a fixed period of time does not ensure that the skin samples are perturbed to any significant extent. Indeed, skin permeability enhancement is usually modest under this type of treatment protocol, since LFS

application for 10 minutes results in just a 1.5-fold enhancement in skin electrical resistivity.[12] Note that this is a very small extent of skin electrical resistivity enhancement, considering that skin hydration itself can cause similar extents of enhancement during a 24-hour period.[12] Accordingly, in the present study, it was required that LFS be applied to attain greater enhancements in skin electrical resistivity, which allows us to better understand the effect of the purely physical enhancement mechanism associated with LFS, relative to the combined physical and chemical enhancement mechanisms associated with LFS/SLS.

Along the lines discussed above, the objectives of the present study are to explain: i) how the extent of skin perturbation differs between skin samples treated with LFS/SLS and LFS, in the context of the APPM, ii) how ε/τ ratios differ between skin samples treated with LFS/SLS and LFS, iii) how the amount of mechanical support (i.e., the thickness of the dermis in the skin model considered) affects the extent of skin perturbation in samples treated with LFS/SLS and LFS , and iv) how the reproducibility and predictability of skin permeability enhancement and treatment times of skin samples treated with LFS/SLS compares to those of skin samples treated solely with LFS. Addressing (i) – (iv) will help explain the role of SLS in inducing skin structural perturbation, including the role of SLS in enhancing transdermal transport.

5.2 Materials and Methods

5.2.1 Materials

Phosphate buffered saline tablets (PBS; 0.01 M phosphate, 0.137 M NaCl) and SLS were obtained from Sigma Chemical Company (St. Louis, MO). C_{14}-labeled sucrose (specific activity of 600 mCi/mmol) was obtained from American Radiolabeled Chemicals (St. Louis, MO).

Hionic-Fluor, a scintillation cocktail, was obtained from Perkin-Elmer (Waltham, MA). All chemicals were used as received. Deionized water from a Milli-Q water purification system (Millipore, Bedford, MA) was used for the preparation of all solutions.

5.2.2 Preparation and Pre-Treatment of Skin Samples by LFS/SLS

Previously published protocols were utilized for the storage and preparation of skin samples. [19, 20] This procedure has been approved by the MIT Committee on Animal Care. Briefly, skin was harvested from the back and flank of Female Yorkshire pigs, sectioned into 25-mm strips, and stored at -85 °C for up to 6 months. Before use in experiments, the skin was thawed for 1 hour in PBS and all excess hair and subcutaneous fat were removed. Full-thickness skin (FTS) samples were utilized without further preparation, while split-thickness skin (STS) samples were dermatomed to 700 μm thickness using an electric reciprocating dermatome (Zimmer Orthopedic Surgical Products, Dover, OH). The skin was then cut into 25 mm by 25 mm samples, for use in the 15-mm inner diameter diffusion cells (PermeGear, Hellertown, PA).

LFS/SLS and LFS pre-treatment of skin samples was carried out according to previously published methods.[12, 13, 17, 19, 20, 23] Skin treatment was carried out with a 20 kHz ultrasound horn (VCX 500, Sonics and Materials, Inc., Newtown, CT), under the following experimental conditions: intensity - 7.5 W/cm^2, duty cycle - 50% (5 s on, 5 s off), and tip displacement - 3 mm. Two different coupling media were utilized to treat the skin samples: i) 1% SLS in PBS solution (LFS/SLS treatment), and ii) PBS solution alone (LFS treatment). Samples were treated with LFS until they reached currents ranging from 5 μA (low level of LFS treatment) to 200 μA (high level of LFS treatment), in order to test a wide range of LFS-induced

skin perturbation (higher currents suggest higher levels of skin perturbation). Note that the range of skin currents used here is similar to previously reported ranges used with LFS.[19, 24] After each minute of LFS treatment, the coupling medium was changed in order to minimize thermal effects (maintain the temperature within 10 °C of room temperature), and the electrical current of the skin samples was measured to determine if a desirable skin current had been attained. Following LFS treatment, samples were rinsed thoroughly with PBS in order to remove all excess SLS from the skin surface, and the coupling medium was replaced with PBS prior to the sucrose permeability experiments.

5.2.3 Skin Electrical Resistivity Measurements

Skin electrical resistivity, R, has been shown to be an accurate and instantaneous indicator of the structural state of the skin.[9, 19, 25] Previously published methods[9, 23, 24] were followed to measure R and are summarized next. A signal generator (Hewlett-Packard, model HP 33120A) was used to generate an AC voltage at 100 mV and 10 Hz. The voltage was applied across the skin using two Ag/AgCl electrodes (In Vivo Metrics, Healdsburgh, CA). The skin electrical current was measured using a multimeter (Fluke Corporation, Model 189) and the skin electrical resistance was calculated using Ohm's Law. R was then calculated by subtracting the background resistance and then multiplying the resulting skin electrical resistance by the area of the skin sample. In order to ensure that the skin was intact prior to experimentation, the initial R value of a skin sample was required to be above 50 kOhm·cm^2.[26-28]

5.2.4 Calculating the Steady-State Sucrose Skin Permeability

Following the LFS/SLS or LFS treatments, the steady-state sucrose skin permeability was determined. Sucrose was chosen as a model hydrophilic permeant because it has previously been utilized in the context of the APPM to accurately describe skin perturbation with LFS/SLS through the measurement of aqueous pore radii and the calculation of ε/τ values.[19, 20] Before commencing the permeability experiments, skin samples were remounted into clean, dry diffusion cells, and filled with 12 mL of PBS in the receiver chamber. For both the LFS/SLS-treated and the LFS-treated skin samples, 2 mL of donor solution containing 0.3-5 μCi/mL of C_{14}-labeled sucrose was utilized. For the passive skin samples, 0.75-1.0 mL of donor solution containing 25-50 μCi/mL of C_{14}-labeled sucrose was utilized (note that a higher concentration is necessary because of the low permeability of the untreated skin samples, and therefore, a smaller donor volume is utilized to minimize the amount of radiolabeled chemicals used). The radiolabeled sucrose concentrations were chosen such that the level of radioactivity in the receiver chamber aliquots was significantly greater than the background radioactivity levels (approximately 10-fold greater). The receiver chambers were stirred magnetically at 400 rpm.

The diffusion cells were sampled every two hours, between 18 and 26 hours, in order to measure the steady-state sucrose permeability of the skin samples. Note that this time frame has previously been established as being appropriate for measuring the steady-state permeability of sucrose through porcine skin.[19, 20] For skin samples treated with LFS/SLS or LFS, 200-μL aliquots of the donor solutions and 400-μL aliquots of the receiver solutions were withdrawn at each time point, in addition to measuring R. For passive skin samples, 20-μL aliquots of the donor solutions and 500-μL aliquots of the receiver solutions were withdrawn at each time point.

Upon withdrawal of solution from the receiver chamber, an identical volume of PBS was added in order to keep the solution level constant. The concentration of sucrose in each sample was measured by adding 5 – 15 mL of scintillation cocktail to each sample and then analyzing the samples on a Tri-Carb 2810TR liquid scintillation counter (PerkinElmer, Waltham, MA).

The permeability of sucrose through the skin, P, was calculated at steady-state, infinite sink conditions using the following equation:[20]

$$P = \frac{V}{AC_d}\left(\frac{\Delta C}{\Delta t}\right) \tag{5.1}$$

where A is the area of skin available for permeation, V is the volume of PBS in the receiver chamber, C_d is the average sucrose concentration in the donor chamber over the sampling period, and $(\Delta C/\Delta t)$ is the rate of change of sucrose concentration in the receiver chamber (where replacement of the sampled aliquots by PBS is taken into account).

5.3 Theory

5.3.1 The Aqueous Porous Pathway Model

By assuming that a hydrophilic permeant, such as sucrose, follows a similar path through the skin as the current carrying ions (for PBS, the dominant ions are Na^+ and Cl^-), one can utilize the APPM to calculate meaningful structural parameters of the skin.[20] This model utilizes hindered-transport theory[29] in order to quantify the steric hindrance exerted by the finite radius of the skin pores on the fluxes of the aqueous permeant and the current carrying ions through the skin. The hindrance factors corresponding to both species are related solely to the radius of each

permeant and to the average radius of the aqueous skin pores, r_{pore}. Then, by equating the diffusion of the aqueous permeant, which is related to the skin permeability, P, and the diffusion of the current carrying ions, which is related to the skin electrical resistivity, R, one can determine a log C value (see Eq. (5.2) below), which is related to r_{pore} and the extent of skin structural perturbation.

The relation between skin permeability, P, and skin electrical resistivity, R, in the context of the APPM, is given by:[20]

$$\log P = \log C - \log R \tag{5.2}$$

where C is defined as follows:

$$C = \frac{kT}{2z^2 F c_{ion} e_0} \cdot \frac{D_p^{\infty} H(\lambda_p)}{D_{ion}^{\infty} H(\lambda_{ion})} \tag{5.3}$$

where z is the electrolyte valence, F is Faraday's constant, c_{ion} is the electrolyte molar concentration, e_0 is the electronic charge, k is the Boltzmann constant, T is the absolute temperature, D_i^{∞} is the infinite-dilution diffusion coefficient of solute i, $H(\lambda_i)$ is the hindrance factor for solute i, and λ_i is defined as the ratio of the radius of solute i, r_i, to the radius of the aqueous skin pores, r_{pore}.[13] The most up-to-date expression for $H(\lambda_i)$, which is valid for $\lambda_i \leq 0.95$, is given by:[14, 19, 29]

$$H(\lambda_i) = 1 + \frac{9}{8}\lambda_i \ln \lambda_i - 1.56034\lambda_i + 0.528155\lambda_i^2 + 1.91521\lambda_i^3 \tag{5.4}$$

$$-2.81903\lambda_i^4 + 0.270788\lambda_i^5 + 1.10115\lambda_i^6 - 0.435933\lambda_i^7$$

It is important to note that the only variable in (5.3) that depends on the intrinsic properties of the skin is r_{pore} (which appears through λ_p and λ_{ion}). All the other variables are either constants or are properties of the permeants used. Therefore, once an experimental C value is determined using Eq. (5.2), r_{pore} can be determined by iteratively solving Eq. (5.3) until it converges.

Before applying the APPM to an experimental data set, it is first necessary to determine whether the model is applicable. To this end, a linear regression is fit to each set of log P versus log R data sets, and only if a 95% confidence interval on the slope of the regression includes the theoretical value of -1 (see Eq. (5.2)) and the linear regression is found to be statistically significant, is the model assumed to be valid. For a more detailed discussion on the applicability of the APPM, see Seto *et. al.*[19] After confirming that the data set can be described by the APPM, a log C value is determined using Eq. (5.2) for each data point contained within the data set. Subsequently, all the individual log C values are averaged to yield the log C value corresponding to that data set. The average log C value can then be utilized to calculate r_{pore} and to assess the structural perturbation of the skin.

It is important to stress that, for any aqueous permeant utilized (with given hydrodynamic radius), only a certain range of r_{pore} values can be determined. In fact, for any permeant, there will be an upper bound on the value of r_{pore} that can be probed depending on the hydrodynamic radius of the permeant (the hydrodynamic radius of sucrose is estimated to be 5.5 Å[20]). This follows, because as the pores become increasingly large, the amount of hindrance exerted by the pores on the diffusing permeants becomes increasingly small as the hindrance factor approaches unity. Recall that hindrance factors range from 0 to 1, where a hindrance factor of 1 corresponds

to no hindrance, and a hindrance factor of 0 corresponds to infinite hindrance. Beyond a certain r_{pore} value, the hindrance exerted by the pores on the permeant becomes statistically indistinguishable from the diffusion of the permeant at infinite dilution, which corresponds to the upper bound of r_{pore} (calculated from the corresponding upper bound on log C) that can be probed with that permeant. This infinite-dilution limit (or infinite-pore limit) will be attained at lower r_{pore} values for smaller permeants and will be higher for larger permeants. The infinite-pore limit for sucrose has been previously established to be ~120 Å (based on Eq. (5.4)).[19, 20] Therefore, for pore radii which are larger than the upper bound for sucrose, log C values can still be used to compare relative skin perturbations of different skin samples.

In addition to calculating log C and r_{pore} values in the context of the APPM, this model can also be used to compute the porosity-to-tortuosity ratio (ε/τ) of the skin samples. This allows us to gain deeper insight into the transdermal pathways present within the skin, by understanding the importance of the area of skin pores present on the skin surface (reflected in ε) relative to the length of the aqueous pathways present in the skin (reflected in τ). Specifically, ε/τ is given by the following expression:[20]

$$\left(\frac{\varepsilon}{\tau}\right)=\frac{1}{\left(\frac{R}{\Delta x}\right)\sigma_{sol}H\left(\lambda_{ion}\right)} \tag{5.5}$$

where σ_{sol} is the electrical conductivity of PBS (0.012 $\Omega^{-1}\text{cm}^{-1}$),[20] $H\left(\lambda_{ion}\right)$ is the hindrance factor for an ion calculated using Eq. (5.4), and Δx is the thickness of the skin layer that provides the primary barrier to transport, which is assumed to be the thickness of the stratum corneum (13.1 μm).[13, 30]

5.4 Results

5.4.1 Analysis of the Experimental Data in the Context of the Aqueous Porous Pathway Model

In order to verify that the APPM is valid over the range of R values attained using the LFS/SLS and LFS skin treatments, it was determined if the regressed slopes are not significantly different from the theoretical value of -1 (see Eq. (5.2)). The log P-log R plots generated for this analysis are reported in Figure 5-1, with the resulting linear regression parameters listed in Table 5-1. Note that a subset of the LFS/SLS data has been published in [19]. Table 5-1 shows that the 95% confidence intervals on the slopes of all 6 sample sets tested include the theoretical value of -1, thus validating use of the model.[1] After establishing the applicability of the APPM, the skin structural parameters are calculated to assess the effect of SLS on skin perturbation, when utilized simultaneously with LFS.

5.4.2 Evaluation of Skin Perturbation through a Comparison of Log C Values

To assess the overall skin perturbation of the two LFS/SLS-treated and two LFS-treated skin models, an analysis-of-variance (ANOVA) test was performed on all the log C values corresponding to the four sample groups tested (see Table 5-2). The ANOVA test yielded

[1] Note that for the passive skin samples (samples with no LFS/SLS or LFS treatments), there is greater uncertainty in the slope of the data, as reflected in the large range for the 95% confidence intervals for these two data sets (1.48 and 0.87, respectively). This is expected, because the passive skin samples have very similar electrical resistivities due to the inherent barrier properties of the skin, and because it is required that the skin samples have a certain initial electrical resistivity to ensure their integrity. Therefore, any natural variation in skin permeability, or in skin pore radius distribution, will result in relatively large deviations from expected values and cause greater uncertainty in the regressed values.

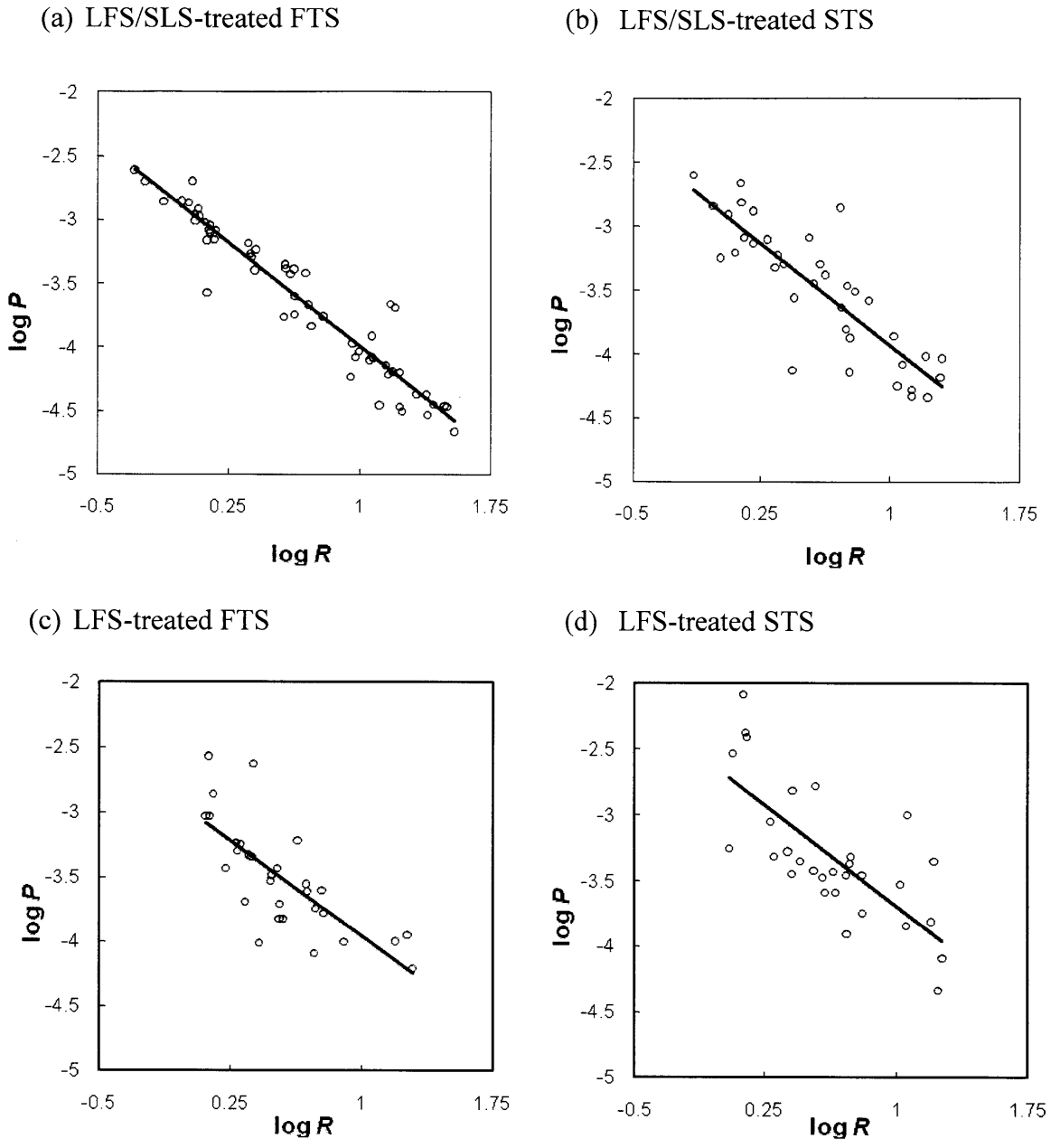

Figure 5-1. Log *P*-log *R* plots for LFS/SLS-treated and LFS-treated skin samples. The solid line on each plot corresponds to the linear regression fitted to each data set. The regression parameters are listed in Table 5-1.

Table 5-1. Model validation for the skin treatments and skin thicknesses tested.

Treatment	Thickness	n	Linear Regression Parameters	
			Slope[a]	r^2
LFS/SLS	FTS	58	-1.08 ± 0.09	0.92
LFS/SLS	STS	37	-1.07 ± 0.22	0.73
LFS	FTS	30	-0.98 ± 0.33	0.57
LFS	STS	30	-1.02 ± 0.37	0.53
None	FTS	8	-1.01 ± 1.48	0.32
None	STS	11	-1.80 ± 0.87	0.71

[a] Range corresponds to a 95% confidence interval.

$P<0.0001$ (note that, at 95% confidence, P must be below 0.05 to reject the null hypothesis that all the sample groups tested have the same population mean), indicating that one or more of the four sample groups do not contain the same population mean. Additional analysis showed that there is no statistical difference in the log C values of the two LFS/SLS-treated skin models (FTS and STS), while there is significant statistical difference between FTS and STS treated solely with LFS ($P<0.0001$). Next, an ANOVA test was performed on the LFS/SLS-treated FTS and STS models, along with the LFS-treated FTS model, and no statistical difference in the log C values of these three skin models was observed. Pairwise t-tests assuming unequal variances between the log C values of all the four skin models confirmed that the LFS-treated STS model exhibits a significantly different extent of skin perturbation compared to the other three skin models tested, while none of the other three skin models tested are statistically different from each other.

As a reference point, log C values for untreated FTS and STS were also determined, and the two LFS/SLS-treated and two LFS-treated skin models were found to have significantly different log C values than the untreated skin samples (pairwise t-tests at 95% confidence). Furthermore, a comparison of untreated FTS and untreated STS showed no statistical difference in their log C values. Utilizing Eqs. (5.3) and (5.4), the average aqueous pore radius of untreated FTS was found to be 16.4 Å (95% confidence interval of [13.6 Å, 21.8 Å]), and that of STS was found to be 16.6 Å (95% confidence interval of [14.2 Å, 20.5 Å]). Note that because the log C values for the LFS/SLS-treated and LFS-treated skin samples were above the infinite-pore limit, suggesting that the skin is exerting no hindrance or negative hindrance on the diffusing permeants, it is therefore not valid to utilize the APPM to calculate average pore radius values. Therefore, only

Table 5-2. Structural parameter values for FTS and STS samples treated with LFS/SLS and LFS.

Treatment	Thickness	n	log C [a,b]	$\varepsilon/\tau \cdot 10^6$ [a]
LFS/SLS	FTS	58	-2.96 ± 0.05	45.6 ± 12.7
LFS/SLS	STS	37	-2.90 ± 0.09	45.6 ± 13.3
LFS	FTS	30	-2.96 ± 0.10	42.0 ± 9.06
LFS	STS	30	-2.68 ± 0.13	36.1 ± 10.9
None	FTS	8	-3.35 ± 0.15	2.07 ± 0.50
None	STS	11	-3.34 ± 0.11	2.81 ± 0.40

[a] Range corresponds to a 95% confidence interval.

[b] log C is equivalent to the y-intercept of a linear regression of log P vs. log R with a slope equal to -1.

log C values were used to compare the extent of skin structural perturbation of these skin models, as the validity of the APPM is in question for these data sets. However, it is still valid utilize log C values to compare the extent of skin perturbation with different skin treatments, as previously reported in the literature.[19]

5.4.3 Evaluation of the Skin Structural Parameter, ε/τ

ε/τ values were calculated using Eq. (5.5) for the two LFS/SLS-treated and two LFS-treated skin samples, as well as for untreated FTS and STS. These results are reported in Table 5-2. The ε/τ values of both LFS/SLS-treated FTS and STS are identical, while the ε/τ values of the LFS-treated FTS and STS groups are lower, and generally decrease with decreasing skin thickness. There is no statistical difference between the ε/τ values of untreated FTS and STS. On average, ε/τ was found to increase approximately 20-fold between untreated skin samples and samples that were treated with LFS/SLS or LFS, suggesting an increase in the number of pores on the skin (reflected in a larger ε value) or the creation of more direct (less tortuous) paths through the skin (reflected in a smaller τ value) following treatment of the skin.

5.4.4 Treatment Time Required to Reach Specific Skin Electrical Resistivity Levels

In order to assess reproducibility and predictability of the LFS/SLS and LFS treatment regimens, in addition to the regression analyses (r^2 values and 95% confidence intervals) reported in Tables 5-1 and 5-2, treatment times were compared for each of the two treatment conditions (with and

Table 5-3. Skin treatment times associated with three levels of skin electrical resistivity,[a] for FTS and STS models treated with LFS/SLS and LFS.

		1.5 ± 0.6 kΩ·cm^2		4.0 ± 1.6 kΩ·cm^2		10.0 ± 4.0 kΩ·cm^2	
Treatment	Thickness	n	time (min)[b]	n	time (min)[b]	n	time (min)[b]
LFS/SLS	FTS	15	2.4 ± 0.4	11	2.0 ± 0.9	12	1.4 ± 0.6
LFS/SLS	STS	11	2.8 ± 1.2	10	1.8 ± 0.8	9	1.2 ± 0.4
LFS	FTS	10	14.0 ± 3.9	14	22.1 ± 5.3	4	16.5 ± 5.7
LFS	STS	8	13.1 ± 4.1	14	12.2 ± 4.7	6	6.4 ± 3.3

[a] These three ranges of R values were chosen in order to make useful statistical comparisons between the treatment times.

[b] Range corresponds to a 95% confidence interval.

without SLS) at three separate skin perturbation levels (as quantified by R values of 1.5, 4.0, and 10.0 $k\Omega \cdot cm^2 \pm 40\%$). Note that a smaller skin electrical resistivity value corresponds to a greater extent of skin perturbation (less resistance of the skin membrane). This data is reported in Table 5-3. For LFS/SLS-treated skin samples, treatment times increased monotonically with decreasing skin electrical resistivity. In addition, treatment times were not significantly different between FTS and STS samples at each of the skin electrical resistivities considered. On the other hand, the treatment times for skin samples treated solely with LFS did not behave in a straightforward manner, and took 5-fold to 12-fold longer to reach skin electrical resistivity levels similar to those of skin samples treated with LFS/SLS. In addition, no statistically significant difference was found between the treatment times required to reach any of the three skin electrical resistivities considered in the case of LFS-treated FTS.

5.5 Discussion

5.5.1 Effect of SLS on the Structural Perturbation of LFS-Treated Skin

The primary criterion that was used to quantify skin perturbation utilizes the effective radii of the hydrophilic diffusive pathways in the skin models tested, which scale directly with log C in the context of the APPM (see Eqs. (5.2) – (5.4)). A less negative log C value indicates an increase in the pore radius, suggesting increased perturbation of the skin samples by the treatment administered. The main objective was to compare the results for skin samples treated with LFS/SLS with those for skin samples treated only with LFS, in order to understand the effect of SLS on skin perturbation when used simultaneously with LFS. In addition, in order to test the effect of the skin mechanical support on skin perturbation, for the two skin treatments used (LFS/SLS and LFS), both FTS (typical thickness of 1.5-1.8 mm) and STS (thickness of 0.70

mm) models were tested. It is important to recognize that both the FTS and STS models are equivalent, in the context of the APPM, prior to treatment, as clearly reflected in their: (i) nearly identical log C values (see Table 5-2, corresponding to pore radii of 16.4 Å and 16.6 Å, respectively), and (ii) their statistically similar values of ε/τ (see Table 5-2). Therefore, any observed increases in log C or ε/τ in the treated skin samples can be attributed solely to the LFS/SLS or LFS treatments applied to those skin samples.

5.5.1.1 Comparison of the LFS/SLS-Treated FTS and STS Models

A comparison of the skin structural parameters of LFS/SLS-treated FTS and STS shows that: (i) their log C values are statistically similar (see Table 5-2), and (ii) their ε/τ values are essentially identical (see Table 5-2). Furthermore, Table 5-3 shows that the treatment times associated with the three levels of skin electrical resistivity for FTS and STS are statistically similar for the three skin electrical resistivities analyzed. This confirms that, irrespective of the skin thicknesses studied, skin perturbation induced by LFS/SLS is generated in a consistent and similar manner. In other words, the FTS and STS models are identical in terms of their response to the LFS/SLS treatment. This important conclusion is consistent with the recent findings by Seto *et al.*[19]

5.5.1.2 Comparison of log C Values for LFS/SLS-Treated and LFS-Treated Samples

For LFS-treated FTS, the extent of skin perturbation, as quantified by the log C values, is statistically similar to both LFS/SLS-treated FTS and LFS/SLS-treated STS. However, as Table 5-2 shows, the log C value corresponding to LFS-treated STS is significantly less negative than

those corresponding to the other three skin sample groups tested (pair-wise t-tests comparing LFS-treated STS to the other three sample groups yields $P \leq 0.006$). This interesting finding follows because: i) in the absence of SLS, skin samples must be treated for much longer time periods to reach similar skin electrical resistivity values (see Table 5-3), and ii) the thinner STS model does not respond to the physical enhancement mechanism (cavitation) associated with LFS in the same manner as the thicker FTS model. Simply stated, the stresses put on the thinner, less mechanically robust STS during the long LFS treatment induce significantly greater skin perturbation than that observed in: (i) the more mechanically robust FTS model, and (ii) the combined chemical/physical enhancement induced by the shorter LFS/SLS treatment. This finding also shows that, although the skin electrical resistivity is a good quantitative measure of skin perturbation, the extent to which it scales with skin permeability depends on both the skin model and skin treatment regimen used.

5.5.1.3 Comparison of ε/τ Values for LFS/SLS-Treated and LFS-Treated Samples

Table 5-2 shows that the ε/τ values for the LFS-treated samples decrease with decreasing skin thickness, and are generally lower than those corresponding to the LFS/SLS-treated samples. Although the observed differences are not statistically significant to 95% confidence, they are nevertheless interesting because they provide some insight into the role that SLS plays in perturbing the skin, when combined with LFS. More specifically, although the LFS/SLS-treated samples are subjected to 5- to 12-fold shorter treatments (see Table 5-3), these samples still have higher ε/τ values, suggesting that they are either more porous (larger ε value) and/or less tortuous (smaller τ value) than those treated only with LFS. It is not likely that an increase in ε

can explain the difference in ε/τ values for LFS/SLS-treated and LFS-treated skin samples. This is because previous studies have shown that the radius of impinging cavitation microjets and the overall number of cavitation events observed near the skin surface decreases in LFS/SLS-treated samples, with respect to samples treated solely with LFS.[11, 12] Since cavitation bubble collapse near the skin surface is the primary mechanism of new pore formation and permeability enhancement for skin treated with LFS/SLS and LFS, this would in fact suggest that the porosity of LFS-treated samples should be greater than the porosity of LFS/SLS-treated samples (which is further enhanced because LFS treatments are an order-of-magnitude longer than LFS/SLS treatments). Therefore, the most likely explanation for the observed increase in ε/τ in LFS/SLS-treated samples, with respect to LFS-treated samples, is the ability of SLS to fluidize/disorder lipid bilayers and expand lacunar regions, thereby creating less tortuous and more direct permeation pathways through the skin membrane. Note that this explanation is consistent with the findings of Paliwal *et al.*, who showed that, in LFS-treated skin, the number density of lacunar regions increases significantly with respect to those in untreated and LFS/SLS-treated skin (which suggests greater porosity).[18] In addition, Paliwal *et al.* showed that in LFS/SLS-treated skin, the number density of lacunar regions did not increase with respect to that in untreated skin, although the total area of the lacunar regions did increase. This suggests increased length and connectivity of the lacunar regions, which could be explained by an inter-connected three-dimensional network of pores (which suggests decreased tortuosity).[18] Accordingly, the ability of LFS and SLS to work in concert, in order to permeabilize skin in both a physical and chemical manner, leads to the observed higher ε/τ values for the LFS/SLS-treated samples, compared to the samples treated only with LFS.

5.5.2 Reproducibility and Predictability of Skin Perturbation in Samples Treated with LFS/SLS and LFS

Reproducibility and predictability of skin perturbation are important characteristics of any skin treatment regimen. Clinically, not all patients have skin with similar thickness, elasticity, or other biomechanical properties.[31, 32] Therefore, a robust skin treatment protocol is ideal. Consequently, examining the data presented in this study, it is not surprising that a combination of LFS/SLS is presently used in clinical applications of LFS (the company commercializing this technology is Echo Therapeutics, Franklin, MA).[21, 22]

An examination of the log *P*-log *R* plots shown in Figure 5-1 reveals much greater variability in the regression lines shown for samples treated solely with LFS (Figures 5-1(c) and 5-1(d)), compared to those treated with LFS/SLS (Figures 5-1(a) and 5-1(b)). This is also shown quantitatively in Tables 5-1 and 5-2, where the 95% confidence intervals for both the slope of the linear regression and the log *C* values are broader for the LFS-treated samples (0.33-0.37 and 0.10-0.13, respectively) compared to those for the LFS/SLS-treated samples (0.09-0.22 and 0.05-0.09, respectively). Similarly, the r^2 values for the linear regressions of the LFS-treated data (0.53-0.57) are smaller than those of the LFS/SLS-treated data (0.73-0.92), thus demonstrating that skin perturbation, and the resulting skin permeability enhancement, are less predictable for skin treated solely with LFS.

Another significant difference between the LFS/SLS-treated and LFS-treated samples is in the observed trends in treatment times (see Table 5-3). Specifically, samples treated with LFS/SLS take nearly an order-of-magnitude less time to reach similar skin electrical resistivities than LFS-

treated samples do. Note that the observed decrease in treatment time is consistent with the previous finding that the energy density threshold required to observe skin permeability enhancement in LFS/SLS-treated skin is an order-of-magnitude smaller than that for LFS-treated skin (note that energy density scales with treatment time).[11] In addition, LFS/SLS-treated samples behave in a more predictable manner, where: (i) treatment times decrease with increasing skin electrical resistivity, and (ii) the treatment times necessary to reach the various skin electrical resistivity levels considered are not significantly different for the FTS and STS samples. On the other hand, for FTS samples treated solely with LFS, treatment times show no statistically significant difference to reach the three skin electrical resistivity levels reported in Table 5-3 (an ANOVA analysis yielded a p-value of 0.172, which was confirmed by pairwise t-tests at 95% confidence), while the treatment times for LFS-treated STS samples decrease in a non-linear manner with increasing skin electrical resistivity levels. In addition, a comparison of treatment times for the LFS-treated FTS and STS samples reveals that, at the 1.5 $k\Omega \cdot cm^2$ skin electrical resistivity level, the treatment times are statistically similar, while they are statistically significantly different (95% confidence) at both the 4 and 10 $k\Omega \cdot cm^2$ levels. This again points to the lack of predictability and reproducibility of skin samples treated only with LFS, where some skin samples respond much more favorably to the LFS treatment than others. With all of the above in mind, it is quite clear that it is extremely advantageous to treat skin with a combination of LFS/SLS. Not only are the required treatments much shorter using LFS/SLS, but also the combined chemical and physical enhancement mechanisms involved in skin perturbation using LFS/SLS induce much more predictable trends in skin perturbation than those induced by the purely physical mechanism associated with LFS.

The most significant implications of these findings involve an improved mechanistic understanding of the combined effect of LFS and SLS on skin perturbation. Specifically, it was shown that, although not intuitive, the combination of both a chemical and physical skin penetration enhancer can, in fact, be less perturbing to the skin (based on log C values) than a physical skin penetration enhancer alone. Furthermore, the results show that the addition of SLS to the LFS coupling medium not only allows the delivery of permeants in an equivalent manner to LFS alone, but also induces less perturbation to the skin membrane in a much shorter, reproducible, and predictable manner. Clearly, the reduction in treatment time in the presence of SLS is a great advantage clinically, because it would require health personnel an order of magnitude more time to treat patients with LFS alone. Furthermore, the importance of decreased skin perturbation and shorter application time is very significant with respect to patient safety and compliance. Future research in this area should be aimed at identifying surfactants that can provide similar, or greater, levels of skin permeability enhancement when combined with LFS, than LFS/SLS, while inducing even less skin perturbation and irritation. To this end, *in vivo* studies on the irritancy potential of the LFS/surfactant treatment of skin should be considered.

5.6 Conclusions

In this study, the effect of SLS on skin perturbation was investigated, when utilized simultaneously with LFS, by treating two skin models, pig FTS and pig STS, with two treatment regimens, LFS/SLS and LFS, to reach a range of skin electrical resistivity levels. The LFS/SLS treatment was found to provide consistent extents of skin perturbation, as quantified using the log C and ε/τ values obtained. Skin samples treated solely with LFS yielded less consistent results, where the log C values of the FTS and STS skin models were statistically significantly

different. Additionally, the ε/τ values for LFS-treated skin samples were generally less than those for LFS/SLS-treated samples, suggesting that SLS acting on the skin creates more direct paths through the skin membrane by the disordering/fluidization of lipid bilayers, denaturation of keratin fibers, and expansion of lacunar regions. An analysis of the variability in the log P-log R linear regression parameters and log C values revealed greater variation in samples treated solely with LFS, resulting in lower r^2 values and broader confidence intervals for the regression parameters and log C values, with respect to LFS/SLS-treated samples. Additionally, the LFS-treated samples required 5-fold to 12-fold longer treatment times than the LFS/SLS-treated samples to reach similar skin electrical resistivity levels. Treatment times for the LFS/SLS-treated samples behaved predictably, decreasing monotonically with increasing skin electrical resistivity level, showing no significant difference in treatment times between FTS and STS samples at each of the skin electrical resistivity levels analyzed. On the other hand, LFS-treated samples were perturbed in a less predictable manner, with large variations and no statistical significance in treatment times between the skin electrical resistivity levels considered.

In summary, SLS has a generally positive impact on skin structural perturbation when utilized in combination with LFS, compared to LFS treatment alone, by: (i) requiring equal, or less, skin perturbation to reach similar skin electrical resistivity values (as reflected in the log C values), (ii) reaching similar skin electrical resistivity levels in much shorter treatment times (about an order-of-magnitude decrease in treatment times), and (iii) inducing skin perturbation in a significantly more reproducible and predictable manner.

5.7 References

[1] S. Mitragotri, in: T. Desai, S. Bhatia and M. Ferrari (Eds.), BioMEMS and Biomedical Nanotechnology. , Vol. 3, Springer, New York, 2006, pp. 223-236.

[2] S. Mitragotri, J. Kost, Low-frequency sonophoresis: a review. Adv Drug Deliv Rev 56(5) (2004) 589-601.

[3] M. Johnson, S. Mitragotri, A. Patel, D. Blankschtein, R. Langer, Synergistic effects of chemical enhancers and therapeutic ultrasound on transdermal drug delivery. J Pharm Sci 85(7) (1996) 670-679.

[4] D. Levy, J. Kost, Y. Meshulam, R. Langer, Effect of ultrasound on transdermal drug delivery to rats and guinea pigs. J Clin Invest 83(6) (1989) 2074.

[5] S. Mitragotri, D. Blankschtein, R. Langer, Ultrasound-mediated transdermal protein delivery. Science 269(5225) (1995) 850-853.

[6] S. Mitragotri, D. Blankschtein, R. Langer, Transdermal drug delivery using low-frequency sonophoresis. Pharm Res 13(3) (1996) 411-420.

[7] H. Tang, C. Wang, D. Blankschtein, R. Langer, An investigation of the role of cavitation in low-frequency ultrasound-mediated transdermal drug transport. Pharm Res 19(8) (2002) 1160-1169.

[8] A. Tezel, A. Sens, S. Mitragotri, Investigations of the role of cavitation in low-frequency sonophoresis using acoustic spectroscopy. J Pharm Sci 91(2) (2002) 444-453.

[9] H. Tang, D. Blankschtein, R. Langer, Effects of low-frequency ultrasound on the transdermal permeation of mannitol: comparative studies with in vivo and in vitro skin. J Pharm Sci 91(8) (2002) 1776-1794.

[10] S. Mitragotri, Synergistic effect of enhancers for transdermal drug delivery. Pharm Res 17(11) (2000) 1354-1359.

[11] S. Mitragotri, D. Ray, J. Farrell, H. Tang, B. Yu, J. Kost, D. Blankschtein, R. Langer, Synergistic effect of low-frequency ultrasound and sodium lauryl sulfate on transdermal transport. J Pharm Sci 89(7) (2000) 892-900.

[12] A. Tezel, A. Sens, J. Tuchscherer, S. Mitragotri, Synergistic effect of low-frequency ultrasound and surfactants on skin permeability. J Pharm Sci 91(1) (2002) 91-100.

[13] J. Kushner, D. Blankschtein, R. Langer, Experimental demonstration of the existence of highly permeable localized transport regions in low-frequency sonophoresis. J Pharm Sci 93(11) (2004) 2733-2745.

[14] B.E. Polat, P.L. Figueroa, D. Blankschtein, R. Langer, Transport pathways and enhancement mechanisms within localized and non-localized transport regions in skin treated with low-frequency sonophoresis and sodium lauryl sulfate. J Pharm Sci 100(2) (2011) 512-529.

[15] I. Lavon, N. Grossman, J. Kost, The nature of ultrasound-SLS synergism during enhanced transdermal transport. J Control Release 107(3) (2005) 484-494.

[16] A. Dahlan, H. Alpar, P. Stickings, D. Sesardic, S. Murdan, Transcutaneous immunisation assisted by low-frequency ultrasound. Int J Pharm 368(1-2) (2009) 123-128.

[17] J. Kushner, D. Kim, P. So, D. Blankschtein, R. Langer, Dual-channel two-photon microscopy study of transdermal transport in skin treated with low-frequency ultrasound and a chemical enhancer. J Invest Dermatol 127(12) (2007) 2832-2846.

[18] S. Paliwal, G. Menon, S. Mitragotri, Low-frequency sonophoresis: ultrastructural basis for stratum corneum permeability assessed using quantum dots. J Invest Dermatol 126(5) (2006) 1095-1101.

[19] J. Seto, B. Polat, R. Lopez, D. Blankschtein, R. Langer, Effects of ultrasound and sodium lauryl sulfate on the transdermal delivery of hydrophilic permeants: Comparative in vitro studies with full-thickness and split-thickness pig and human skin. J Control Release 145(1) (2010) 26-32.

[20] H. Tang, S. Mitragotri, D. Blankschtein, R. Langer, Theoretical description of transdermal transport of hydrophilic permeants: application to low-frequency sonophoresis. J Pharm Sci 90(5) (2001) 545-568.

[21] B. Becker, S. Helfrich, E. Baker, K. Lovgren, P. Minugh, J. Machan, Ultrasound with topical anesthetic rapidly decreases pain of intravenous cannulation. Acad Emerg Med 12(4) (2005) 289-295.

[22] A. Farinha, S. Kellogg, K. Dickinson, T. Davison, Skin impedance reduction for electrophysiology measurements using ultrasonic skin permeation: initial report and comparison to current methods. Biomed Instrum Techn 40(1) (2006) 72-77.

[23] J. Kushner, D. Blankschtein, R. Langer, Evaluation of hydrophilic permeant transport parameters in the localized and non-localized transport regions of skin treated simultaneously with low-frequency ultrasound and sodium lauryl sulfate. J Pharm Sci 97(2) (2008) 906-918.

[24] J. Kushner, D. Blankschtein, R. Langer, Evaluation of the porosity, the tortuosity, and the hindrance factor for the transdermal delivery of hydrophilic permeants in the context of the aqueous pore pathway hypothesis using dual-radiolabeled permeability experiments. J Pharm Sci 96(12) (2007) 3263-3282.

[25] P. Karande, A. Jain, S. Mitragotri, Relationships between skin's electrical impedance and permeability in the presence of chemical enhancers. J Control Release 110(2) (2006) 307-313.

[26] G. Kasting, L. Bowman, Dc Electrical-Properties of Frozen, Excised Human Skin. Pharm Res 7(2) (1990) 134-143.

[27] G. Kasting, L. Bowman, Electrical Analysis of Fresh, Excised Human Skin - a Comparison with Frozen Skin. Pharm Res 7(11) (1990) 1141-1146.

[28] J. Rosell, J. Colominas, P. Riu, R. Pallasareny, J. Webster, Skin Impedance from 1 Hz to 1 Mhz. IEEE T Bio-Med Eng 35(8) (1988) 649-651.

[29] P. Dechadilok, W. Deen, Hindrance factors for diffusion and convection in pores. Ind Eng Chem Res 45(21) (2006) 6953-6959.

[30] M. Johnson, D. Blankschtein, R. Langer, Evaluation of solute permeation through the stratum corneum: Lateral bilayer diffusion as the primary transport mechanism. J Pharm Sci 86(10) (1997) 1162-1172.

[31] A. Cua, K. Wilhelm, H. Maibach, Elastic properties of human skin: relation to age, sex, and anatomical region. Arch Dermatol Res 282(5) (1990) 283-288.

[32] C. Edwards, R. Marks, Evaluation of biomechanical properties of human skin. Clin Dermatol 13(4) (1995) 375-380.

Chapter 6

Thesis Summary, Evaluation of Low-Frequency Ultrasound-Mediated Transdermal Delivery, and Future Research Directions

6.1 Thesis Summary

The primary focus of this thesis has been to extend current knowledge on the role of cavitational and surfactant effects in skin permeability enhancement by low-frequency sonophoresis (LFS), especially with regards to elucidating previously unexplained phenomena such as heterogeneous transport and synergism between LFS and chemical penetration enhancers (CPEs). In Chapter 2, the permeation pathways within highly-perturbed regions of LFS-treated skin, localized transport regions (LTRs), and non-LTRs were investigated. This allowed me to identify the mechanisms of skin permeability enhancement in each skin region, and to demonstrate that cavitation microjet collapses within LTRs play a significant role in skin perturbation. Chapter 3 focused on

the effect of non-traditional surfactants when combined with LFS treatment. Specifically, it was found that even common dyes, which are typically assumed to be inert constituents of LFS coupling solutions, can have dramatic effects on bulk and interfacial solution properties due to their amphiphilic nature. These effects can also significantly affect skin perturbation caused by LFS treatment. Chapter 4 began the study into the synergism between LFS and CPEs. In this chapter, I presented a flux model that explains the synergism between both amphiphilic and non-amphiphilic CPEs by explaining how in each of these cases there is increased CPE penetration into the LTRs and non-LTRs of LFS-treated skin. This flux model was also able to explain why amphiphilic CPEs are expected to have a greater flux into the skin relative to non-amphiphilic CPEs, which in turn explains why amphiphilic CPEs are generally observed to have greater synergism with LFS treatment. Finally, in Chapter 5 I further studied the synergism between LFS and an amphiphilic CPE, sodium lauryl sulfate (SLS), albeit from the unique perspective of the effect of SLS on the skin structure when combined with LFS treatment. The findings show that, in spite of utilizing two types of skin permeability enhancers (chemical and physical), the inclusion of SLS in the coupling medium results in milder treatment with more reproducible and predictable enhancements in skin permeability. In the rest of this section, the major conclusions of this thesis will be discussed in more detail.

6.2 Major Thesis Conclusions

In Chapter 2, the aqueous porous pathway model was utilized to study the frequency dependence in pore size within LTRs and non-LTRs of LFS-treated skin. It was shown that the pore radii in the non-LTRs are independent of ultrasound frequency, ranging from 18.2 – 18.5 Å. In addition, it was determined that the pore radii in the non-LTRs are statistically significantly larger than the

values for the native skin samples (13.6 Å), suggesting that a frequency-independent enhancement process is at play in these skin regions. Additional experiments were carried out to quantify the amount of SLS penetrating into LTRs and non-LTRs relative to native skin, and it was found that nearly twice as much SLS penetrates into the non-LTRs per unit area than into untreated skin. Furthermore, by studying different mechanisms of SLS penetration into skin, it was shown that boundary-layer reduction caused by acoustic streaming is the most likely cause for the increased SLS uptake within non-LTRs. Therefore, recognizing that SLS itself can increase pore radii in the skin, it was concluded that a frequency-independent process, such as acoustic streaming, causes increased penetration of SLS into the skin, with SLS acting on the skin being the main contributor to the observed increase in pore radius. In the LTRs, it was observed that the pore radii increase dramatically with decreasing frequency (161 Å, 276 Å, and ∞ for 60 kHz, 40 kHz, and 20 kHz LFS, respectively). Accordingly, strong support was provided to the proposal that transient cavitation events near the skin surface, which are known to be frequency dependent, are the primary mechanism of skin permeability enhancement in LTRs. The variation of the skin radii with ultrasound frequency in the LTRs also suggests that transient cavitation microjets impinging on the skin surface can explain the observed changes in pore radii.

In Chapter 3, a fluorescent dye, sulforhodamine B (SRB), commonly used in LFS treatments, was studied first with regards to characterizing its amphiphilicity and then to quantify its effect on skin permeability enhancement with LFS. It was demonstrated that SRB is an amphiphilic molecule that preferentially adsorbs at an air/water interface, bringing about a considerable decrease in the surface tension of pure water (23 mN/m reduction). MD simulations revealed that

SRB is thermodynamically stable in its adsorbed state, both as monomers and dimers, with clearly defined head and tail regions as quantified by the hydration of its atomic groups, similar to conventional surfactants. Furthermore, SRB was shown to be able to incorporate into SLS micelles, which results in a dramatic decrease in the cmc of SLS. Because of its incorporation into SLS micelles, SRB was observed to have a significant shift in color and opacity in aqueous solution with increasing SLS concentration. MD simulations revealed that the SRB molecules reside mainly in the palisade layer of the SLS micelles. With respect to skin permeability enhancement with LFS treatment, SRB was shown to increase skin permeability significantly when combined with LFS treatment, acting as a CPE itself. However, when combined with SLS, SRB had an antagonistic effect. This was attributed to a decrease in the cmc of SLS and the growth of SLS micelles with the incorporation of SRB, leading to lower amounts of SLS delivered into the skin.

In Chapter 4, a physical mechanism that explains how LFS increases the transdermal uptake of CPEs was presented. Specifically, it was found that the origin of the observed synergism between LFS and CPEs is the ability of LFS to increase the penetration and dispersion of CPEs by direct deposition of CPEs into the LTRs of LFS-treated skin through the collapse of acoustic cavitation microjets. Moreover, amphiphilic CPEs were found to exhibit even greater synergism with LFS than non-amphiphilic CPEs because their flux into the skin is further enhanced by the adsorption of amphiphilic monomers to the surface of the cavitation bubbles. Therefore, in addition to a convective flux induced by the collapse of acoustic cavitation microjets that drives all CPEs, amphiphilic CPEs adsorbed to cavitation bubbles are also directly deposited into the skin. More modest increases in the uptake of CPEs into the non-LTRs of LFS-treated skin,

relative to untreated skin, were also observed and found to be consistent with the prediction of the flux model proposed.

In Chapter 5, the effect of SLS on skin perturbation, when utilized simultaneously with LFS, was investigated by treating two skin models, pig FTS and pig STS, with two treatment regimens, LFS/SLS and LFS, to reach a range of skin electrical resistivity levels. The LFS/SLS treatment was found to provide consistent extents of skin perturbation, as quantified using the log C and porosity-to-tortuosity (ε/τ) values obtained. Skin samples treated solely with LFS yielded less consistent results, where the log C values of the FTS and STS skin models were statistically significantly different. Additionally, the ε/τ values for LFS-treated skin samples were generally less than those for LFS/SLS-treated samples, suggesting that SLS acting on the skin creates more direct paths through the skin membrane by the disordering/fluidization of lipid bilayers, denaturation of keratin fibers, and expansion of lacunar regions. An analysis of the variability in the log P-log R linear regression parameters and log C values revealed greater variation in samples treated solely with LFS, resulting in lower r^2 values and broader confidence intervals for the regression parameters and log C values, with respect to LFS/SLS-treated samples. Additionally, the LFS-treated samples required 5-fold to 12-fold longer treatment times than the LFS/SLS-treated samples to reach similar skin electrical resistivity levels. Treatment times for the LFS/SLS-treated samples behaved predictably, decreasing monotonically with increasing skin electrical resistivity level, showing no significant difference in treatment times between FTS and STS samples at each of the skin electrical resistivity levels analyzed. On the other hand, LFS-treated samples were perturbed in a less predictable manner, with large variations and no statistical significance in treatment times between the skin electrical resistivity levels considered.

Therefore, it was concluded that SLS has a generally positive impact on skin structural perturbation when utilized in combination with LFS, compared to LFS treatment alone, by: (i) requiring equal, or less, skin perturbation (based on log C values) to reach similar skin electrical resistivity values (as reflected in the log C values), (ii) reaching similar skin electrical resistivity levels in much shorter treatment times (about an order-of-magnitude decrease in treatment times), and (iii) inducing skin perturbation in a significantly more reproducible and predictable manner.

6.3 Evaluation of the Current Prospects and Future Trends of Low-Frequency Ultrasound-Mediated Transdermal Delivery

The use of LFS has shown great promise in the transdermal delivery of therapeutics, including hydrophilic drugs and macromolecules. Since the initial investigations of transdermal delivery utilizing ultrasound frequencies between 20 and 100 kHz two decades ago, this technology has already spawned a number of startups, received FDA approval for the topical delivery of local anesthetics, and is currently being investigated for other clinical applications, such as skin permeabilization for non-invasive blood glucose monitoring. With this strong beginning, LFS-mediated transdermal delivery has the potential to gain an even stronger clinical foothold by exploiting the unique strengths of this technology. For example, LFS can be utilized for systemic, regional, and local delivery, with the ability to control the transdermal delivery profile of the active therapeutic compound by varying the ultrasound treatment parameters. Therefore, in addition to the systemic delivery of proteins, such as insulin, local delivery of drugs to treat skin disorders may be an area where LFS can exploit its ability to permeabilize skin in a controlled manner. This may be particularly relevant to skin disorders where the delivery of

active therapeutics through the skin represents a limiting transport step, and the number of side effects can be limited by localized therapy, such as in the case of psoriasis plaques.[1, 2]

Another application where LFS may be able to distinguish itself from other physical skin permeability enhancers is in the development of a closed-loop system for the monitoring of blood analytes and the subsequent delivery of appropriate therapeutics. The advancement of the cymbal array device by Smith *et al.*[3] has now opened the door to a wearable LFS device. Additionally, the feasibility of LFS for non-invasive blood-glucose monitoring has already been established.[4-6] Therefore, the technology necessary to create such a device already exists. Nevertheless, many obstacles still need to be overcome before a device is ready for use in the clinic. For example, potential challenges include the development of efficient algorithms involved in sensing and delivery (because there is a lag-time associated with both transdermal blood-glucose monitoring and the transdermal delivery of insulin, accurate predictions will be crucial), and in the design of a battery system that would be powerful enough to drive the LFS cymbal array, while still being small enough to allow for a wearable device.

A final exciting area where LFS could have a significant impact is in the field of transdermal vaccination. The feasibility of transdermally delivering high-molecular weight vaccines, such as tetanus toxoid, by LFS has already been established in *in vitro* and *in vivo* animal models.[7, 8] It is also known that targeting of the Langerhans cells in the skin can result in an enhanced immune response with respect to vaccine injection.[9, 10] However, in addition to allowing increased amounts of antigens to reach the Langerhans cells by increasing skin permeability, the LFS treatment itself has been shown to activate the Langerhans cells and elicit an immune

response.[7, 11] In fact, Tezel *et al.* have shown that the immune response induced by the delivery of 1.3 μg of tetanus toxoid (TT) to the Langerhans cells by LFS is equal to that of 10 μg of TT injected subcutaneously in mouse models.[7] Clearly, more research is needed to fully understand, characterize, and control this effect. This would involve not only studying delivery of antigens and the resulting immune response, but also the formulation of vaccines for delivery via the transdermal route. An additional variable that could also be studied is the addition of a co-enhancer during the LFS treatment, because it has been shown that the immune response elicited by tetanus toxoid can increase with the inclusion of SLS in the LFS coupling medium, although the response is not directly proportional to the SLS concentration.[8]

In addition to the specific areas discussed above, additional research is needed on the general safety of the technology. If a closed-loop device for glucose monitoring and insulin delivery is developed, long-term safety studies are necessary to determine whether repeated treatments with LFS are safe. Current safety studies have only been conducted for relatively short times (a maximum of 24 – 48 hours), and usually following only a single LFS treatment. Moreover, if drugs are to be systemically and repeatedly delivered by LFS, more research is needed into the reproducibility of skin permeability induced by the LFS treatments, both between different patients and after repeated treatments in a single patient. Additionally, further research on the generation of more uniform skin permeability enhancement would greatly benefit LFS treatments. Under current treatment protocols with SLS, only 5-25% of the skin surface treated by LFS contains LTRs, which are the skin regions through which the majority of transdermal transport occurs.[12] If one could increase the size of the LTRs to cover the entire skin surface treated, the area of skin treatment sites could decrease by up to 20-fold. This would result in

decreased power needed to operate the LFS device and aid in further miniaturization of a clinical device. For example, Paliwal *et al.* have recently shown that an aqueous mixture of 0.5% 3-(decyl dimethyl ammonio) propane sulfonate and polyethylene glycol dodecyl ether induced three times more LTR area than 1% SLS.[13] Therefore, research on cavitation enhancers for use with LFS, including more potent synergistic chemical enhancers, deserve further investigation.

In conclusion, LFS-mediated transdermal delivery of hydrophilic drugs and macromolecules shows great promise to address key needs in the medical field, such as developing a closed-loop system for tighter glycemic control, treating localized skin disorders, and transdermal vaccination. However, there are still opportunities to make technological and mechanistic advances with this technology that can increase its clinical utility. To reach the ultimate goal of positively affecting patients' lives, LFS researchers must focus on the unique advantages offered by LFS, including exploiting these advantages when investigating new treatments involving LFS.

6.4 Proposed Future Directions

6.4.1 Ultrasonic Transcutaneous Immunization (TCI) via a High-Throughput Approach

LFS has been shown to act as an adjuvant,[7] but still little is known about how immune response varies with ultrasound parameters and how to optimize the transdermal delivery of vaccines. The aims of this type of work would be to formulate better transdermal vaccines and to optimize skin treatments in order to create a platform for transdermal vaccination.

TCI would allow for the elimination of many safety concerns associated with needle usage, such as needle misuse and re-use, especially in developing or third-world countries.[14] Additionally, it has previously been shown that the amount of antigen required to generate a similar immune response is nearly an order-of-magnitude less with ultrasonic TCI than with injection, which could provide added safety benefits.[7] Furthermore, immunization via the transdermal route (targeting of Langerhans cells or dermal dendritic cells) generates both systemic (IgG and IgM) and mucosal (IgA) humoral immune responses, while injection-based vaccines produce only systemic immune response. Finally, utilizing physical (LFS) and chemical (CPE) stimuli to produce a biological signal (immune response) are not straightforward,[7] and better mechanistic understanding of these processes would undoubtedly result in a more rational design of TCI platforms.

The approach of this work could be to test different parameters associated with LFS-treatment prior to the application of different model antigens. First, LFS treatment parameters should be tested *in vitro*, to test for lead candidates. This would be followed by investigation of selected candidates with *in vivo* mouse models for immune response. The initial ultrasound parameters to be tested, in a combinatorial approach, include treatment time, intensity, duty cycle, tip displacement, and frequency. Additionally, the combination of LFS with specific CPEs, or a mixture of CPEs for synergistic effects, could also be tested. Because this entails a large number of experiments, it would be necessary to manufacture multi-cell diffusion arrays, to be used with multi-element ultrasound probes, which can be ordered in arrays as large as 96 elements commercially. Following treatment, skin samples would be exposed to model antigens (e.g.,

ovalbumin or tetanus toxoid) *in vitro* and the quantity of antigen present in the receiver compartment of the skin or penetrating into the skin quantified through fluorescence- or radio-labeling. This would allow for a high-throughput screening approach to identify lead treatment conditions for delivery of antigens. These candidate treatments could then be tested with *in vivo* mouse models, with various toxoids (e.g., tetanus, influenza, and hepatitis, among others) for immunological response by activation of the Langerhans cells and dermal dendritic cells, through fluorescently-labeled antibody techniques, and for antibody levels by using enzyme-linked immunosorbent assay (ELISA).[7]

6.4.2 Non-Invasive Local Delivery of Genetic Drugs and Therapeutics

Delivery of active therapeutics to treat skin disorders is often limited by the barrier properties of the skin, which does not allow for effective delivery of molecules larger than a few hundred Daltons in molecular weight or those that are hydrophilic in nature. Delivery is often further limited by the disorder itself, such as in the case of psoriasis, where over proliferation of the skin causes the formation of white, scaly plaques. In other cases, such as with melanomas, drugs must be delivered to deeper tissues of the epidermis or dermis, and therefore topical delivery is not always appropriate. Often, topical chemotherapy is only possible with small molecules, such as 5-fluorouracil (MW=130 g/mol). Conversely, larger or hydrophilic molecules require injection or IV administration for the necessary therapeutic effect to be achieved. These modes of administration can cause increased systemic side-effects, such as cardiotoxicity, and, for the case of injection, only allows for the administration of a bolus, which may provide sub-optimal delivery profiles.

Additionally, recent research has demonstrated that mutations in certain genes (e.g., B-Raf) can regulate protein synthesis and signaling cascades in melanomas.[15] Some of these complex signals, although not fully understood, are known to lead to cancer progression. However, by utilizing RNA interference, the activity of such genes can be decreased in a very specific manner. In fact, siRNA have been identified that target only mutations in B-Raf, and not the wild-type, which can lead to far fewer side-effects related to treatment.[15] Delivery of siRNA can be a significant challenge, however, as they are known to degrade quite rapidly in the body when not protected[16] and are generally too large to be administered topically through intact skin.[17] However, encapsulating siRNA and utilizing a controlled method of skin perturbation may allow for increased penetration of siRNA into the epidermal/dermal junction and dermis where melanoma and melanoma metastases occur. Furthermore, combination therapies of siRNA, to minimize cancer progression, with chemotherapeutics may allow for an improvement, or even synergism, in melanoma therapies.

The aim of this research would be to investigate the delivery of siRNA to melanomas in order to knockdown genes that encode for proteins (e.g. B-Raf) that promote cancer progression, including combination therapies of siRNA with chemotherapeutics, by developing and utilizing a dual-frequency ultrasonic transdermal delivery platform. In addition, a further application could be to increase the penetration of therapeutics, such as the anti-psoriatic drug methotrexate, into deeper tissue layers to treat diseases of the skin.

A multi-frequency ultrasound method could be developed to deliver nude active therapeutics or liposome encapsulated biologics (for the case of siRNA). Synthesis and loading of liposomes

with siRNA should initially be conducted according to previously published methods.[18] However, anti-psoriatic and chemotherapeutic agents could be delivered in initial experiments without encapsulation. Preliminary experiments would be conducted *in vitro*, with porcine skin. Skin samples would be initially treated with LFS (20-60 kHz), in order to increase the permeability of the skin. Parameters tested could include ultrasound frequency and intensity, as well as the composition of the coupling solution (e.g., inclusion of CPEs). Following skin perturbation by LFS, a coupling solution containing the active therapeutic would then be applied to the treated skin area and high-frequency ultrasound would be applied (1-3 MHz). High-frequency sonophoresis (HFS) can induce convective currents by acoustic streaming, which can lead to increased penetration of compounds into the skin, without appreciable degradation of compounds, as is the case with LFS. Therefore, the combination of LFS and HFS in-series should allow for increased penetration of therapeutics. After identification of the optimal treatment parameters for delivery of each drug type, the studies involving treatment of melanoma could be continued with *in vitro* melanoma-containing skin reconstructs in order to understand the response of the cancer to the identified treatments. If the skin reconstructs, grown from human melanoma and keratinocyte cell lines,[18] cannot mechanically withstand treatment by LFS, experiments could be continued with *in vivo* nude mouse models. Delivery and response studies with both chemotherapeutic agents and siRNA may be investigated, as well as combination therapies including both types of agents. For studies involving anti-psoriatic agents, preliminary experiments may involve experiments with an *in vitro* psoriasis model,[19] to test for efficacy of treatment. Further experimentation could be conducted with *in vivo* mouse psoriasis models.[20] For anti-psoriatic agents, a solely HFS treatment approach may also be tested, in addition to the combined LFS/HFS approach.

6.5 References

[1] B. Nickoloff, F. Nestle, Recent insights into the immunopathogenesis of psoriasis provide new therapeutic opportunities. Journal of Clinical Investigation 113(12) (2004) 1664-1675.

[2] V. Dubey, D. Mishra, T. Dutta, M. Nahar, D.K. Saraf, N.K. Jain, Dermal and transdermal delivery of an anti-psoriatic agent via ethanolic liposomes. Journal of Controlled Release 123(2) (2007) 148-154.

[3] N. Smith, S. Lee, E. Maione, R. Roy, S. McElligott, K. Shung, Ultrasound-mediated transdermal transport of insulin in vitro through human skin using novel transducer designs. Ultrasound Med Biol 29(2) (2003) 311-317.

[4] J. Kost, S. Mitragotri, R. Gabbay, M. Pishko, R. Langer, Transdermal monitoring of glucose and other analytes using ultrasound. Nat Med 6(3) (2000) 347-350.

[5] H. Chuang, E. Taylor, T. Davison, Clinical evaluation of a continuous minimally invasive glucose flux sensor placed over ultrasonically permeated skin. Diabetes Technol The 6(1) (2004) 21-30.

[6] H. Chuang, M. Trieu, J. Hurley, E. Taylor, M. England, S. Nasraway Jr, Pilot Studies of Transdermal Continuous Glucose Measurement in Outpatient Diabetic Patients and in Patients during and after Cardiac Surgery. J Diabetes Sci Technol 2(5) (2008) 595-602.

[7] A. Tezel, S. Paliwal, Z. Shen, S. Mitragotri, Low-frequency ultrasound as a transcutaneous immunization adjuvant. Vaccine 23(29) (2005) 3800-3807.

[8] A. Dahlan, H. Alpar, P. Stickings, D. Sesardic, S. Murdan, Transcutaneous immunisation assisted by low-frequency ultrasound. Int J Pharm 368(1-2) (2009) 123-128.

[9] J. Mikszta, J. Alarcon, J. Brittingham, D. Sutter, R. Pettis, N. Harvey, Improved genetic immunization via micromechanical disruption of skin-barrier function and targeted epidermal delivery. Nat Med 8(4) (2002) 415-419.

[10] P. Karande, S. Mitragotri, Transcutaneous immunization: an overview of advantages, disease targets, vaccines, and delivery technologies. Annu Rev Chem Biomol Eng 1 (2010) 175-201.

[11] C. Scarponi, F. Nasorri, F. Pavani, S. Madonna, R. Sestito, M. Simonacci, O. De Pità, A. Cavani, C. Albanesi, Low-Frequency Low-Intensity Ultrasounds Do Not Influence the Survival and Immune Functions of Cultured Keratinocytes and Dendritic Cells. J Biomed Biotechnol (2009).

[12] B.E. Polat, P.L. Figueroa, D. Blankschtein, R. Langer, Transport pathways and enhancement mechanisms within localized and non-localized transport regions in skin treated with low-frequency sonophoresis and sodium lauryl sulfate. J Pharm Sci 100(2) (2011) 512-529.

[13] S. Paliwal, M. Ogura, S. Mitragotri, One-step acquisition of functional biomolecules from tissues. P Natl Acad Sci USA 107(33) (2010) 14627.

[14] M. Prausnitz, R. Langer, Transdermal drug delivery. Nat Biotechnol 26(11) (2008) 1261-1268.

[15] A. Sharma, N.R. Trivedi, M.A. Zimmerman, D.A. Tuveson, C.D. Smith, G.P. Robertson, Mutant V599EB-Raf Regulates Growth and Vascular Development of Malignant Melanoma Tumors. Cancer Res 65(6) (2005) 2412-2421.

[16] D.H. Kim, J.J. Rossi, Strategies for silencing human disease using RNA interference. Nat Rev Genet 8(3) (2007) 173-184.

[17] G.M.M.E. Maghraby, A.C. Williams, B.W. Barry, Can drug-bearing liposomes penetrate intact skin? J Pharm Pharmacol 58(4) (2006) 415-429.

[18] M. Tran, R. Gowda, A. Sharma, E. Park, J. Adair, M. Kester, N. Smith, G. Robertson, Targeting V600EB-Raf and Akt3 using nanoliposomal-small interfering RNA inhibits cutaneous melanocytic lesion development. Cancer Res 68(18) (2008) 7638.

[19] J. Jean, M. Lapointe, J. Soucy, R. Pouliot, Development of an in vitro psoriatic skin model by tissue engineering. J Derm Sci 53(1) (2009) 19-25.

[20] H.-L. Ma, S. Liang, J. Li, L. Napierata, T. Brown, S. Benoit, M. Senices, D. Gill, K. Dunussi-Joannopoulos, M. Collins, C. Nickerson-Nutter, L.A. Fouser, D.A. Young, IL-22 is required for Th17 cell-mediated pathology in a mouse model of psoriasis-like skin inflammation. J Clin Invest 118(2) (2008) 597-607.